Exploring the role of polymers in scaling up the manufacturing of solid-state batteries

Ronan Chometon

Sorbonne Université

Laboratoire de Chimie de la Matière Condensée de Paris

Ecole doctorale - ED 397 - Physique et Chimie des Matériaux

Collège de France

Laboratoire de Chimie du Solide et Energie

Blue Solutions

Convention CIFRE

Exploring the role of polymers in scaling up the manufacturing of solid-state batteries

Ronan CHOMETON

Doctoral thesis in Physics and Chemistry of Materials

Directed by Christel Laberty-Robert and Jean-Marie Tarascon

Presented and defended in public on 23rd April 2024 in front of the jury,

Dr. Cristina Iojoiu	Research director, LEPMI, Université Grenoble-Alpes	President Referee
Pr. Marnix Wagemaker	Professor, SEE, TU Delft	Referee
Dr. Felix H. Richter	Group leader, Justus-Liebig Universität Gießen	Examiner
Dr. Florencia Marchini	Senior Project Manager, Umicore	Examiner
Dr. Anthony Bonnet	Director Materials for Energy, Arkema	Examiner
Pr. Christel Laberty-Robert	Professor, LCMCP, Sorbonne Université	Director
Pr. Jean-Marie Tarascon	Professor, CSE, Collège de France	Director
Dr. Marc Deschamps	Director Electrochemistry, Blue Solutions	Supervisor

Sorbonne Université

Laboratoire de Chimie de la Matière Condensée de Paris

Ecole doctorale - ED 397 - Physique et Chimie des Matériaux

Collège de France

Laboratoire de Chimie du Solide et Energie

Blue Solutions

Convention CIFRE

Le rôle des polymères dans les batteries tout-solide et leur mise à l'échelle

Ronan CHOMETON

Thèse de doctorat en Physique et Chimie des Matériaux

Dirigée par Christel Laberty-Robert et Jean-Marie Tarascon

Présentée et soutenue publiquement le 23 Avril 2024 devant un jury composé de

Dr. Cristina Iojoiu	Directrice de recherche, LEPMI, Université Grenoble-Alpes	Présidente Rapporteuse
Pr. Marnix Wagemaker	Professeur, SEE, TU Delft	Rapporteur
Dr. Felix H. Richter	Group leader, Justus-Liebig Universität Gießen	Examinateur
Dr. Florencia Marchini	Senior Project Manager, Umicore	Examinatrice
Dr. Anthony Bonnet	Directeur Matériaux pour l'énergie, Arkema	Examinateur
Pr. Christel Laberty-Robert	Professeure, LCMCP, Sorbonne Université	Directrice
Pr. Jean-Marie Tarascon	Professeur, CSE, Collège de France	Directeur
Dr. Marc Deschamps	Directeur Electrochimie, Blue Solutions	Superviseur

Acknowledgements

First and foremost, I would like to express my most sincere gratitude to Professor Christel Laberty-Robert, for these three and a half exciting years. Your supervision helped me to go through the intricate adventure of the PhD, thanks to your continuous availability, your trust, your scientific expertise, and your always kind guidance.

I surely am more than grateful to Professor Jean-Marie Tarascon for welcoming me in his laboratory, at Collège de France. Over these years, you transmitted your passion for science through your guidance, high standard and frankness.

I wish to convey my appreciation to Marc Deschamps for his supervision, trust and advice, and Blue Solutions for funding this work through the CIFRE program.

Overall, I want to deeply thank my supervisors for their collaboration as a team and for the precious freedom they gave me to explore, fail and succeed, which undoubtedly helped me build confidence over these years. I am glad to continue research with all three of you on another thrilling scientific journey.

I wish to thank Cristina Iojoiu and Professor Marnix Wagemaker for willing to undertake the task of refereeing this thesis. I also thank Felix Richter, Florencia Marchini and Anthony Bonnet for agreeing to be part of the jury.

This thesis would not have been the same without the great help of Professor Michaël Deschamps in carrying out the NMR experiments, which was initiated with Professor Christel Gervais and Cristina Coelho. I also thank Christophe Méthivier for the XPS analysis, Jacques Louis for the help with XRD measurements, Elisa Quemin for making impedance spectroscopy a bit less complicated to me, Benjamin Hennequart for many discussions regarding solid-state batteries (with Elisa), Arnaud Perez for pertinent advice, Jessica Duvoisin for her invaluable administrative support and finally, Romain Dugas for all his help with both engineering and scientific problems.

For their warm welcome in Blue Solutions, I thank Nour Daher, Jonathan Szymczak, Patrick Leblanc and Margaud Lécuyer.

I wish to thank Francois Ribot and Christian Bonhomme for welcoming me in LCMCP, and Hélène Gervais, Corinne Pozzo di Borgo and Diana Lesueur for their help.

The PhD journey would not have been as enjoyable without my amazing colleagues and now friends Elisa and Benjamin. I have been lucky to be part of the solid-state team with you and other past and present members: Romain, Tuncay, Wei, Maria, Horyung and Florencia. I do not forget my office mates and all the funny discussions: Elisa, John, Juan, Zhenying, Aleksandra, Xu, Tatjana, Bernard and others. Special mentions for Ivette, Damien, Alexia, Elisa G., Clémence, Gwen, Laura, Elisabeth, Conrad, Florian, Cédric, Simon and to all the former, current and future CSE lab members. I do not forget my wonderful colleagues at LCMCP and especially in the RMES team: Agathe, Thibaut, Léna, Adeline, Milad, Kethsovann, Morgan, and others.

Enfin, je terminerai en français pour remercier chaleureusement mes amis, avec qui pour certains nous avons partagé les hauts et les bas de la vie de thésard. Bien sûr, mes colocs Jacques, Jules D. et M., Baptiste, qui m'ont supporté au quotidien ces trois ans et demi.

A mes parents pour leur soutien inconditionnel tout au long de mes études et plus généralement, dans la vie. A mes frères et ma sœur, qui me rendent fier.

Une pensée toute particulière pour mes grands-parents, et à leur encouragement, d'où qu'ils soient.

Enfin, à Jordane, merci pour tout.

Table of contents

Broader context

In the late 18th century, the Industrial Revolution marked a milestone in human history, igniting an era of unprecedented economic growth and major technology advancements. The widespread adoption of fossil fuels, initially coal and subsequently oil and natural gas, supplied the rapid expansion of industry and transportation, thanks to their energy density (around 50 $MJ.kg^{-1}$ for oil and natural gas versus 1 $MJ.kg^{-1}$ for a standard lithium-ion battery)[1], cost-effectiveness, abundance and ease-of-use. In a world driven by economic growth, contemporary societies became increasingly reliant on the combustion of fossil fuels. This dependence has been causing a concerning surge of anthropogenic greenhouse gas (GHG) emissions (**Figure 0.1b**), whose unequivocal consequence is the ongoing global temperature rise, currently of 1.1°C compared to 1850-1900 period (**Figure 0.1a**). The most recent report from the International Panel on Climate Change (IPCC)[2] predicts a temperature increase from 1.5 to more than 4°C by the end of the century, depending on the present and future policies and the resulting intensity of GHG emissions mitigation (**Figure 0.1c**).

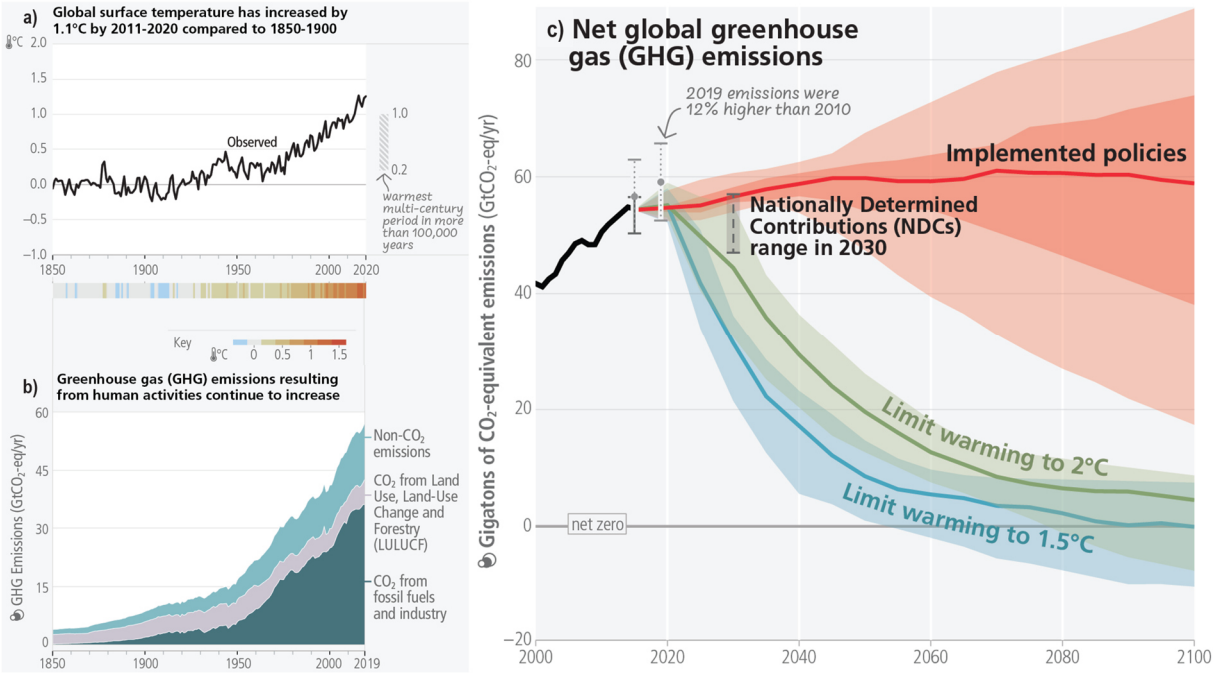

Figure 0.1 (a) Global surface temperature from 1850 to 2020 (b) Global net anthropogenic GHG emissions including CO_2 from fossil fuel combustion and industrial processes (dark green); net CO2 from land use, land-use change and forestry (grey); CH4; N2O; and fluorinated gases (light blue). (c) Projected global GHG emissions depending on the followed mitigation scenario (blue and green) compared to currently adopted policies (red). Adapted from IPCC's AR6 Synthesis report[2]

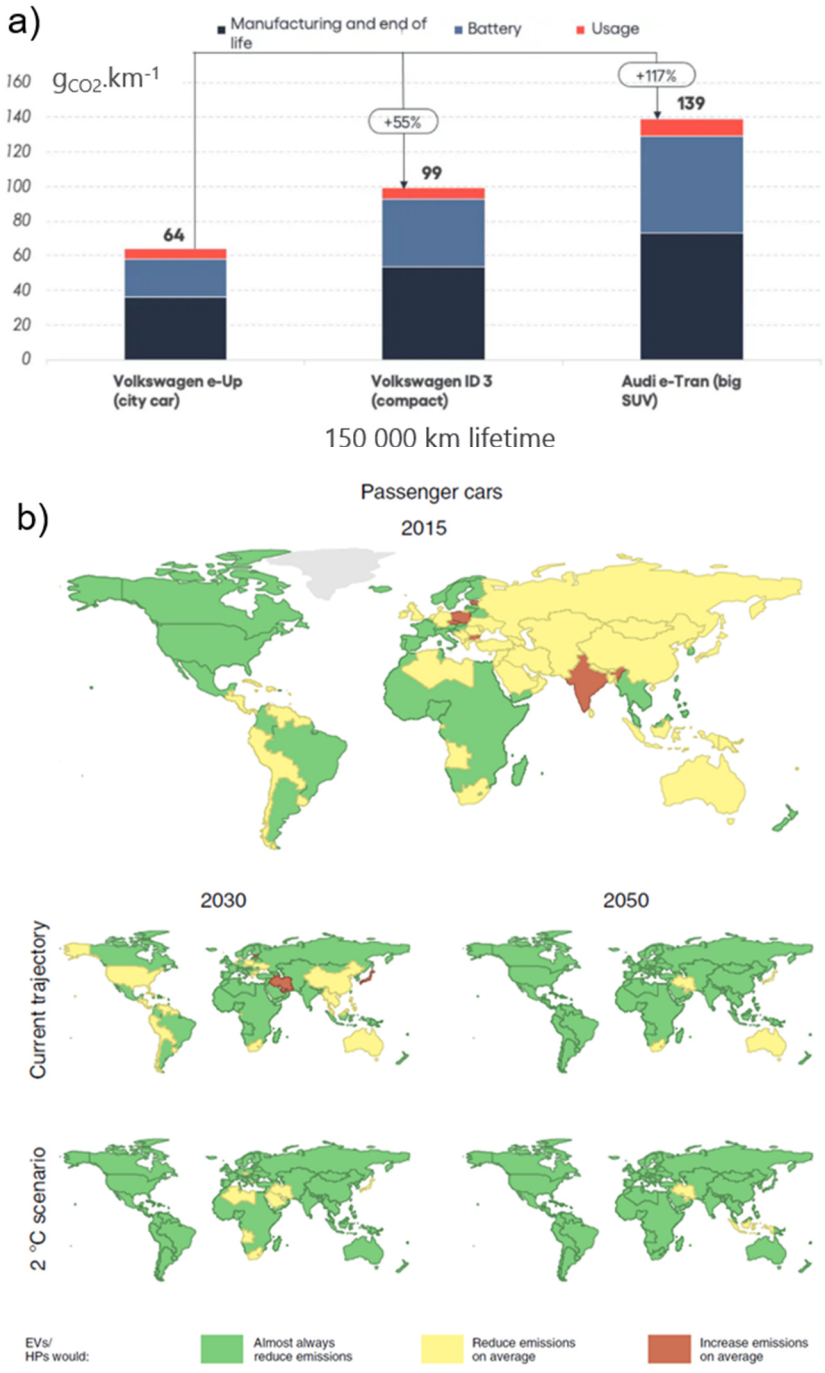

Figure 0.2 (a) Average carbon footprint of EVs in France depending on the model.[3] (b) Relative GHG emission intensities of EVs around the world.[4]

These policies consistently endorse a rapid transition from carbon-intensive to low-carbon and renewable sources of energy, such as wind and photovoltaics, which are already economically competitive when compared to fossil fuels[2]. Additionally, the IPCC strongly recommends electrifying transportation, which still overwhelmingly relies on combustion engines. However, it is crucial to bear in mind that the local electrical mix directly affects the

carbon footprint of electrical vehicles (EV), as well as the size and weight of the vehicle (**Figure 0.2a**). Even though the transition to low-carbon energy sources may be slow, a faster adoption of EVs would lead to a quasi-systematic reduction of GHG emissions throughout the world in the near future (2030 to 2050 – **Figure 0.2b**). In both sectors, the ongoing revolution relies on our capacity to store generated electricity in a sustainable, cost-effective, and reliable manner. The grid management already relies on various energy-storage systems (ESS), such as electrical, mechanical, thermal and electrochemical devices, to ensure flexible and steady power supply. Among them, electrochemical ESS, which convert chemical energy into electricity, have become indispensable, especially lithium-ion batteries. Thanks to fifty years of continuous development, their high energy density (250 – 300 $Wh.kg^{-1}$) and competitive cost (150$.kWh^{-1} in 2022)[5] makes them today a decisive asset towards the necessary electrification of transportation and energy supply. The ever-increasing demand of batteries calls for a diversification of technologies in order to meet different requirements for different applications. Large-scale storage requires cheaper and long-lasting batteries (e.g. lithium iron phosphate – LFP chemistry or secondary use of EV batteries), while EVs market pushes for devices with higher energy density and enhanced safety (e.g. nickel manganese cobalt NMC chemistry or solid-state batteries). This thesis therefore aims to contribute towards the development of solid-state batteries, as outlined below.

Thesis outline

This thesis will specifically focus on exploring the role of polymers as a binder in inorganic-based solid-state batteries and their potential for scaling up their fabrication. This work is structured in four chapters as detailed below:

Chapter 1 introduces the paradigm shift from established lithium-ion technology to solid-state batteries, examining the diverse landscape of solid electrolytes and their chemo-mechanical properties. It emphasises the importance and challenges of scaling up manufacturing processes for practical implementation, exploring the potential of hybrid solid electrolytes, as well as the role of non-conductive binders.

Chapter 2 concentrates on the development of a specific hybrid solid electrolyte, based on PEO:LiTFSI and Li_6PS_5Cl, to prepare self-standing solid-state separators. The optimisation of formulation gives insights into the complex conduction mechanism, supported by additional characterisation of the resulting interphase.

Chapter 3 focuses on the integration of PVDF-HFP as non-conductive binder to prepare sheet-type electrodes and separators, via a tape-casting method. The meticulous optimisation of the fabrication process, giving promising results, paves the way for assembling self-standing solid-state batteries.

To conclude, **Chapter 4** provides a comprehensive summary of the findings from this thesis and offers valuable insights and guidance for future research to build upon the work presented in this study.

Chapter 1 – General introduction towards scaling up solid-state batteries manufacturing

1.1 – From lithium-ion to solid-state batteries: prospects and challenges

The inception of electrochemical storage dates to the year 1800 when Alessandro Volta pioneered the first battery known as the Voltaic Pile.[6] This device, composed of zinc and copper electrodes immersed in brine, utilised a chemical reaction for the storage and delivery of electric charges. Subsequent systems, including the Daniel cell[7] with its copper-zinc configuration in sulphuric acid, were fundamentally primary batteries, designed for single use. A significant breakthrough occurred in 1859 when Gaston Planté introduced the lead-acid battery[8]. This design featured lead and lead dioxide electrodes in sulphuric acid, marking the world's first rechargeable battery. Remarkably, the lead-acid battery remains in use today, primarily in the automotive industry, standing as the pioneering secondary battery. Various chemistries were explored throughout the 20th century, including nickel-cadmium, alkaline, and nickel metal-hydride. However, it was not until the 1970s that the lithium-ion technology emerged.

1.1.1 Principles of secondary batteries operation

A battery primarily consists of three essential features: a positive electrode (cathode), a negative electrode (anode), both immersed in an electrolyte. The electrolyte serves the crucial function of conducting ions while remaining insulative to electrons. The electrons circulate through the external electrical circuit connected to both electrodes. During operation, electrochemical reactions occurring at the electrodes modify the thermodynamics of the cell. The overall voltage U can be evaluate through the Nernst equation at each electrodes:

$$x\mathrm{Ox} + ne^- \leftrightarrow y\mathrm{Red} \qquad \textbf{Equation 1.1}$$

$$E_{electrode} = E^\circ{}_{electrode} - \frac{RT}{nF} \cdot \ln \frac{a_{\mathrm{Red}}^{y}}{a_{\mathrm{Ox}}^{x}} \qquad \textbf{Equation 1.2}$$

$$U = E_{cathode} - E_{anode} \qquad \textbf{Equation 1.3}$$

In secondary batteries, the reactions taking place at the electrodes are reversible, enabling the system to store (charge) and release (discharge) energy depending on the direction of electron flow. Each electrode is characterised by its energy storage capability, also known as the specific capacity (Q). It is defined as the theoretical amount of charged species that the electrode can store or release in the active material (AM), as expressed below:

$$Q = \frac{z \cdot F}{3600 \cdot M_{AM}} \text{ ; in } Ah.g^{-1} \quad \textbf{Equation 1.4}$$

where z is the number of electrons involved in the electrochemical reaction, $F = 96485\ C.mol^{-1}$ the Faraday constant and M_{AM} the molecular mass of the AM. From these figures, the amount of energy stored in the battery can be calculated. Gravimetric and volumetric energy densities (E) are determined by multiplying the specific capacity by the cell voltage and are expressed per unit of weight ($Wh.kg^{-1}$) and per unit of volume ($Wh.L^{-1}$), respectively.

$$E = Q \cdot U \quad \textbf{Equation 1.5}$$

Energy density stands as the primary metric that researchers and industry professionals continually seek to maximise in batteries. However, various other metrics are crucial to evaluating the performance of such system, including power density, calendar life, safety, cost, and environmental footprint, among others. To grasp an understanding of the incremental advancements in secondary batteries, subsequent sections will delve into the recent history of the most widely used Li-ion technology and the shift towards "next-generation" solid-state batteries.

1.1.2 Developments of the lithium battery technology

Lithium (Li) is very attractive for electrochemical storage as the lightest solid element of the periodic table (6.94 g.mol^{-1}), with the lowest electrochemical potential ($E°_{Li^+/Li}$ = -3.04V versus Standard Hydrogen Electrode – SHE) and one of the highest theoretical capacity (3862 mAh.g^{-1}). In the 1970s, research into lithium-based materials gained significant momentum, with M. Stanley Whittingham's discovery of titanium disulphide (TiS_2), a chalcogenide intercalation compound.[9–11] This lithium-free layered compound is able to insert lithium ions without significant change in its crystallographic structure.

At cathode $TiS_2 + Li^+ + e^- \rightleftarrows LiTiS_2$ **Equation 1.6**

At anode $Li \rightleftarrows Li^+ + e^-$ **Equation 1.7**

It was employed as a positive electrode, combined with Li-metal as the negative electrode, to form the first rechargeable lithium battery. Even though the industrial development initiated

with ExxonMobil was stopped due to severe oil price drop at that time, others continued to believe in the Li-metal battery. Until 1989, Moli Energy Ltd. exploited the Canadian natural resources of molybdenum disulphide (MoS_2), a similar compound to TiS_2, to produce the first Li-metal based battery.[12] Despite a commercial success with Japanese electronics manufacturers, safety issues of fire and explosion sealed the fate of this technology, ultimately resulting in a comprehensive product recall. The primary reason was identified as short-circuits arising from the uncontrolled growth of whisker-like structures on the lithium metal anode. In 1980, John B. Goodenough played a pivotal role by introducing lithium cobalt oxide ($LiCoO_2$ - LCO) as a cathode material[13], providing higher cell potential (around 4V vs Li^+/Li) given the greater electronegativity of oxygen compared to sulphur, as well as improved air stability compared to TiS_2. To address the lingering safety concerns linked with Li-metal, the concept of Li-insertion chemistry was extended to the anode, an idea originally proposed by Michel Armand[14] and realised by Bruno Scrosati with the "rocking chair" cell.[15] In 1983, Akira Yoshino published a decisive work in which he combined LCO with petroleum coke to build a cell based on the "rocking chair" concept.[16]

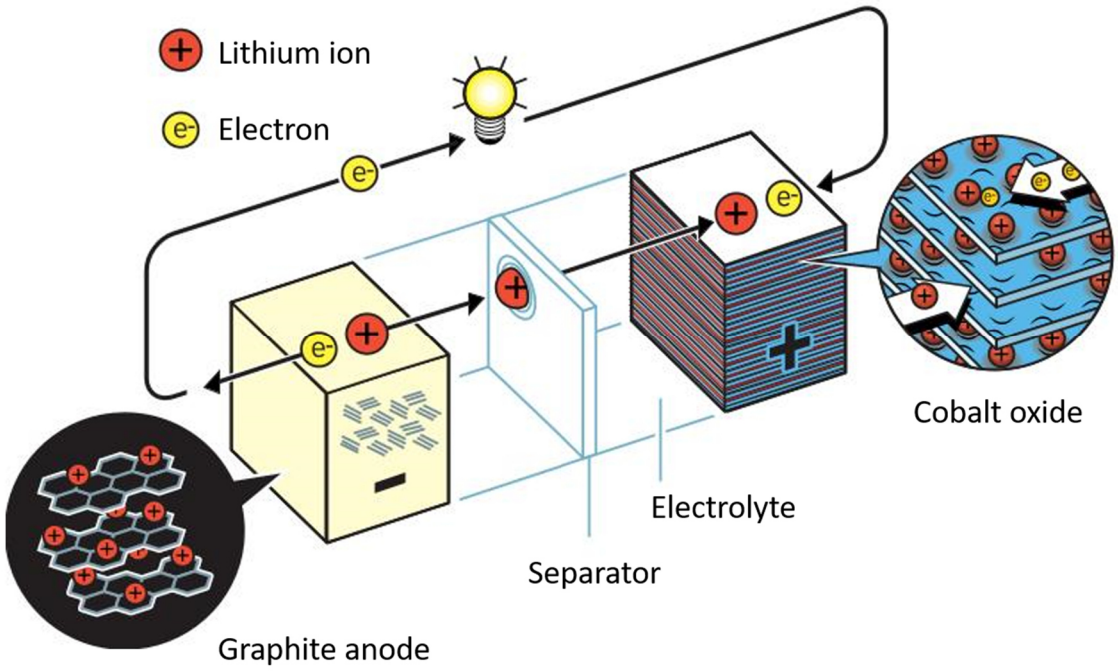

Figure 1.1 Scheme of the typical lithium-ion battery based on LCO at the cathode and graphite at the anode. Adapted from reference.[17]

Further improvement of the anode made possible the use of graphite[18] and ethylene carbonate-based electrolyte[19], resulting in a stable and safer battery. This research led to the commercialization of the first lithium-ion battery (LIB) by Sony in 1991 (**Figure 1.1**).

At cathode $LiCoO_2 \rightleftarrows Li_{1-x}CoO_2 + xLi^+ + xe^-$ **Equation 1.8**

At anode $C_n + xLi^+ + xe^- \rightleftarrows Li_xC_n$ **Equation 1.9**

In the pursuit of better batteries, the research community has been working over the following decades to improve the specific capacity and the stability of cathode materials. Significant progress has been achieved in the layered oxide cathodes family through the partial substitution of cobalt in LCO to other transition metals such as nickel and manganese. High-nickel content cathodes, especially NMC622 ($LiNi_{0.6}Mn_{0.2}Co_{0.2}O_2$) and NMC811 ($LiNi_{0.8}Mn_{0.1}Co_{0.1}O_2$), have gained widespread adoption in the LIB industry.[20] Compared to LCO (140 mAh.g^{-1}), they offer increased practical specific capacity (180 – 200 mAh.g^{-1}), lower cost, and contribute to addressing ethical concerns associated with cobalt sourcing.[21] Simultaneously, alternative compounds have been developed to eliminate the need for cobalt, including the spinel $LiMn_2O_4$ (LMO) and the polyanionic $LiFePO_4$ (LFP).[22,23] LFP, owing to its environmentally friendly attributes and the abundance of its source materials, has emerged as a strong competitor to NMC cathodes in the electric vehicle (EV) industry, where cost reduction is a major driving force.[20] Another primary target of the industry is the maximization of the cell energy density. After years of development, LIBs have reached energy densities of approximately 300 to 350 Wh.kg^{-1} at the cell level, approaching their theoretical limits. Achieving further improvements necessitates a shift in paradigm. One approach involves substituting the graphite anode with alloy anodes, such as silicon, deviating from the conventional rocking-chair concept. Silicon can alloy with up to 4.4 Li per Si and delivers a remarkable theoretical specific capacity of 4200 mAh.g^{-1}.[24] However, it undergoes unavoidable mechanical degradation due to substantial volume change (exceeding 300%), resulting in a poor capacity retention over cycling.[25] The alternative approach involves the use of the original lithium metal anode to take advantage of its exceptional specific capacity. The need for systems that can prevent the growth of dendrites and ensure safety of Li metal anode has brought solid-state batteries into the spotlight, along with the expectations associated with this technology.

1.1.3 Shifting to solid-state batteries: a change of paradigm

○ Expected benefits of solid-state batteries

The underway adoption of batteries in the field of transportation and energy storage intensifies the aspiration for safer, high energy density and long-lasting systems. In this context, solid-state batteries (SSBs) have caught the attention of the academic and industrial communities as they offer several potential gains. The substitution of the flammable organic liquid electrolyte with a solid ionic conductor has the potential to address the prime safety concern of LIBs, which is the fire hazard due to electrolyte leakage.[26] Moreover, the solid characteristic of the electrolyte may pave the way for the resurgence of the lithium metal anode, acting as barrier to dendrites. Thanks to the exceptional specific capacity of lithium metal, SSBs could offer a significantly increased theoretical energy density compared to LIBs (350 – 400 $Wh.kg^{-1}$)[27] (**Figure 1.2**). Theoretical calculation predict a 70% increase in volumetric energy density and a 40% higher gravimetric energy density.[28] Additionally, SSBs are expected to exhibit improved cycling kinetics, as ceramic electrolytes provide a Li^+ transference number of one[29], eliminating concentration polarization, a phenomenon typically observed in liquid systems with mobile anions.

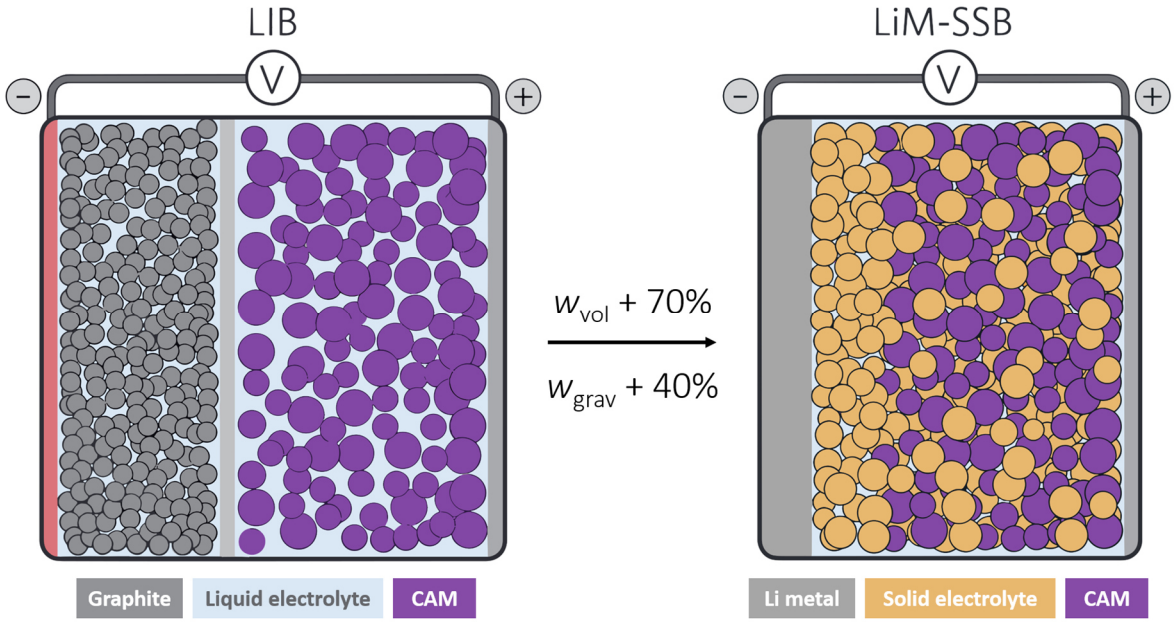

Figure 1.2 Schematics of a typical lithium-ion battery (LIB) based on liquid electrolyte (left) compared with a lithium metal solid-state battery (LiM-SSB) based on solid electrolyte (right). Adapted from reference.[28]

In addition to the previously mentioned benefits of SSBs, this technology could offer other potential attributes, such as the suppression of the chemical crosstalk between electrodes[28], thereby extending the operating lifespan. The adjustable chemistry of solid electrolytes (SEs – oxide, sulphide, halide or polymer) opens the perspective of using high voltage (up to 5V vs Li^+/Li) cathode active materials (CAM) and operating in a wider window of temperature, enhancing energy density and safety respectively.[28,30] Another possible improvement lies in the ability to design the cell based on the concept of bipolar stacking.[31] This approach will be discussed later in section **1.3.2**. Despite the enthusiasm sparked by the potential performances improvement, several challenges persist before practical SSBs realisation, including the enhancement of the SE's characteristics, the stability of the interfaces and the process of assembly.

○ Remaining challenges for solid-state batteries realisation

SSBs are governed by solid-solid interfaces, which give rise to most of the challenges associated to their realisation (**Figure 1.3**). In these complex systems, chemistry and mechanics are closely intertwined and (electro-)chemical events can produce a mechanical response, and *vice versa*.[32] On the anode side, it is challenging to form and maintain an adequate contact between the lithium metal and the solid electrolyte separator. In particular, both interfacial voids[33,34] and lithium dendrites[35–37] can form during cycling, leading to cell instability. Additionally, most of SEs are not stable against the low potential of lithium metal[38], which can affect the electrochemistry and the wetting at the interface. In the separator layer, the ease of Li^+ transport is highly dependent on the interparticle contact and its stability during operation, as porosity and cracking hinder the conduction between the electrodes. SEs are also susceptible to degradation depending on the conditions of separator manufacturing, such as moisture traces in the working environment[39] and solvent processing of the material.[40] Last but not least, the cathode composite presents several challenges in achieving a functional SSB. The Li^+ transfer during charge and discharge can be obstructed by contact loss due to the CAM internal volume change upon (de-)lithiation.[41,42] The SE electrochemical instability at high voltage is another factor impeding ionic exchange in the cathode.[43] The arrangement of CAM and SE particles determines the tortuosity of the composite, a critical factor that describes the accessibility of CAM particles.[44]

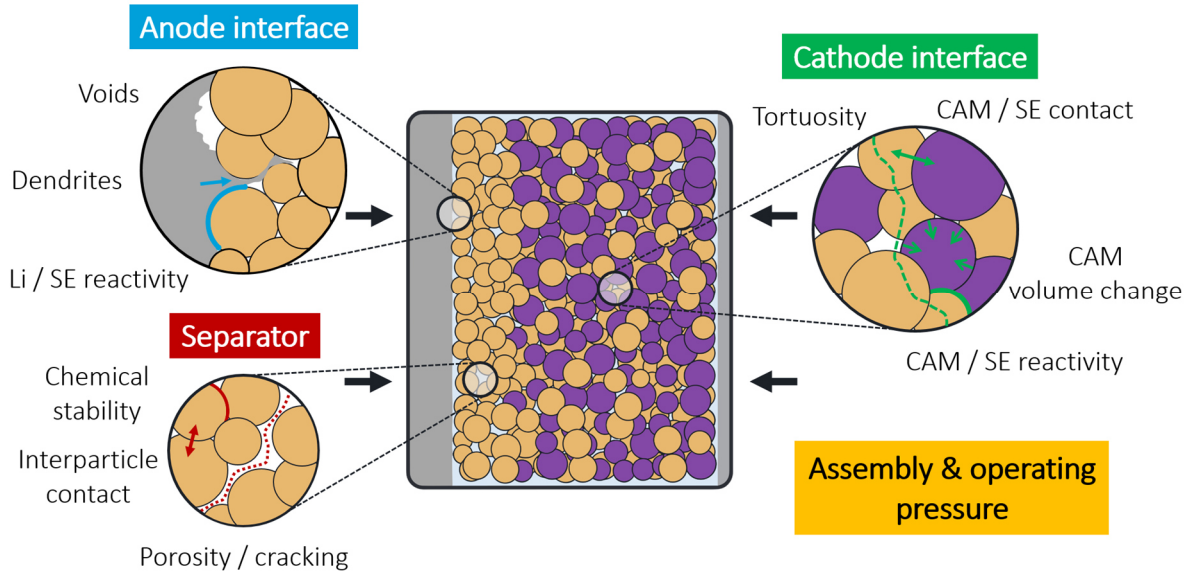

Figure 1.3 Illustration of the recurring challenges for SSB development. Adapted from reference.[28]

Since solid-solid contacts constitute the core of SSB mechanisms, pressure during both assembly and operation is a key parameter that can either mitigate or contribute to the previously described issues.[45] Reaching sufficient interparticle contact is typically achievable by applying high external pressure (in the order of 100 MPa) to the cell[46], but this is incompatible with the use of lithium, a soft metal prone to creeping within the porosity and causing a mechanically induced short-circuit.[47] Operating SSBs at more reasonable pressures (in the order of 1 MPa) is imperative for the practical implementation of this technology.

1.2 – The journey towards better solid electrolytes

1.2.1 Solid electrolytes: their properties and own particularities

Selecting the appropriate SE is paramount when realizing a SSB, as most of the previously mentioned challenges arise from its (electro-)chemical or mechanical properties. Intensive research in the field of solid ionic conductors, driven by the pursuit of a functional SSB, has resulted in the development of a diverse range of SEs over the years.

Going back to the early 19th century, Michael Faraday was the first to observe ionic mobility in a solid, which were Ag_2S and PbF_2 in heated state.[48] Highlighting some pivotal milestones, β-alumina stands out as the first fast ionic conductor for several cations (Li^+, Na^+, K^+, H_3O^+, Ca^{2+}, Mg^{2+}), but it was soon discarded for SSB development due to its brittleness.[49] John B. Goodenough played also a major role in the SSB field by introducing the NASICON-

type electrolytes (Sodium SuperIonic CONductor) in 1976 - $Na_{1+x}Zr_2Si_xP_{3-x}O_{12}$, $0 \leq x \leq 3$.[50] Another key discovery was brought to light by Peter V. Wright in 1973 and Michel Armand in 1978 when the first one observed ionic conductivity by dissolving alkali metal salts in poly(ethylene oxide) (PEO)[51], and the second build a SSB with this polymer electrolyte.[52] With the pace of new discoveries accelerating, a natural categorisation emerged, classifying most-used SEs in four different families. These includes the inorganic families composed of oxides, sulphides and halides, and the organic family, which encompasses all the polymer-based electrolytes.

To meet the expectations of SSBs, a SE has to fulfil several requirements: a high lithium ionic conductivity at room temperature (> 10^{-3} S.cm^{-1}), a negligible electronic conductivity, a large electrochemical stability window (0 – 5 V versus Li^+/Li at best), good chemical stability against the CAM, lithium metal and moisture, and facile processing properties. Each family exhibits its own strengths and weaknesses (**Figure 1.4**).

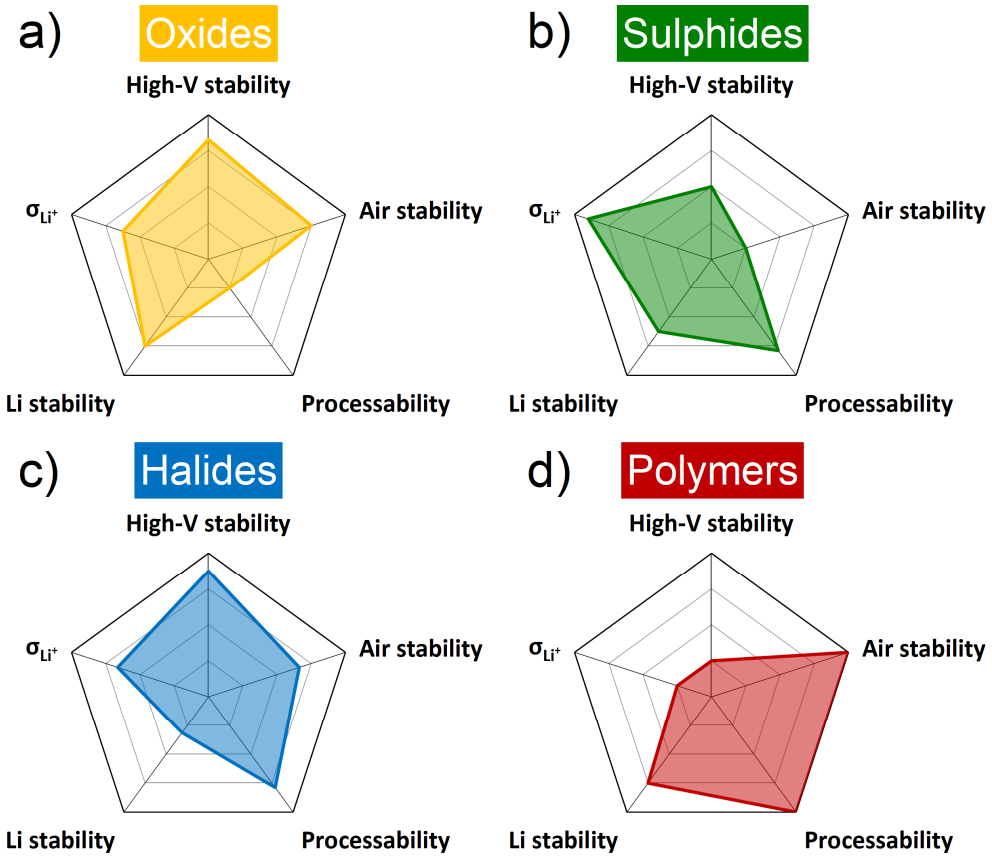

Figure 1.4 Spider charts comparing SEs requirements in the four families. Adapted from reference[53]

The **oxide** SEs family expanded by deriving the early introduced NASICON structure to Li-conducting materials, such as $Li_{1+x}Al_xTi_{2-x}(PO_4)_3$ (LATP)[54] and $Li_{1+x}Al_xGe_{2-x}(PO_4)_3$ (LAGP)[55], which displays high ionic conductivities (around 10^{-3} S.cm^{-1}). In parallel, perovskite-type and garnet-type compounds were also successfully developed, with $Li_{3x}La_{2/3-x}TiO_3$ (LLTO)[56] and $Li_7La_3Zr_2O_{12}$ (LLZO)[57] respectively. Oxide-based ionic conductors often demonstrate significant assets in terms of moisture and thermal stability, and exhibit a broad electrochemical stability window.[58] Therefore, they are good candidates for utilization with high-voltage CAM and lithium metal anode. Regarding their synthesis, they can usually be prepared in open-air atmosphere but require very high sintering temperature (> 1000°C) to attain their final ionic conductivity, by reducing the grain boundary resistivity.[59] Overall, their mechanical rigidity (E = 150 GPa and H = 6 GPa for LLZO)[60] poses a challenge for integration into SSBs, primarily due to the difficulty of creating optimised interfaces under practical processing conditions.

Sulphide-based ionic conductors have their roots in the development of glassy Li_2S-P_2S_5 and its counterparts, which exhibit around 10^{-4} S.cm^{-1} in room temperature (RT) ionic conductivity.[61] The early 21st century witnessed a significant advancement thanks to Ryoji Kanno and his group, when they introduced the thio-LiSICON SEs family (Lithium SuperIonic CONductors) $Li_xM_{1-y}M'_xS_4$ (M = Si, Ge and M' = P, Al, Zn, Ga, Sb).[62–64] This family demonstrated an improved ionic conductivity, reaching around 10^{-3} S.cm^{-1}. A ground-breaking discovery occurred in 2011, when they introduced $Li_{10}GeP_2S_{12}$, displaying an ionic conductivity of 10^{-2} S.cm^{-1}, comparable to current liquid electrolytes.[65] This new material marked a crucial milestone, reviving interest and investment in SSBs research and development. Simultaneously, various chemistries were investigated, and notably, the argyrodite-type SEs (Li_6PS_5X – X = Cl, Br, I) emerged as serious competitors for sulphide-based SSBs.[66] These materials display ionic conductivity in the range of 10^{-3} S.cm^{-1}, and halide substitution can elevate this conductivity to 10^{-2} S.cm^{-1}, as demonstrated recently by Linda Nazar's group with $Li_{5.5}PS_{4.5}Cl_{1.5}$.[67] In general, sulphides SEs tend to outperform oxide-based ionic conductors both in terms of processing and ionic conductivity. Their ductile nature allows for RT densification (E = 18.5 GPa and H = 2 GPa for Li_6PS_5Cl)[60], thus facilitating SSBs fabrication while preventing temperature-induced degradation.[68] However, they are more susceptible to degradation, particularly from moisture[39], chemical instability with positive and negative electrode materials due to a narrow electrochemical stability window.[38]

Another family has recently gained much interest in the SSB field: the **halide**-based SEs. Originally, simple lithium halides have been studied (LiX – X = F, Cl, Br, I), only exhibiting very low ionic conductivity (< 10^{-7} S.cm^{-1}).[69] More recently, metal-halide SEs (Li_aMX_b – M = In, Zr, Y, Sc) have proved significantly higher ionic conductivities at RT (10^{-3} S.cm^{-1}), such as Li_3InCl_6 and Li_3YBr_6.[70,71] Compared to sulphides, halide SEs benefit from a better high-voltage stability (4.25 V vs Li^+/Li for Li_3YCl_6)[72] and better deformability (H = 0.3 GPa for Li_3YBr_6)[73], enabling RT densification. However, they face challenges such as poor electrochemical stability in reduction[72] and high hygroscopicity, leading to rapid liquefaction when exposed to moisture.[74]

Polymer solid electrolytes (PSEs) are typically approached and studied differently from inorganic solid electrolytes (ISEs) due to their distinct physical and chemical characteristics. Following Wright and Armand's landmark work on conductivity in salt-containing polymers, a crucial development occurred in 1983 with the introduction of lithium bis(trifluoromethanesulfonyl)imide (LiTFSI) as conducting salt.[75] Thanks to a low binding energy between $TFSI^-$ and Li^+, the ionic conductivity of PEO:LiTFSI stood out from other reported PSEs at that time, reaching 10^{-3} S.cm^{-1} at 80°C. Since Li^+ conductivity can only occur in non-crystallised domains of PEO, one approach to achieving sufficient conductivity is by operating the battery in the polymer-melted state. Another strategy involved incorporating inorganic particles to reduce crystallinity, as suggested by Scrosati.[76] Despite prolific research on modifying both the polymer (copolymers[77], comb-like polymers[78]) and the salt (single-ion PSE[79], hydrogen-containing anion[80]), PEO:LiTFSI remains the most widely used system to date. It serves as the basis for Blue Solutions' current commercial batteries, which combine LFP and Li metal electrodes and operates around 60°C.[81] Contrary to ISEs, PSEs are flexible (E = 0.14 GPa and H = 5 MPa for PEO:LiTFSI)[82] and relatively easy to process in films, either by tape-casting (wet route) or by extrusion (dry route), which facilitates the battery manufacturing. However, they are limited by low RT conductivity (10^{-7} – 10^{-5} S.cm^{-1}) and small transference number ($t^+ \approx 0.2 – 0.5$)[83], which usually impose operating the SPE-based SSB at elevated temperature (> 60°C).[77]

1.2.2 A comparative description of two representative solid electrolytes: Li_6PS_5Cl and PEO:LiTFSI

To provide a representative and detailed examination of SE properties, we conduct here a comparative analysis of two extensively used SEs: PEO:LiTFSI and Li_6PS_5Cl (also referred

as argyrodite). Belonging to distinct families, they exhibit unique characteristics in terms of ionic conductivity mechanisms, (electro-)chemical reactivity, mechanical properties and processing methods.

○ Conduction mechanisms

The assessment of ionic conductivity in solid electrolytes is conducted through electrochemical impedance spectroscopy (EIS). In this method, a layer of SE (typically a densified pellet for ISEs or a membrane for organic counterparts) is sandwiched between blocking electrodes, often made of stainless steel, titanium, sputtered gold, or carbon. EIS measurements are then carried out at a specific temperature. The resulting Nyquist plot allows the extraction of ionic resistance R_{ionic} (**Figure 1.5**). The conductivity σ is subsequently calculated, with e representing the thickness of the solid electrolyte, and S denoting its area.

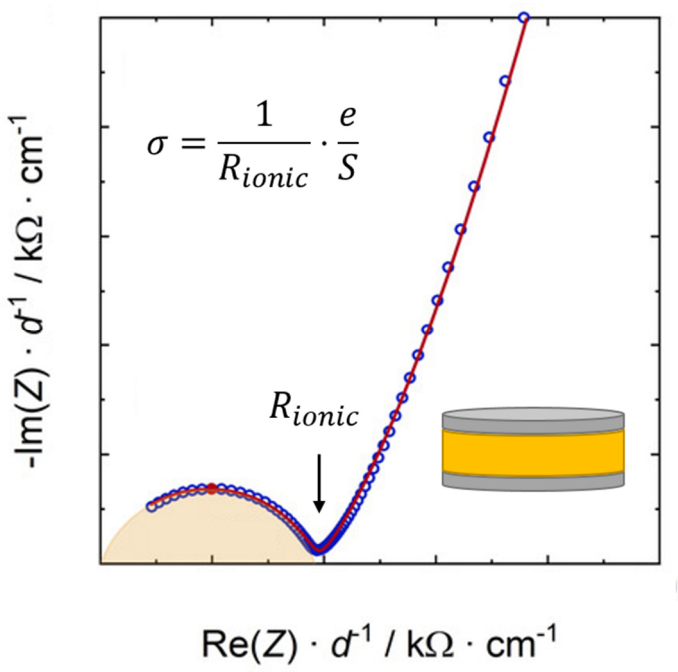

Figure 1.5 Typical Nyquist plot obtained from EIS of a SE layer and the associated equation to extract the SE ionic conductivity. Adapted from reference.[40]

The conduction of lithium ions in inorganic and organic SEs obeys different mechanisms. In ceramic SEs like Li_6PS_5Cl, Li^+ hopes from a position to another within the lattice.[84] In the crystalline structure of argyrodite, chlorine Cl^- forms a face-centred cubic framework, while nonbonded sulphur S^{2-} and PS_4^{3-} units occupy the tetrahedral and octahedral voids, respectively (**Figure 1.6**). Lithium ions Li^+ form a cage around S^{2-} and their

exact position depends on local site disorder (i.e., inversion of sulphur and chlorine positions). Three types of Li^+ displacement are reported in this structure: the doublet, the intra-cage and the inter-cage jumps.[85] The movement of Li^+ at the atomic scale is responsible for the observed ionic conductivity with an SE particle at larger scale.

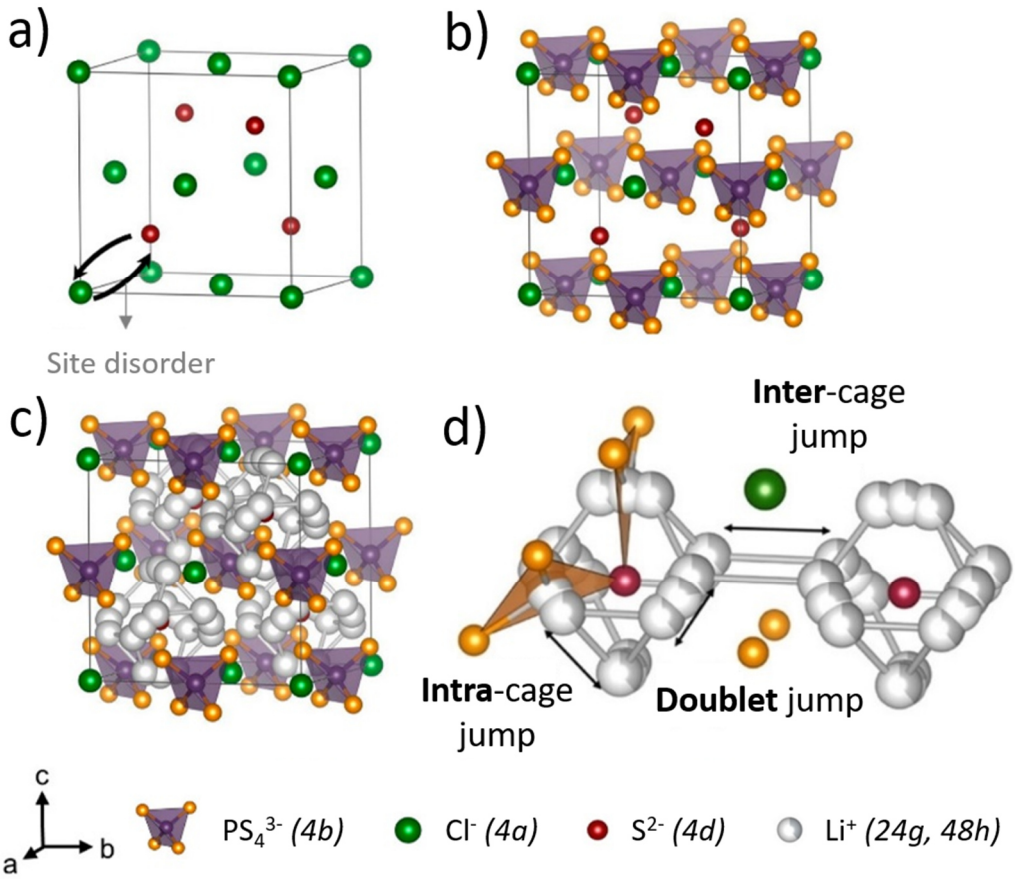

Figure 1.6 Unit cell of the Li_6PS_5Cl cubic polymorph: (a) Cl^- anions form a face-centred cubic structure with S^{2-} ions in half of the tetrahedral voids and (b) PS_4^{3-} units in the octahedral interstices. (c) Li^+ sites form cage-like structures around the free sulphide positions. (d) Possible jumps between Li^+ positions: doublet, intra- and inter-cage jumps. Reproduced from references[84,85]

This conductivity is known to be dependent on temperature as the microscopic jumps are thermally activated events. This dependence is commonly described by the Arrhenius law[86], as expressed below:

$$\sigma = \frac{\sigma_0}{T} \cdot \exp\left(-\frac{E_a}{k \cdot T}\right) \qquad \textbf{Equation 1.10}$$

where σ_0 is the pre-exponential factor, E_a the activation energy and k the Boltzmann constant.

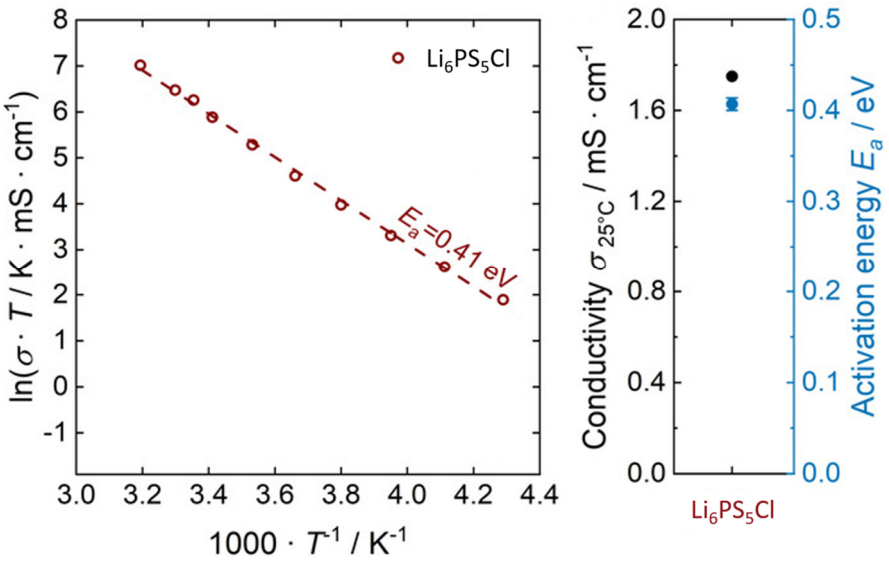

Figure 1.7 Temperature-dependence of Li_6PS_5Cl ionic conductivity: (a) Arrhenius plot and (b) conductivity and activation energy at 25°C. Adapted from reference.[40]

The typical Arrhenius plot of argyrodite Li_6PS_5Cl in **Figure 1.7** illustrates this relationship, showing an activation energy of approximately 0.4 eV, consistent with findings in other studies.[87,88]

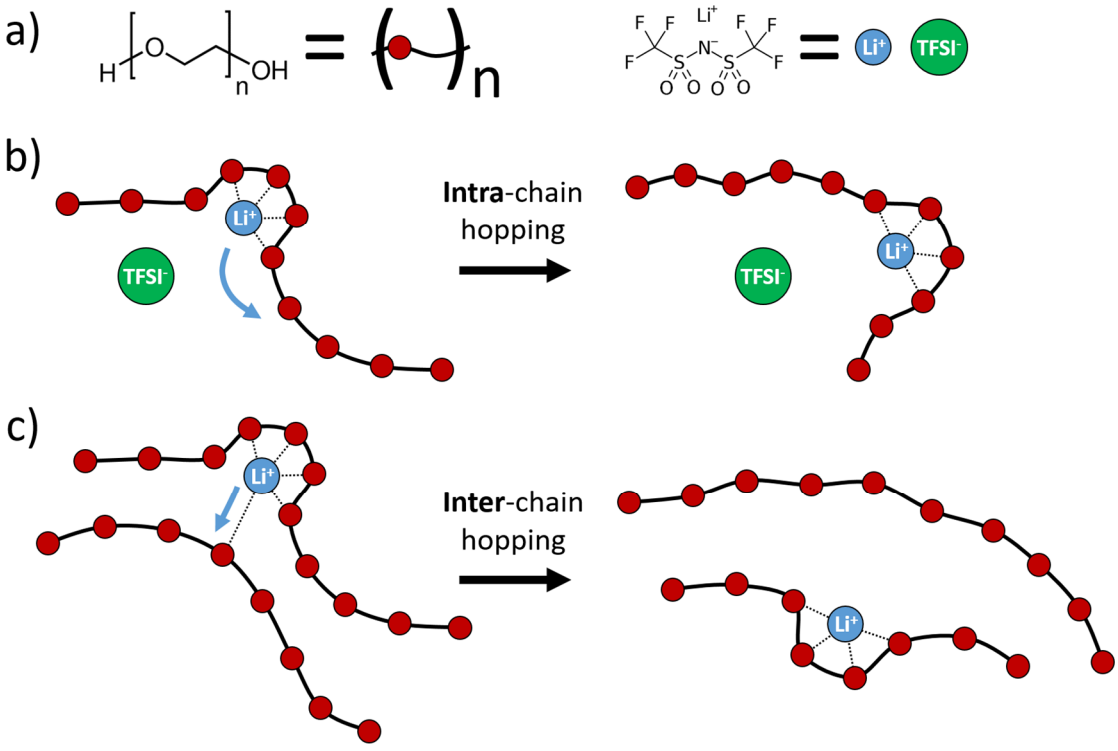

Figure 1.8 (a) Formula of poly(ethylene oxide) – PEO and lithium bis(trifluoromethanesulfonyl)imide – LiTFSI. Schematics illustrating lithium ion mechanisms for displacement along the PEO chain (b) and between chains (c). Adapted from reference.[77]

Conduction in PEO-based electrolytes relies on two concomitant phenomena. Illustrated on **Figure 1.8** the coordination of Li^+ by the ether oxygen, acting as a Lewis base with a high donor number, enables its displacement along the chain (intra-chain hopping) or between chains (inter-chain hopping).[89] Simultaneously, there is a segmental motion of the polymer chains themselves. The two combined mechanisms result in a long-range displacement of lithium ions, contributing to the electrolyte conductivity.

PEO is in a crystalline state at RT and can solubilise salts, such as LiTFSI, leading to its partial amorphisation. Since crystalline domains of PEO are poorly Li^+-conductive, increasing the ratio of amorphous domains, where segmental mobility is possible, positively affects the ionic conductivity.[90] As demonstrated by differential scanning calorimetry (DSC) in **Figure 1.9a**, an increase in salt concentration (or a decrease in the molar ratio EO:Li ; EO accounts for ethylene oxide unit) results in a decrease in both the crystalline PEO enthalpy of fusion and its associated melting temperature.

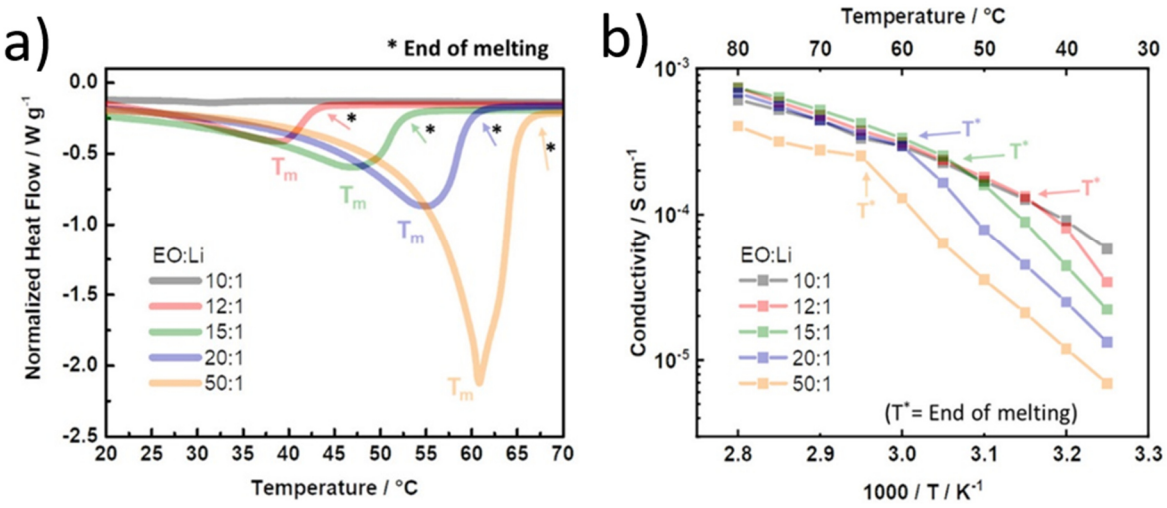

Figure 1.9 (a) Normalised heat flow of PEO_x:LiTFSI electrolyte (x = 10, 12, 15, 20, 50) as a function of temperature. The endothermic peaks represent the melting of PEO crystalline phase. (b) Associated ionic conductivity as a function of temperature. Reproduced from reference.[90]

Specifically, the system with EO:Li = 10:1 exhibits no melting event, indicating its fully amorphous nature. This correlates well with higher RT conductivity, facilitated by easier segmental motion and enhanced Li^+ mobility (8-fold increase of D_{Li^+} from EO:Li = 50:1 to 10:1).[90] As observed in **Figure 1.9b**, ionic conductivity becomes independent of salt concentration above the melting temperature, determined by DSC. Below this temperature, PEO undergoes partial crystallization, especially at lower salt concentrations, resulting in a

corresponding drop in conductivity. The empirical model of Vogel-Fulcher-Tammann (VFT)[91–93] typically describes the temperature dependence of ionic conduction in such amorphous electrolytes, above their glass transition temperature T_g.

$$\sigma = \frac{\sigma_0}{T} \cdot \exp\left(-\frac{B}{k \cdot (T - T_0)}\right)$$ **Equation 1.11**

In this equation derived from the Arrhenius model, B is the pseudo-activation energy and T_0 is the Vogel temperature, equal to T_g in ideal glasses but generally set 50°C below T_g for salt-in-polymer complexes, such as PEO:LiTFSI.[89,94] Other than salt concentration and temperature, the molar mass of the PEO also plays a role on the electrolyte viscosity. Shorter chains lead to a decrease of the matrix viscosity and favour segmental mobility, thus higher ionic conductivity. This phenomenon was described by Devaux *et al.*[95] (**Figure 1.10**).

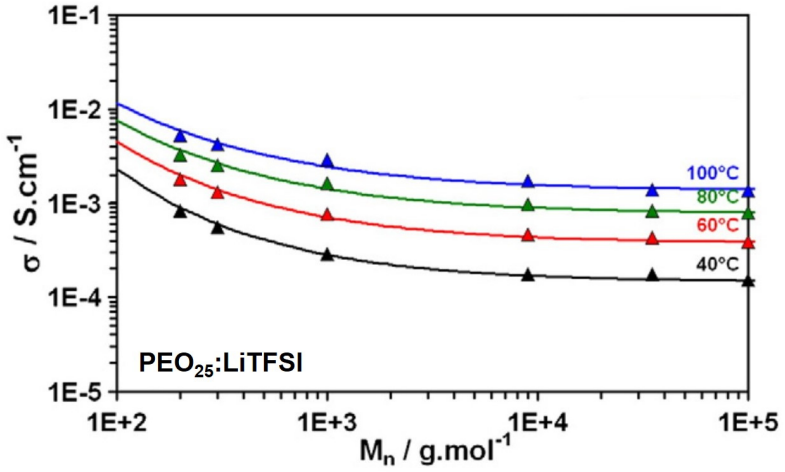

Figure 1.10 Isothermal variation between 40 and 100°C of the ionic conductivities according to M_n for the PEO_{25}:LiTFSI polymer electrolyte. Adapted from reference.[95]

○ (Electro-)chemical reactivity

As highlighted earlier in this manuscript, the performances of SSBs are significantly influenced by solid-solid interfaces. In particular, the electrochemical stability of the SE-electrodes interfaces raises concern due to the high potential of advanced CAM and the strong reduction capability of lithium metal. At those interfaces, three potential situations can arise (**Figure 1.11**).

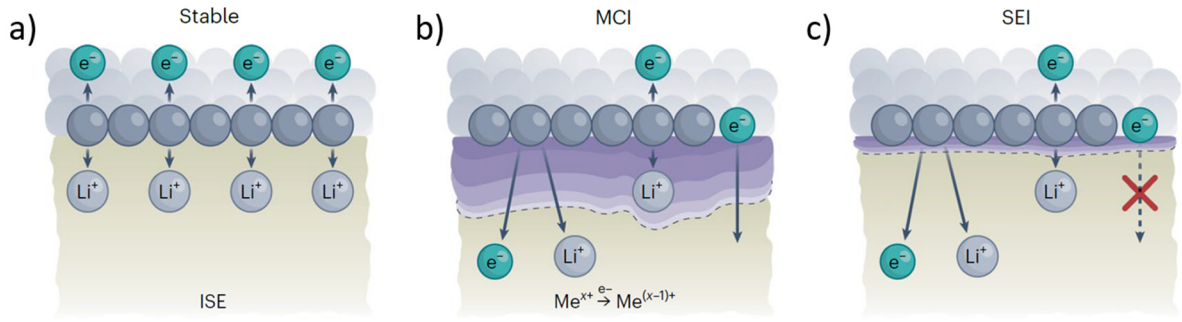

Figure 1.11 Illustration of the three types of interfaces that can form at the SE-electrode interface. (a) *Thermodynamically stable interface* – absence of chemical reactivity. (b) *Non-passivated Mixed-Conductive Interphase (MCI)* – formation of a mixed ionic-electronic interphase that continuously grows until short-circuit. (c) *Passivated Kinetically Stable Interphase (SEI)* – formation of an electronically insulative interface that can conduct ions, exhibiting a self-passivating behaviour. Reproduced from reference.[96]

Similar to many sulphide SEs, the argyrodite Li_6PS_5Cl suffers from a narrow thermodynamic stability window (1.7 – 2.0 V vs Li^+/Li), that is typically assessed by density functional theory (DFT) calculation[97] or via cyclic voltammetry (CV).[98] Beyond these voltage boundaries, the SE undergoes degradation, resulting in the formation of insulative species that passivate both the CAM and Li metal interfaces. Based on X-ray photoelectron spectroscopy (XPS) measurements at various potentials in a half-cell configuration, Tan *et al.*[98] proposed the following mechanism of degradation:

$$\text{Oxidation: } Li_6PS_5Cl \rightarrow LiCl + \frac{1}{2}P_2S_5 + \frac{5}{2}S + 5Li^+ + 5e^- \qquad \textbf{Equation 1.12}$$

$$\text{Reduction: } Li_6PS_5Cl + 8Li^+ + 8e^- \rightarrow LiCl + Li_3P + 5Li_2S \qquad \textbf{Equation 1.13}$$

Additional to its intrinsic thermodynamic reactivity, argyrodite can experience (electro-)chemical degradation against both electrodes. On the cathode side, reactivity occurs with transition metal oxides at high potential as demonstrated by Janek *et al.*[43] using time-of-flight secondary-ion mass spectrometry (ToF-SIMS) and XPS (**Figure 1.12a**). In their study, the formation of sulphate (SO_x) and phosphate (PO_x) species at the interface between NMC622 and Li_6PS_5Cl correlates well with a long-term capacity fading. On the anode side, the reduction of argyrodite in contact with lithium metal leads to a self-passivation of the interface, as illustrated with XPS in Wenzel *et al.* study (**Figure 1.12b**).[99]

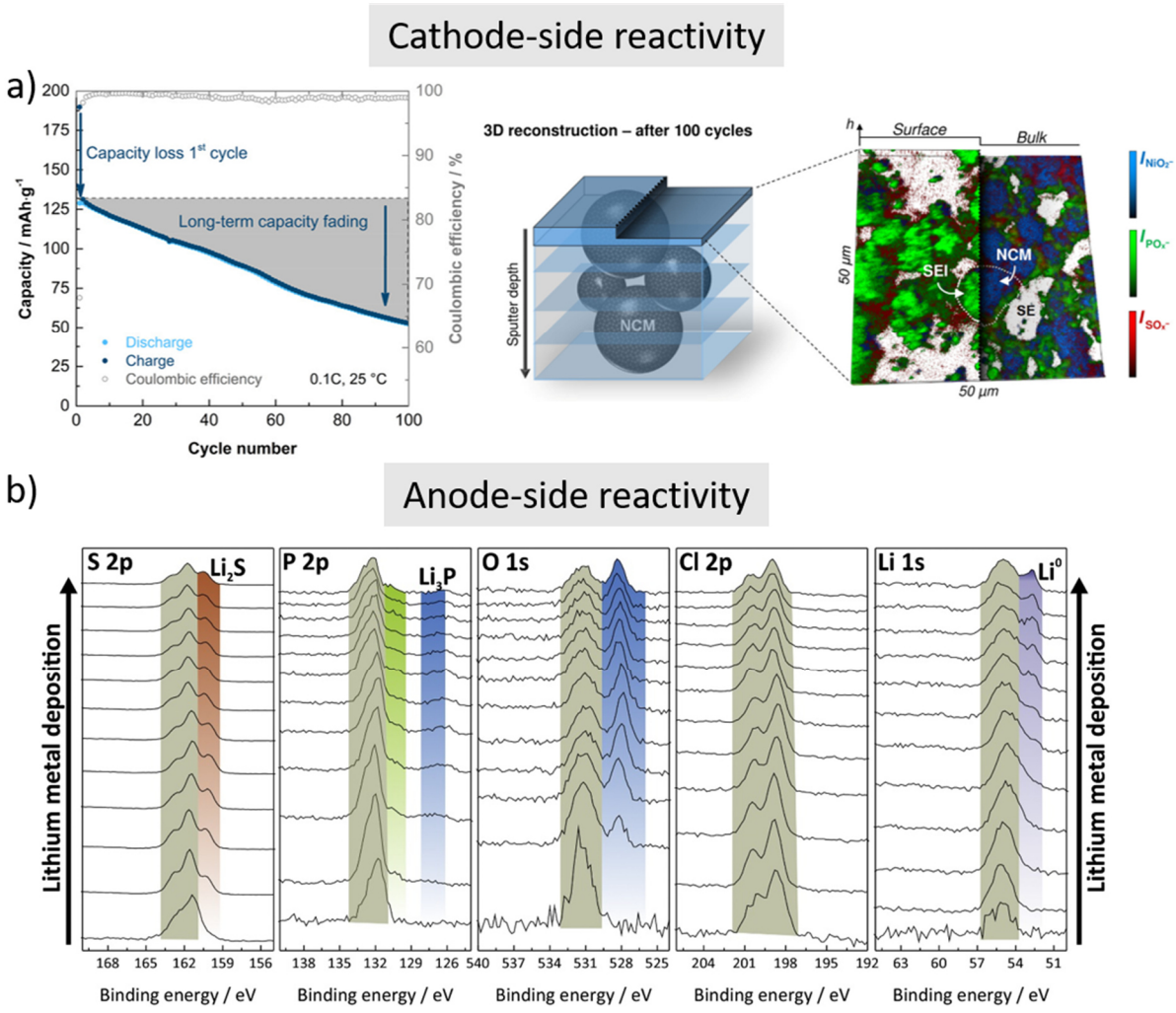

Figure 1.12 Reactivity of Li_6PS_5Cl at the electrodes interface. (a) Cathode side: Capacity retention of an NMC622: Li_6PS_5Cl | Li_6PS_5Cl | LiIn cell – Three-dimensional reconstruction of the ToF-SIMS depth profile of the cycled composite cathode. (b) *In situ* XPS of argyrodite during sequential lithium metal deposition, unravelling the associated degradation products. Reproduced from references.[43,99]

The cathodic stability of PEO:LiTFSI is often debated due to the inconsistency in reported oxidation onset potential, ranging from <4.0 to >5.0 V. This variability stems from various experimental conditions used to determine it. The potentiodynamic method (CV) is typically used for its ease of implementation, but it suffers from uncertainty in determining the current threshold at which the system is considered unstable. Additionally, the choice of the electronic surface can impact the kinetics of degradation, altering the observed oxidation onset. To overcome these limitations, Homann *et al.*[100] proposed a galvanostatic approach applied to practical composite cathodes based on various active materials and PEO:LiTFSI (**Figure 1.13a**). During the charging of electrodes, they systematically observe a potential plateau at 4.6V vs Li^+/Li.

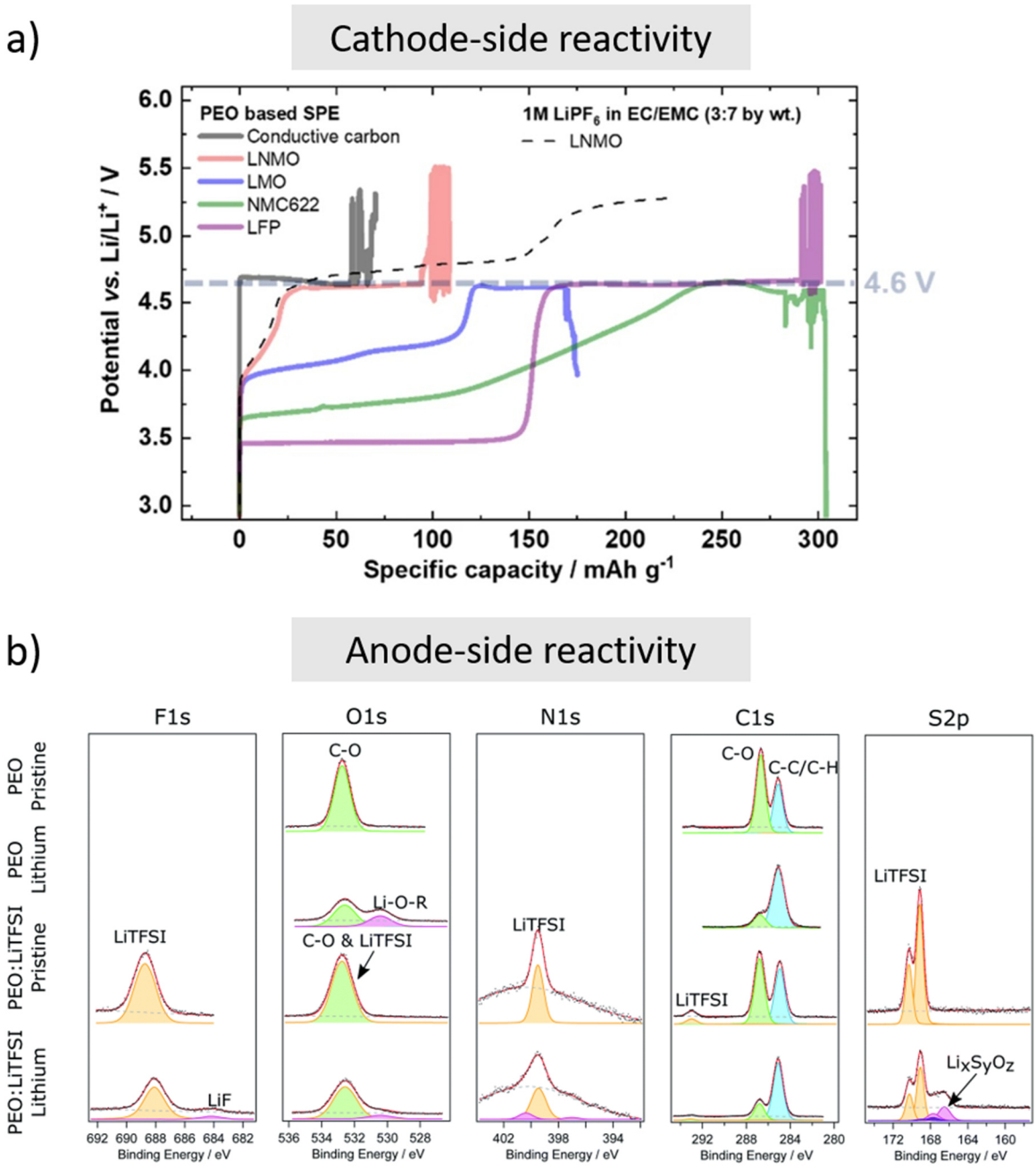

Figure 1.13 Reactivity of PEO:LiTFSI at the electrodes interface. (a) Determination of the onset of main oxidation via overcharge of the positive electrode using different active materials. (b) XPS of PEO and PEO:LiTFSI before and after lithium metal deposition, unravelling the associated degradation products. Reproduced from references.[100,101]

This plateau is unrelated to each material's delithiation process and points to the main oxidation reaction of the organic SE. A plausible mechanism[102] suggests that dehydrogenation of PEO occurs at high potential, leading to the neutralization of TFSI anion into the strong acid HTFSI. The latter further causes chain scissions and the formation of volatile molecules, including H_2. On the anode side, PEO:LiTFSI can be reduced by the low potential of lithium

metal. As demonstrated by XPS analysis (**Figure 1.13b**)[101], the polymer chain undergoes partial C-O bond breaking, while the salt undergoes partial degradation to form LiF and sulphur oxyanions $Li_xS_yO_z$.

- Mechanical properties

Beyond the critical properties of ionic transport and stability, the mechanical characteristics of SEs are also crucial to the battery design. They play a decisive role in both assembly and operation, determining the quality and stability of the solid-solid contacts between the SE and the electrodes.[60] As volume expansion often occurs during lithiation of the electrodes[41], local stress may increase at the solid-solid interfaces and is often accommodated by the appearance of fractures, thus compromising the cell integrity. Simultaneously, contraction mainly occurs during delithiation, leading the formation of voids and the loss of solid-solid contacts.

Considering their distinct physical nature, the two electrolytes studied in this section exhibit very different mechanical behaviours. The polymeric nature of PEO:LiTFSI makes it suitable for extrusion and calendaring processes, benefiting from low glass transition and melting temperatures ($T_g \approx -50°C$ and $T_m \approx 65 - 70°C$ for pure PEO).[103] This makes it easier to form stable contact with soft materials like lithium metal and better wetting of CAM particles. PEO:LiTFSI is a versatile material, as the amount of salt dissolution significantly impacts the mechanics of the SE, with higher concentrations leading to less crystalline and softer electrolytes. A simple compression test illustrates the decrease of elastic resistance (or Young's modulus) as the EO:Li ratio decreases, as shown in the study by Stolz *et al.* (**Figure 1.14a-b**).[90] However, some minimal mechanical strength is necessary to ensure the integrity of the battery and prevent dendrite growth. One strategy, proposed by the same group, is to shift from linear chains to a reticulated network of PEO, increasing the stiffness but slowing down the ionic conductivity (**Figure 1.14c-d**)[104], which illustrates a common trade-off between mechanical and conduction properties in SSBs. By employing a reticulated electrolyte in an NMC | Li full cell instead of PEO:LiTFSI, they demonstrated the elimination of "voltage noise", a phenomenon characteristic of Li dendrite-induced micro short circuits. However, lithium dendrites appearance is not solely linked to the rigidity of the SE, since they can grow in soft media, like PEO:LiTFSI[105], as well as hard but brittle ones, like LLZO.[106] This phenomenon is

multifactorial since it is influenced by several parameters, including the lithium purity, the SE wettability on Li and the plating/stripping current density.

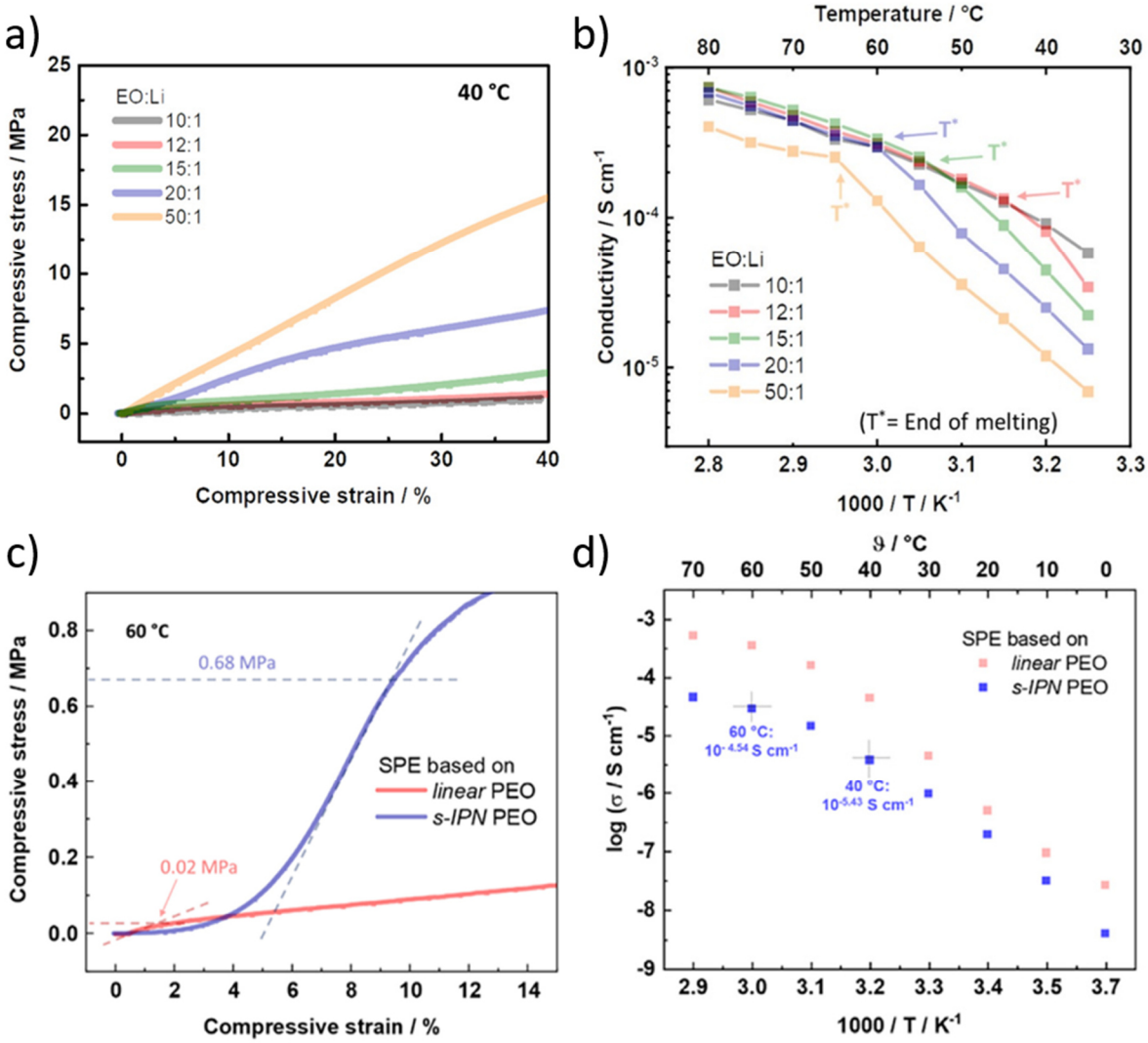

Figure 1.14 Correlation between mechanical properties and ionic conductivity in PEO:LiTFSI systems. Compression curves under different conditions: (a) varying EO:Li ratio and (c) with or without reticulation. Related ionic conductivities in temperature: (b) varying EO:Li ratio and (d) with or without reticulation.[90,104]

Processing Li_6PS_5Cl differs significantly from polymer electrolytes due to its ceramic nature. Being sulphide-based, argyrodite is a relatively "soft" ceramic compared to oxide SEs, allowing densification at high pressure (100 – 400 MPa leading to 68 – 77 % relative density)[46] and room temperature into pellets. However, it remains inherently brittle, especially due to remaining porosity within the compacted powder.[47] Additionally, it is significantly less prone to elastic deformation than the PEO:LiTFSI system, with respective Young's moduli of $E_{Li_6PS_5Cl} \approx 25\ GPa$ and $E_{PEO_{10}:LiTFSI} = 0.4\ MPa$ at RT.[107,108] In this case, several mechanical issues are often reported with batteries based on Li_6PS_5Cl, including loss of contact with the

CAM, penetration of lithium metal within the SE layer leading to fracture, and appearance of voids at the anode interface.[33,42,109]

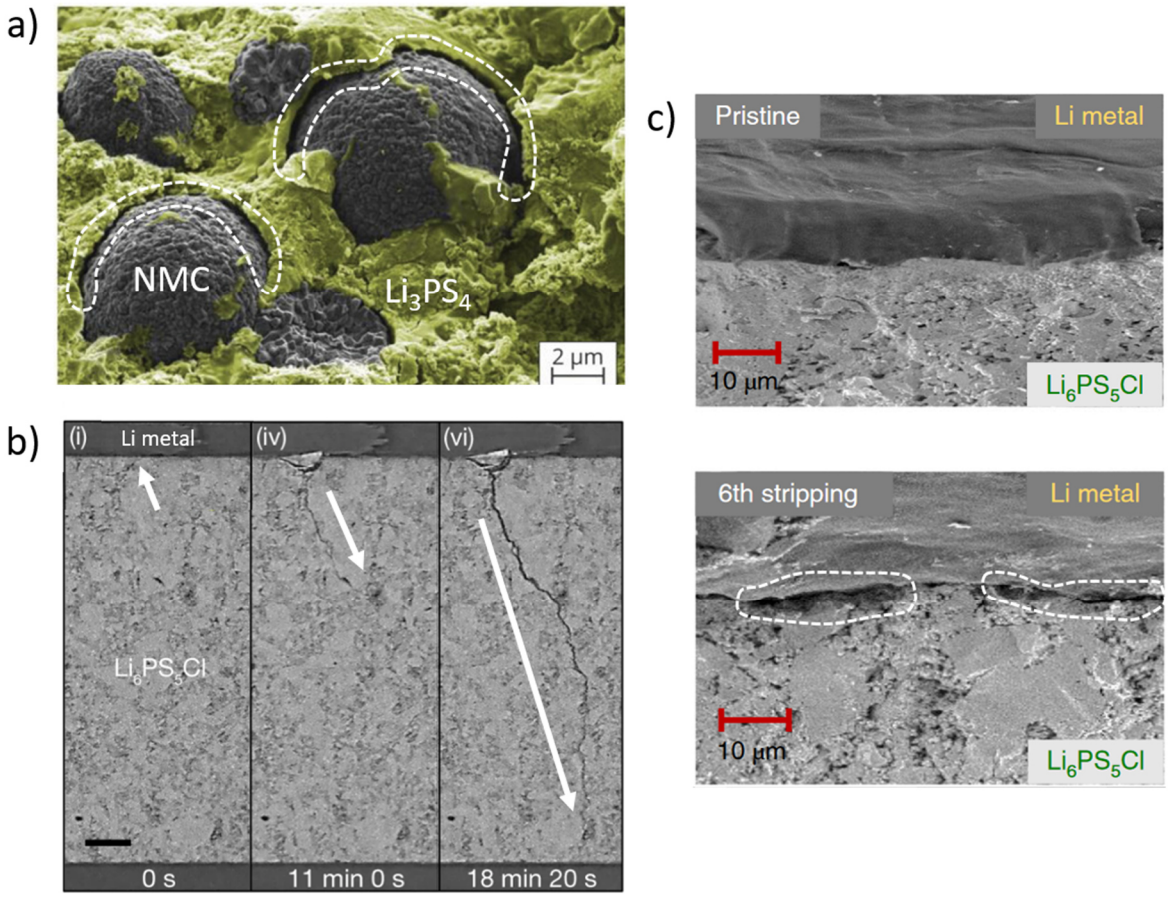

Figure 1.15 Typical mechanical issues in occurring in SSBs based on ceramic electrolyte. Dotted lines highlight the presence of voids at the electrode-SE interface. (a) Scanning electron micrographs (SEM) of cathode composite NMC811:Li_3PS_4 in discharge state after 50 cycles. (b) Operando X-ray computed tomography (XCT) cross-sectional image slices showing the initiation of a lithium dendrite accompanied with the propagation of a crack (white arrow) in a symmetric Li | Li_6PS_5Cl | Li cell. (c) SEM cross-sections of the interface between lithium metal and Li_6PS_5Cl after 6 cycles of plating and stripping in symmetric cell configuration. Reproduced from references.[33,42,109]

1.2.3 Hybrid solid electrolytes: a continuous compromise

As organic and inorganic solid electrolytes each have their advantages and drawbacks concerning conduction and mechanical properties, a potential approach is to fabricate hybrid materials that combine the strengths of both.

- Non-conductive inorganic fillers

The historical approach of hybrid solid electrolytes (HSEs) involves the dispersion of non-conductive inorganic fillers in a matrix of polymer electrolyte. In typical organic SEs like

PEO:LiX (LiX for lithium salt), the addition of ceramic nanoparticles such as Al_2O_3, TiO_2 and SiO_2 mainly has a plasticizing effect, disrupting the crystallinity. In 1999, Croce *et al.*[110] studied the effect of the addition of 10 wt.% of nanosized Al_2O_3 to the polymer electrolyte PEO_8:$LiClO_4$ (**Figure 1.16a-c**). They demonstrated by DSC that the amorphisation of the HSE was permanent over days in the presence of Al_2O_3, while recrystallization occurred after several days in the ceramic-free SE. They correlated this amorphous structure with a significant increase in RT ionic conductivity, thanks to facilitated mobility of the charges.

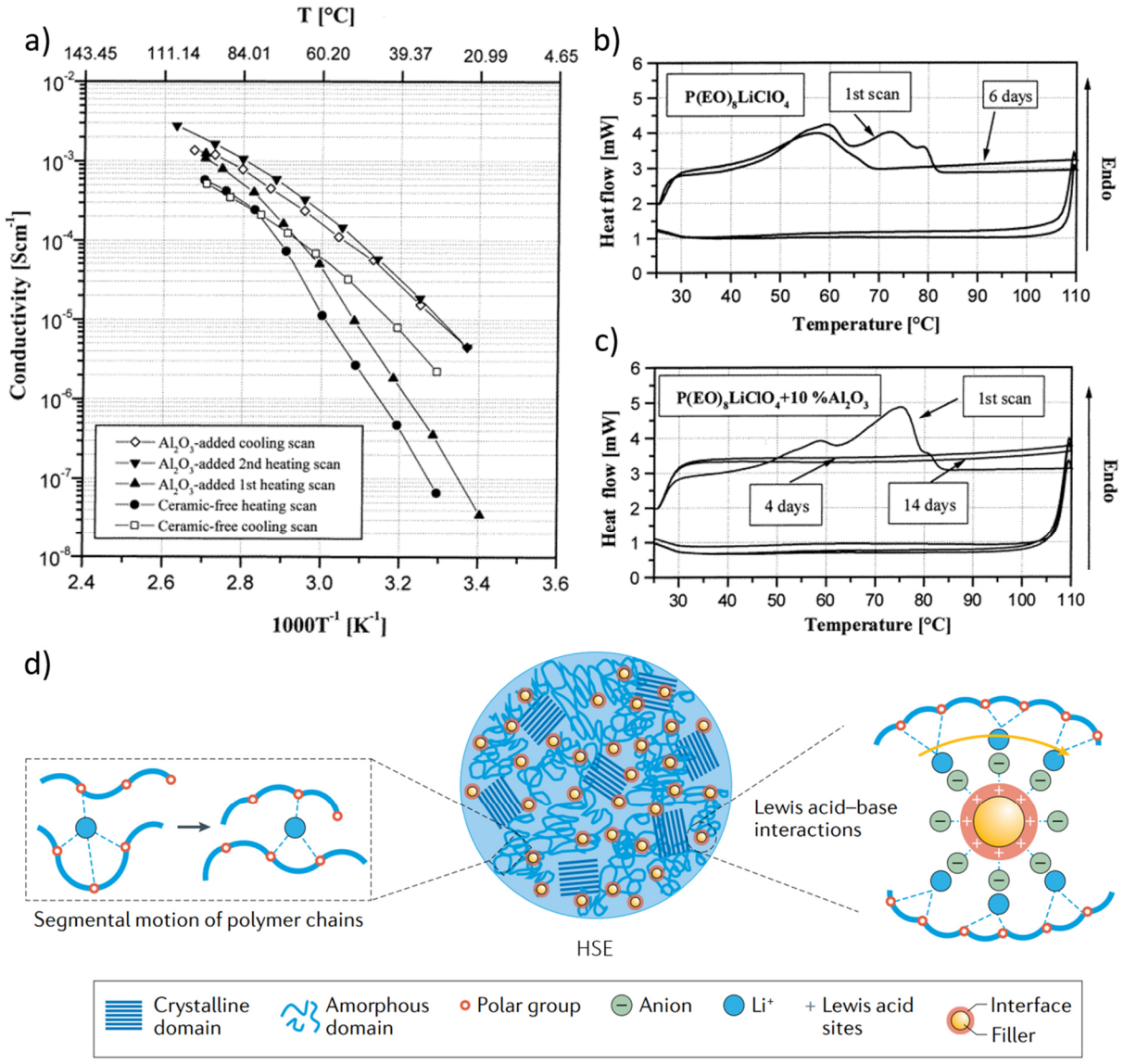

Figure 1.16 Influence of nanofiller addition (Al_2O_3) to a partially crystallised polymer electrolyte (PEO_8:$LiClO_4$). (a) Ionic conductivity in temperature of ceramic-free and nanocomposite polymer electrolytes. (b-c) The associated DSC thermograms of the as-prepared samples and after a different number of days of RT storage (rate 10°C.min^{-1}). (d) Schematics of Li^+ ion transport in HSE containing ceramic fillers with Lewis-acid sites. Reproduced from references.[110,111]

These Lewis-acid groups compete with the formation of complexes with the polymer (Li^+ - PEO), as well as with the anion of the salt (Li^+ - X^-). This competition favours salt dissociation and conduction at the ceramic surface, resulting in an increased fraction of "free" Li^+ ions. In a study by Croce *et al.*[112] in 2020, the addition of 10 wt.% acidic Al_2O_3 to PEO_{20}:$LiCF_3SO_3$ demonstrated an increase in the transference number from 0.46 to 0.63, highlighting the enhancement of Li^+ conductivity.

- Inorganic – polymer interface in hybrid solid electrolytes

With the emergence of highly conductive ISEs, a more recent approach to fabricating HSEs consists in dispersing Li^+-conducting particles within a polymer electrolyte matrix. The purpose is to achieve synergy between the high conductivity of the ISE and the desirable mechanical properties of the PSE. Understanding the contribution of each phase to Li^+ conduction within the HSE is crucial for assessing the effective benefits of their combination. To ensure these benefits, effective transfer of lithium ions between the inorganic and polymer phases is necessary, involving a transition from one conduction mechanism to another. There is also a significant mismatch of lithium concentrations between the PSE and the ISE (e.g., $C^{Li}_{PEO_{10}:LiTFSI} = 1.9\, mol.L^{-1}$ and $C^{Li}_{Li_6PS_5Cl} = 36.7\, mol.L^{-1}$), which leads to a gap of Li^+ chemical potentials at the interface, making its crossing an energy-demanding step. Moreover, the contact between these two phases introduces a new interface within the HSE, which should be mechanically and chemically stable with the lowest resistance possible to ensure effective Li^+ transfer. To assess these characteristics, conducting EIS measurements on a PSE | ISE layered structure is a valuable technique that can disclose the interface resistivity and the activation energy associated to Li^+ transfer. While most studies focus on oxide SEs interfaced with a PSE, Simon *et al.*[113] directed their interest on the PEO_{10}:LiTFSI | Li_6PS_5Cl interface (**Figure 1.17**). By employing a four-point EIS measurement on a Li | SPE | ISE | SPE | Li layered structure, they could unravel the resistivity and activation energy of two processes: the Li^+ charge transfer (CT) between the SPE and the ISE, and the formation of an intermediate layer of degradation products (SPEI). In comparison with similar studies on oxide SEs and various PSEs, they demonstrated that this system exhibited one of the lowest interface resistances and activation energies among PSE | ISE interfaces.[114] This makes it a promising candidate for fabricating HSEs or utilizing it as a buffer layer at the Li metal anode interface.

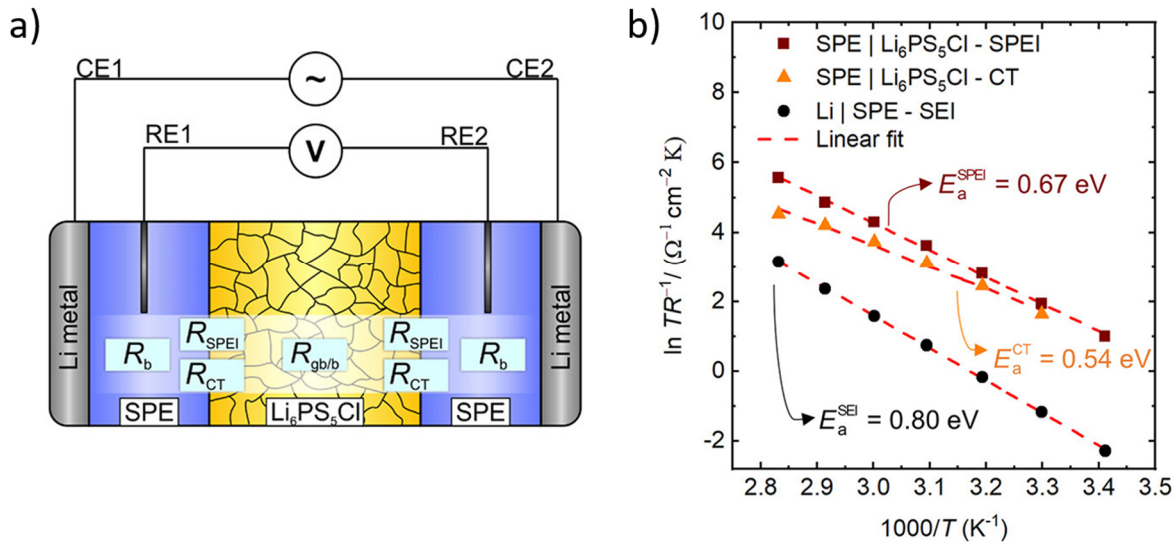

Figure 1.17 (a) Schematics of the four-point cell setup to study the PEO_{10}:LiTFSI | Li_6PS_5Cl interface. (b) Temperature-dependent resistances of the solid-polymer electrolyte interphase (SPEI), ionic charge transfer (CT) and the Li | PEO_{10}:LiTFSI solid electrolyte interphase (SEI). Reproduced from reference.[113]

Furthermore, gaining insights into the chemical properties at the interface through surface-sensitive techniques, such as XPS and ToF-SIMS, can provide a more comprehensive understanding of the interface. In the same study, Simon *et al.* employed both techniques to unravel the degradation products forming the interphase, predominantly LiF and polysulphides, and to monitor its growth after thermal aging.

○ Conduction mechanisms in hybrid solid electrolytes

When transitioning from a well-defined layered structure to more complex particles-in-matrix systems, the crucial parameter in this case becomes the ratio between the ISE and the PSE. Two distinct approaches emerge from the prolific literature on the topic: (i) the addition of a small amount of ceramic filler to disturb the crystallinity of the organic phase, known as a *ceramic-in-polymer* system; (ii) and its opposite, in which the polymer electrolyte, in low content, acts primarily as a binder, called *polymer-in-ceramic*. In both cases, the preparation method must ensure the intimate mixing of the two components. This can be achieved either by casting a slurry, prepared from powders dispersed in an inert solvent, or by following a solvent-free route that involves the application of shear forces (via hand-grinding or extrusion), possibly coupled with temperature, to achieve an homogeneous HSE. It is also crucial to remove any residual water and solvent in the HSE by careful drying to prevent misinterpretation of the ionic conductivity and possible degradation of the ISE.[40,115,116]

Within an HSE, there are multiple theoretical pathways available for the lithium ions migration: either solely through a percolating PSE network (respectively ISE network), which is more probable in low ISE content (respectively low PSE content), along the boundaries between the two phases, or through a mixed ISE-PSE network, implying the ability to cross the interface (**Figure 1.18**).[117] There is no consensus on the actual conduction mechanisms occurring in the reported HSEs. Indeed, they depend on many parameters, including the polymer chemistry and its molecular weight, the choice of Li salt anion and its concentration, the type of ceramic electrolyte and its particle size and surface chemistry, the organic-to-inorganic ratio, the presence of plasticiser and the mixing route (wet or dry). As a result to this complexity, a wide range of ionic conductivities is reported, with some indicating a synergistic effect[88,118], while others exhibit reduced values compared to their initial components.[119,120] However, in cases where synergy is observed, it was also shown that the polymer crystallinity was reduced by the presence of the inorganic filler, meaning that a mixed ISE-PSE conduction network is not certain.[118]

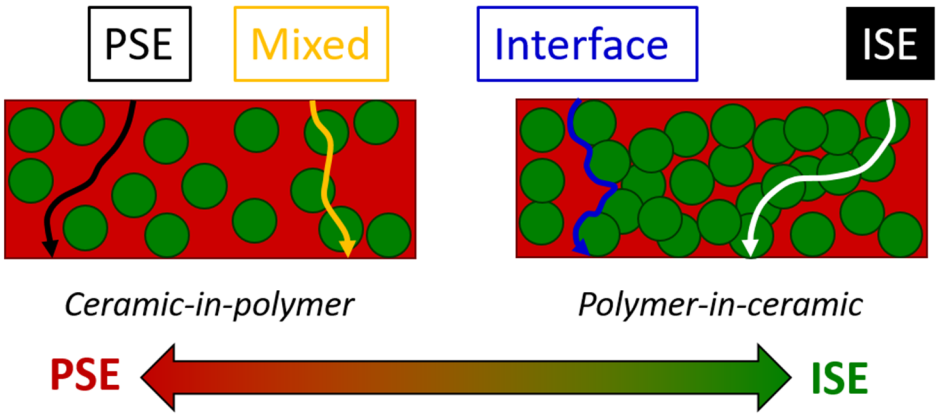

Figure 1.18 Schematics of the theoretical pathways for Li^+ migration through an HSE and representation of the two formulation approaches according to PSE – ISE ratio. Adapted from reference.[117]

A proposed method to elucidate the conduction mechanism involves the use of solid-state nuclear magnetic resonance (ssNMR).[121,122] By polarizing a symmetric cell ^{6}Li | HSE | ^{6}Li, the partial replacement of the naturally abundant ^{7}Li (92.5 at.%) by ^{6}Li leaves a trail within the HSE. An increase in certain peak intensities on the subsequent ^{6}Li ssNMR spectrum should highlight the preferred environments for Li^+ conduction. While the strategy is very elegant, and the outcome should be unambiguous, the experimental conditions should be scrutinised carefully. Reported studies systematically perform alternating polarization but do not mention

the capacity moved from one electrode to the other.[121,123] Alternating plating and stripping of the lithium metal electrode are not consistent with the purpose of the experiment, as mostly ^{7}Li is plated on both electrodes, originating from the HSE. When inverting the polarization, primarily the top part of this electrode, mostly composed of ^{7}Li, is stripped. Additionally, a significant amount of lithium needs to be exchanged to ensure a detectable evolution of the ssNMR peak intensities, before and after the polarization. The absence of an estimation for the percentage of lithium replacement in the HSE raises questions on the validity of the conclusions. However, an interesting study on PEO:LiTFSI – LGPS HSEs by Zheng *et al.*[122] concludes that ionic transport preferably occurs at the interface, as proven by tracer-exchange ^{6}Li ssNMR using a one-way polarisation.

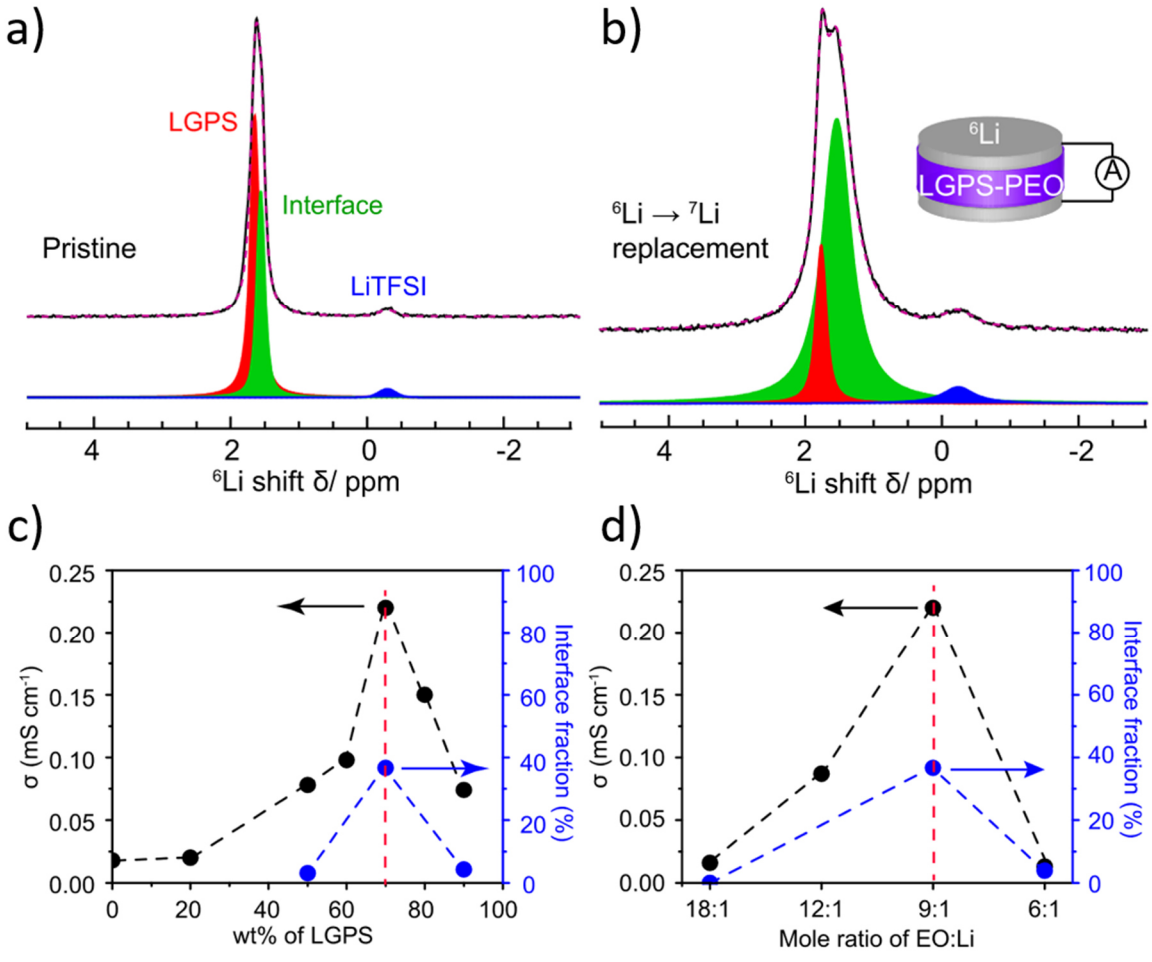

Figure 1.19 ^{6}Li magic angle spinning NMR of an PEO:LiTFSI – LGPS hybrid electrolyte film before (a) and after (b) ^{6}Li → ^{7}Li tracer-exchange. (c) Conductivity and interface fraction of PEO_9:LiTFSI – LGPS as a function of LGPS content. (d) Conductivity and interface fraction of PEO_x:LiTFSI – LGPS = 30:70 (w) as a function of the EO:Li = x:1 ratio. Reproduced from reference.[122]

They were able to demonstrate a positive correlation between ionic conductivity and the amount of interface quantified by ^{6}Li ssNMR, which is function of LGPS content and salt concentration (**Figure 1.17**).[122] A previous work led by the same group concluded differently on the PEO:$LiClO_4$ – LLZO system.[121] The tracer-exchange experiment suggests a preferred Li^+ conduction through the LLZO network. However, the chosen formulation of 20 vol.% of LLZO is below the percolation threshold of inorganic particles, questioning the conclusion of the ssNMR measurements, which are not supported by ionic conductivity values.[124]

In 2022, Liu *et al.*[125] reported a different role of the interface in an HSE based on PEO:LiTFSI – Li_6PS_5Cl, investigated by ssNMR. They noted the absence of ion transfer at the interphase, mainly composed of poorly conductive products of degradation. They strategically incorporated insoluble ionic liquid (PP13-TFSI) into the formulation, which positioned itself at the particles interface, and served as a bridge for lithium ion transport, ultimately enhancing conductivity.

Altogether, these studies highlight the complexity of HSE systems in which the conduction mechanism is fully composition-dependent and where the interface is key. To attain the desired synergy between ionic conductivity and mechanical properties, the formulation of an HSE requires careful adjustment of the available parameters, with the organic-to-inorganic ratio and the salt concentration being of prime importance. A systematic approach should allow understanding their contribution of each them, helping to reach the best compromise for practical application. The potential of this strategy will be investigated within the scope of this thesis.

1.3 – Scaling up the manufacturing of solid-state batteries

Despite major developments at the SEs level and innovative strategies attempting to combine their assets, one emerging challenge is the ability to manufacture SSBs out of it, with a needed transition from the laboratory to the pilot scale. Several points are of prime importance to achieve this task: the stability of materials in an industrial environment, the mixing quality of solid components, the preparation of self-standing electrodes and separator and the process of SSBs assembly, with the challenging integration of the lithium metal anode.

1.3.1 Electrodes and separator fabrication

○ Environmental stability of Li_6PS_5Cl

To fabricate tape electrodes and separators, a careful evaluation of the materials stability towards their environment is necessary. Sulphide-based SEs are highly sensitive to ambient moisture, which is why experiments are general done in an argon-filled glovebox (H_2O < 1 ppm). Chen *et al.*[126] reported the chemical evolution of Li_6PS_5Cl when exposed to ambient air. The hydrolysis of argyrodite leads to irreversible sulphur loss by the formation of hydrogen sulphide gas (H_2S), as confirmed by X-ray diffraction (XRD).

$$Li_6PS_5Cl + 4\,H_2O \rightarrow LiCl + Li_2S + Li_3PO_4 + 4\,H_2S\uparrow \qquad \textbf{Equation 1.14}$$

Additional analysis, including XPS, NMR, Raman and Fourier transform infrared spectroscopy (FTIR), unravelled the formation of hydrated species (oxysulphides) and carbonates after air exposure.

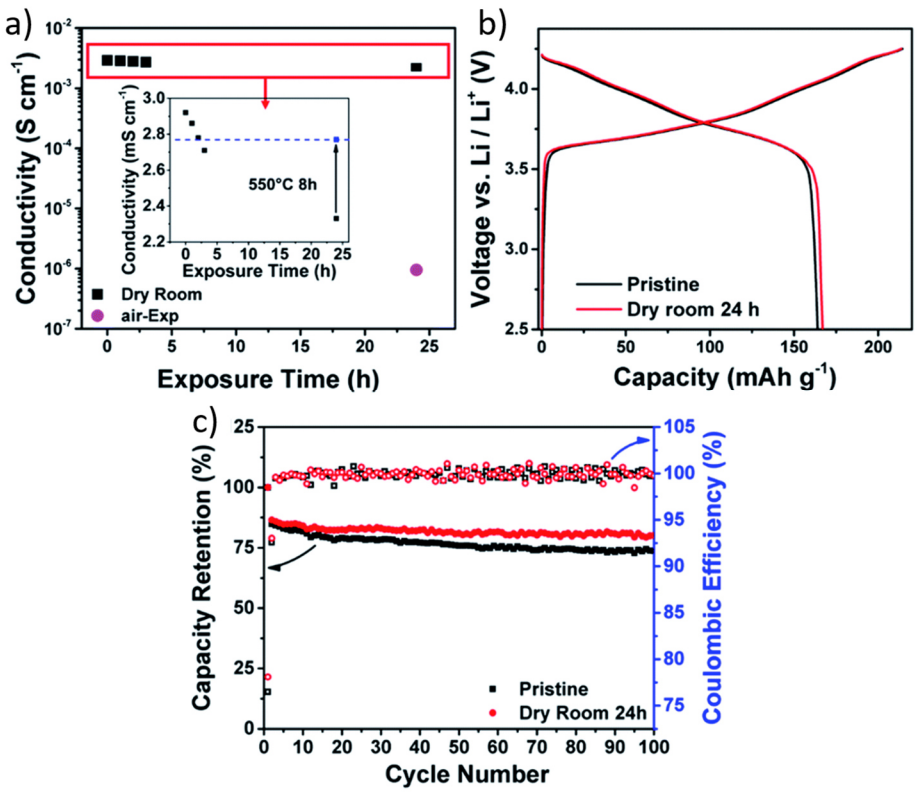

Figure 1.20 (a) Ionic conductivity of dry room exposed Li_6PS_5Cl samples as a function of time, a heat-treated sample following 24 hours of dry room exposure, and an air-exposed sample. (b) First cycle voltage profiles (C/10), (c) capacity retention (C/3) and Coulombic efficiency of NCM811|Li_6PS_5Cl|LiIn cells assembled using pristine or 24h dry room exposed Li_6PS_5Cl. Reproduced from reference.[126]

However, the researchers demonstrated that in a controlled environment, such as a dry room (H_2O < 100 ppm), Li_6PS_5Cl could retain most of its ionic conductivity after 24 hours of exposure (**Figure 1.20**). Solid-state NMC | LPSCl | LiIn cells exhibited similar performances with or without the dry air exposure, providing strong evidence for the feasibility of large-scale sulphide-based SSBs in dry rooms.

Since H_2S is a flammable and toxic gas, considering the safety requirements for handling hazardous materials is of prime importance when anticipating a scale-up in manufacturing. Singer *et al.*[39] investigated the parameters influencing the generation of H_2S in a dry room environment for self-standing films of Li_6PS_5Cl. They identified the dew point level (i.e., water content in the atmosphere) and the exposed surface (film porosity and geometry) as the two main factors that dictate the amount of generated gas. As shown in **Figure 1.21**, they highlighted the correlation between the H_2S generation rate and the water content and put these dew-point dependant rates in perspective with the German safety limits of 5 and 10 ppm for long-time and ceiling exposures, respectively.[127] Based on their investigation, the researchers advocate for a working environment with a maximum dew point of -40°C (≈ 140 ppm) to ensure workers' safety and product quality. However, it is important to point that workers' olfactory comfort is here not taken into account, since the human limit of detection lies between 0.02 and 0.1 ppm of H_2S, with a smell close to "rotten eggs".[128]

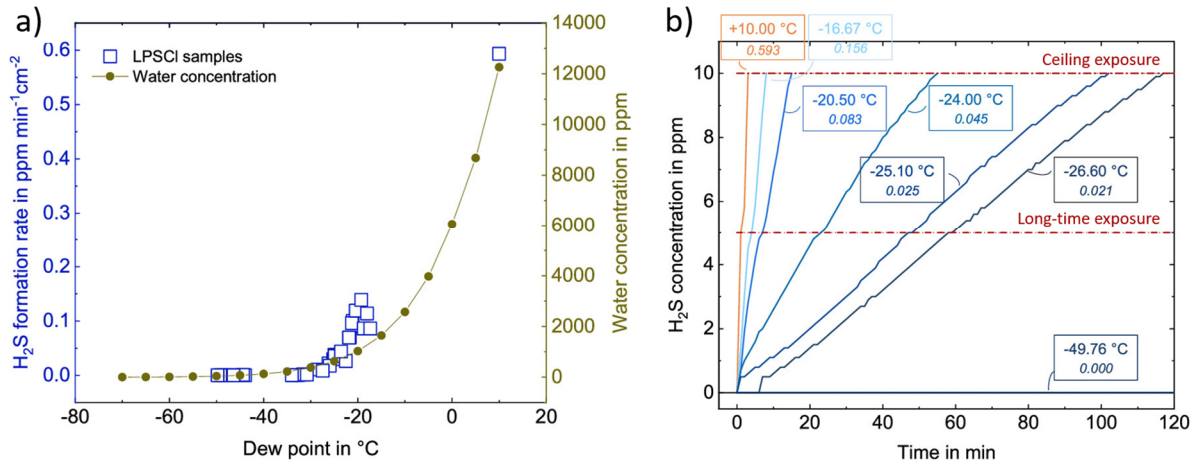

Figure 1.21 (a) H_2S formation rate normalised by exposed surface as a function of dew point. (b) H_2S concentration over time under different dew points, compared to long-time and ceiling exposure limits. Reproduced from reference.[39]

Various strategies are being explored to enhance the chemical stability of Li_6PS_5Cl towards its environment, as well as high potential CAMs and lithium metal. One favoured method involves applying a nanometric protective coating on the particles, either through vapour-phase deposition of a hydrophobic polymer layer or using atomic layer deposition (ALD) to form an inorganic protection at the surface.[129,130] A more promising and straightforward approach involves the formation of a thin carbonate layer through a simple treatment under CO_2-rich atmosphere, leading to a spontaneous gas-solid reaction.[131] This Li_2CO_3 protective coating improves the ionic conductivity retention of argyrodite in ambient air and enhances stability against high voltage cathodes, demonstrating excellent capacity retention of 90% after 2000 cycles (**Figure 1.22**).

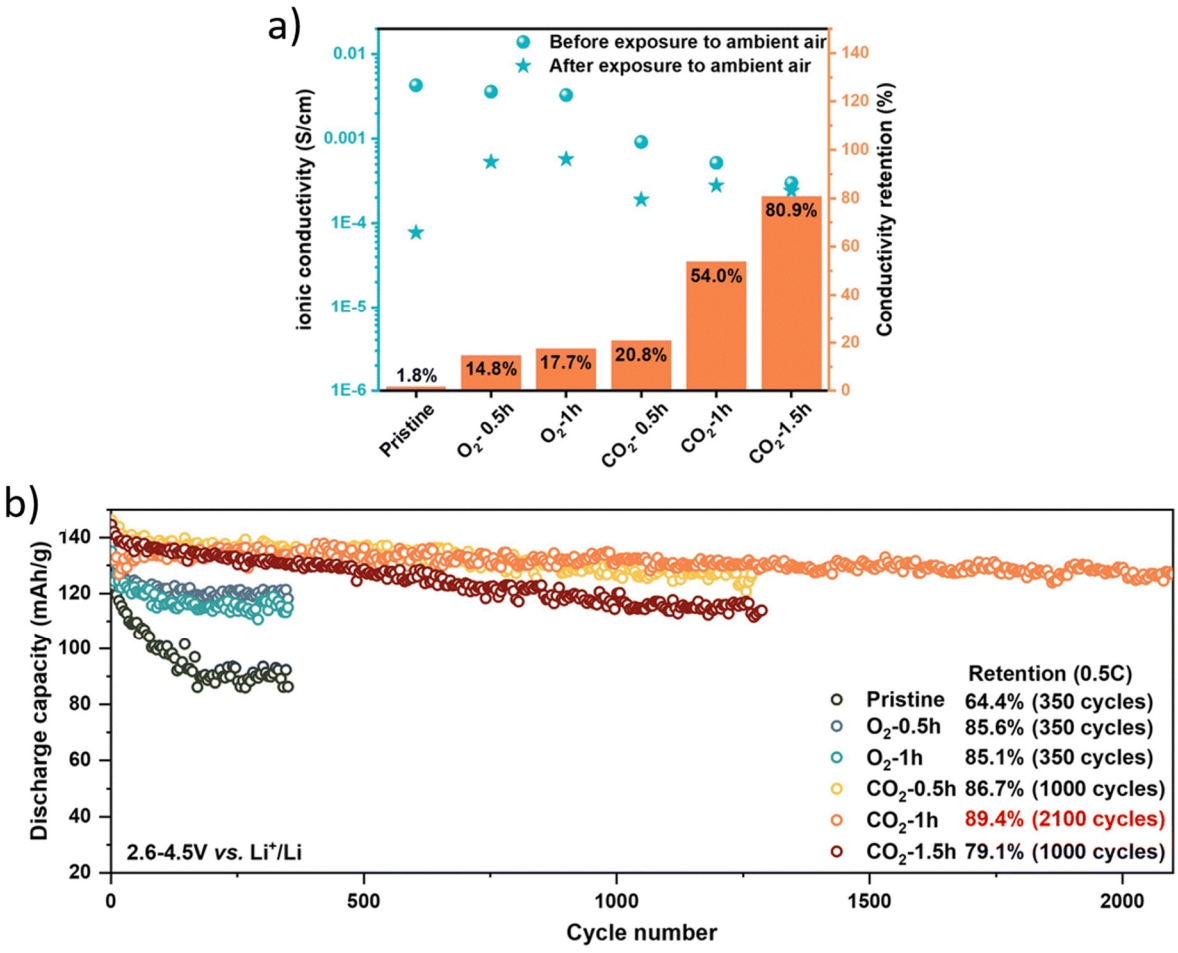

Figure 1.22 (a) Ionic conductivity and conductivity retention (in %) of CO_2 or O_2 gas-treated Li_6PS_5Cl samples before and after exposure to ambient air with a relative humidity of 17% for 1 hour. (b) Long-term cycling performance (0.5C) of $LiCoO_2$ and gas-treated Li_6PS_5Cl cathode composite-based SSBs. Reproduced from reference.[131]

○ Optimization of the cathode composite

The cathode composite is a highly intricate part of the SSB, consisting of up to four materials: the CAM, the SE, an electronically conductive additive (typically vapour-grown carbon fibres – VGCF) and a polymer binder, in the case of sheet-type electrodes. Given their diverse chemical and mechanical properties, understanding their interactions is vital for optimizing formulation and processing. An effective composite must meet several requirements, including achieving high ionic and electronic percolation, maintaining low tortuosity, minimizing porosity, achieving high CAM loading while minimizing the presence of electrochemically inactive components (SE, conductive and polymer additives). Ultimately, it should result in a SSB delivering high energy and power density with loading levels aligning with industrial standards (> 5 mAh.cm^{-2})[132], thereby enabling competitive performance against current LIBs.

To ensure the maximum utilization of the CAM, fine-tuning of the CAM:SE ratio and their respective particle size is of paramount importance. Both theoretical and experimental studies show how these parameters influence tortuosity and ionic-electronic percolation within the composite cathode.[44,133,134] **Figure 1.23** displays a visualization of a modelled CAM:SE mix of spherical particles and highlights the need for a minimal amount of SE (> 25 vol.%) and critical maximum particle size ratio of $\lambda = \frac{D_{CAM}}{D_{SE}} \geq 1.5$ ($D_{CAM} = 5\ \mu m$).

The morphology of the CAM particles is also crucial, with a choice between monolithic and polylithic structures.[135] Polylithic particles, formed by the agglomeration of small primary particles with different orientations, are typically used for LIBs but pose challenges in SSBs due to a lack of mechanical integrity during cycling and the inability of the SEs particles to recover the contact, unlike liquid electrolytes.[135] Monolithic particles are thus favoured for SSBs.

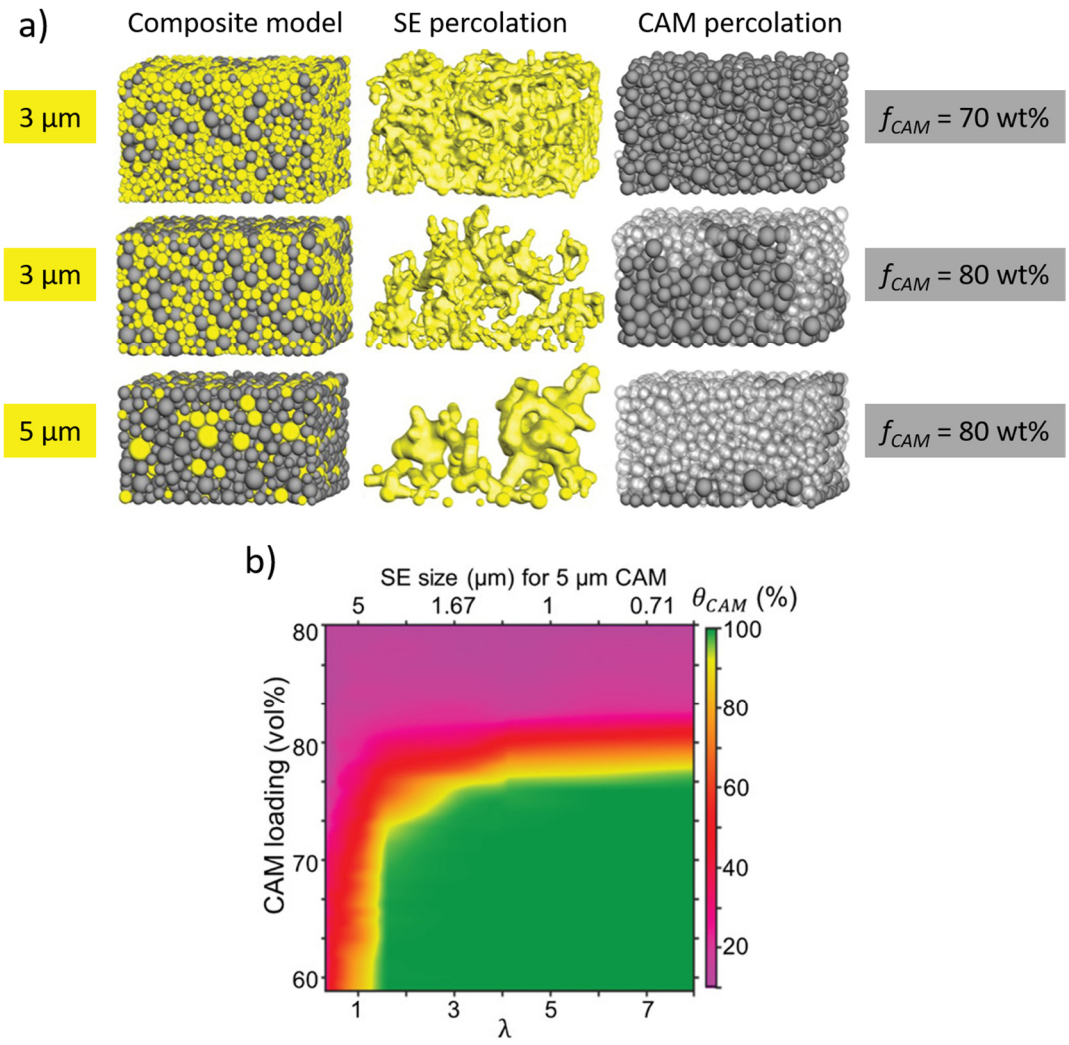

Figure 1.23 (a) Visualization of modelled cathode composites, with various SE particle size and CAM loading, and the resulting SE and CAM percolations. (b) Computed CAM utilization ($\boldsymbol{\theta_{CAM}}$) as a function of CAM loading and $\boldsymbol{\lambda}$. Adapted from reference.[44]

Ensuring intimate and durable solid-solid contacts within the cathode composite is essential and mostly determined by the mechanical properties of the SE. To withstand the stresses generated by significant volume change during (de-)lithiation of the CAM (up to 7%)[41], the SE should be easily deformable. A recent theoretical study by Farzanian *et al.*[60] emphasises the critical role of hardness (resistance to localised plastic deformation) and elasticity (ability to reversibly deforms) in the occurrence of mechanical defects at the CAM:SE interface over cycling (porosity, contact loss and volume expansion). They conclude that an SE displaying low elastic and hardness moduli should minimise the appearance of such defects and allow for lower external pressures during cell operation (**Figure 1.24**). Li_6PS_5Cl is already a promising candidate for low-pressure cycling thanks to its ductile nature, contrary to brittle LLZO.

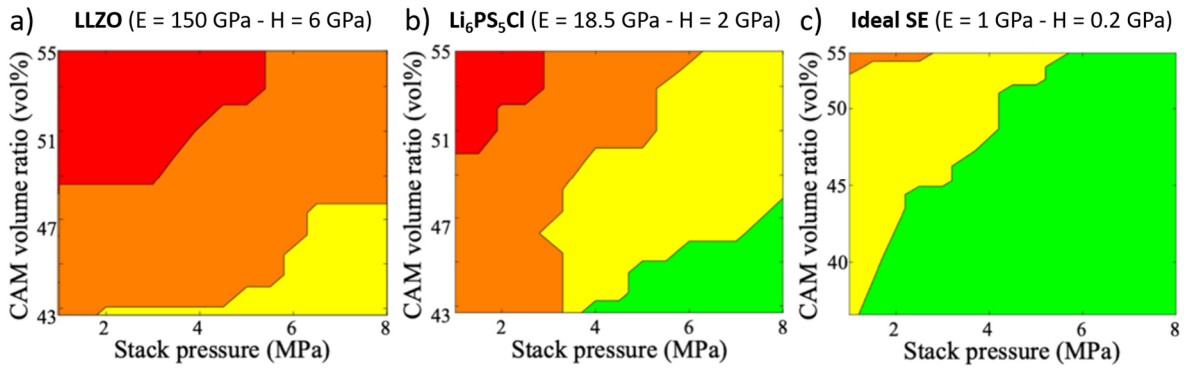

Figure 1.24 Design principle for an NMC-based cathode composite with (a) LLZO, (b) Li_6PS_5Cl, and (c) a SE with a low Young's modulus (E) and hardness (H). The contour in each plot represents the degree of defect in the cathode composite from green (no defect) to red (four defects). Adapted from reference.[60]

It is clear that the formulation of the cathode composite, including the choice of particle size, the SE's mechanical properties and the ratio of the different components, determines the performances of the SSB under practical conditions. However, the processing method also plays a decisive role by influencing the microstructure of the final electrode.

○ Processing of self-standing films

Different options are available to prepare a cathode composite, but every one of them should ensure a homogeneous repartition of the different components with minimal porosity and maximum interparticle contact. Dry processing remains the most common technique used at the laboratory scale and generally consists in hand grinding the CAM, the SE and the carbon additive using an agate mortar and a pestle. Despite being easy to implement, this approach lacks repeatability from the operator and ability to upscale.

That is why current research is exploring an alternative way consisting in the ball milling of powders.[136] This technique involves many parameters (rotation speed, mass of powder, number and characteristic of balls, milling duration, etc.) and requires precise engineering to achieve the required reproducibility and composite quality for large-scale manufacturing. A promising recent development relies on the mechano-fusion advanced technique to prepare high CAM loading composites with enhanced CAM:SE contacts (**Figure 1.25**).[137] The high shear and compression forces enable the formation of a thin coating layer of SE on the surface of the CAM. Thanks to these optimised contacts, a significant improvement of the performances despite the reduction of both the SE content (up to 10 wt.%) and the operating pressure (down to 3 MPa) was made possible.

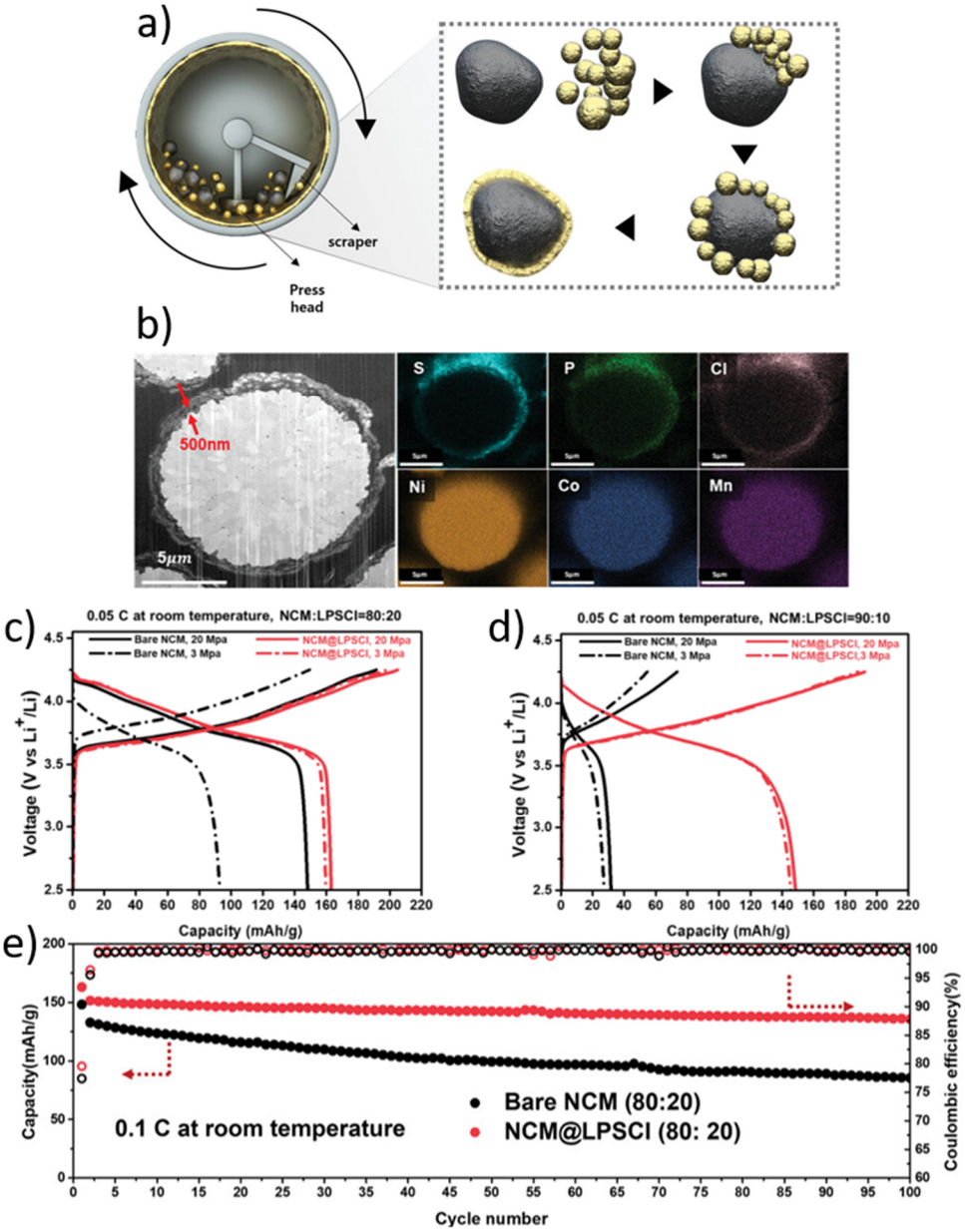

Figure 1.25 (a) Illustration of the mechano-fusion process. (b) FIB cross section of NMC:Li_6PS_5Cl = 80:20 (w) composite electrode observed with SEM and the corresponding EDS mapping. First galvanostatic cycles of bare NMC and NMC: Li_6PS_5Cl composite electrode at 20 and 3 MPa with NMC to Li_6PS_5Cl ratios of (c) 80:20 and (d) 90:10 and (e) capacity retention of the 80:20 ratios. Adapted from reference.[137]

To meet industrial standards, a shift from pellet-type to sheet-type batteries is necessary in order to increase the cell-level energy density and the feasibility of large area SSBs. At the laboratory scale, cells are assembled by compacting powders, firstly of the separator and subsequently of the electrodes (**Figure 1.26a**).[138] This design results in low energy density cells because of thick pellets, which cannot apply to large area batteries.

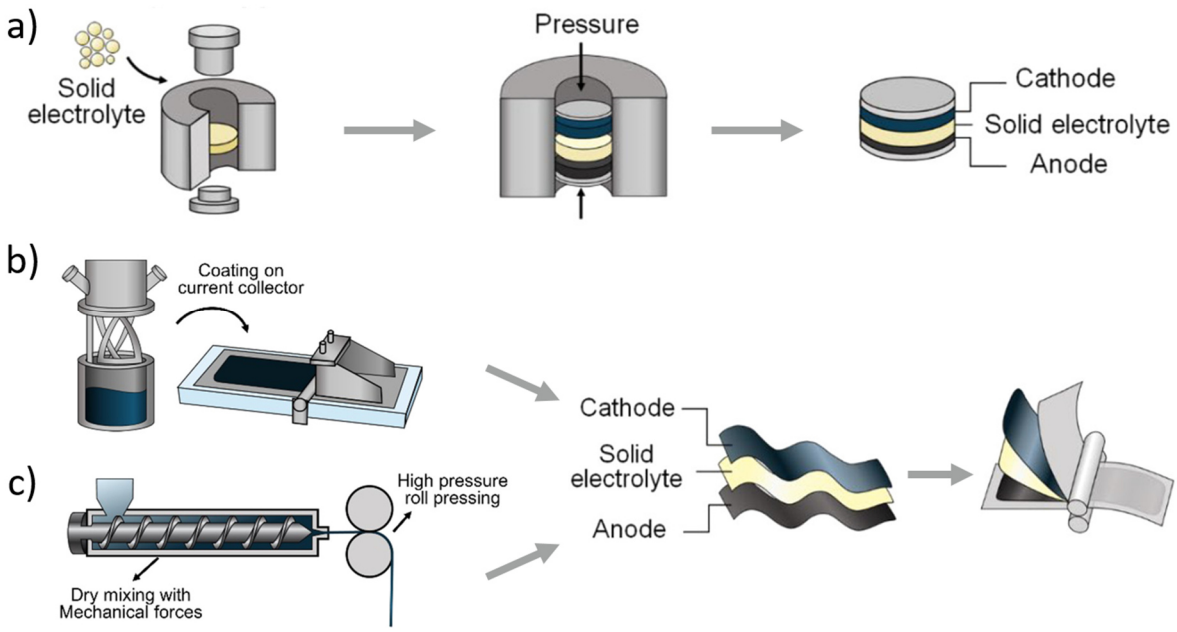

Figure 1.26 Schematics of a cell fabrication with a pellet-type design (a) or a sheet-type architecture via a wet route (b) or a dry process (c). Adapted from reference.[138]

Taking inspiration from the current LIBs manufacturing process, the production of sheet-type electrodes and separator would be more practical and more compatible with existing LIB production lines. The addition of a polymeric binder is then necessary to ensure their mechanical cohesion and easy handling. Its incorporation can be either achieved through a dry process, involving extrusion of powders (**Figure 1.26c**), or a wet process, consisting in the preparation of a slurry which is subsequently coated on a substrate (**Figure 1.26b**).

The dry process of electrodes and separator requires a polymer that has the ability to spread through the particles and bind them together without the help of a solvent. In this regard, polytetrafluoroethylene (PTFE) is the most promising candidate thanks to its fibrillation characteristics (**Figure 1.27a**). A two-steps process is required, involving the high shearing mixing to initiate binder fibrillation and ensure its good repartition, followed by the roll pressing of the paste to obtain the film. Following this strategy, Hippauf *et al.*[139] reported the fabrication of a self-standing cathode containing only 0.1 wt.% binder (**Figure 1.27b**) with a high areal capacity of 6.5 mAh.cm^{-2}, demonstrating cycling performances comparable to a binder-free cathode.

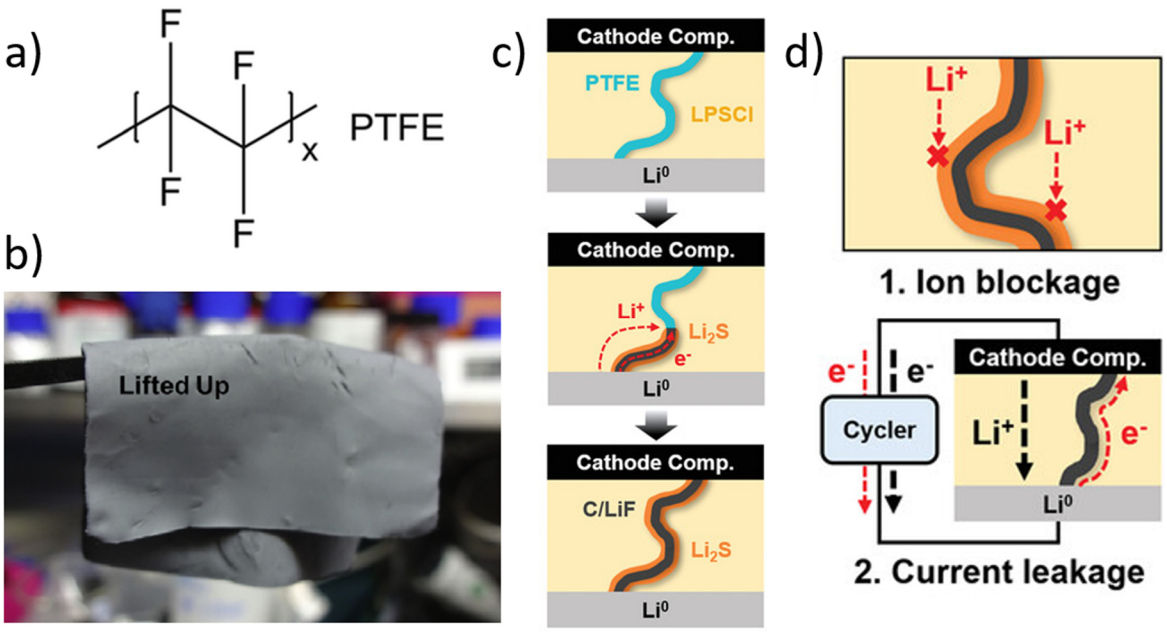

Figure 1.27 (a) Chemical formula of polytetrafluoroethylene (PTFE). (b) Free-standing film of NMC:Li_6PS_5Cl cathode composite using 0.3 wt.% of PTFE binder. (c) Schematic of the proposed reduction mechanism of PTFE in SE film contacting Li metal and (d) the resulting possible failure mechanisms. Reproduced from references.[139,140]

However, PTFE cannot be used in the separator and be in direct contact with a low-potential anode, like lithium metal. Indeed, the fibres are defluorinated following a reduction reaction leading to the formation of LiF and conductive carbon species. The resulting network of reduced PTFE forms an electronic pathway through the SE separator and ultimately leads to the cell failure (**Figure 1.27c-d**).

The other strategy to manufacture sheet-type electrodes and separator is the wet route, relying on the use of a solvent as the dispersing and spreading medium. After mixing the powders and the binder solution, the obtained slurry is coated with a doctor-blade on a current collector, when preparing electrodes, or on a plastic substrate, when preparing the separator. The main challenge lies in identifying the adequate solvent-binder pair. First, the binder must be soluble in the solvent. Second, the SE has to be chemically stable versus the solvent. Third, the binder must provide satisfactory mechanical properties to obtain a self-standing film or sufficiently adhesive electrodes. The main limitation of sulphide SEs is their dissolution occurring in polar solvents, with a collapsing of their lattice structure, resulting in a drastic loss of ionic conductivity.

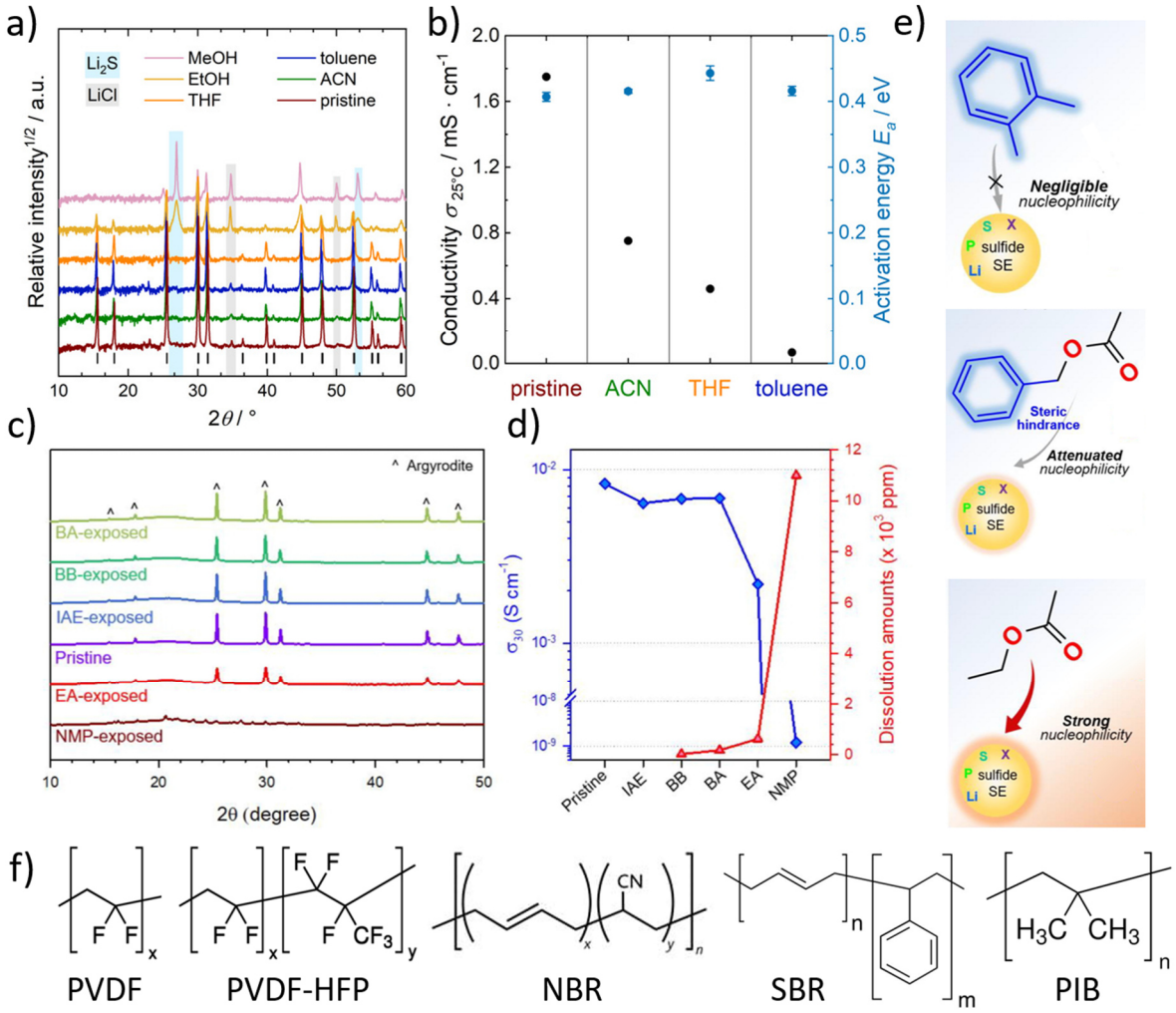

Figure 1.28 Chemical compatibility of Li_6PS_5Cl with various solvents (methanol – MeOH, ethanol – EtOH, tetrahydrofuran – THF, toluene, acetonitrile – ACN, benzyl acetate – BA, butyl butyrate – BB, isoamyl ether – IAE, ethyl acetate – EA, N-methyl pyrrolidone – NMP). (a), (c) XRD patterns and (b),(d) ionic conductivity of solvent-exposed argyrodite samples. (e) Schematics illustrating nucleophile interaction of Li_6PS_5Cl with o-xylene, benzyl acetate and ethyl acetate (from top to bottom). (f) Typical binders for SSBs. Adapted from references.[40,141]

In the same time, polar solvents are favourable to dissolve binders displaying good adhesion and cohesion properties, which highlights the necessity of trade-off in the tape formulation. Stability of argyrodite with various solvents have been reported (**Figure 1.28**).[40,141] The usual ones for electrodes manufacturing are not suitable for Li_6PS_5Cl processing (NMP, ethanol, tetrahydrofuran, acetonitrile, etc.) since they are too polar and display a strong nucleophilicity with these inorganic particles. One promising family of solvents is the alkyl-esters, which are able to solubilise suitable binders, including poly(vinylidene fluoride-co-hexafluoropropylene) – PVDF(-HFP) – and rubbers – styrene or nitrile butadiene rubber (SBR, NBR). However, the presence of bulky groups (linear or branched alkyl chains, aromatic cycle) is mandatory to

weaken the nucleophilicity and ensure the retention of ionic conductivity. Xylene solvent can also dissolve apolar binders, including polyisobutylene (PIB) and the aforementioned rubbers, and is inert towards Li_6PS_5Cl but harmful to the user, contrary to alkyl-esters. Simultaneously, rigorous attention must be paid to the qualitative mechanical properties of the fabricated sheets. This is crucial for the fine-tuning of the binder nature and content, ensuring the production of resilient tapes that can be effortlessly peeled off the substrate, particularly in the context of self-standing separators. An alternative strategy to ensure higher cohesion is to reinforce the self-standing separator layer with a structural backbone, such as a nonwoven polymer scaffold as proposed by Nam *et al.*[142], however at the cost of increased dead mass (14 wt.%) and volume resulting in lower ionic conductivity.

Finding the best compromise for electrode and separator sheets fabrication does not hold a single answer given the variety of solvent and binder available. A recent review on self-standing sulphide-based separators report over thirty different formulations, highlighting the complexity of the matter.[143] After the individual manufacturing of cathode and separator sheets, their following assembly with lithium metal poses additional challenges. The remaining obstacles and the most promising solutions will be explored in the following section.

1.3.2 Assembly and operation of a solid-state battery

o The challenge of lithium metal implementation

The appealing prospect of increasing energy density when shifting from LIBs to SSBs is only possible at the condition of using a high capacity anode, with lithium metal standing out as the optimal candidate (3860 $mAh.g^{-1}$ and 2061 $mAh.cm^{-3}$).[144] However, the processing and integration of lithium metal anodes still entail several difficulties related to chemical compatibility and morphological mismatch at the interface, along with stability of cell operation.

Because of its low redox potential, lithium metal is prone to strong reactivity, especially with components of ambient air (N_2, O_2, H_2O, CO_2) leading to the formation of native passivation layers that contains Li_3N, Li_2O, LiOH and Li_2CO_3.[145] Contamination of lithium is thus difficult to avoid, even in dry room conditions, and can affect the interface stability with the SE.[146] Additionally, the choice of SE is crucial to obtained either a non-reactive (e.g. LLZO) or a self-passivating interface (e.g. Li_6PS_5Cl) with lithium metal.[144] In self-passivating sulphide-

based electrolytes like Li_6PS_5Cl, the main degradation mode of the Li – SE interface stems from current focusing leading to dendrite growth through the separator (**Figure 1.29**). Several factors cause the Li^+ inhomogeneous distribution and instable morphology, including the wettability of lithium with the SE, the interface roughness and the cell assembly.

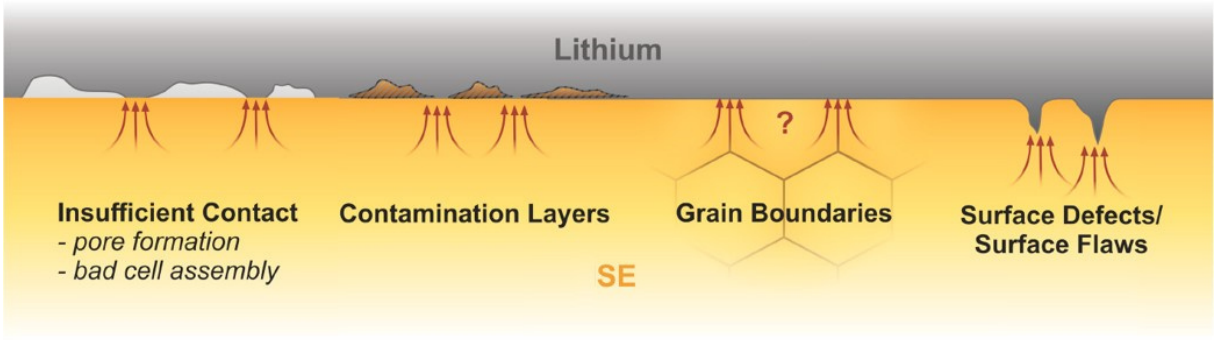

Figure 1.29 Different causes for current focussing at the Li – SE interface. Reproduced from reference.[144]

Addressing the morphological stability of the interface, the applied pressure during assembly and operation plays a crucial role in maintaining proper contact between the solid electrolyte (SE) and lithium metal. As a soft metal with a yield strength of 0.7 MPa[144], lithium undergoes plastic deformation when exposed to pressures surpassing this threshold. Doux *et al.*[47] demonstrated that lithium metal anodes can properly operate at pressures lower than 5 MPa, to avoid mechanical extrusion through the SE separator. However, a minimum pressure (3 – 7 MPa)[33] is necessary to prevent contact losses and pore formation, which can subsequently lead to current focussing and dendrite growth.

Several strategies are being explored to facilitate the integration of lithium metal anode in SSBs. One promising approach involves alloying lithium with other metals such as Ag, Au, Si, Mg, etc.[147] in order to stabilise the cyclability of the anode. In laboratory SSBs research, the indium-lithium alloy is already widely adopted. Its biphasic domain, In + InLi, is characterised by a long voltage plateau at 0.622 V vs Li^+/Li (< 45 at.% Li)[148], making it an ideal candidate for use as a counter electrode in half-cells. Additionally, the alloy becomes brittle once formed, which is convenient for high-pressure cycling, a common practice in SSBs research. However, indium is heavy (7.3 $g.cm^{-3}$ versus 0.5 $g.cm^{-3}$ for lithium), electrochemically inactive and the resulting alloy anode has a higher potential than lithium, rendering it impractical in terms of energy density. Another strategy relies on incorporating an interlayer at the interface between the SE and lithium metal. This interlayer can be metallic (Si, Au,

…)[149,150], inorganic (Li_3N, LiF, Al_2O_3, …)[151,152] or polymeric (PEO:LiTFSI, PEDOT, …).[153,154] The primary objective is to serve as a contact mediator and modify the diffusion properties at the interface, ultimately enhancing the morphological stability. If lithium metal interface with inorganic SEs remains a challenge, the mastering of the interface with PSE has been achieved by Blue Solutions company, which currently commercialise LFP | SPE | Li metal cells.[81] Polymeric interlayers in inorganic-based SSBs hold a lot of promises for practical realization.

From a manufacturing perspective, production and handling lithium metal foils is pose significant challenges. The conventional approach involves the extrusion of lithium ingot followed by roll pressing (**Figure 1.30**).[155] To enhance mechanical resistance, particularly for thin foils (< 20 µm) that are highly fragile, a current collector can be laminated onto the lithium foil. Alternative manufacturing processes are being investigated, taking a bottom-up approach, such as physical vapour deposition (PVD)[156] or slurry coating[157]. However, these alternatives still face scalability issues and encounter challenges with highly divided and reactive lithium metal.

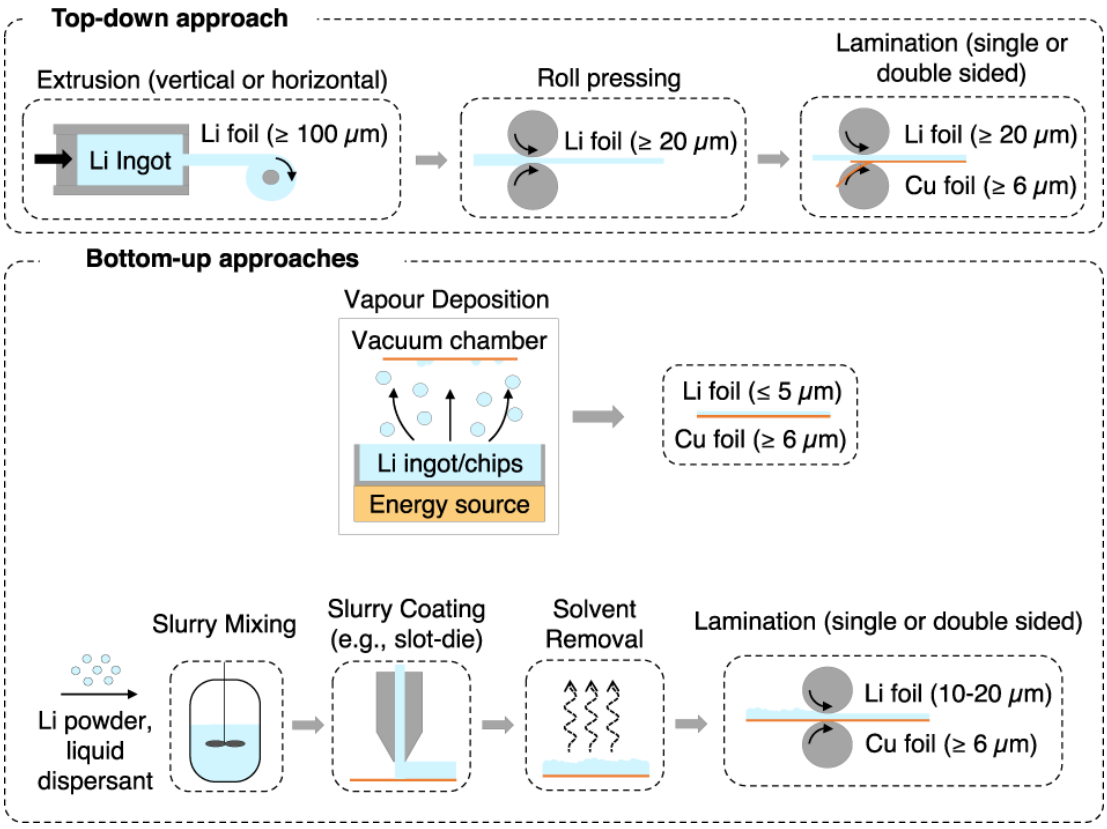

Figure 1.30 Production methods of lithium metal foils. Top-down approach including the extrusion of lithium ingot followed by roll pressing of the obtained foil down to ≥ 20µm. Bottom-up approaches: physical vapour deposition onto a copper current collector, and lithium slurry coating on copper current collector, followed by roll pressing. Reproduced from reference.[155]

Once the three components of the solid-state battery (SSB) are in sheet form (cathode, separator, lithium anode), the next step involves assembling them to create the final stack.

○ Towards pilot scale solid-state battery

Transitioning from laboratory to pilot scale requires additional considerations dealing with pressure application. Indeed, densification of electrodes and separator is essential to reduce the porosity and increase the solid-solid contacts between particles. The shift in cell form factor, from pellets (< 1 cm^2) to large area pouch cells (tens of cm^2), calls for a change in the method of compaction. With typical pellet-type cells, powders are densified at high pressure (> 300 MPa) via uniaxial compression, using a laboratory hydraulic press (**Figure 1.31a** - middle). However, this strategy is inapplicable to pouch cells since the needed tons-force linearly increase with the area, requiring a proportionally larger hydraulic press. To overcome this hurdle, alternative densification techniques must be considered. Calendaring, or line pressing, is widely used in the LIB industry to reduce the porosity in electrodes and could possibly be applied to SSBs, as it stands out in terms of scalability and high throughput (**Figure 1.31a** - left). However, the large forces applied for SSB densification may lead to thickness inhomogeneity and cracks within the sheets. Another technique, called isostatic pressing, is based on an isotropic application of the pressure using a fluid (**Figure 1.31a** - right). It has recently gained increasing interest as it can deeply densify SSBs of any size achieving high homogeneity and improved electrode – separator contacts (**Figure 1.31b**). It can be performed at room temperature (cold isostatic pressing – CIP) or using a heated fluid (warm / hot isostatic pressing – WIP / HIP).[158] The current limitations to this technique are the size of the vessel and the high cost of implementation.

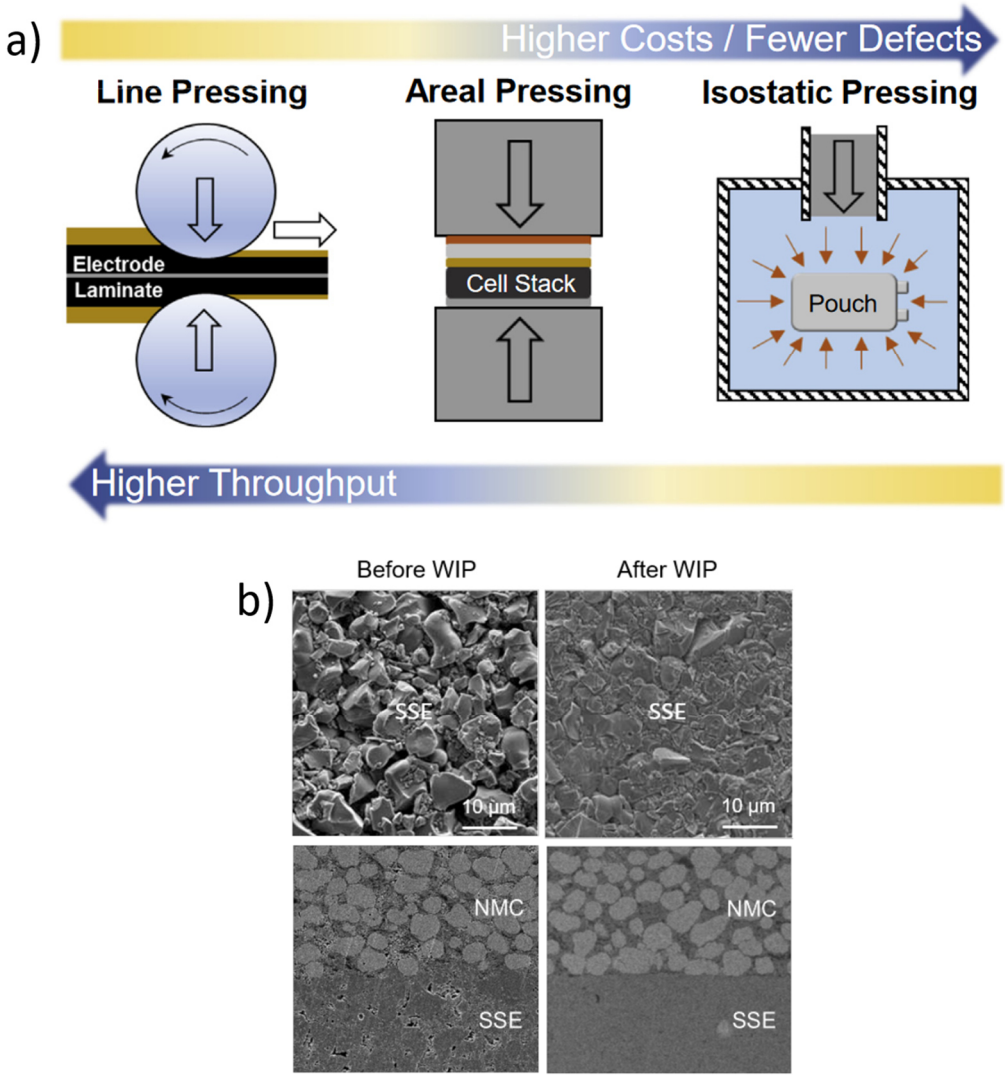

Figure 1.31 (a) Schematic of the three major strategies to achieve densification of pouch-type cells ASSBs. (b) Effect of isostatic pressure on tape solid electrolyte and electrodes. Changes in interfacial properties between each component in the cell after pressurisation using WIP (490 MPa) as observed by SEM. Reproduced from references.[159,160]

Various approaches in the assembly strategy can potentially improve the energy density of the SSB (**Figure 1.32a**). Reducing the SE separator thickness is a requirement to minimise materials' amount without affecting the cell capacity, with 30 µm being the limit to compete with LIBs energy density (**Figure 1.32b-c**). Additionally, a thick cathode electrode (≤ 5 mAh.cm^{-2}) is more attractive concerning energy density than the multiplication of low loading unit cells, as it saves inactive material from current collectors. On the negative side, the use of advanced anode system, including lithium metal, silicon alloy anode and anodeless configuration, is necessary to achieve higher energy densities compared to current LIB technology. In the absence of liquid electrolyte, bipolar stacking is possible in SSB systems. It consists of an arrangement in series of consecutive unit cells, with the anode and the cathode

being placed on opposite sides of a bipolar current collector. This would replace the classical parallel cell stack, which utilises monopolar current collectors that are double-coated with the same electrode. It has the potential to enhance power and energy density *via* inactive material reduction and electron flow homogeneity. However, the main hurdle remains the absence of control of each individual cell potential within the stack, which requires a very high uniformity of cells manufacturing and cycling behaviour.

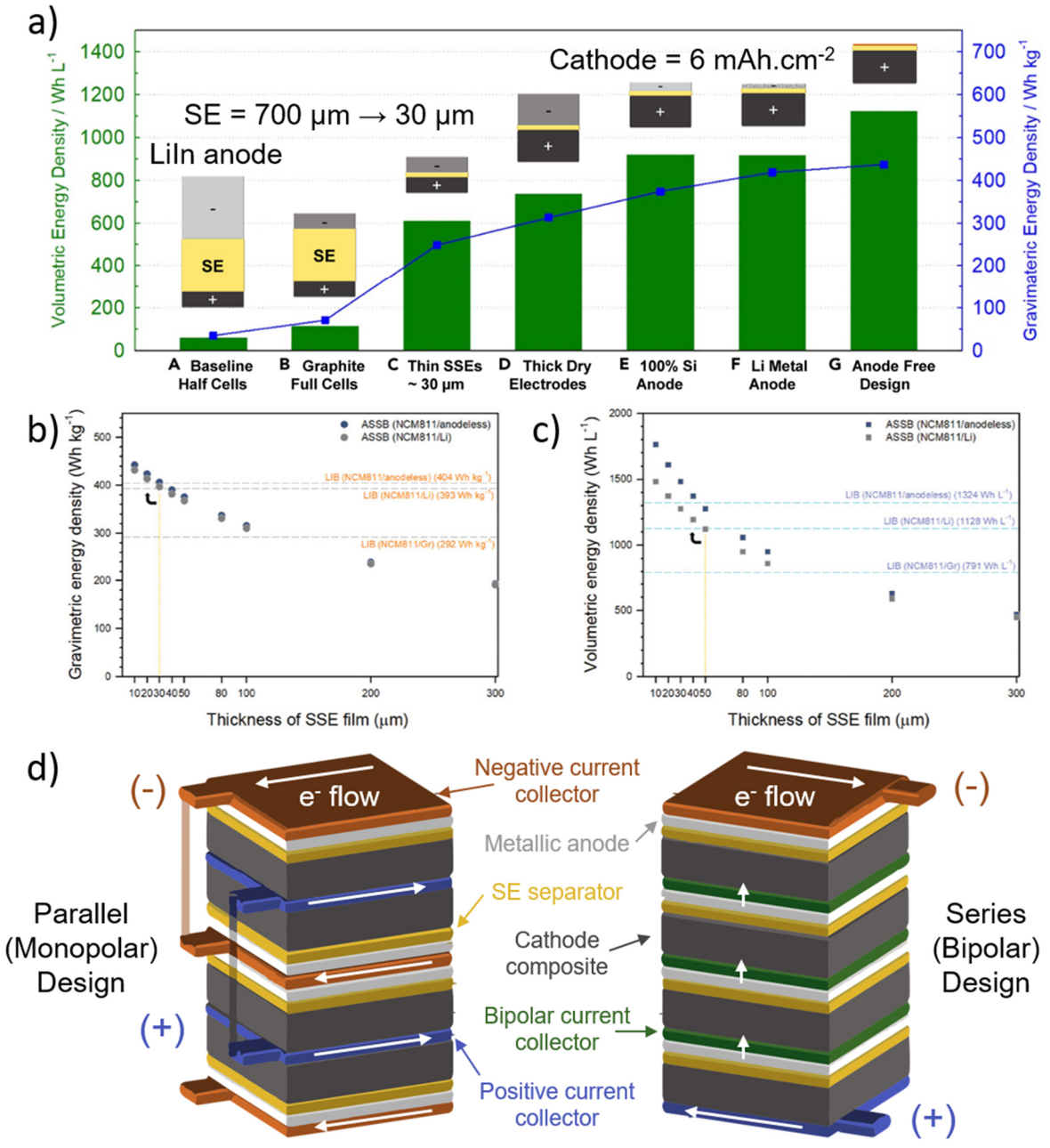

Figure 1.32 (a) Calculated volumetric and gravimetric energy densities as a function of SSB cell parameters and (b,c) as a function of separator thickness. (d) Schematics of parallel (monopolar) versus series (bipolar) stacking design and direction of the electron flow (in white). Adapted from references.[143,159]

After assembly, pressure application remains of particular importance to mitigate contact loss stemming from electrodes volume change. There is no consensus on the required pressure value during SSB operation, as it involves two conflicting criteria: the cathode composite require high pressure to maintain solid-solid contacts (≈ 50 – 200 MPa)[147,161], while the lithium metal anode can only withstand low pressure (≤ 5 MPa) to avoid mechanical extrusion and electrochemically grown dendrites.[33,47] However, the homogeneity of the stack pressure is of paramount importance to ensure repeatability of the performances, especially at low pressure. An adequate SSB module for pouch cell requires both springs and rubber gaskets, for constant and homogeneous pressure application (**Figure 1.33a-b**). In practical applications, the operation of SSBs at high pressures is not a viable option since it requires a significant amount of hardware to apply and maintain such large forces, leading to a drop in the gravimetric and volumetric energy densities at the module level (**Figure 1.33c-d**). A critical size of the system is also needed to compete with current LIB module efficiencies.

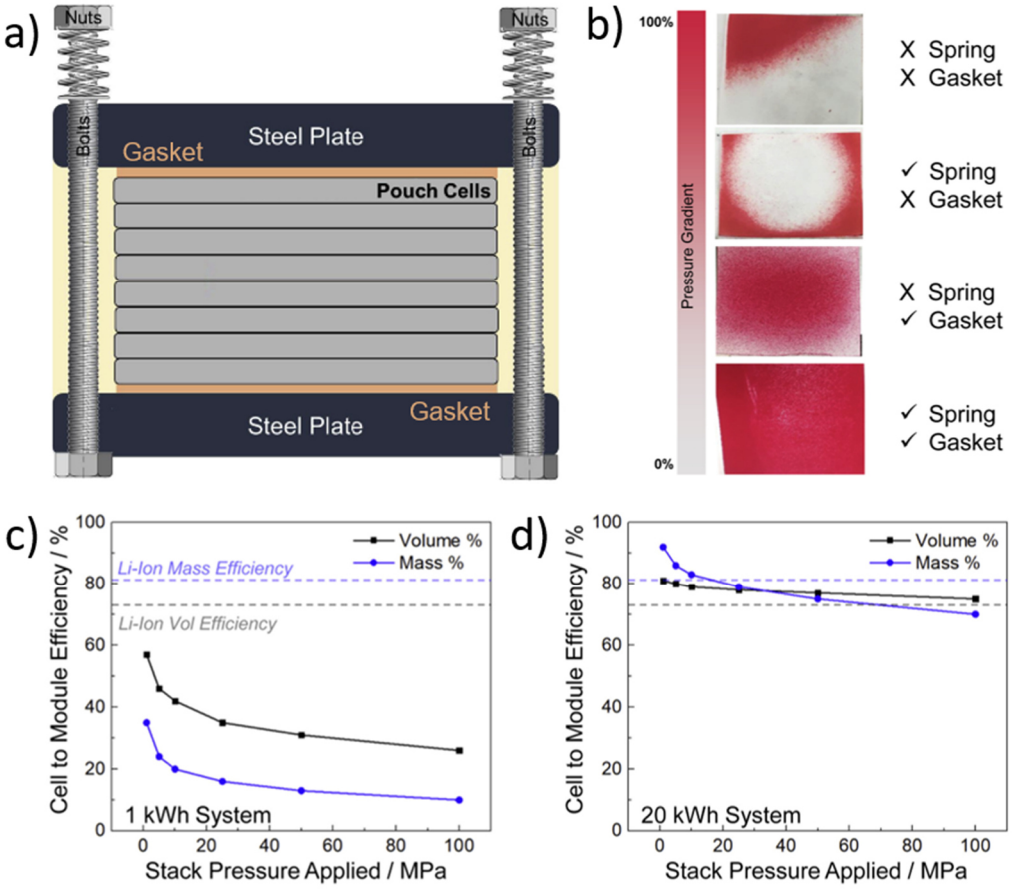

Figure 1.33 (a) Schematic of typical ASSB module assembly under stack pressure. (b) Importance of applying uniform stack pressure with the use of springs and gaskets as revealed with pressure paper. Cell to module conversion efficiencies versus stack pressure based on a system size of (c) 1 kWh and (d) 20 kWh. Li-ion cell to module conversion efficiencies by mass and volume are displayed for reference. Adapted from reference.[159]

As of today, SSBs are at a milestone of their development, transitioning from laboratory scale fundamental understanding to prototyping level where upscaling hurdles are mainly dealt with engineering solutions. A few recent studies attempt to bridge the gap between those two areas by introducing innovative strategies to achieve performances and critical size SSB cells, approaching industrial goals.

1.3.3 State-of-the-art solid state batteries

A pioneering study that achieved a SSB approaching industrial requirements was published in 2020 by Lee *et al.*, an industrial research group.[160] They reported a prototype pouch cell of 0.6 Ah at a moderate pressure (2 MPa), based on an NMC:Li_6PS_5Cl:VGCF high-loading cathode (6.8 mAh.cm^{-2}) and a Li_6PS_5Cl separator in an anodeless system, with no excess lithium. To prevent the formation of dendrites, the authors implemented an innovative interlayer on the anode side, composed of silver nanoparticles and carbon black (**Figure 1.34a**).

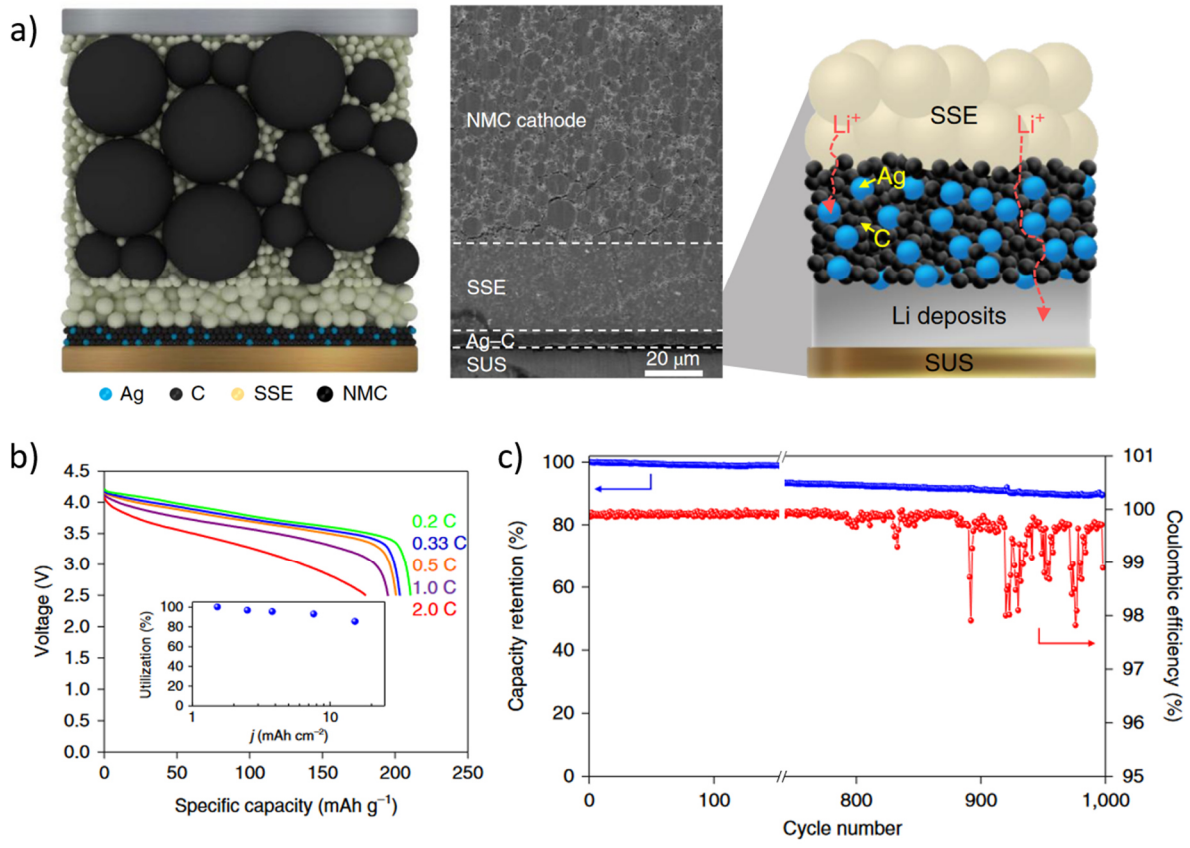

Figure 1.34 (a) Schematic and SEM cross-section of an anodeless SSB implementing the Ag-C interlayer. (b) Rate capability in discharge at 60°C with constant current – constant voltage (CC-CV) mode (C/10 – 4.25V) in charge. (c) Capacity retention and Coulombic efficiency of the 0.6 Ah pouch cell plotted against the cycle numbers. Cycling was done in CC mode at C/2 between 2.5 and 4.25V vs Li^+/Li at 60°C. Adapted from reference.[160]

Taking advantage of the alloying process between lithium and silver, this system enabled homogeneous plating and stripping for over 1000 cycles retaining 89% of the initial capacity, demonstrating long cycle life, high energy density (> 900 $Wh.L^{-1}$) and good rate capability (**Figure 1.34b-c**). It is noteworthy that this is the first study reporting the utilisation of isostatic pressing (490 MPa) during the SSB assembly, highlighting its strength in reducing porosity and improving contacts (**Figure 1.31b**). They also proved the feasibility of manufacturing SSB with sheet-type electrodes and separator, using a PTFE-based dry process for the cathode and a wet process for the separator, with rubber binder, and the interlayer, with PVDF. However, it is crucial to keep in mind that the operation temperature of 60°C is far from practical application and was necessary to obtain a dendrite-free and high-capacity long cycling.

Another breakthrough study for the SSB community came out in 2021 with Tan *et al.*[147] reporting the successful implementation of a silicon anode (**Figure 1.35a**), benefiting from an energy density competitive with lithium metal. They paired it with a Li_6PS_5Cl separator and a high-loading NMC:Li_6PS_5Cl:VGCF cathode (25 $mg_{NMC}.cm^{-2}$ – 5 $mAh.cm^{-2}$) and demonstrated long cycling capability at 1C and 50 MPa, reaching 80% capacity retention after 500 cycles (**Figure 1.35c**).

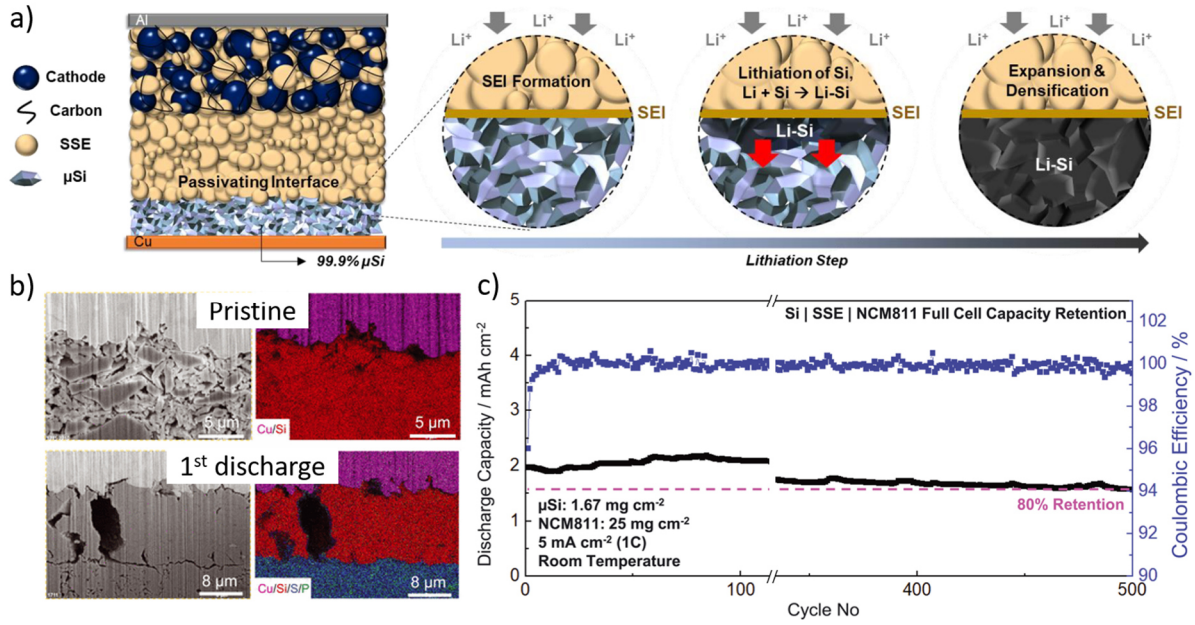

Figure 1.35 (a) Schematics of the NMC | Li_6PS_5Cl | µSi cell and proposed lithiation and SEI formation mechanism. (b) Visualisation of µSi anode densification after first cycle with SEM cross-section and EDS mapping. (c) Long cycling performance of the cell under 50 MPa pressure. Adapted from reference.[147]

However, the fast C-rate implied an utilisation of less than half of the NMC practical capacity (2 vs 5 mAh.cm^{-2}), hiding possible long-term cathode instability. The outstanding performance of the anode relies on the intrinsic property of large volume expansion of silicon during lithiation, resulting in the beneficial densification of the anode after a first cycle at 370 MPa (**Figure 1.35b**).

Concerning lowering of the operation pressure, it is worth mentioning again the study of Kim *et al.* [137] based on the disruptive mechano-fusion technique for the cathode composite preparation. As shown in **Figure 1.25**, they were able to fully retain the cell capacity when shifting from 20 to 3 MPa. Another recently published work succeeded to prepare a sheet-type cathode with PVDF-HFP as a binder and reported a capacity retention of 95% at room temperature after decreasing the operating pressure from 70 to 2 MPa in an NMC | LiIn cell.[162] These studies, among others, reinforce the prospect of operating sulphide-based SSBs at practical low pressures, which remains one of the major impediment.

1.4 – Conclusion of the chapter

In this introductory chapter, we have explored the principles and historical evolution of the widely adopted lithium-ion battery. Driven by the quest of performance, a shift from liquid-based to solid-state batteries has the potential to unlock the current energy density limit, by reintroducing the lithium metal anode. SSBs are currently experiencing significant momentum in both academic and industrial communities, marked by prolific research efforts. However, the promises of improved performance and safety should not overshadow the persistent challenges, notably related to the (electro-)chemical and mechanical stability of solid-solid interfaces.

At the core of SSBs, the solid electrolyte holds most of the issues and solutions, stemming from a wide range of chemistries and their inherent chemo-mechanical characteristics. To illustrate these differences, we conducted a comparative study on two distinct SEs, PEO:LiTFSI and Li_6PS_5Cl. We then explored the potentials and limits of combining SEs, especially polymer and inorganic ones, to create self-standing hybrid solid electrolytes, with a special interest on the interfaces and the resulting conduction mechanism.

Beyond SE improvement, the transition from laboratory to pilot-scale SSBs remains a challenge. Integration of polymer binders for fabricating sheet-type batteries raises questions

about material stability and processing. Lithium metal incorporation and interfacial stability are among the biggest remaining challenges. Moving towards larger-scale batteries calls for a redesign of the assembly and operating procedures to achieve the long-awaited SSB performances. Innovative researchers are addressing these challenges by introducing innovative cell designs, getting closer to the practical application.

Playing our part in this challenging enterprise, this thesis will initially focus on the formulation of hybrid solid electrolyte in **Chapter 2**, exploring their strengths and weaknesses. Shifting from conductive polymer electrolytes to non-conducting polymer binders, **Chapter 3** will delve into the fabrication of sheet-type battery components and their assembly in pouch cell SSBs operating at low pressure.

Chapter 2 – Meaningful metrics for an efficient formulation of polymer – argyrodite hybrid solid electrolyte

2.1 – Introduction

In the previous chapter, we introduced solid-state batteries (SSBs) which have gathered significant attention thanks to their potential performance enhancement. However, they are still constrained by several difficulties regarding the processing of the materials, which lacks the possibility to scale up. Especially, the different families of solid electrolytes (SEs) come with their own set of advantages and limitations. Inorganic SEs are generally good ionic conductors but suffer from their brittle nature, while polymer SEs (PSEs) often display poor conductive properties but stand out in terms of processing. Since a single SE cannot display both sufficient conductivity and desirable mechanical properties, one strategy consists in the hybridisation of these SEs to achieve a synergy. This approach has been extensively explored in the literature, yet no general tendency has emerged and materials synergy is not always achieved.[163] This stems from the various formulations and results reported, often lacking a rational formulation study, which is essential for understanding the governing parameters and the underlying conduction mechanism.

Thus, to fill this gap, this chapter presents a systematic formulation of a hybrid solid electrolyte (HSE) based on two widely used and easily available SEs: the salt-in-polymer PEO:LiTFSI (poly(ethylene oxide) and lithium bis(trifluoromethanesulfonyl)imide) and the sulphide-based argyrodite Li_6PS_5Cl. The primary objectives of this work are to meet two practical criteria: achieving sufficient HSE ionic conductivity (10^{-4} S.cm^{-1} at RT) and the ability to prepare a self-standing film. Various parameters will be systematically explored and adjusted, including the salt concentration, the polymer molar mass and the organic-to-inorganic ratio. We will give special attention at understanding the Li^+ conduction mechanisms involved and correlating them with the nature of the internal reactivity of the HSE. Finally, the study will delve into the practical applications of such HSE, from dry room manufacturing to its cell cycling performance.

2.2 – Formulation of the HSE by the optimization of selected metrics

2.2.1 Characterisation of the precursor electrolytes

To lay the groundwork for the HSE study, we initially conducted a characterisation of the precursor electrolytes, encompassing studies on ionic conductivity, morphological features, thermal behaviour and chemical properties.

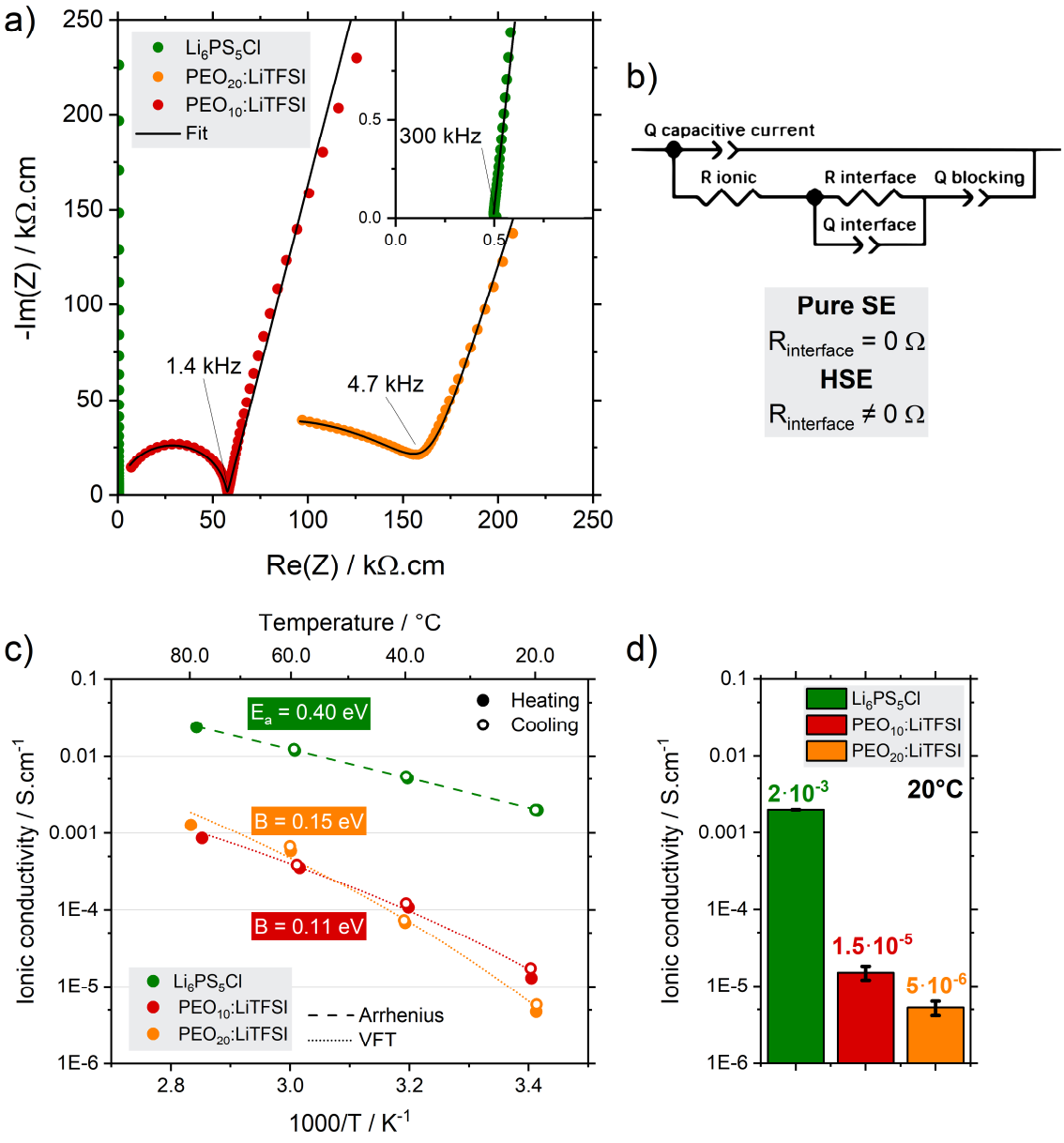

Figure 2.1 Ionic conductivity characterisation of the precursor electrolytes. (a) EIS spectra at 20°C normalised by the pellet (Li_6PS_5Cl – e = 1.2 mm) or the film (PEO_x:LiTFSI – e = 50 – 100 µm) form factor and their related fit. (b) Model fitting the EIS data in ion-blocking electrodes configuration. Details are available on **Scheme S2.1**. (c) Temperature-dependant ionic conductivity, in the range of 20 – 80 °C, fitted according to the adequate activation mechanism (Arrhenius or VFT) and the associated (pseudo) activation energy E_a (or B). (d) Ionic conductivity at 20°C averaged over heating and cooling steps.

We first confirmed the ionic conductivity and the activation mechanism associated to the precursor electrolytes by performing electrochemical impedance spectroscopy (EIS) in temperature (**Figure 2.1**). Using dedicated cells for pellet (Li_6PS_5Cl) or film (PEO:LiTFSI) characterisation (**Figure S2.1**) could obtain reliable impedance data in an ion-blocking electrodes configuration, and extract the ionic resistance by model fitting. Starting with commercial argyrodite powder (Li_6PS_5Cl – NEI corporation), we confirmed excellent ionic conductivity at 20°C (2 $mS.cm^{-1}$). The activation mechanism follows the Arrhenius law with an activation energy of 0.40 eV, in good agreement with previous studies.[40,87] The dependence of ionic conductivity in temperature is described by the following equation (details available in section **1.2.2**):

$$\sigma = \frac{\sigma_0}{T} \cdot \exp\left(-\frac{E_a}{k \cdot T}\right) \qquad \textbf{Equation 2.1}$$

where σ_0 is the pre-exponential factor, E_a the activation energy and k the Boltzmann constant.

The morphology of the particles was observed by scanning electron microscopy (SEM – **Figure 2.2**) and revealed a wide range of particle size, from 30 to less than 1 µm in diameter. The presence of large particles and its consequence on HSEs preparation will be further discussed in the following sections of this chapter.

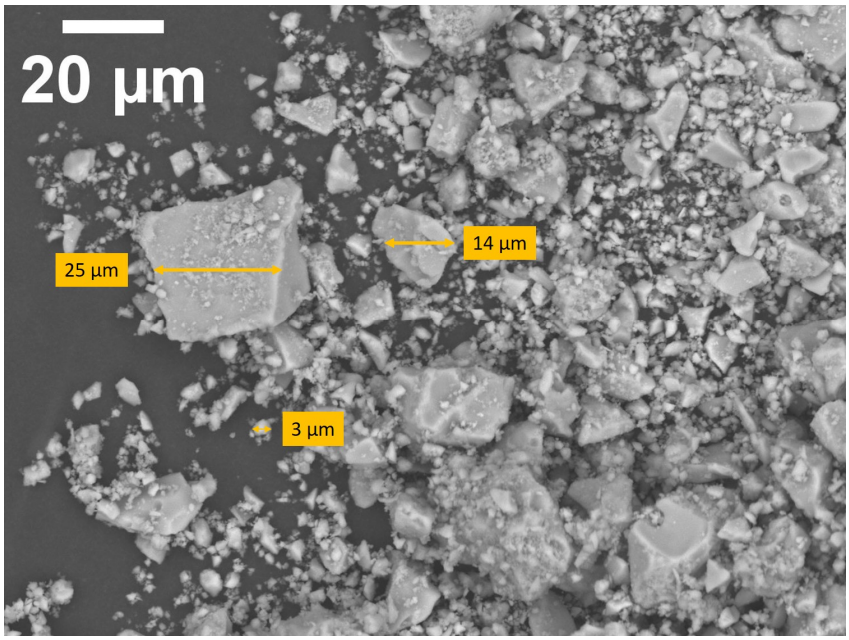

Figure 2.2 Morphological aspect of Li_6PS_5Cl powder observed by SEM, with particle size ranging from 30 to 1 µm.

Moving to the PSEs, we prepared them following a solvent-free route. The dissolution of LiTFSI (99.9 % purity) in high molar mass PEO (M = 600 kg.mol^{-1}) was done by applying shear forces to the materials, in an agate mortar with a pestle. The resulting gums were subsequently hot-pressed at 80°C several times, to ensure their homogeneity, and translucent thin films were obtained (e ≈ 50 – 100 µm). In accordance with literature, a higher salt concentration (EO:Li = 10:1 – C_{Li} = 2.0 mmol.cm^{-3}) results in a higher room temperature ionic conductivity (**Figure 2.2c**). Varying the temperature, the conductivity data fit well with the empirical model of Vogel-Fulcher-Tammann (VFT - **Figure S2.2**), confirming a lower pseudo-activation energy B with a higher salt concentration (**Figure 2.1b**).[89,94] The VFT model equation is recalled here (details available in section **1.2.2**):

$$\sigma = \frac{\sigma_0}{T} \cdot \exp\left(-\frac{B}{k \cdot (T - T_0)}\right) \qquad \textbf{Equation 2.2}$$

In this equation derived from the Arrhenius model, B is the pseudo-activation energy and T_0 is the Vogel temperature, equal to T_g in ideal glasses but generally set 50°C below T_g for salt-in-polymer complexes, such as PEO:LiTFSI.

Thermal analysis (**Figure 2.3**), performed with differential scanning calorimetry (DSC), confirmed that the increase of room temperature conductivity is due to the disappearance of pure PEO crystalline domains, which are poorly Li^+-conductive. With an EO:Li ratio of 10, the degree of crystallinity χ_c drops to 1% while remaining at 67% with a less concentrated electrolyte (EO:Li = 20:1 – C_{Li} = 1.1 mmol.cm^{-3}). Additionally, this experiment shows that Li_6PS_5Cl is stable in the -70 – 200°C temperature range, with the absence of thermal event.

Lastly, the surface chemistry of the precursor electrolytes was probed by X-ray photoelectron spectroscopy (XPS – **Figure 2.4**). No contamination was detected since only expected peaks were observed and assigned to the PS_4^- unit for Li_6PS_5Cl (S2p) and to LiTFSI functional groups ($-SO_2CF_3$ on S2p and $-CF_3$ on F1s). This is in accordance with the expected values obtained with EIS and DSC measurements.

Considering its ionic conductivity and absence of crystallinity, the highly-concentrated PEO_{10}:LiTFSI was selected as the organic phase for the subsequent HSE preparation. This choice aims to maximise the ionic conductivity of the HSE, given that the PSE serves as the limiting phase in conduction. Moreover, the presence of inorganic particles will not disrupt the crystallinity of the already amorphous PSE.

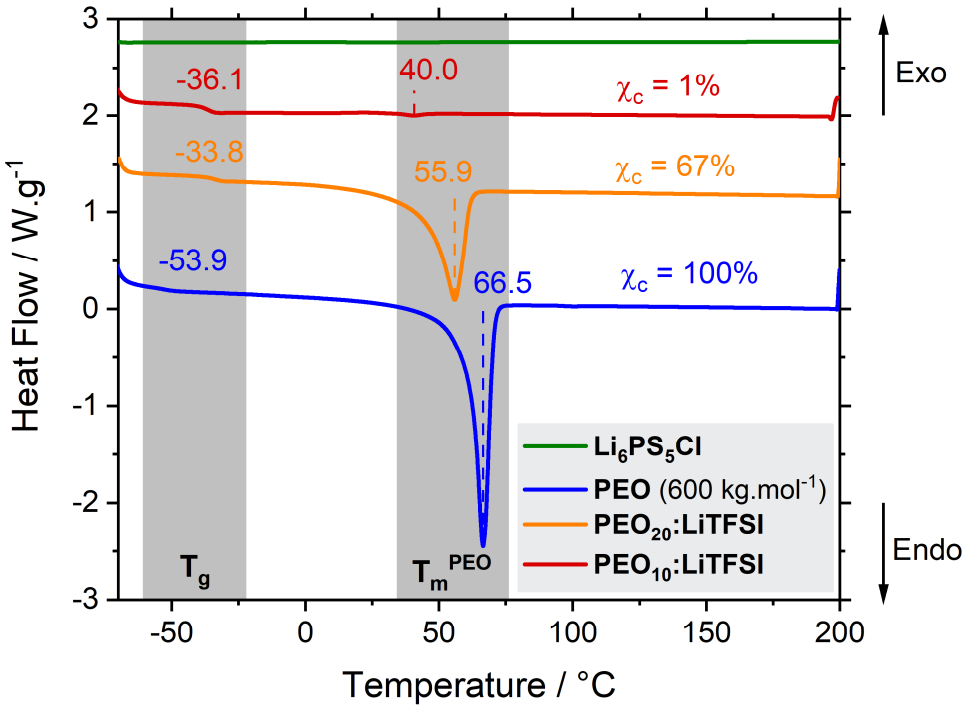

Figure 2.3 Thermal analysis of the precursor materials by DSC with a heat rate of 10°C.min^{-1} in argon atmosphere. Identification of the glass transition (T_g) and melting (T_m^{PEO}) temperatures, with the calculated degree of crystallinity (χ_c).

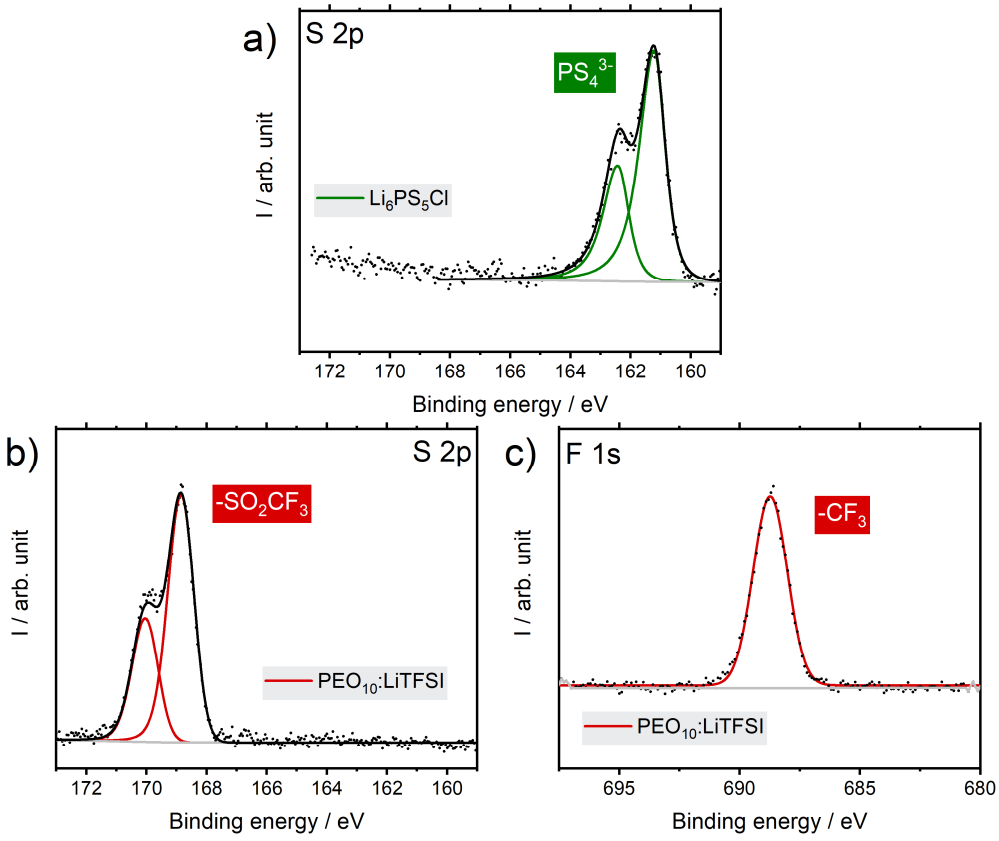

Figure 2.4 Surface chemistry of the precursor electrolytes probed by XPS analysis. (a) S2p spectrum of Li_6PS_5Cl. (b) S2p spectrum of PEO_{10}:LiTFSI. (c) F1s spectrum of PEO_{10}:LiTFSI.

2.2.2 Choice of the preparation route

To prepare composite materials, two distinct strategies can be considered to obtain an intimate mixing of the materials: with or without the assistance of a solvent. To determine the most suitable option, we conducted both for comparison. The wet route involves the use of a solvent to disperse the inorganic particles and dissolve the polymer and salt.[111] For this, we employed tetrahydrofuran (THF – dried over molecular sieves 4Å) to prepare the slurry that was then casted to form a film after drying.[88] The alternative route is based on the dry mixing of the powders, applying high shear forces and/or temperature.[164] We conducted both strategies to prepare an HSE based on 60 wt.% of PEO_{10}:LiTFSI and 40 wt.% of Li_6PS_5Cl. No significant effect could be disclosed according to the measurement ionic conductivity at 20°C (**Figure 2.5a**). However, the XPS analysis reveals a degradation process initiated through the wet route. Additional species, including polysulphides ($-S_x^0-$) and lithium fluoride (LiF), are identified in the S2p and F1s domains (**Figure 2.5d-e**). They remain absent on the dry route XPS data which display only the contribution attributed to both initial phases of the HSE (**Figure 2.5b-c**).

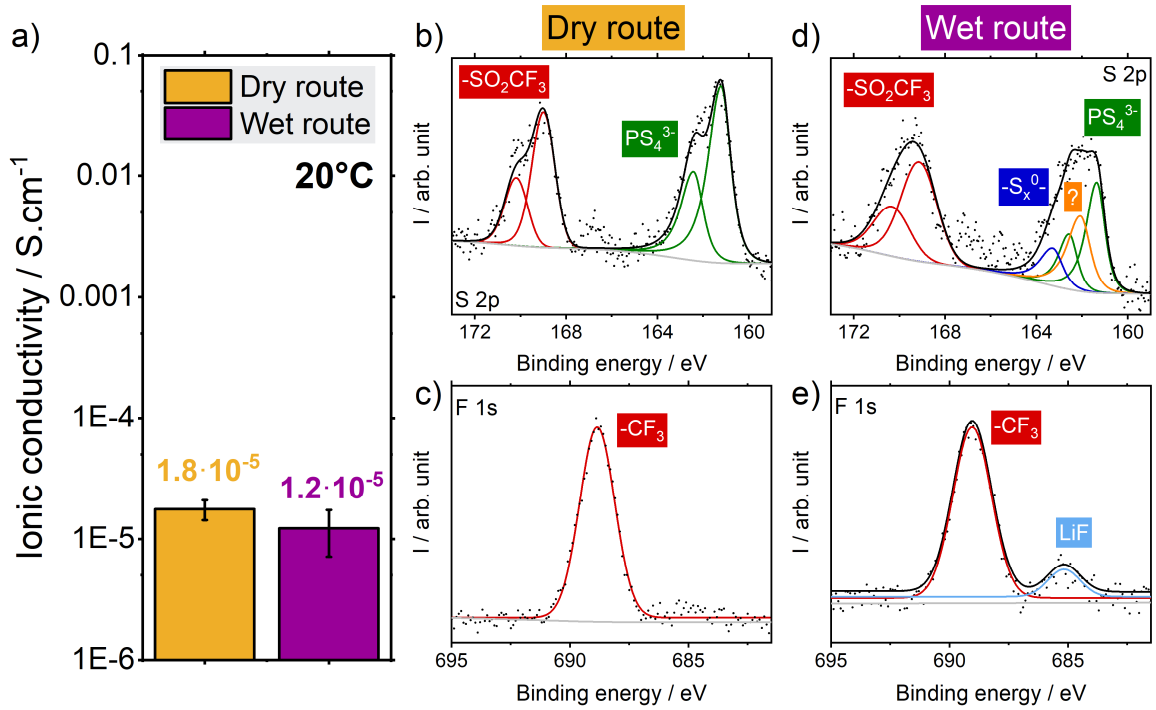

Figure 2.5 Comparison of dry and wet routes in the preparation of an HSE (PSE:ISE = 60:40 – w). (a) Ionic conductivity at 20°C. (b) S2p and (c) F1s XPS spectra for dry route. (d) S2p and (e) F1s XPS spectra for wet route.

Based on these preliminary findings, we decided to select the dry route strategy for the rest of the study on HSEs. However, this result could have been anticipated as the instability of argyrodite toward THF was already reported ($\sigma_{pristine}$ = 1.7 mS.cm^{-1} versus σ_{THF} = 0.46 mS.cm^{-1} at 25°C).[40]

2.2.3 Understanding the role of the organic-to-inorganic ratio

Following the dry route strategy, we prepared HSEs covering the whole range of organic-to-inorganic ratio (from 20 to 95 wt.% of Li_6PS_5Cl in PEO_{10}:LiTFSI). The mechanical properties of the films obtained differ according to the quantity of ceramic particles. HSEs with an inorganic content of 60 wt.% (56 vol.%) or less are flexible, self-supporting films (**Figure 2.6a**). On the other hand, HSEs with more than 75wt.% (72 vol.%) Li_6PS_5Cl are not cohesive and the resulting material is brittle (**Figure 2.6b**). Depending on the ratio, the prepared films exhibit a mechanical behaviour close to either a polymer (≤ 60 wt.% ceramic) or a ceramic (≥ 75 wt.%). Scanning electron microscopy (SEM) images of the HSE cross-sections show a homogeneous distribution of the ceramic particles within the organic matrix at a large scale (> 100µm) (**Figure 2.6c-f**). However, heterogeneity is significant at the micron level, mostly due to Li_6PS_5Cl particle size ranging from 1 to 30 µm (**Figure 2.2**) and the ease of mixing, resulting in increased roughness for HSEs with high inorganic content.

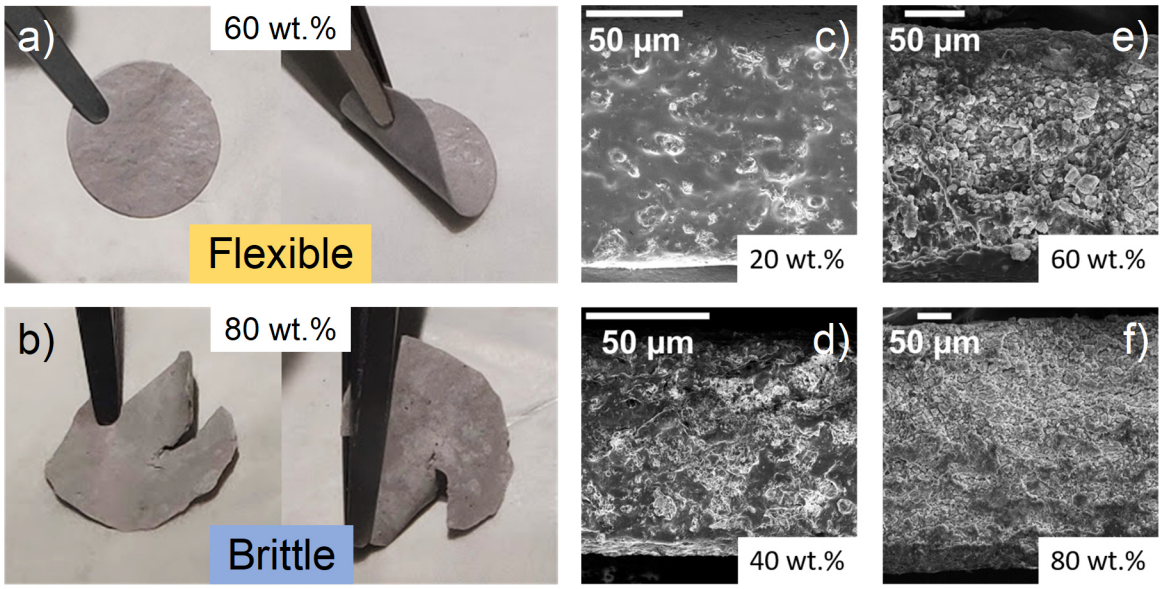

Figure 2.6 Influence of organic-to-inorganic ratio on HSE preparation. Images of (a) flexible HSE (60 wt.% Li_6PS_5Cl) and (b) brittle HSE (80 wt.% Li_6PS_5Cl). (c) to (f) SEM cross-section pictures of HSE according to the ceramic content.

We then performed ionic conductivity measurements on the prepared HSE films, using an in-house designed SSB cell device with stainless steel blocking electrodes (**Figure S2.1**). **Figure 2.7a** displays the EIS spectra of two representative HSEs, a *ceramic-in-polymer* (20 wt.% - 18 vol.%) and a *polymer-in-ceramic* (75 wt.% - 72 vol.%) system. They are fitted with an equivalent circuit taking into account the bulk and organic-inorganic interfacial resistive contributions, with the capacitive response of the blocking electrodes interface (**Figure 2.1** and **Scheme S2.1**).

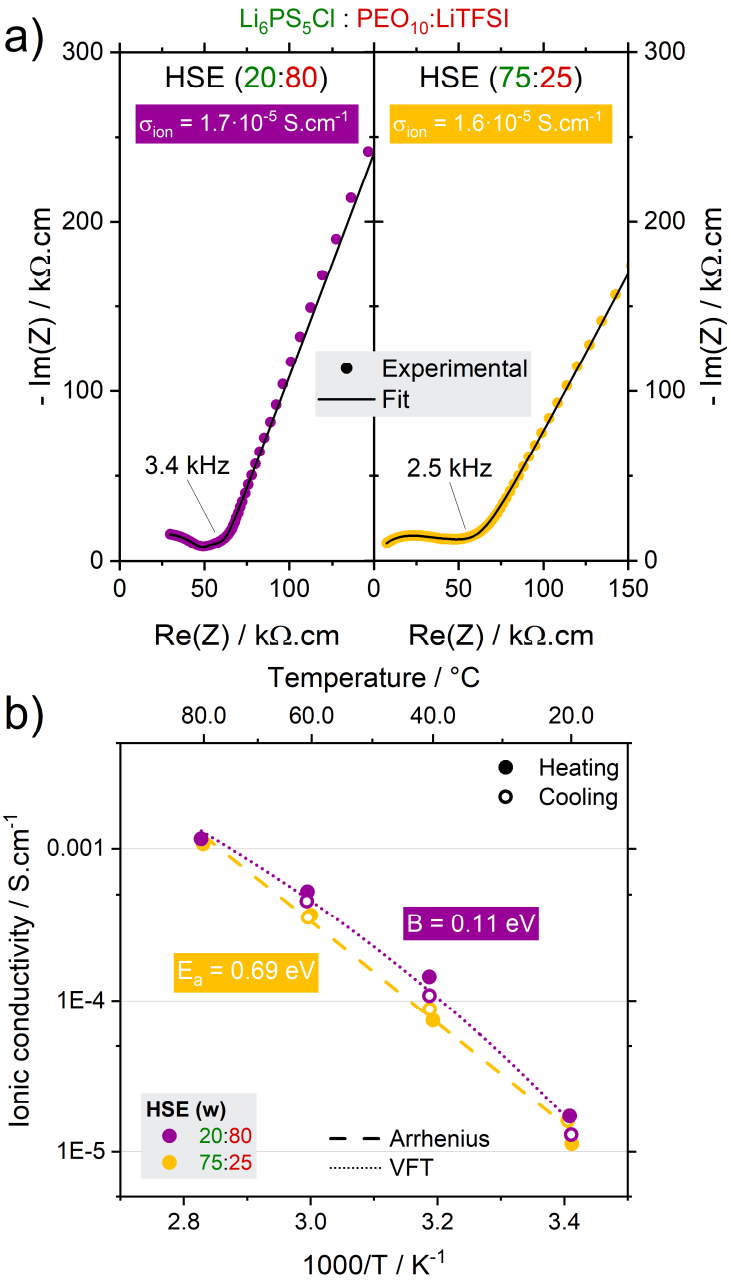

Figure 2.7 (a) EIS spectra of two HSEs (20 and 75 wt.% of ceramic) at 20°C and their related fit. (b) Temperature-dependant ionic conductivity in the range of 20 – 80 °C, fitted according to the adequate activation mechanism (Arrhenius or VFT) and the associated (pseudo) activation energy.

The resistance of electrolyte and interface are both taken into account to calculate the overall ionic conductivity of the HSE. The two HSEs shown here have similar ionic conductivity at 20°C, yet they differ regarding the activation mechanism (**Figure 2.7b**). The polymer-rich HSE can be fitted with a VFT law, displaying a pseudo-activation energy B = 0.11 eV similar to PEO_{10}:LiTFSI. Conversely, the ceramic-rich HSE follows an Arrhenius law despite being in the same range of ionic conductivity. However, the associated activation energy E_a = 0.69 eV is significantly higher than pure Li_6PS_5Cl (E_a = 0.40 eV). The choice of the adequate model is based on the highest correlation coefficient obtained when linear fitting ln(σT) versus 1000/T (**Figure S2.3**).

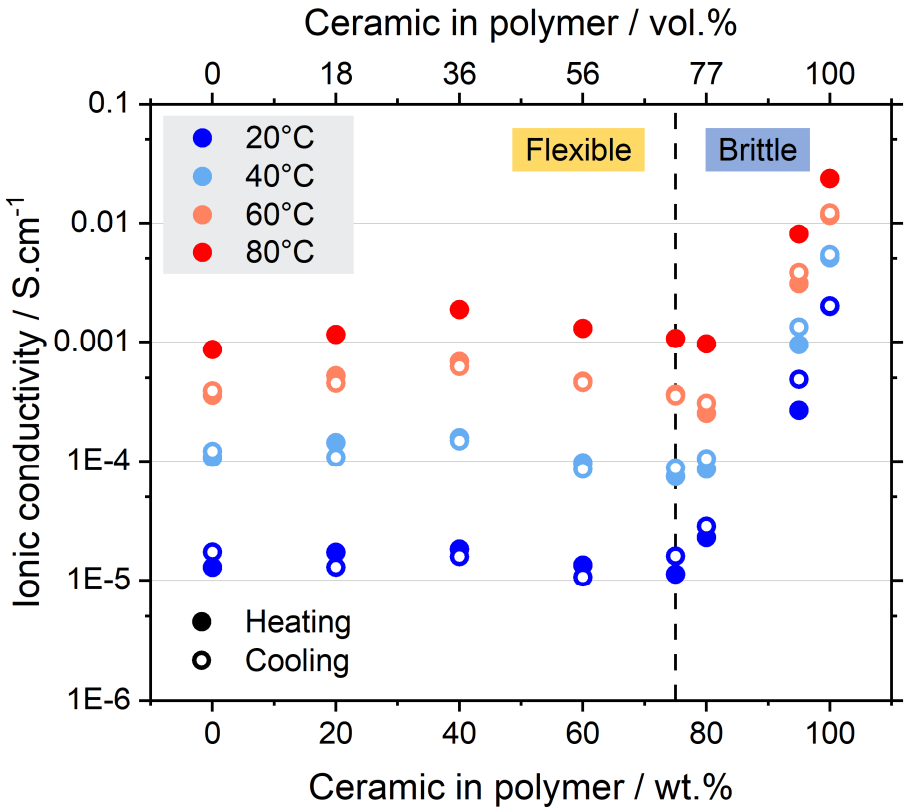

Figure 2.8 HSE ionic conductivity according to the organic-to-inorganic ratio and temperature. Qualitative mechanical properties (flexible versus brittle) are highlighted according to ceramic content. Incertitude on calculated conductivities mainly stems from the thickness of the film, which can slightly vary between the heating and the cooling steps.

Extending the ionic conductivity measurement to the whole range of organic-to-inorganic ratio and at different temperatures, we could reveal two distinct behaviours related to conduction and mechanical properties (**Figure 2.8**). Regarding ionic conductivity, there is no noticeable effect of adding ceramic to the polymer electrolyte up to 75 wt.%, regardless of the temperature. In contrast, the addition of a small amount of PEO_{10}:LiTFSI (from 5 to 20

wt.%) to the ceramic powder results in a significant decrease in the ionic conductivity of the HSE, with a similar trend at each temperature. The threshold at which conductivity starts to increase, around 75 wt.% of ceramic, corresponds well to the transition from a flexible, self-standing film to a brittle mixture. This implies that a compromise between mechanical and conductivity properties will be necessary to meet the expected HSE requirements.

In order to perform activation mechanism fitting on all HSEs, it is necessary to determine the glass transition temperature (T_g) of the electrolytes as it is involved in the VFT model (refer to section **1.2.2**). DSC measurements between -70°C and 100°C revealed that T_g increases linearly with Li_6PS_5Cl content in the HSE (**Figure 2.9**). Similarly, Comer *et al.*[165] reported a linear increase of the relaxation temperature (T_α), measured by dynamic mechanical analysis (DMA), with the content of both SiO_2 and MgO filler in a cross-linked PEO based nanocomposite. They suggest that the increase of T_α, equivalent to T_g measured by DSC, stems from favourable interaction between the polymer phase and the inorganic filler, which thus limit the mobility of the chains. In our case, this interaction may be associated to an interphase formation, as chemical reactivity may occur between the organic and the inorganic phases. This matter will be discussed in section **2.3** of this chapter.

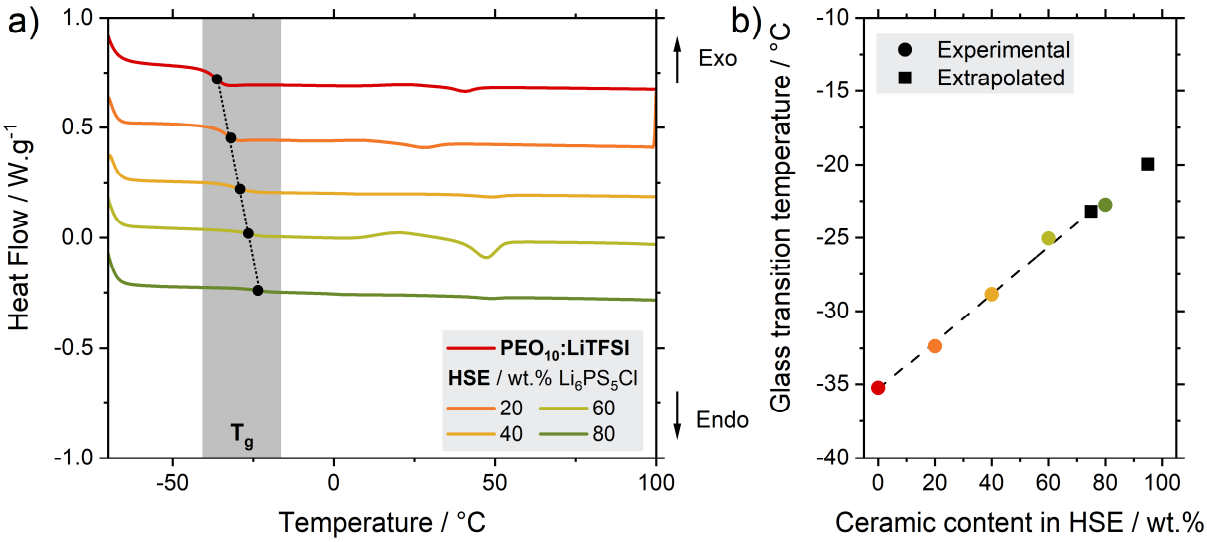

Figure 2.9 (a) Thermal analysis of the HSEs by DSC in argon atmosphere with a heat rate of 10°C.min^{-1} and varying content of Li_6PS_5Cl. (b) Evolution of the glass transition temperature (T_g) according to the ceramic content. Extrapolated values for missing points are obtained by linear fitting of the experimental data.

Having measured ionic conductivity in temperature and the glass transition temperature, we performed both Arrhenius and VFT fitting for all the prepared HSEs (**Figure**

S2.3). The model that best describes their activation mechanism for each formulation was chosen based on the highest value of the correlation coefficient R^2 (**Figure 2.10a**). Interestingly, the two domains of the organic-to-inorganic ratio appear again (**Figure 2.10b**). HSEs with ≤ 60 wt.% of ceramic behave like PEO_{10}:LiTFSI following a VFT model, while HSEs with ≥ 75 wt.% follow an Arrhenius activation similar to Li_6PS_5Cl. The addition of ceramic particles (from 20 to 60 wt.%) to the organic matrix has no significant effect on the pseudo-activation energy B, which remains stable around 0.11 eV, in the same way as conductivity.

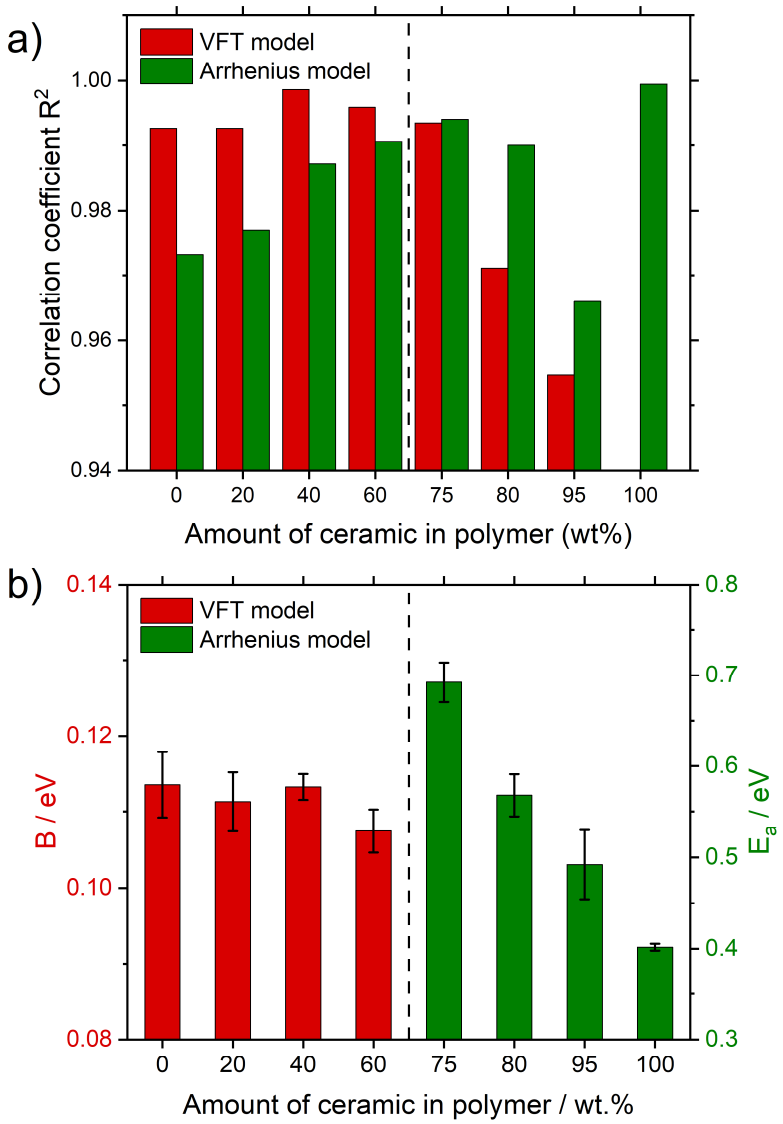

Figure 2.10 (a) Arrhenius and VFT models correlation coefficients evolution with ceramic content. (c) Selected fitting model for activation mechanism of HSEs according to ceramic content and evolution of the associated (pseudo) activation energy. Error bars are calculated from the fit parameters standard errors. The transition from VFT to Arrhenius "domains" is marked by the dashed line (between 60 and 75 wt.% of Li_6PS_5Cl).

Clearly, the absence of PEO crystalline domains in the starting polymer phase (**Figure 2.3**) makes the presence of inorganic fillers insignificant, as long as the organic phase percolation is maintained (< 30 vol.%).[124] To confirm this hypothesis, we prepared an HSE without LiTFSI to suppress the conductivity of the organic phase, with equal volume content of PEO and Li_6PS_5Cl (**Figure S2.4**). The resulting HSE conductivity ($1.4 \cdot 10^{-6}$ S.cm^{-1}) is ten times lower than the one containing LiTFSI ($1.2 \cdot 10^{-5}$ S.cm^{-1} with 56 vol.% of Li_6PS_5Cl). In the absence of LiTFSI, the ionic pathway must occur through the network of Li_6PS_5Cl which is very tortuous and thus, impeded by non-conductive PEO. With LiTFSI, the organic network can conduct lithium ions faster than the Li_6PS_5Cl tortuous network. When following a *polymer-in-ceramic* approach, the addition of a small amount of organic phase (from 5 to 25 wt.%) results in a higher activation energy from 0.49 to 0.69 eV, directly linked to a downward trend in ionic conductivity (**Figure 2.8**). The presence of a less conductive phase, PEO_{10}:LiTFSI, located between Li_6PS_5Cl particles increases tortuosity within the highly conductive ceramic percolating network. As the organic phase content increases, the tortuosity of the lithium conduction paths increases, resulting in in an overall decreased lithium conductivity.

Concluding this section, we propose to use the activation mechanism fitting as an easily accessible metric to gain a deeper understanding of the HSE ionic pathway. Overall, these results support the hypothesis of Li^+ conduction via the organic matrix in HSEs with 20 to 60 wt.% of ceramic, while Li_6PS_5Cl particles may be the preferred pathway for lithium ions at higher ceramic contents (75 to 95 wt.%). As expected, the organic-to-inorganic ratio is a decisive parameter for HSE formulation, yet the simultaneous enhancement of ionic conductivity and mechanical properties has not been achieved by solely varying it.

2.2.4 Optimizing the selected metrics

○ Influence of the polymer molar mass

To reach our conductivity and mechanical criteria, we took advantage of the wide range of molar masses commercially available for PEO and studied the effect of reducing its molar mass on the ionic conductivity for both pure polymer electrolytes and HSEs. We set the inorganic content at 75 wt.% as it represents the current best compromise between achieving satisfactory mechanical properties and ionic conduction based Li_6PS_5Cl percolation. **Figure 2.11a** shows the increase of conductivity in PEO_{10}:LiTFSI systems due to polymer shortening (from 600 to 0.4 kg.mol^{-1}), as previously observed by Devaux *et al.*[95] A lower molar mass

decreases the glass transition temperature and increases chain mobility due to a greater amount of end groups, which are more mobile than the backbone. The consequence is an increase of free volume and hence ionic conductivity.[89] Reducing the molar mass of PEO from 600 to 0.4 kg.mol^{-1} results in a three-fold gain of the conductivity, from (1.5 ± 0.3) to (4.5 ± 0.4) · 10^{-5} S.cm^{-1} at 20°C.

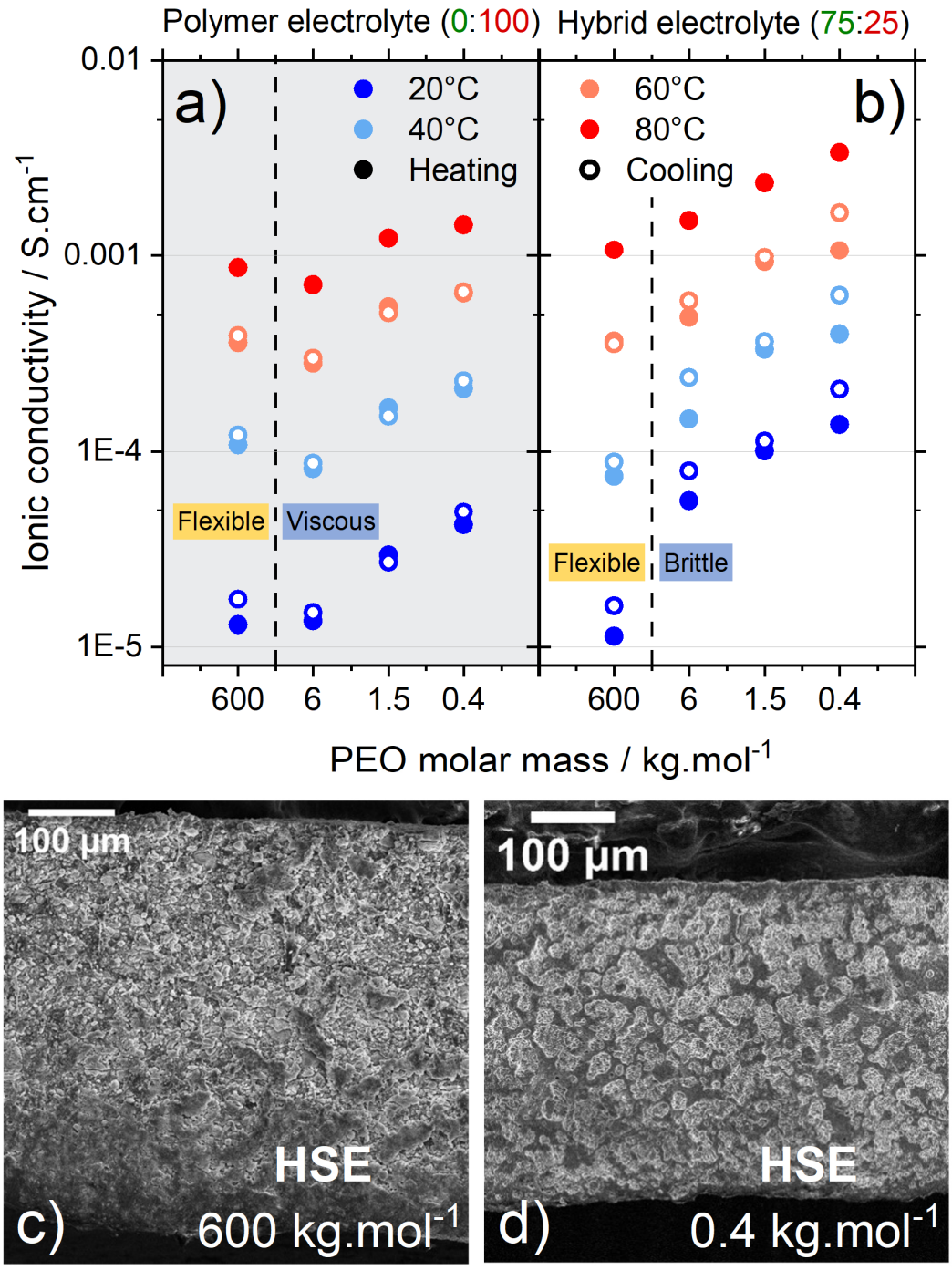

Figure 2.11 Temperature-dependent ionic conductivity of (b) HSE (75 wt.% Li_6PS_5Cl) compared to (a) polymer electrolyte according to PEO molar mass. Cross-section SEM images of HSE with (c) high (600kg.mol^{-1}) and (d) low (0.4 kg.mol^{-1}) PEO molar mass.

The effect is significantly higher when we switch to an HSE system with high inorganic content (PEO_{10}:LiTFSI : Li_6PS_5Cl = 25:75 (w) – **Figure 2.11b**). The benefit is in this case twelve-fold, from (1.4 ± 0.3) to (17 ± 5) · 10^{-5} $S.cm^{-1}$. This means that the addition of Li-conductive ceramic particles has a clear positive impact on the ionic mobility through the HSE, regardless of the initial conductivity of the organic phase. The quality of the mixing between the two precursor electrolytes may explain the difference between high and low molar mass systems. At room temperature, PEO_{10}:LiTFSI (600 $kg.mol^{-1}$) is in solid-state, requiring hot-processing (around 80°C) to mix it with Li_6PS_5Cl. In contrast, PEO_{10}:LiTFSI (0.4 $kg.mol^{-1}$) is in viscous liquid-state at 25°C, making mixing easier and more complete. PEO chain length can also have an impact on the arrangement of ceramic particles within the organic matrix, as shown on SEM cross-section images with different organization of phases (**Figure 2.11c-d**). The percolation of the inorganic phase is easier to access in a low molar mass system since the viscosity of the organic phase is lower[95], which explains the beneficial effect on ionic conductivity. While the conductivity criterion is met for the low molar mass PEO system (0.4 $kg.mol^{-1}$) with a conductivity over 10^{-4} $S.cm^{-1}$ at room temperature, this HSE suffers from poor mechanical properties, as it is a brittle material that cannot be processed as a thin and flexible self-standing film.

○ Strategy of mixing polymers of different molar masses

Given that high molar mass PEO can act as a flexible backbone[166] and based on our findings that a low molar mass PEO (referred as PEG in the following text) allows a better mixing and therefore higher conductivity, the logical approach is to formulate an HSE based on an organic phase with mixed molar masses. To this end, PSEs were prepared with PEO (600 $kg.mol^{-1}$) and PEG (0.4 $kg.mol^{-1}$) at different mass ratios (1:0, 2:1, 1:1, 1:2 and 0:1 (w)). They were subsequently mixed with 75 wt.% of Li_6PS_5Cl to obtain a range of high ceramic-loading HSEs, whose ionic conductivities were measured in a range of temperature from 20°C to 80°C (**Figure 2.12**).

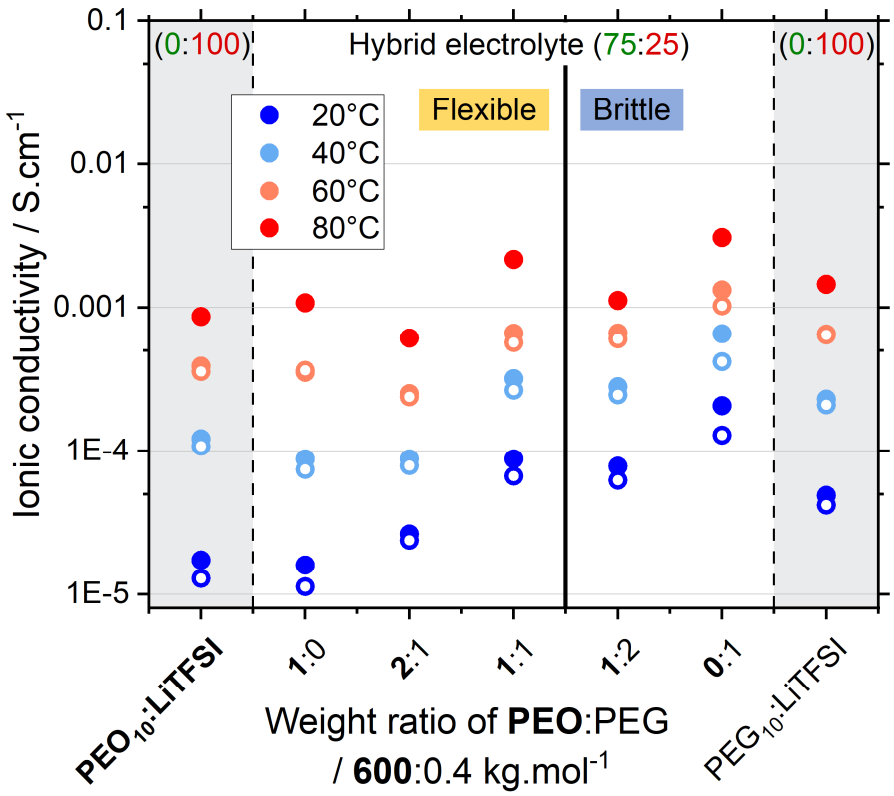

Figure 2.12 Effect of PEO:PEG weight ratio in the organic phase to the HSE ionic conductivity in temperature. Qualitative mechanical properties (flexible versus brittle) are highlighted according to this ratio.

As predicted from previous discussion, increasing the amount of PEG improves the ionic conductivity at 20°C. Up to 50 wt.% (ratio 1:1), this benefit is significant with a five-fold increase, from (1.4 ± 0.3) to (8 ± 1) · 10^{-5} S.cm^{-1}. For higher amounts of PEG, the gain in conductivity is smaller (only twofold from 50 to 100 wt.%) and the loss of mechanical properties is too important to be interesting in terms of formulation. HSE with the polymer blend PEO:PEG=1:2 (w) is indeed a brittle material. The final organic phase is thus chosen as [PEO:PEG = 1:1 (w)]$_{10}$:LiTFSI. As a summary, **Figure 2.13a** shows the ionic conductivity of the precursor electrolytes and the HSEs as a function of temperature and their respective activation mechanisms (refer to **Figure S2.5** for choice of mechanism). It appears that the HSE with the modified organic phase (OP) follows an Arrhenius law and has a higher activation energy (0.52 eV) compared to pure Li_6PS_5Cl (0.41 eV). Here, shifting from the initial PEO_{10}:LiTFSI to the modified [PEO:PEG = 1:1 (w)]$_{10}$:LiTFSI polymeric matrix enables a significant reduction in activation energy from 0.69 to 0.52 eV. The conductivity criterion is reached here with 10^{-4} S.cm^{-1} at room temperature (25°C).

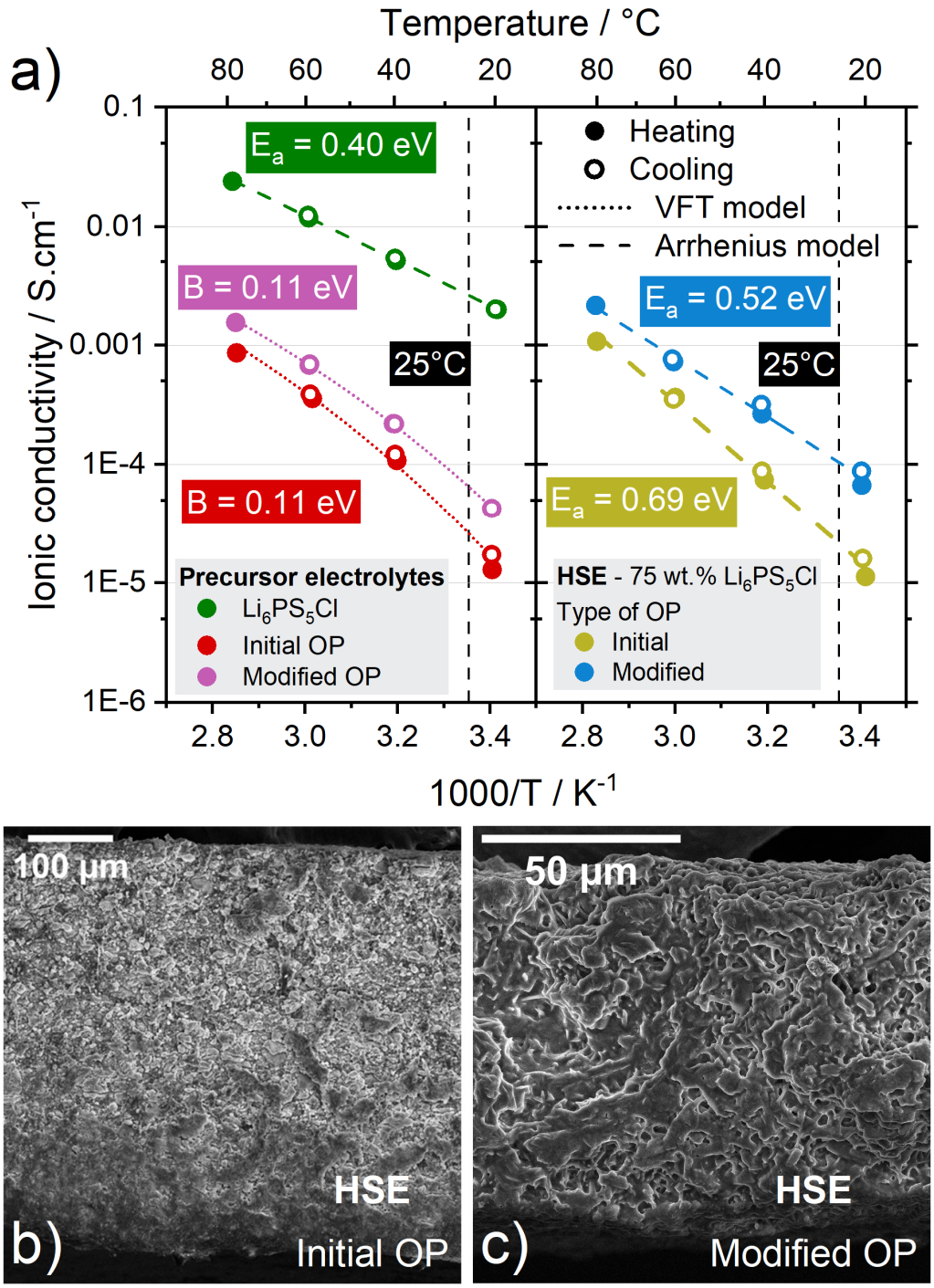

Figure 2.13 (a) Temperature-dependant ionic conductivity and activation mechanism for precursor electrolytes and HSEs (75 wt.% Li_6PS_5Cl). Initial organic phase (OP): PEO_{10}:LiTFSI – Modified OP: $[PEO:PEG = 1:1\ (w)]_{10}$:LiTFSI. Cross-section SEM images of HSE with (b) initial OP and (c) modified OP.

The SEM cross-section (**Figure 2.13c**) shows the overall homogeneity with smoother surface and the possibility of processing the optimised HSE as thin membranes (< 100 µm). This feature is essential to ensure low ohmic drop and high energy density in a complete cell configuration.

As a point of comparison, a conductivity of $6 \cdot 10^{-5}$ S.cm^{-1} at 30°C was obtained by Simon *et al.*[88] using 40 wt.% of Li_6PS_5Cl and 60 wt.% of PEO_{20}:LiTFSI, which is close to our measurements (**Figure 2.8**). Following a similar solvent-based route, Li *et al.*[167] explored HSEs based on $Li_{10}GeP_2S_{12}$ (LGPS – σ_{ion} = 10^{-2} S.cm^{-1}) and PEO_{10}:LiTFSI. They obtained a maximum conductivity of 10^{-5} S.cm^{-1} at 20°C with 90 wt.% of LGPS, indicating no synergy between the phases. Our systematic approach successfully reaches higher room temperature conductivity following a straightforward solvent-free process.

2.3 – Characterisation of the HSE internal reactivity

When preparing an HSE composed of electrolytes with different chemical natures, it is essential to investigate their compatibility and assess the feasibility of ionic transfer at their interface. As a preliminary experiment, we compared XPS spectra of an HSE (40 wt.% Li_6PS_5Cl) before and after a storage of six days at 80°C, to accelerate the ageing process and trigger possible reactivity between the inorganic and the organic SEs (**Figure 2.14**). Comparison of the S2p spectra shows a direct impact of temperature on the stability of the ceramic in contact with the polymer phase. Degraded sulphide species are formed with the appearance of a polysulfide peak, with a similar effect to solvent exposure (**Figure 2.5**). It highlights the necessity of using the HSE at room temperature in order to prevent Li_6PS_5Cl degradation.

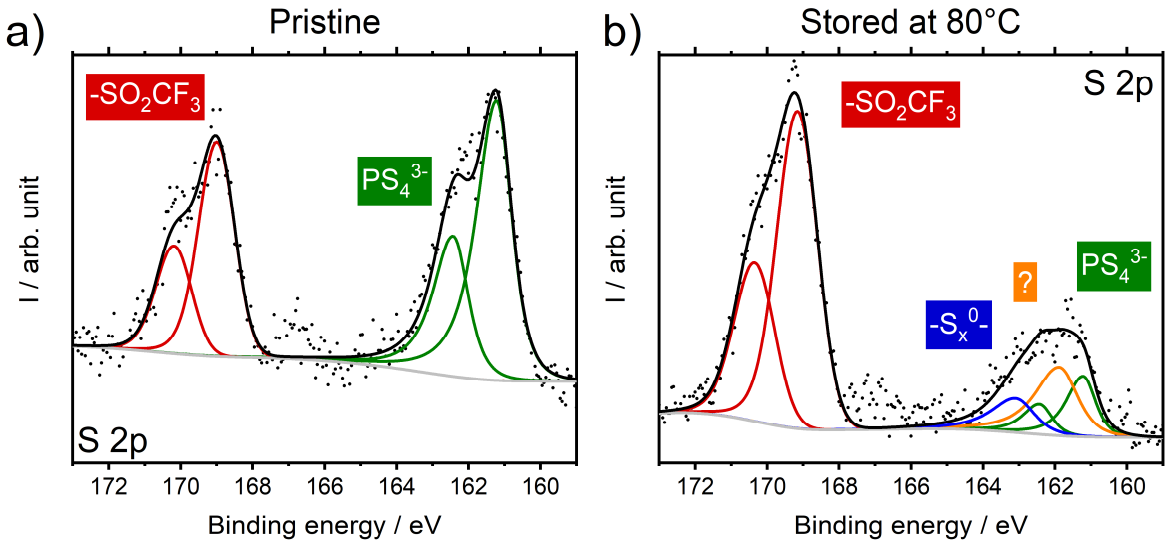

Figure 2.14 X-ray photoelectron spectroscopy (XPS) analysis of an HSE (60 wt.% PEO_{10}:LiTFSI + 40 wt.% Li_6PS_5Cl) at (a) pristine state and (b) after a storage of six days at 80°C.

2.3.1 Ionic transfer at the organic-inorganic interface

To gain a better understanding on the conductivity mechanism in our HSE, we characterised the ionic transfer at the interface with impedance measurements. They were performed on a trilayer stack PEO:LiTFSI | Li_6PS_5Cl | PEO:LiTFSI, varying the organic layer salt concentration (EO:Li = 10 – 20 – 40). A pressure of 4.5 MPa was applied in a dedicate cell (**Figure S2.1c**) to prevent the creeping of the polymer films. It has the advantage to simplify the interface to a planar surface between the organic and inorganic phases. The EIS spectra were fitted according to the model for HSE conductivity, taking into account the electrolytic and the interfacial contributions (**Scheme S2.1**).

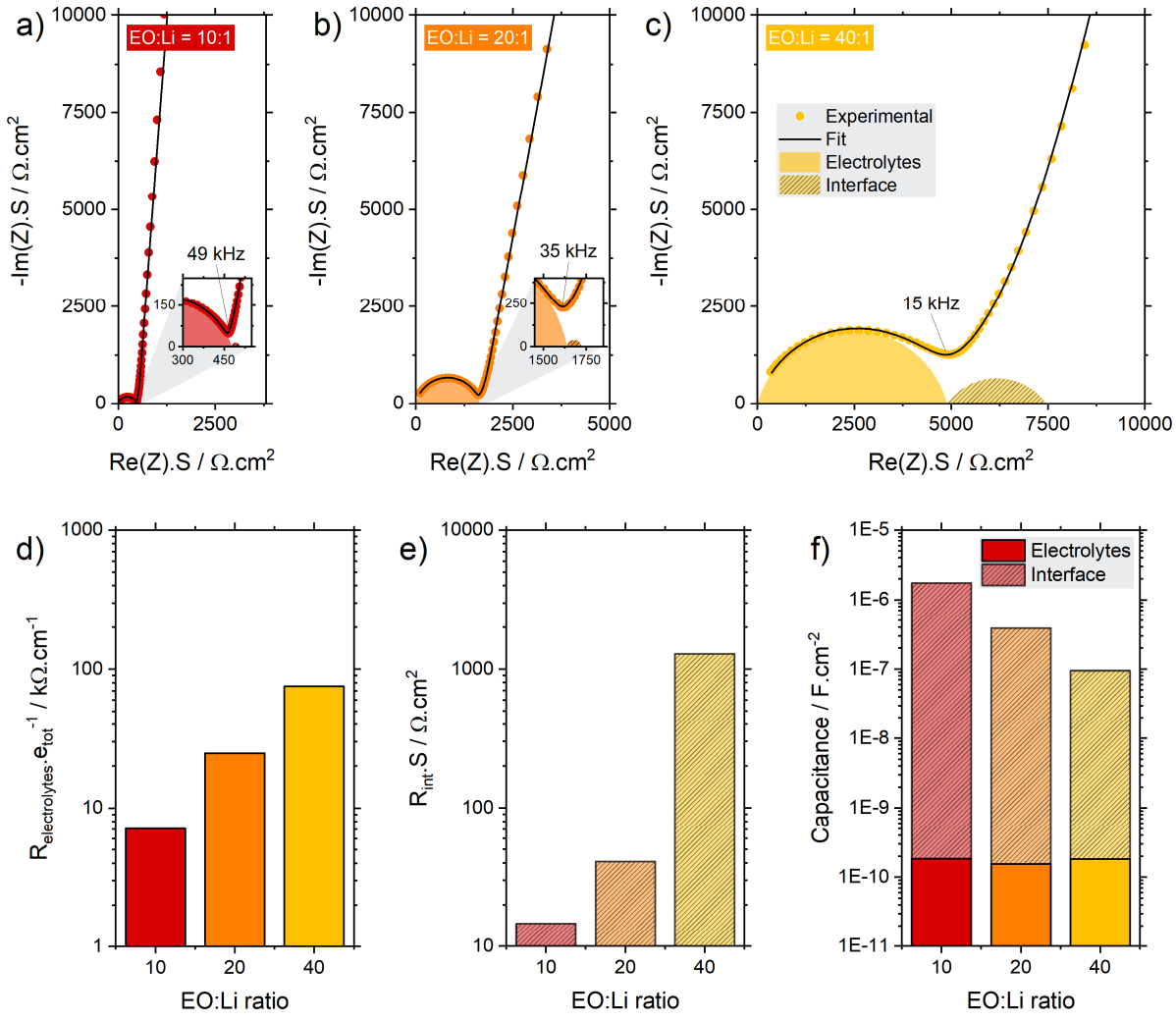

Figure 2.15 Influence of EO:Li ratio (i.e. salt concentration) on the organic-inorganic interface. EIS spectra at room temperature of the trilayer stack PEO_x:LiTFSI | Li_6PS_5Cl | PEO_x:LiTFSI, with (a) x = 10, (b) x = 20 and (c) x = 40. The associated fit and the electrolytic and interfacial contributions are highlighted. Evolution of (d) electrolytic resistance, (e) interfacial resistance and (f) both associated capacitance according to EO:Li ratio.

They show similar responses at different EO:Li ratios in the PSE (**Figure 2.15a-c**). Two contributions are identified at high and medium frequencies, with a transition around 10 – 50 kHz. However, the associated impedance magnitude increases with lower salt concentrations. Indeed, the high-frequencies contribution can be assigned to conduction within the bulk of both organic and inorganic electrolytes. The associated resistance $\frac{R_{electrolytes}}{e_{tot}}$ increases (e_{tot} represents the thickness of the trilayer stack) with higher EO:Li ratio (**Figure 2.15d**), as expected given that the PSE is less conductive with a lower salt concentration.[90] The corresponding capacitance remains constant around 10^{-10} F.cm^{-2} (**Figure 2.15f**). Concerning the interface contribution at medium frequencies (1 – 50 kHz), its resistance significantly increases with a higher EO:Li ratio, while the associated capacitance decreases and lies in the range of 10^{-6} F.cm^{-2} (**Figure 2.15e-f**), in good accordance with a previous study by Simon *et al.*[113] A plausible explanation to these trends is based on the semi-crystalline nature of PEO:LiTFSI. As explained in section **1.2.2**, a lower concentration of salt leads to larger crystalline PEO domains in the electrolyte. It results in a smaller area for ion transfer and consequently, causes a higher resistance and a lower capacitance of interface. Another parameter is the quality of contact between the organic and inorganic phases. PEO:LiTFSI being stiffer with lower salt concentration, the appearance of voids is more likely and can lead to even smaller contact area.[168] It confirms our choice EO:Li = 10:1 for the organic phase, with a higher conductivity and a lower stiffness that ensures better contacts with the ceramic particles.

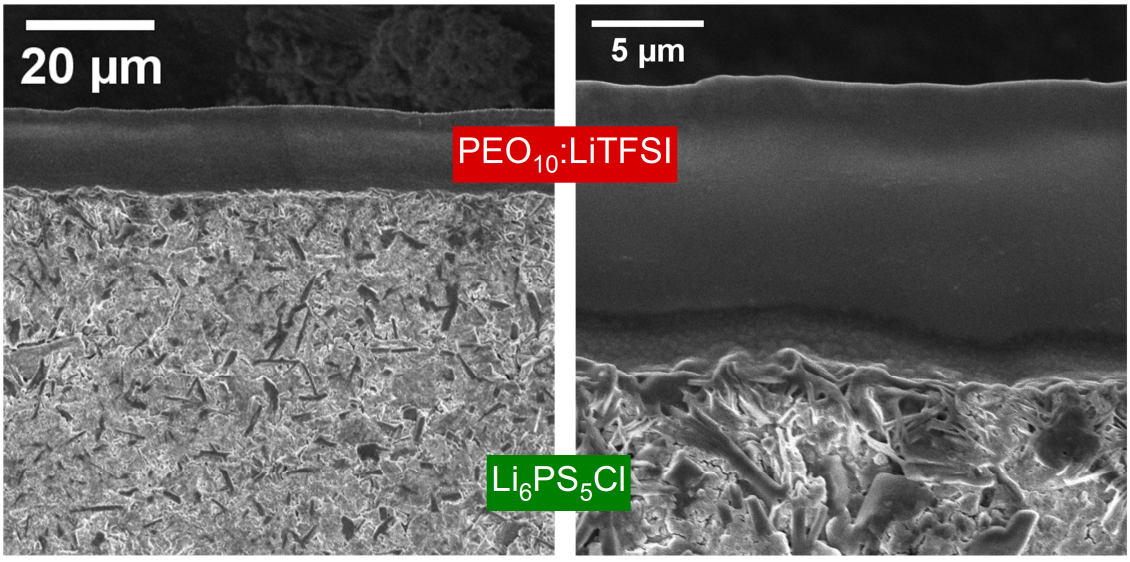

Figure 2.16 SEM cross-section pictures of a film of PEO_{10}:LiTFSI on top of a pellet of Li_6PS_5Cl.

To assess the quality of the interface morphology, we observed by SEM a cross-section of the electrolyte stack at EO:Li = 10:1. We could confirm the adhesion between phases and the flatness of the polymer – ceramic interface, as seen on cross-section images (**Figure 2.16**).

In these conditions, we pursued the characterisation of the interface by submitting the stack to a heat treatment of one hour at 80°C. The resulting impedance spectrum highlights the unambiguous growth of the interface resistance (**Figure 2.17a**), from 10^1 to 10^4 Ω.cm^2. The electrolytes contribution remains constant, as expected given the SEs' intrinsic stability at this temperature. We subsequently performed EIS measurements in a range of temperature to determine the underlying activation mechanisms in this polymer – ceramic stack. Resistance values overlap well during heating and cooling ramps (22h in total), demonstrating the stability of the system after the interphase formation (**Figure 2.17b**). Electrolytes resistance follows a VFT model with the same pseudo-activation energy B = 0.10 eV as PEO_{10}:LiTFSI (**Figure S2.6a**). It confirms that the polymer electrolyte layers are the limiting conduction step, since they have a lower conductivity ($1.5 \cdot 10^{-5}$ S.cm^{-1}) than ceramic ($4 \cdot 10^{-4}$ S.cm^{-1} at 4.5 MPa). Indeed, lowering the pressure affects argyrodite conductivity (from 2 to 0.4 mS.cm^{-1} between 100 and 4.5 MPa – **Figure S2.7**), probably due to the loss of mechanical cohesion between the particles. Considering the interfacial resistance, it follows an Arrhenius law with a high activation energy of 0.83 eV (**Figure S2.6b**). Assuming the formation of an interphase between the organic and inorganic phases (refer to section **2.3.2** for supporting this hypothesis), this is an energetically unfavourable obstacle to the passage of lithium ions, given its high activation energy compared to the pure ceramic phase (0.44 eV) and its high areal resistivity (10^4 Ω.cm^2). This result is in reasonable agreement with the reported value of 0.67 eV, where the authors used a more accurate setup with four-point EIS measurement.[113] Overall, we have identified the negative effect of high temperature on the chemical stability of our HSE via the formation of an interphase with a high activation energy, hence the need for a room temperature processing and operation.

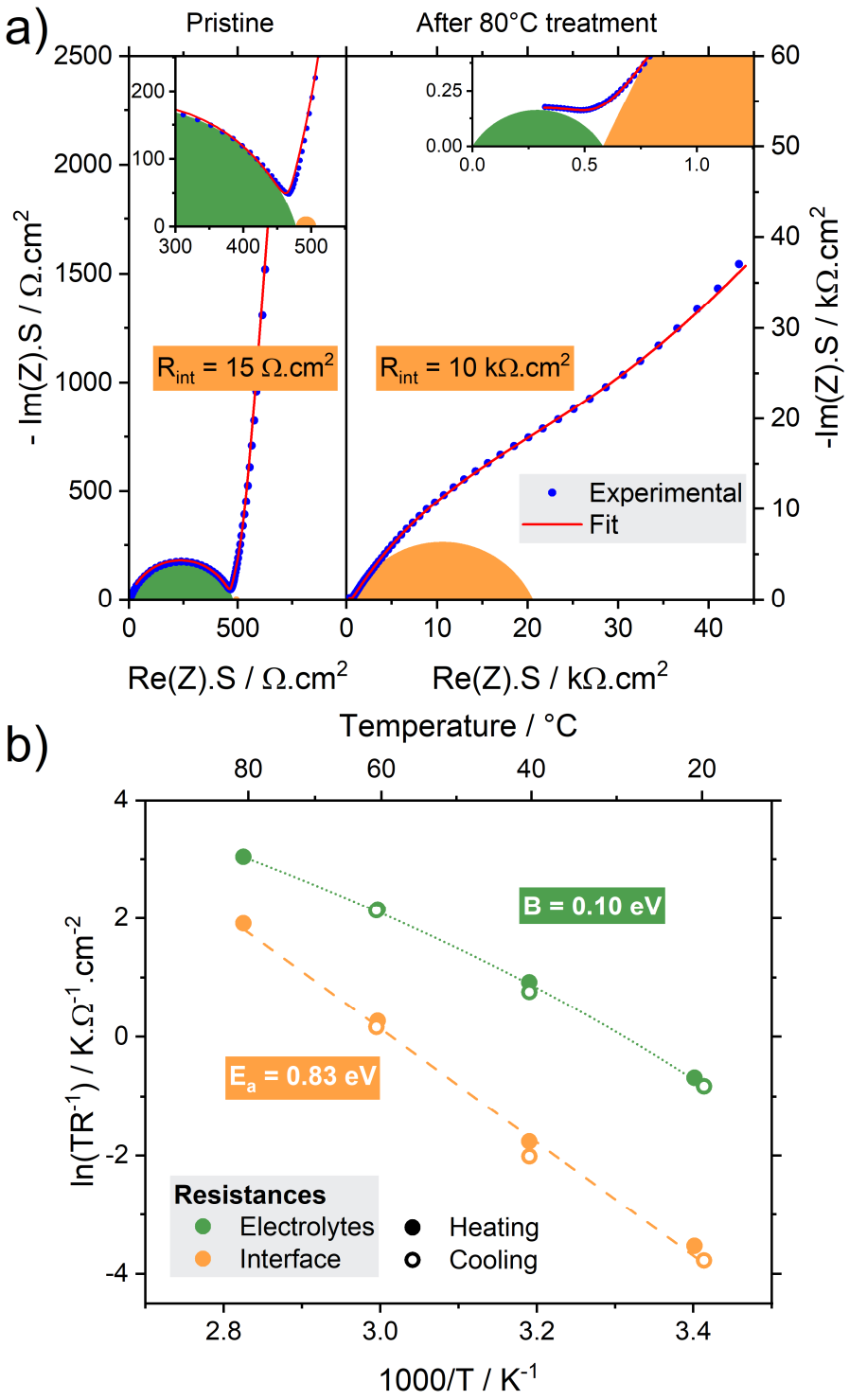

Figure 2.17 Compatibility of ceramic and polymer phases probed by EIS. (a) EIS spectra of trilayer PEO_{10}:LiTFSI | Li_6PS_5Cl | PEO_{10}:LiTFSI before and after an 80°C treatment. (b) Evolution of R_{elec} and R_{int} in temperature and their related activation energies.

2.3.2 Interphase formation probed by ssNMR

With the aim of gaining a finer understanding of the organic – inorganic interface within the HSE, we performed ^{7}Li magic angle spinning (MAS) solid-state nuclear magnetic resonance (ssNMR). This technique allows us to have a closer look at the structural environments of lithium in this complex hybrid material. We first acquired the reference spectra of the precursor electrolytes (**Figure 2.18a-b**), the ceramic Li_6PS_5Cl and the polymer phase [P(EO-co-PO):PEG = 1:1 (w)]$_{10}$:LiTFSI. The switch from the homopolymer PEO to the copolymer P(EO-co-PO) will be discussed in section **2.4.1**. Thankfully, the chemical shifts associated with the inorganic and the organic phases are well apart, thus facilitating the attribution of peaks in the HSE spectrum. On the Li_6PS_5Cl spectrum (**Figure 2.18a**), two components centred on 1.47 ppm are observed accounting for 67.9% (green and sharp) and 32.1% (grey and broad) in intensity. Several factors can explain the presence of these two components. Firstly, ^{7}Li ions are quadrupolar (nuclear spin S = 3/2) and their relaxation is intrinsically biexponential, especially for samples where the correlation time of the environment fluctuations (i.e. site-to-site jumps) is close to the inverse of the Larmor frequency (3 ns for 330 MHz here).[169] In such a case, biexponential relaxation leads to a complex line shape, which is made of two Lorentzian lines. A broad one represents 60% of the signal and a narrower one accounts for the remaining 40%. This applies to a homogeneous sample, whereas our sample exhibits heterogeneity in particle size (**Figure 2.2**). In this case, heterogeneities (magnetic field inhomogeneities, interfaces, defects, differences in lithium mobility) may contribute to additional sources of broadening, resulting in a more complex line shape. The spectrum acquired with the pure polymer electrolyte displays a single component at -1.07 ppm (red – **Figure 2.18b**). When the organic phase is mixed with Li_6PS_5Cl, the resonance from Li^+ in LiTFSI shifts to -0.74 ppm and the peak broadens (**Figure 2.18c**). This indicates a change in the local Li^+ environment within the polymer phase. Indeed, the majority of the volume in the HSE is occupied by ceramic particles (72 vol.%), which alters the global susceptibility and magnetic field experienced by the organic phase. The peak accounts for 2.15% of the signal, as described by the model (**Figure S2.8**), consistent with the theoretical calculation yielding 2.0% of the total lithium content in the organic phase (refer to section **S2.1** for calculation details). Additionally, there is a shift in the Li_6PS_5Cl peak that becomes asymmetric, accompanied by two additional contributions at 1.53 ppm (pink) and 1.36 ppm

(yellow). This once again signifies a widespread disorder within the hybrid sample, and a potential discontinuity in magnetic susceptibilities at the interface between the organic and the inorganic phases. A new feature appears at 0.33 ppm (blue), manifesting as a right shoulder to the ceramic resonance. Its position between the ceramic and the polymer environments suggests that it represents the interphase, the existence of which was previously deduced by EIS analysis (refer to section **2.3.1**).

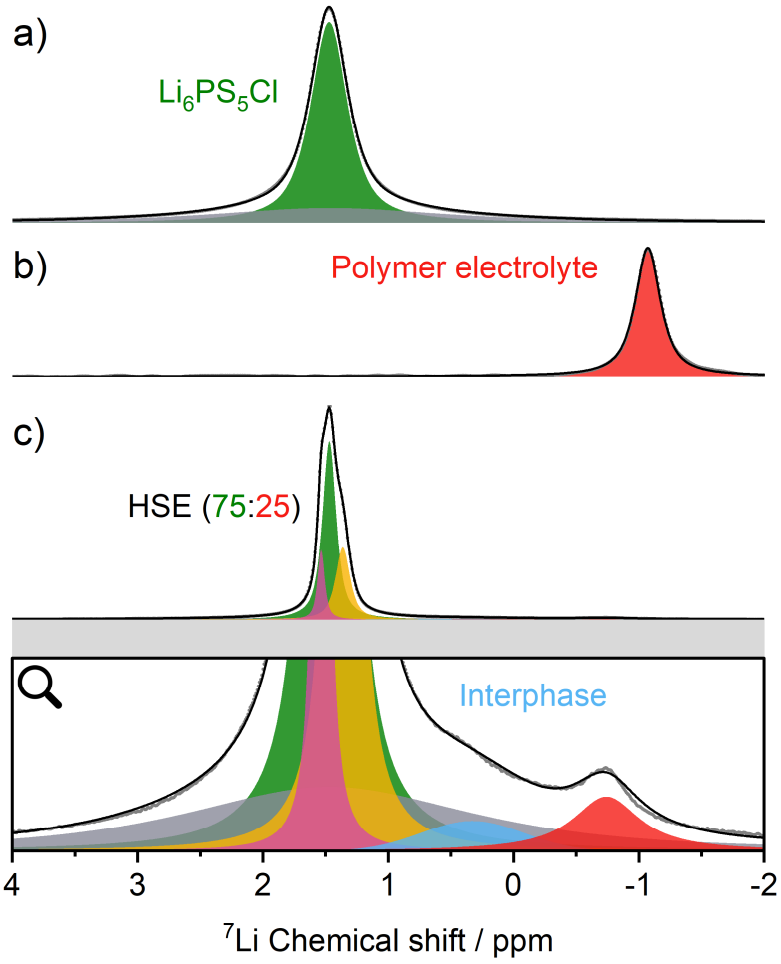

Figure 2.18 ^{7}Li MAS NMR spectra of (a) Li_6PS_5Cl, (b) $[P(EO\text{-}co\text{-}PO):PEG = 1:1\ (w)]_{10}$:LiTFSI and (c) the optimised HSE (75 wt.% Li_6PS_5Cl). The experimental spectrum is shown in grey, the model in black and the fitted contributions in colours (green, grey, pink and yellow – Li_6PS_5Cl; blue – interphase; red – polymer electrolyte).

Since the HSE was prepared immediately before the NMR measurements, we were able to track the evolution of the spectrum over one day (**Figure 2.19a**). Interestingly, we observed an increase and sharpening of the interphase peak concurrently with a decrease in the contribution assigned to the polymer electrolyte. This observation confirms the nature of this new lithium environment, which is trapped within the interphase formed through a slow

chemical reaction. A quantitative analysis of the spectra, acquired at different intervals ranging from few minutes to a day after mixing, gives the intensity evolution of each contribution (**Figure S2.8g**). The intensity ratio between the interphase and the polymer electrolyte was then deduced and its increase over time corroborates the observed evolution of the peaks intensities (**Figure 2.19b**). A rapid increase from 0.5 to 1.0 occurs during the first three hours, followed by a more gradual increase to 1.5, which stabilises after one day. This unequivocally reveals a phenomenon of lithium depletion within the organic phase, feeding the formation of the interphase.

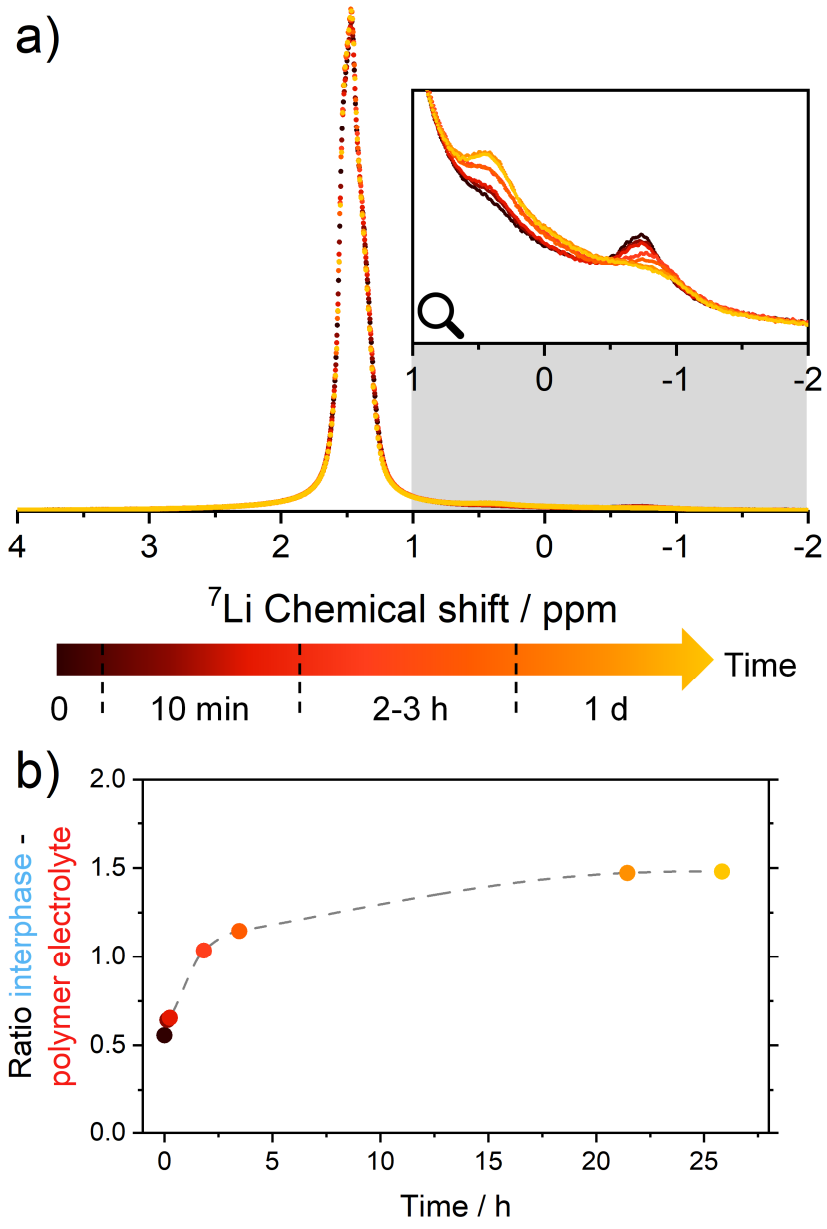

Figure 2.19 (a) Evolution of the ^{7}Li MAS NMR spectrum of the optimised HSE over a period of one day. (b) Ratio of interphase and organic phase intensities, deduced from spectra fitting, as a function of time. The grey dashed line acts as a visual guide.

To assess the lithium exchange ability between the three phases (inorganic | interphase | organic), a homonuclear 2D Exchange SpectroscopY (EXSY) was performed on the HSE (**Figure 2.20**). This powerful technique allows us to probe the ionic mobility at the microscopic scale and gain deeper insights into lithium exchange at the interface. Specifically, we employ a mixing delay of 100 ms under ultra-fast MAS (40 kHz) to quench spin diffusion resulting from weak dipolar interactions. As two ^{7}Li spins separated by 3 Å experience a dipolar interaction of 672 Hz in magnitude, we considered that spin diffusion is negligible at such a fast MAS rate, and that lithium ions should be further apart, particularly in the polymer phase. In the resulting contour plot (**Figure 2.20a**), the intense and broad cross region is the signature of the disordered Li_6PS_5Cl environment. Less intense peaks are identified on the diagonal as the interphase and polymer electrolyte environments.

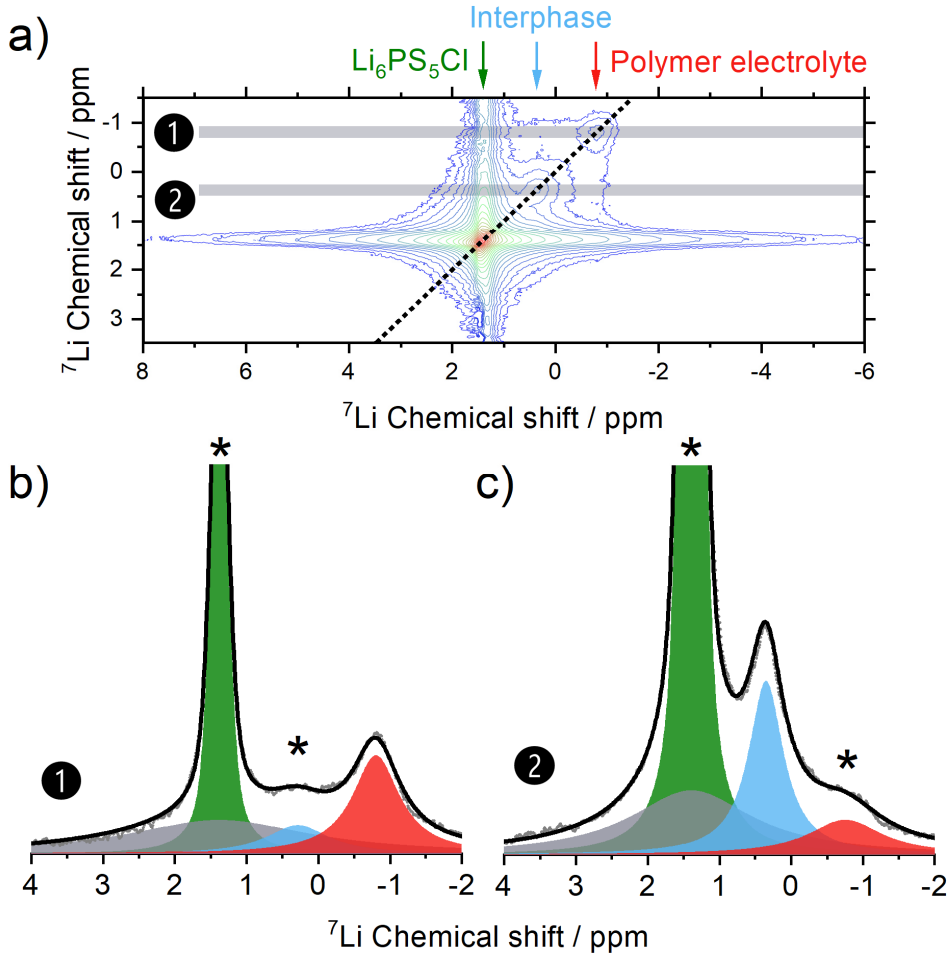

Figure 2.20 Two-dimensional ^{7}Li EXchange SpectroscopY (EXSY) spectrum obtained for the optimised HSE. The unidimensional ^{7}Li spectra are obtained from the sum of 0.234 ppm wide slices to identified off-diagonal peaks (*). Green and grey contributions represents Li_6PS_5Cl, while the blue and red ones account for the interphase and the organic phase, respectively.

Off-diagonal intensity is detected between the interphase, ceramic and organic phase environments. To clearly observe the chemical exchange process, we analysed the 1D cross-sections (grey areas) centred on the organic (1) and interphase (2) environments (**Figure 2.20b**). Both reveal chemical exchange between the interphase, the organic electrolyte and the ceramic phase. Despite the resistive nature of the interphase, previously observed by EIS, this confirms that lithium ions slowly diffuse across the interphase over a 100 ms timescale. However, evidence of lithium exchange at the micrometric scale does not necessarily imply macroscopic lithium conduction through both phases, as clarified with our conductivity measurements and activation mechanism determinations (refer to section **2.2**).

As a conclusion to the ssNMR study, we summarised in the following schematic (**Figure 2.21**) our understanding of the interphase formation within the HSE, by highlighting the process of lithium depletion of the organic phase.

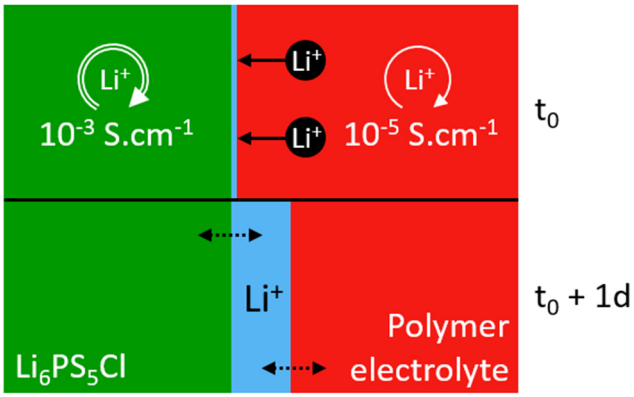

Figure 2.21 Schematic of the interphase formation highlighting the process of the organic phase depletion.

Altogether, our findings reinforce the hypothesis that the chemical interaction between Li_6PS_5Cl and PEO:LiTFSI (as well as its derivatives with PEG and P(EO-co-PO)) leads to the formation of a highly resistive interphase. This newly established environment impedes ionic transfer, as evidenced by the interphase exhibiting a high activation energy of 0.83 eV, as determined by EIS. Additionally, lithium ions can only slowly diffuse across it over a 100 ms timescale, as unveiled by ssNMR.

2.4 – Evaluation of the HSE practical performances

The fabrication of an organic-inorganic HSE was initially motivated by its potentially easier implementation in a real SSB, leveraging a suitable trade-off between conductive and

mechanical properties. In this section, we delve into various aspects of the HSE's practical performances, including its manufacturing under the practical conditions of a dry room (in Blue Solutions' facilities), the characterisation of its mechanical properties and the evaluation of its electrochemical performance.

2.4.1 Benefits and challenges of dry room manufacturing

Moving from the inert and confined environment of a glovebox to a larger and less regulated environment of a dry room presents a considerable challenge when scaling up the manufacturing of SSBs. Water content in the atmosphere is typically higher in a dry room (< 130 ppm – dew point < -40°C) than in an argon-filled glovebox (< 1 ppm). Being aware of the degradation process of argyrodite with water, we studied the evolution of the ionic conductivity when the powder is exposed to a dry atmosphere for more than a day (**Figure 2.22**). Despite a systematic decrease, the magnitude of Li_6PS_5Cl ionic conductivity remains acceptable, above 1 $mS.cm^{-1}$, even after 36 hours of exposure. The water level does not appear to drastically affect the loss of ionic conductivity, even at humidity levels < 300 ppm (location far from dry air blowers). Overall, we were able to evaluate the feasibility of using argyrodite in a dry room, as it has also been confirmed by another study.[126]

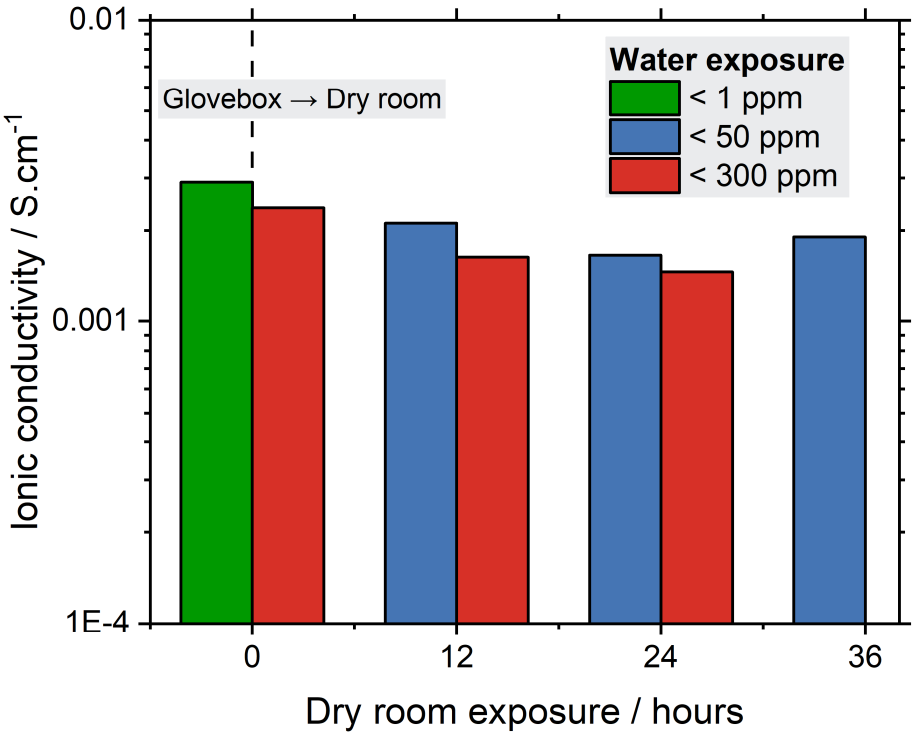

Figure 2.22 Evolution of Li_6PS_5Cl ionic conductivity according to exposure time and water level in a dry room.

In parallel, we performed X-ray diffraction (XRD) measurements to probe potential structural degradation of the argyrodite powder after exposure to the dry room atmosphere (**Figure 2.23a**). Since no additional peak could be detected on the diffractograms, we further characterised the exposed samples by XPS analysis (**Figure 2.23b-d**). It revealed partial oxidation of the material, with the presence of oxidised sulphur at the surface, possibly attributed to bridging sulphur atoms (polysulphides, oxysulphides).[126] However not too detrimental to ionic conductivity, dry room handling time of Li_6PS_5Cl should be minimise to avoid the degradation of the material, even if it is a relatively slow process thanks to the low water level.

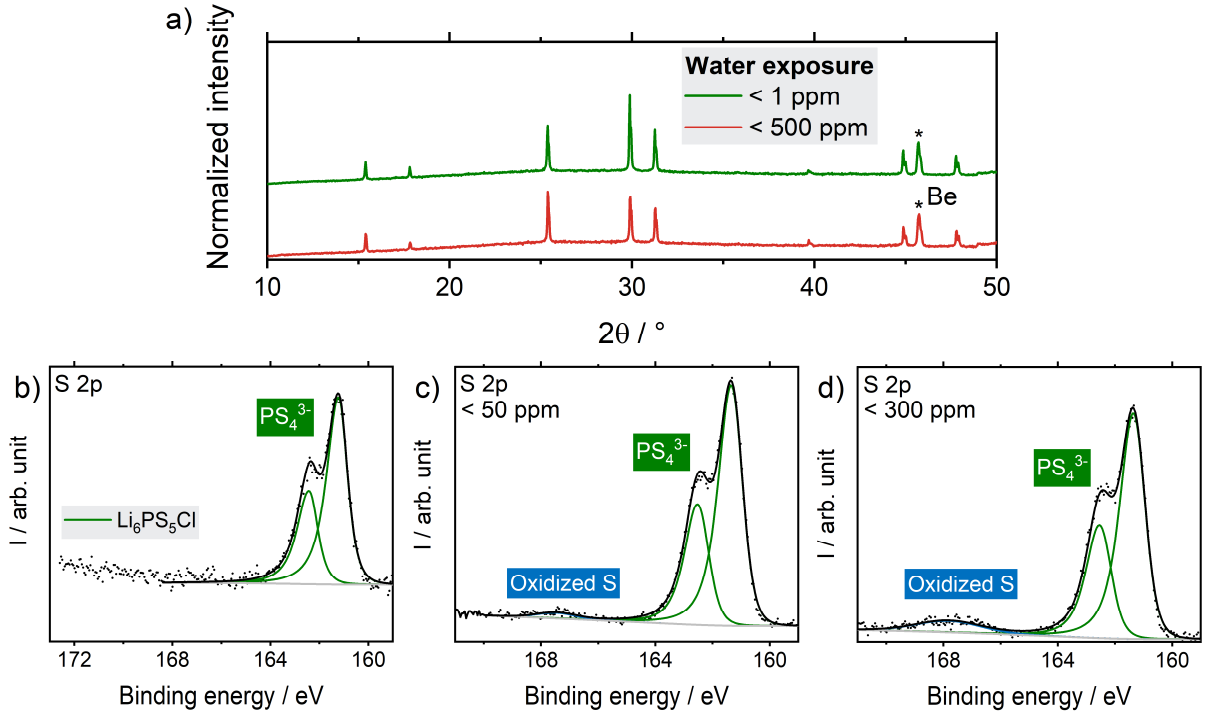

Figure 2.23 (a) X-ray diffractograms of Li_6PS_5Cl samples at pristine state and after 96 hours of exposure in a dry room at a water level of < 300 ppm. X-ray photoelectron spectra (S2p) of Li_6PS_5Cl samples (a) in pristine state and after 96 hours of exposure in a dry room at water levels of (b) < 50 and (c) < 300 ppm.

After ensuring the use of argyrodite in the dry room, we proceeded with experiments to scale up the preparation of the HSE. Moving from preparing less than one gram of material to nearly a hundred grams requires an automated and reliable mixing technique. To achieve this, we adopted the same procedure as employed for the preparation of polymer electrolytes, which involves mixing the polymers and lithium salt in an internal mixer (**Figure 2.24a**). It comprises a chamber equipped with a pair of rotors generating high shear forces, where the materials are mixed together. In our process, we initially mixed together the

polymers P(EO-co-PO) and PEG with the LiTFSI salt to homogenise the organic phase (**Figure 2.24b**). Subsequently, the argyrodite powder was added to disperse within the plastic matrix (**Figure 2.24c**). While the overall mixing appeared homogeneous, the stiffness of the HSE led to local inhomogeneities and induced shear forces that exceeded the capabilities of the mixer (**Figure 2.24d-e**). This was particularly pronounced in the case of the HSE with high-inorganic loading (75 wt.% Li_6PS_5Cl). This test underscored the challenges associated with scaling up the dry mixing of HSE components, potentially necessitating a redesign of existing machines.

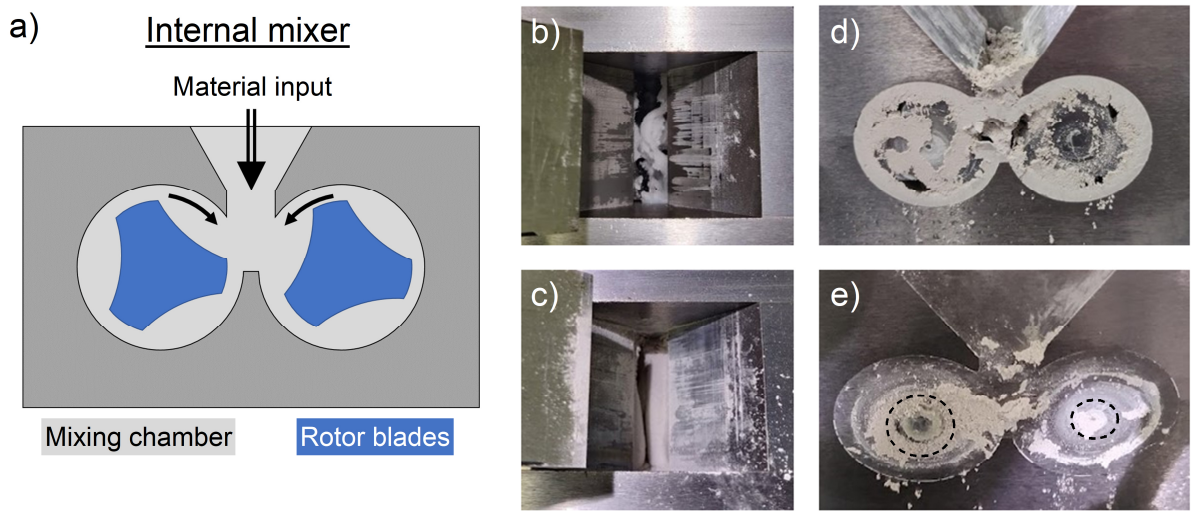

Figure 2.24 (a) Schematics of an internal mixer. Top view of the mixing chamber with (b) only polymer electrolyte and (c) after Li_6PS_5Cl powder addition. (d) View of the chamber after the HSE mixing and (e) inhomogeneities of the mixing: dashed lines highlight non-mixed polymer electrolyte.

After obtaining the paste of HSE, we used a calendering machine to form films, mimicking again the manufacturing process of polymer electrolytes. It is based on rollers that apply pressure, and possibly temperature, on a sheet of material to decrease its thickness, smooth its surface and reduce its porosity. A preliminary test with the optimised formulation based on 25 wt.% $[PEO:PEG = 1:1 (w)]_{10}$:LiTFSI and 75 wt.% Li_6PS_5Cl, as described in section **2.2.4**, showed the systematic appearance of long cracks on the edges. It showed the limits of forming large area films based on the homopolymer PEO (**Figure 2.25a-c**). An alternative was found in replacing it with a more flexible copolymer, the poly(ethylene-co-propylene oxide) P(EO-co-PO) (1000 $kg.mol^{-1}$ – thermoplastic – **Figure 2.25b-d**).

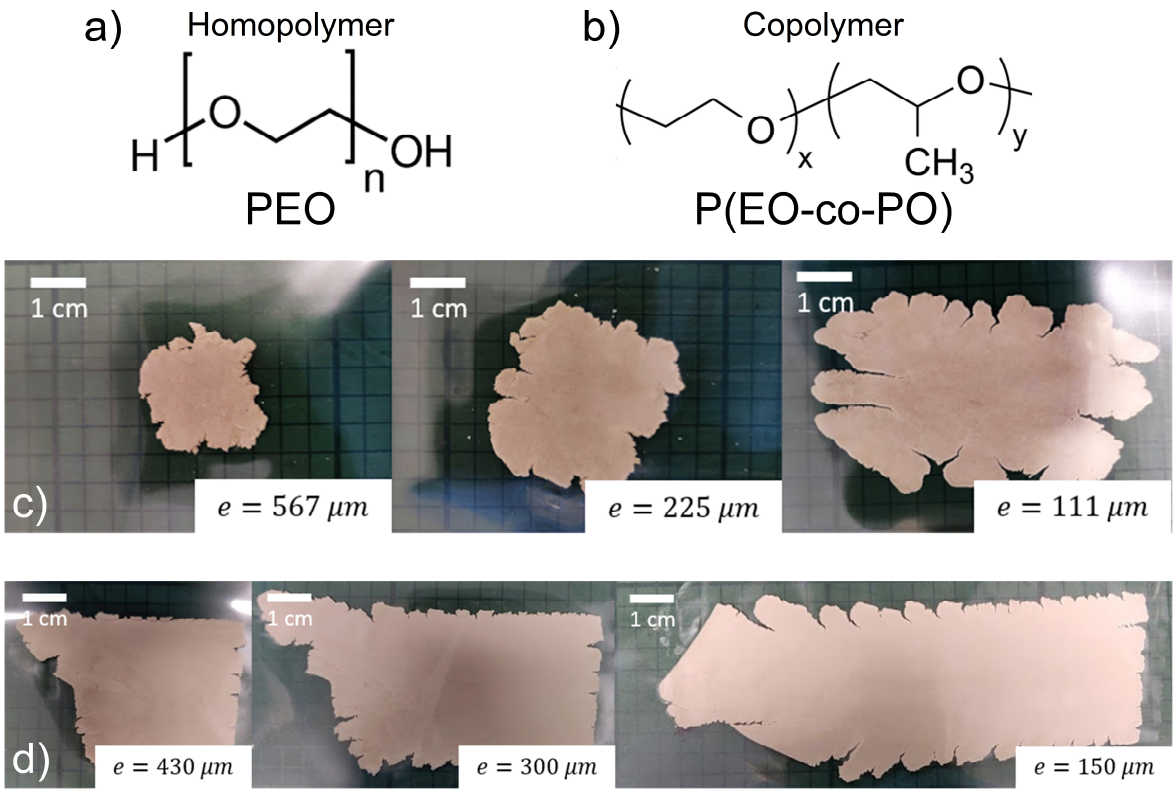

Figure 2.25 Chemical formulas of (a) homopolymer poly(ethylene oxide) PEO and (b) copolymer poly(ethylene-*co*-propylene oxide) P(EO-co-PO). (c) Calendering of the homopolymer-based HSE with crack propagation. (d) Calendering of the copolymer-based HSE limiting crack propagation.

It differs only in the presence of a propylene oxide unit at a 12:1 ratio with ethylene oxide units, which does not affect the HSE room temperature ionic conductivity ($0.9 \cdot 10^{-4}$ S.cm^{-1}). Being less resistant to creep, the copolymer helped in obtaining a large area film without the propagation of cracks from the edges.

Throughout the manufacturing process of the HSE, we measured the water uptake in the materials, using the Karl-Fischer titration (**Figure 2.26**).[170] We confirmed that the precursor materials were sufficiently dried, all of them displaying less than 10 ppm of water. However, the mixing and calendering steps led to a significant water uptake in the HSEs, between 300 and 4000 ppm. This can be explained by the fact that PEO and its derivatives are highly hygroscopic materials.[115] However, degraded Li_6PS_5Cl generates hydrogen sulphide (H_2S) which can perturb the Karl-Fischer titration based on the following reaction between water, iodine and sulphur dioxide, explaining high values:

$$SO_2 + I_2 + 2\,H_2O \rightleftarrows H_2SO_4 + 2\,HI$$ **Equation 2.3**

Anyway, elevated values of "water content" are a sign of degradation within the HSE, with water being the cause and H_2S the consequence. Additionally, the mixing and calendering processes are done in the least air-controlled part of the dry room, displaying 250 ppm of water on average. The difference of "water levels" based on the ceramic content simply originates from the longer time of exposure to dry air, during the fabrication steps of the high-inorganic content HSE (75 wt.% Li_6PS_5Cl), due to its higher stiffness. Overall, the unveiled degradation is preventing the use of HSEs for practical application, due to unavoidable hydrolysis of Li_6PS_5Cl, through organic phase capturing water, which subsequent drying cannot overcome. Therefore, stricter control of water levels is necessary to avoid this constraining phenomenon. Nevertheless, we demonstrate the feasibility of preparing critical-size HSE films using a solvent-free process.

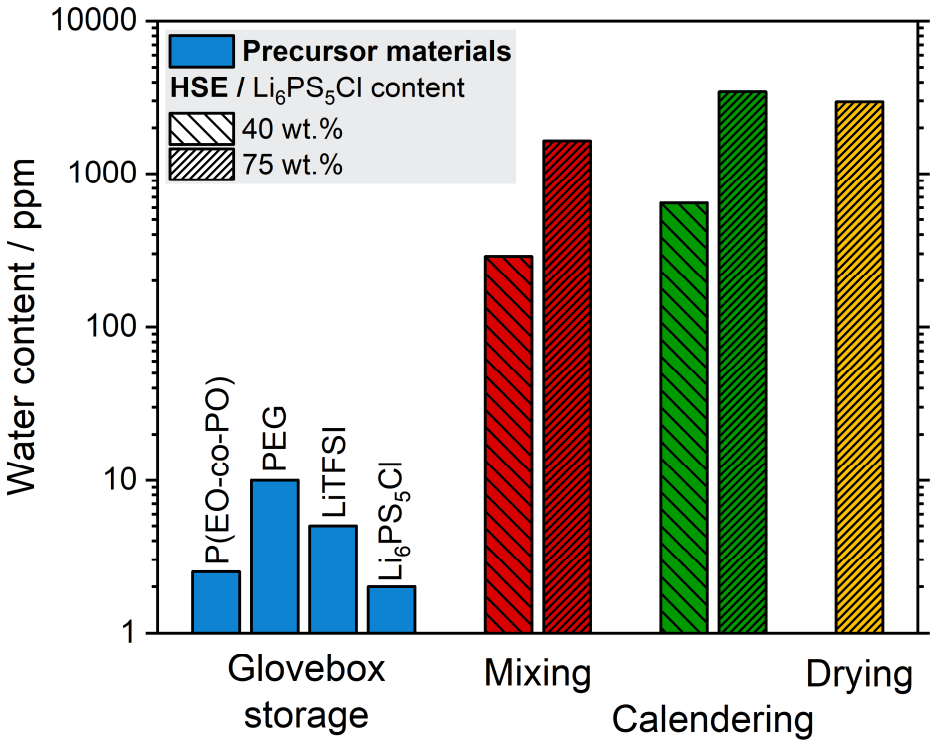

Figure 2.26 Evolution of water content at different stages of the HSE preparation in the dry room: storage of precursor materials, internal mixing, calendering and vacuum drying at 80°C overnight. Water quantification performed following Karl-Fischer titration.

2.4.2 Assessment of the mechanical properties

To characterise the observed difference in the HSE mechanical behaviour according to the ceramic content, we performed tensile test on two representative formulations. Li_6PS_5Cl content was set to 40 and 75 wt.% to compare a *ceramic-in-polymer* system with a *polymer-*

in-ceramic one. The organic phase was kept identical as the optimised one, [P(EO-co-PO):PEG = 1:1 (w)]$_{10}$:LiTFSI. The HSE films were prepared and tested in the dry room following the procedure described in previous section **2.4.1**. The obtained stress-strain curves demonstrate in both cases a good reproducibility between samples (**Figure 2.27**), indicating a good homogeneity of the films obtained by the dry mixing process.

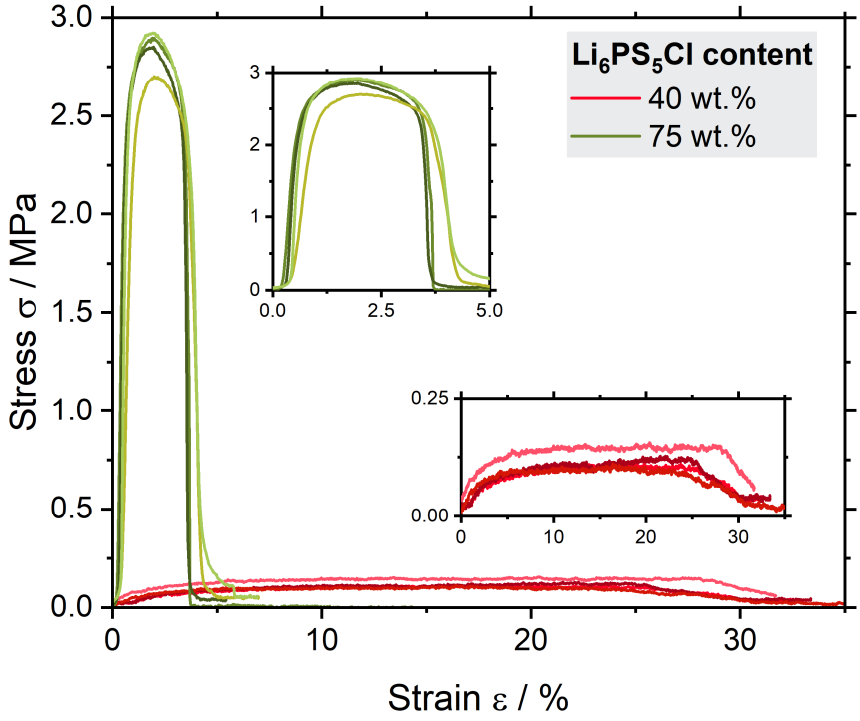

Figure 2.27 Stress-strain curves obtained by tensile test on HSE with two representative amounts of Li_6PS_5Cl (40 and 75 wt.%). Four repetitions were recorded per formulation.

Changing the organic-to-inorganic ratio leads to very different mechanical behaviours. The low ceramic-content HSE (40 wt.%) deforms mainly in a plastic regime (ε = 25%) under a low applied stress (σ = 0.12MPa). This results in a low Young's modulus of 3.6 MPa (**Figure 2.28a**), which is 200 times smaller than the high ceramic-content HSE (75 wt.%). The Young's modulus of 0.82 GPa illustrates the stronger elastic behaviour of the optimised formulation. Overall, the *polymer-in-ceramic* configuration withstands higher stress under elastic (respectively plastic) deformation than the *ceramic-in-polymer* one – yield stress σ_y = 1.8 MPa versus 0.067 MPa (resp. ultimate strength σ_u = 2.8 MPa versus 0.12 MPa). In terms of ability to absorb mechanical energy, the high-ceramic content HSE still outperforms the low content one. The resilience modulus U_r (energy absorbed under elastic deformation i.e. reversible) is 2.1 kJ.m^{-3} compared to 0.68 kJ.m^{-3} (**Figure 2.28b**). In the same trend, the toughness modulus

U_t (energy absorbed before fracture i.e. non-reversible) is almost four times higher (86.5 kJ.m^{-3} versus 24.3 kJ.m^{-3}).

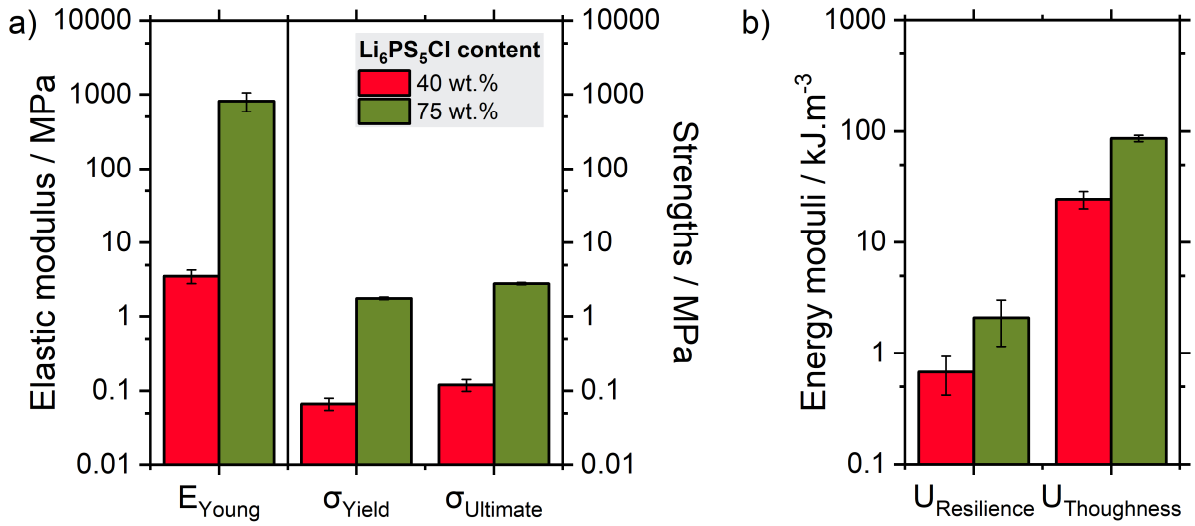

Figure 2.28 Evolution of HSEs tensile properties with ceramic amount: (a) Young's modulus, yield and ultimate strengths, (b) resilience and toughness moduli.

This tensile characterisation demonstrates that the addition of Li_6PS_5Cl particles is beneficial for mechanical resistance of the HSE. As detailed in **Table 2.1**, our HSE outperforms the precursor phase PEO_{10}:LiTFSI, whose tensile properties were assessed by Lopez *et al.*[108]

	E / MPa	**σ_{yield}** / MPa	**U_r** / kJ.m^{-3}	**U_t** / kJ.m^{-3}
PEO_{10}:LiTFSI [108]	0.4	0.04	3	40 – 50
HSE (40 wt.%)	3.6	0.068	0.68	24
HSE (75 wt.%)	820	1.8	2.1	86
Li_6PS_5Cl [107]	22 000 (DFT)	-	-	-

Table 2.1 Summary of mechanical figures for the precursor and hybrid solid electrolytes.

Its yield strength is lower (σ_y = 0.04 MPa) as the material deforms mainly plastically under a long stress plateau. However, resilience (U_r = 3 kJ.m^{-3}) and toughness moduli (U_t = 40 – 50 kJ.m^{-3} – estimated graphically) are comparable. Although our HSE withstands a higher mechanical stress, this means that it is a brittle material compared to the conventional polymer electrolyte, which may be expected given the high content of Li_6PS_5Cl, weakening the elasticity provided by the polymer. Ultimately, we show that a combined increase of ionic

conductivity (σ_{ion} = 10^{-5} to 10^{-4} S.cm^{-1} at 25°C) and mechanical resistance is possible using a systematic formulation approach for HSEs. Improving the mechanical properties of polymer or hybrid electrolytes generally leads to a drop in conductivity. Stolz *et al.*[90] demonstrated the negative correlation between compression resistance and ionic conductivity at 40°C by simply changing the salt concentration in PEO_x:LiTFSI (x = 10 – 50). Lee *et al.*[171] studied an HSE composed of PEO_{20}:LiTFSI and LAGP, and showed that increasing the ceramic amount has a positive impact on the Young's modulus, although it strongly affects the toughness and the ionic conductivity.

2.4.3 Electrochemical performance of HSE-based cells

To conclude the study of the HSE, we explored its applicability as a separator in real electrochemical systems. We first analysed its dynamic behaviour with lithium metal electrodes, in polarised symmetric cells. We subsequently paired the HSE with an NMC-based cathode and evaluated the cell cycling performance.

○ Critical current density determination

The development of SBBs is closely tied to the integration of a lithium metal anode, as we previously detailed in section **1.3.2**. An essential metric to assess the performance of a system utilising a lithium metal is the critical current density (CCD).[172] It is defined as the maximum current density at which a cell can cycle without experiencing any failure, like dendrites formation. One method involves a staircase and symmetric polarisation of a Li | (H)SE | Li cell (**Figure 2.29a**), resulting in alternating plating and stripping at each lithium electrode. Although commonly employed, this method is presently challenged as it presents several limitations, including lack of reproducibility, influence of current density profile on final value and effect of separator thickness.[173] However, we used the same procedure to compare the assembled cells, bearing in mind that the obtained CCD values are not directly applicable to full cell systems.

To evaluate the performance of our HSE, we assembled symmetric cells with homopolymer PEO and copolymer P(EO-co-PO) based optimised HSEs (75 wt.% Li_6PS_5Cl). They were cycled with a starting current density of 20 µA.cm^{-2} for five cycles and a subsequent increase of 20 µA.cm^{-2} every cycle. We also measured the cell impedance at every cycle to probe the evolution of electrolytic and interfacial resistances (**Figure 2.29b**).

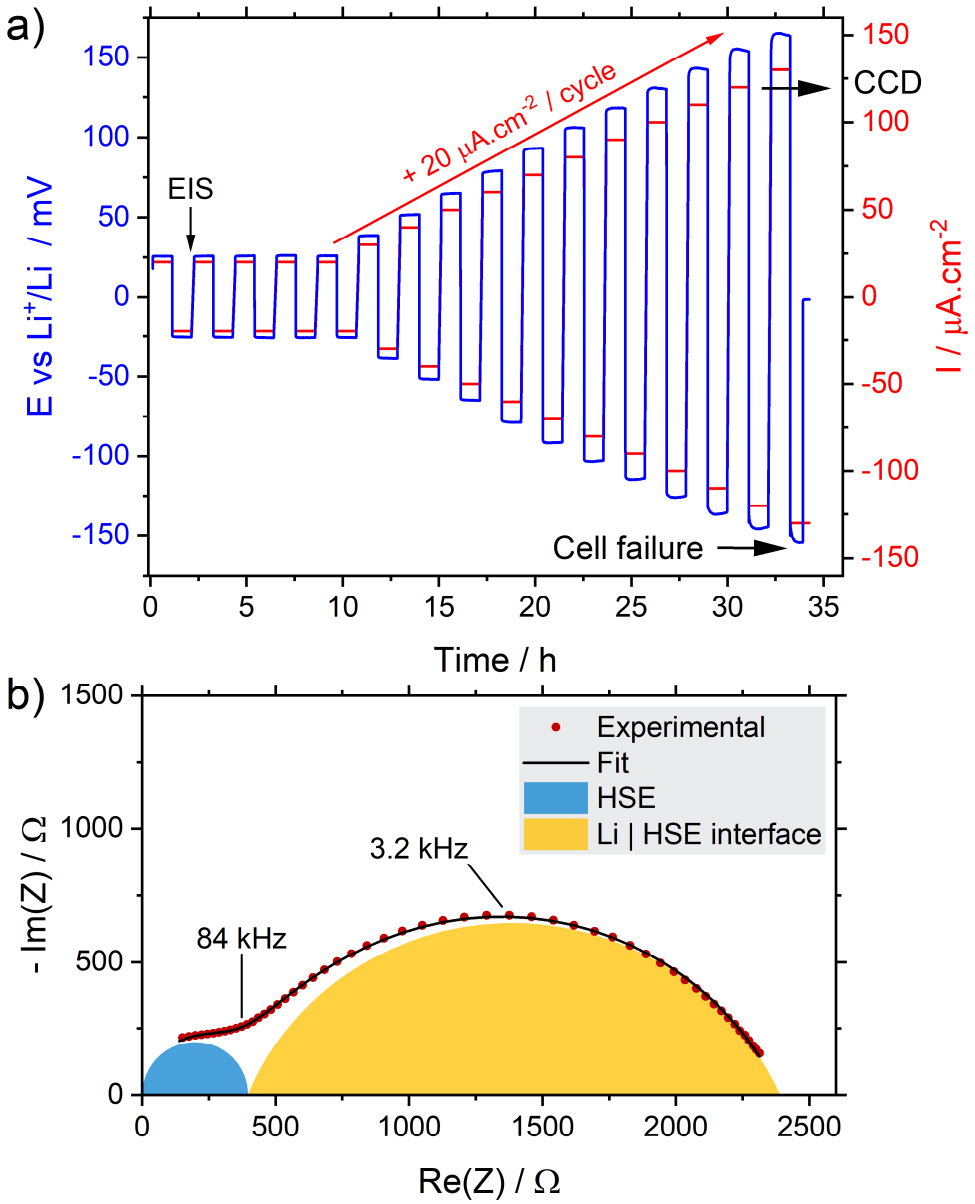

Figure 2.29 (a) Protocol of current staircase (red) for CCD determination with the voltage response (blue). (b) Impedance spectrum of Li | HSE | Li cell with a high-frequency electrolyte contribution (HSE – blue) and a medium-frequency interfacial contribution (Li | HSE interface – yellow).

Typical voltage profiles according to capacity are presented in **Figure 2.30a** & **31a**, for the homopolymer and the copolymer-based HSE cells, respectively. They display a similar behaviour with stable potential at a given current density and a linear evolution of the voltage with the current density. However, the CCD is lower for the homopolymer-based cell (120 $\mu A.cm^{-2}$) than for the copolymer-based cell (180 $\mu A.cm^{-2}$). The electrolytic and interfacial resistances evolve similarly in both cases (**Figure 2.30b-c** & **2.31b-c**).

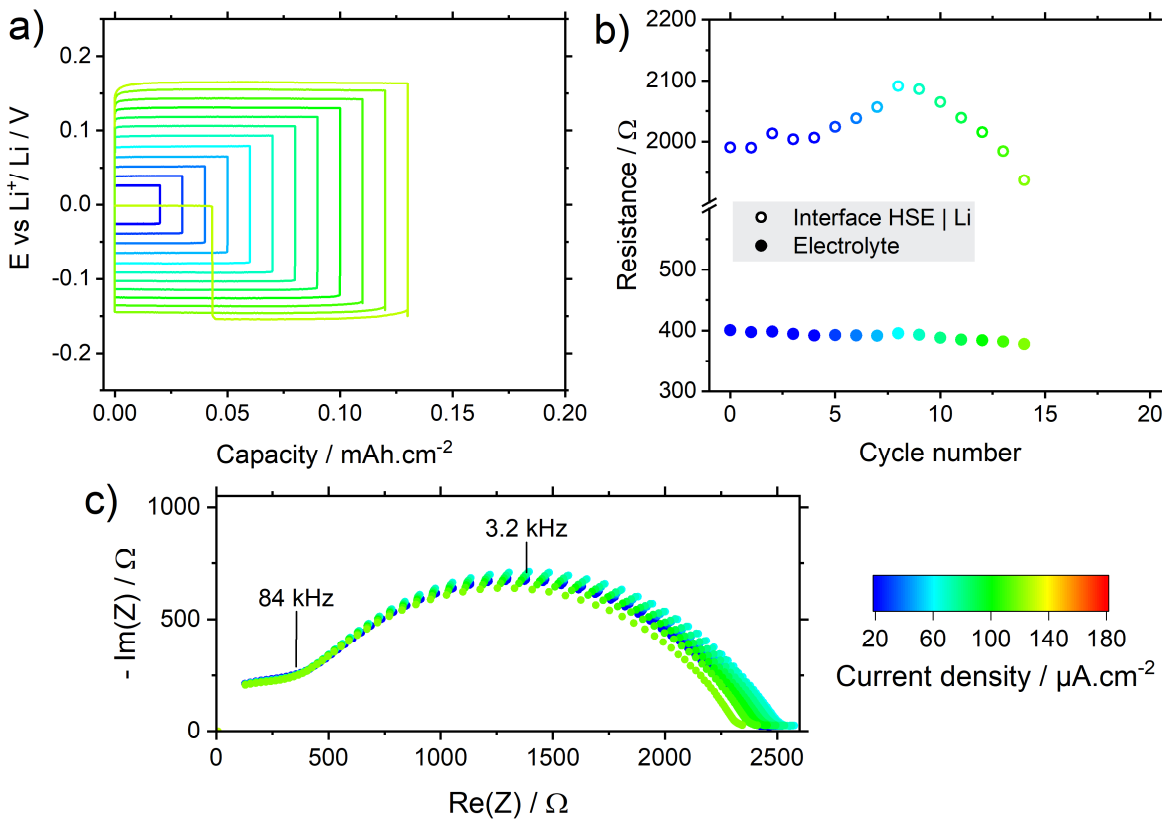

Figure 2.30 Determination of critical current density of the symmetric cell with the optimised HSE based on homopolymer PEO. (a) Voltage profile according to capacity. (b) Evolution of electrolytic and interfacial resistances over cycles. (c) Electrochemical impedance spectra over cycles. Colours represent the current density applied to the symmetric cell.

Interestingly, the resistance stemming from the HSE layer is constant over cycling in both configurations while the interfacial contribution tends to increase before a decrease occurs and ultimately leads to the failure of the cell. It can originate from uneven lithium plating and stripping due to the interface roughness. Some sites are less resistive for lithium exchange and are consequently preferred, leading to an overall decrease of the interfacial resistance. The induced current focussing is then known to be an initiator of dendrites, thus explaining the subsequent short-circuit.[144]

Overall, the CCD determination of HSE-based cells did not prove any benefit of our HSE compared to a classical Li_6PS_5Cl separator. As shown on **Figure 2.32**, there is a slight improvement of the CCD when shifting from PEO (87 ± 31 µA.cm^{-2}) to P(EO-co-PO)-based HSE (147 ± 25 µA.cm^{-2}), but the CCD magnitude remains much lower than what is observed for argyrodite-based cells (646 ± 196 µA.cm^{-2}). Data on pure Li_6PS_5Cl pellets were provided as a courtesy of Dr. Benjamin Hennequart.

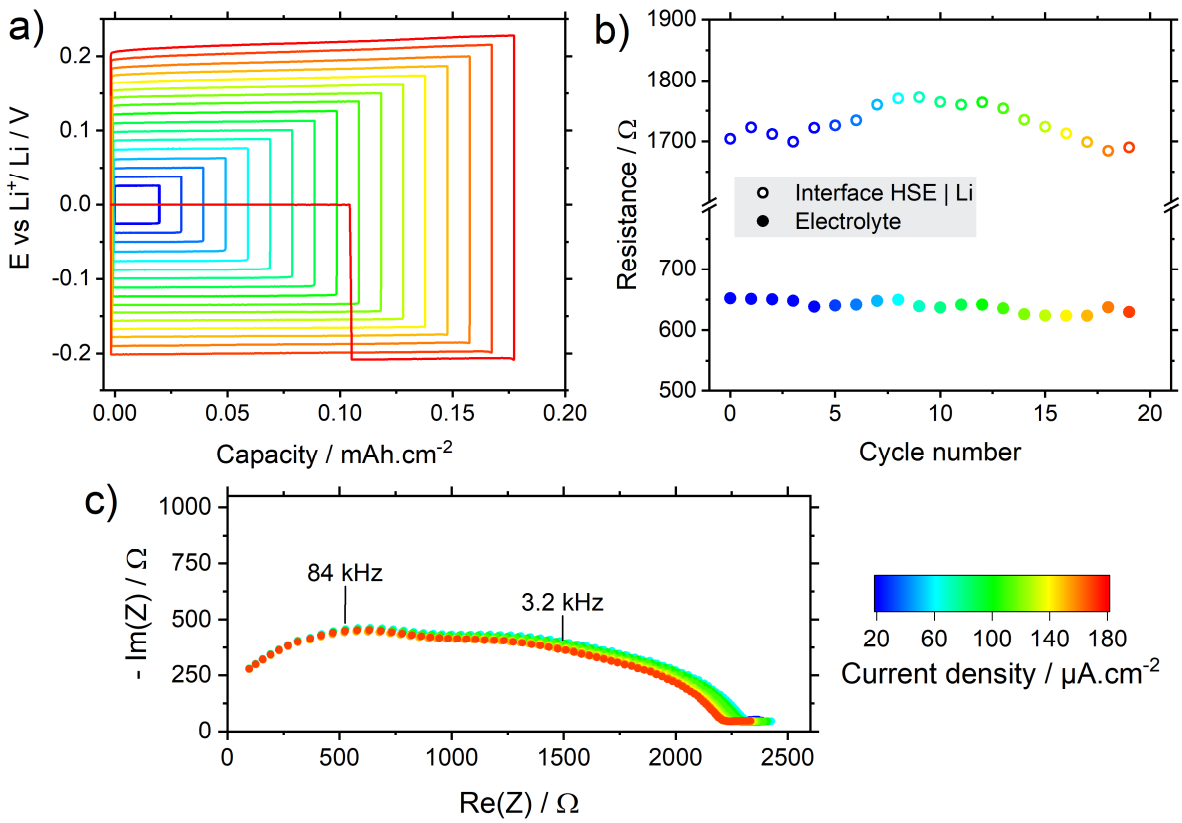

Figure 2.31 Determination of critical current density of the symmetric cell with the optimised HSE based on copolymer P(EO-co-PO). (a) Voltage profile according to capacity. (b) Evolution of electrolytic and interfacial resistances over cycles. (c) Electrochemical impedance spectra over cycles. Colours represent the current density applied to the symmetric cell.

The difference between homopolymer and copolymer systems is too small to give a trustworthy interpretation. We must keep in mind that various parameters can influence the determination of a CCD. The thickness of electrolyte plays a significant role in mitigated the occurrence of dendrites and is here very different between HSE (≈ 150 µm) and Li_6PS_5Cl-based cells (> 1mm). Other factors influence greatly the CCD, including the assembly and cycling temperature and pressure, the SE mechanical properties, the areal capacity, the interfacial chemical stability and the quality of the lithium metal anode. As a result, a large variability is observed in previously reported results,[173] highlighting the complexity of the SE | Li interface and the difficulty in accurately probing it via classical CCD measurements.

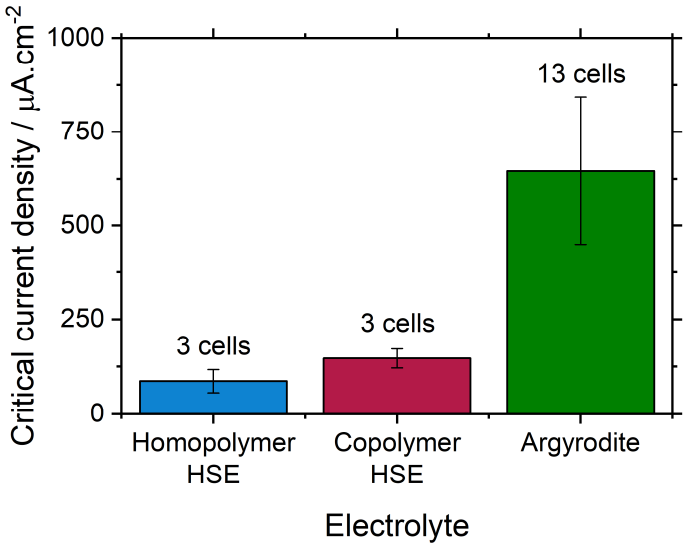

Figure 2.32 Statistics on critical current density measured for argyrodite and HSEs based on homopolymer and copolymer. Argyrodite data available as a courtesy of Dr. Benjamin Hennequart.

○ Half-cell cycling based on the HSE as separator

To approach the final full cell system, we investigated the cycling behaviour of our HSE paired with an NMC-based cathode composite. For this, we employed monolithic particles of $LiNi_{0.6}Mn_{0.2}Co_{0.2}O_2$ (NMC622 – d = 4 µm) as they demonstrate enhanced performance in SSBs.[27] We compared the electrochemical performance with our reference system based on a pure Li_6PS_5Cl separator, employing a relatively low loading around 4 $mg_{NMC}.cm^{-2}$. An in-house prepared cathode composite tape, based on a PVDF-HFP binder (15 mol.% HFP – 300 $kg.mol^{-1}$), is used to ensure good reproducibility between cells, which cycle at a high pressure of 100 MPa, to ensure sufficient contact between particles. The first cycle voltage profile at C/20 reveals a higher polarisation when employing the HSE as a solid-state separator instead of a densified ceramic pellet, despite a lower cathode mass loading (**Figure 2.33a**). The result is a discharge capacity 15% lower for the HSE battery (130.2 $mAh.g^{-1}$) than for the reference batteries (153.25 $mAh.g^{-1}$). This figure is nonetheless encouraging as the thinner hybrid membrane (87 µm) compared with the Li_6PS_5Cl separator (≈ 400 µm) does not compensate for the lower ionic conductivity of the HSE (10^{-4} versus $3 \cdot 10^{-3}$ $S.cm^{-1}$). However, as the ohmic drop becomes significant at a higher C-rate, polarisation increases more rapidly for the HSE battery than for the reference battery, resulting in almost zero capacity at 1C (**Figure 2.33b**). When the current density is reduced to C/5 (**Figure 2.33c-d**), both systems return to their previous capacity levels and show good capacity retention, with a similar decay rate of -0.14 $mAh.g^{-1}.cycle^{-1}$ (resp. -0.155) for the HSE-based battery (resp. pure ceramic batteries). Due to

initial capacity difference, the HSE-based battery reaches 80% discharge capacity faster (Cycle 113) than the reference cells (Cycle 180). Finally, these data indicate that it is possible to operate a battery assembled with our optimised HSE, with low capacity loss at a slow C-rate. However, the insufficient ionic conductivity of the HSE compared with the Li_6PS_5Cl separator affects the capacity accessible at higher C-rates due to greater polarisation. A possible strategy to overcome the poor performances at higher C-rates, or similarly at higher cathode loads, could be to reduce the HSE thickness to less than 10 µm to have an ohmic drop equivalent to that of the reference battery. For the time being, this prospect is limited by the size of Li_6PS_5Cl particles, some of which exceed 30 µm (**Figure 2.2**). On the other hand, the interfaces at the cathode and anode may not be as optimised with the HSE as with pure ceramic, which would require some surface engineering (use of temperature, roll-to-roll assembly).

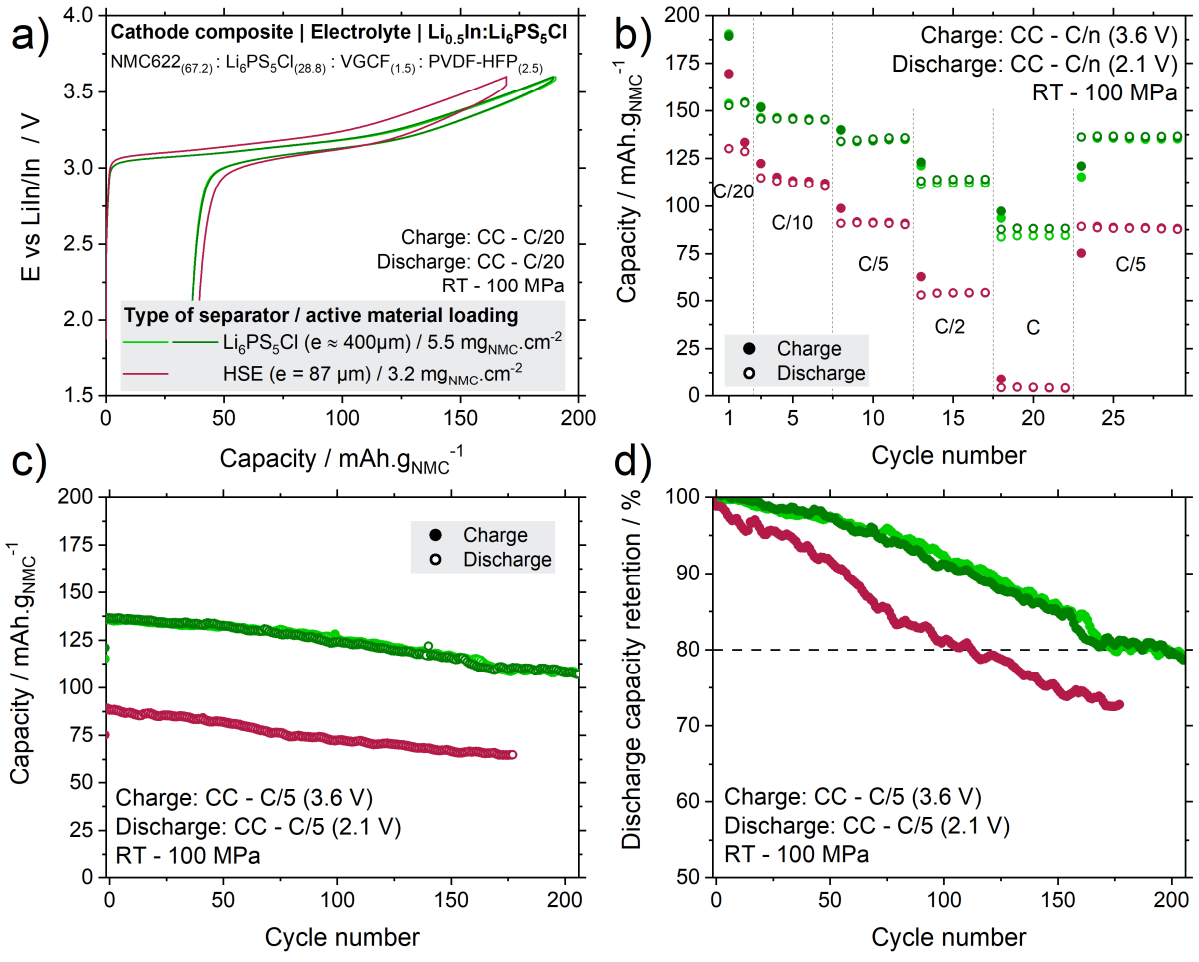

Figure 2.33 Electrochemical performance of an HSE-based battery at room temperature. Comparison between batteries based on HSE (1 cell) or pure Li_6PS_5Cl separator (2 cells): (a) first cycle voltage profile. (b) C-rate behaviour, (c) capacity at C/5 and (d) discharge capacity retention at C/5.

2.5 – Conclusion

In conclusion, **Chapter 2** has presented a thorough study on a hybrid solid electrolyte composed of Li_6PS_5Cl and PEO:LiTFSI (and its derivatives). Our initial ambition was to achieve an HSE in the shape of a thin film that can effectively conduct lithium ions. We set the ionic conductivity target at 10^{-4} $S.cm^{-1}$ at room temperature, while giving particular attention to processability of the HSE (flexible versus brittle).

We first focused on the formulation of the electrolyte and the processing strategy. After eliminating the solvent-based route due to electrolyte degradation issues, we prepared HSEs by dry mixing to explore the range of organic-to-inorganic ratio. The addition of Li_6PS_5Cl improved ionic conductivity beyond 75 wt.%, but it compromised mechanical strength, representing a typical trade-off in HSEs. To address it, we reduced PEO molar mass and proposed a modified organic matrix that combines elasticity and ionic conductivity, resulting in a high-ceramic loading HSE that meets our criteria. Additionally, we introduced a novel approach by utilizing activation mechanism fitting as a powerful metric to elucidate the preferred ionic pathway within HSEs. The VFT model serves as a signature of organic conductivity, while the Arrhenius model characterises ceramic conductivity.

To get a finer understanding of the ionic pathway, we investigated the interface between the inorganic and the organic phases, and its ability to transfer lithium ions. We could detect significant reactivity triggered by temperature, from XPS and EIS measurements. The resulting interphase is obviously detrimental to a joint conduction mechanism since it displays a high energetic barrier for lithium ions to cross it. It was further confirmed by ssNMR analysis with which we detected only slow ionic exchange across the interphase. Interestingly, we could follow the interphase growth in time that relies on the immobilisation of lithium ions initially present in the organic phase.

Keeping in mind the initial purpose of HSE practical application, we studied the potential for scaling up the manufacturing of our HSE in dry room conditions. The main hurdle we encountered lies in the hygroscopicity of the organic phase that leads to the irreversible degradation of the neighbouring inorganic phase. Using common tools for large-scale polymer electrolyte preparation, we applied the same procedure to our HSE and proved the feasibility of manufacturing large area films with it, provided there a stricter control over the ambient

water level. Additionally, enhancement of mechanical properties was observed with a high inorganic content. We finally evaluated the performance of the HSE in batteries, which revealed a non-mastered interface with a lithium metal anode, displaying a low CCD. However, it showed decent cycling figures when paired with an NMC-based cathode.

Overall, the **Chapter 2** has underscored the prime importance of optimizing ionic conductivity and mechanical properties concurrently, for successful HSE formulation. It also provided valuable insights into key conduction mechanisms. Future research should focus on reducing membrane thickness through particle size control and limiting chemical reactivity, by polymer end group modification[174] or particle protective coating[131], to match pure ceramic battery performances. Ultimately, we hope this work serves as guideline for HSEs rational formulation, with emphasis on metric optimization driving further advancements.

Chapter 3 – Tape casting to enable scaling up of solid-state batteries

3.1 – Introduction

Scaling up the manufacturing of solid-state batteries (SSBs) remains one of the greatest challenges of the research field today. The transition from pellet-type to sheet-type SSBs necessitates the incorporation of a polymeric binder to ensure cohesion of the layers. In the previous chapter, we introduced a strategy to achieve both sufficient ionic conductivity and suitable mechanical properties in a solid-state hybrid separator, mixing an organic (PEO:LiTFSI) and an inorganic electrolyte (Li_6PS_5Cl). Although we achieved the desired conductive and mechanical properties, the combination of these two solid electrolytes (SEs) presented several challenges in terms of their chemical compatibility and practical performance in SSBs. This raised the question whether we should use a lithium-conducting binder, such as PEO:LiTFSI, given our findings suggesting that enhanced ionic conductivity was only achievable through conduction within the ceramic network. Additionally, the need for a high-ceramic loading hybrid SE typically compromises the ease of dry mixing and the tape mechanical properties. In light of these results, we questioned the necessity of hybridization for solid-state separators when scaling up SSBs. Shifting to non-conductive binders, commonly used in the lithium-ion batteries (LIBs) industry, became more attractive to reduce polymer content while achieving higher conductivity without compromising mechanical integrity.

As outlined in **Chapter 2**, one promising strategy to manufacture solid-state tapes involves casting an ink composed of ceramic particles (either SE or cathode composite) and binder dispersed in a supporting solvent. Following this strategy, the present chapter introduces the development of self-supporting separators and cathode composite sheets, utilizing the sulphide-based SE Li_6PS_5Cl and the layered oxide $LiNi_xMn_yCo_{1-x-y}O_2$ (NMC) active material (AM). The initial challenge lay in identifying the optimal combination of solvent, binder, and SE. We opted for alkyl-ester solvents capable of dissolving the commonly used poly(vinylidene fluoride-co-hexafluoropropylene) (PVDF-HFP) binder, while preserving the SE's chemical stability. Subsequent steps involved refining the process and optimizing the formulation to produce a cathode composite sheet on an aluminium current collector, with the aim of minimizing the impact of slurry processing on electrochemical performance. Concurrently, self-standing separators were developed using a similar tape casting process, and the influence of various formulation parameters (binder type and content, SE particle size) on the chemicophysical properties (porosity, ionic conductivity, mechanical properties) was

evaluated. Finally, attempts were made to assemble these two layers along with a lithium-indium alloy anode layer to manufacture self-supported SSBs packaged in laminated pouch bags. Different densification strategies were studied, along with their influence on the cell electrochemical performance at significantly reduced pressures compared to conventional testing (≤ 5 MPa). Collectively, these developments bring us closer to practical SSB systems, offering the potential to increase cell area and energy density, thereby paving the way for the integration of the lithium metal anode.

3.2 – Finding the adequate solvent-binder-SE triptych

As mentioned previously in **Chapter 1**, solvent processing of sulphide-based SEs, especially Li_6PS_5Cl, poses a complex challenge due to their strong nucleophilic interaction with most common solvents (e.g. acetonitrile – ACN, tetrahydrofuran – THF, toluene, N-methyl-2-pyrrolidone – NMP, ethanol, water).[40,141] However, these solvents are often preferred for their ability to dissolve common polymeric binders (e.g. PVDF and its HFP-based copolymers, nitrile/styrene butadiene rubber – N/SBR), owing to their sufficient polarity. These two limitations restrict the range of solvents capable of effectively dissolving the chosen polymeric binder, in our case PVDF-HFP, without negatively affecting Li_6PS_5Cl chemicophysical properties.

3.2.1 Possible solvent-binder pairs

Recently alkyl-ester solvents have emerged as promising candidates for wet processing argyrodite with PVDF-HFP.[141,160,162] We investigated three solvents that differ primarily in their steric hindrance, varying in the length of their alkyl chains: ethyl acetate – EA: 2C + 2C, butyl butyrate – BB: 4C + 4C, and hexyl butyrate – HB: 4C + 6C (**Figure 3.1a**). A critical parameter for the processing of solid-state tapes is the boiling point, which naturally increases with bulkier molecules (from 77 to 205°C - **Figure 3.1b**). This parameter affects the drying rate of the coated solid-state tapes and the arrangement of particles within the binder. In 2022, Kim *et al.*[162] reported that the use of a low boiling point solvent, such as EA, lead to fast solvent evaporation and migration of the PVDF-HFP binder to the top of the electrode, causing its delamination. They proposed a mixture of EA and HB solvents to circumvent this issue.

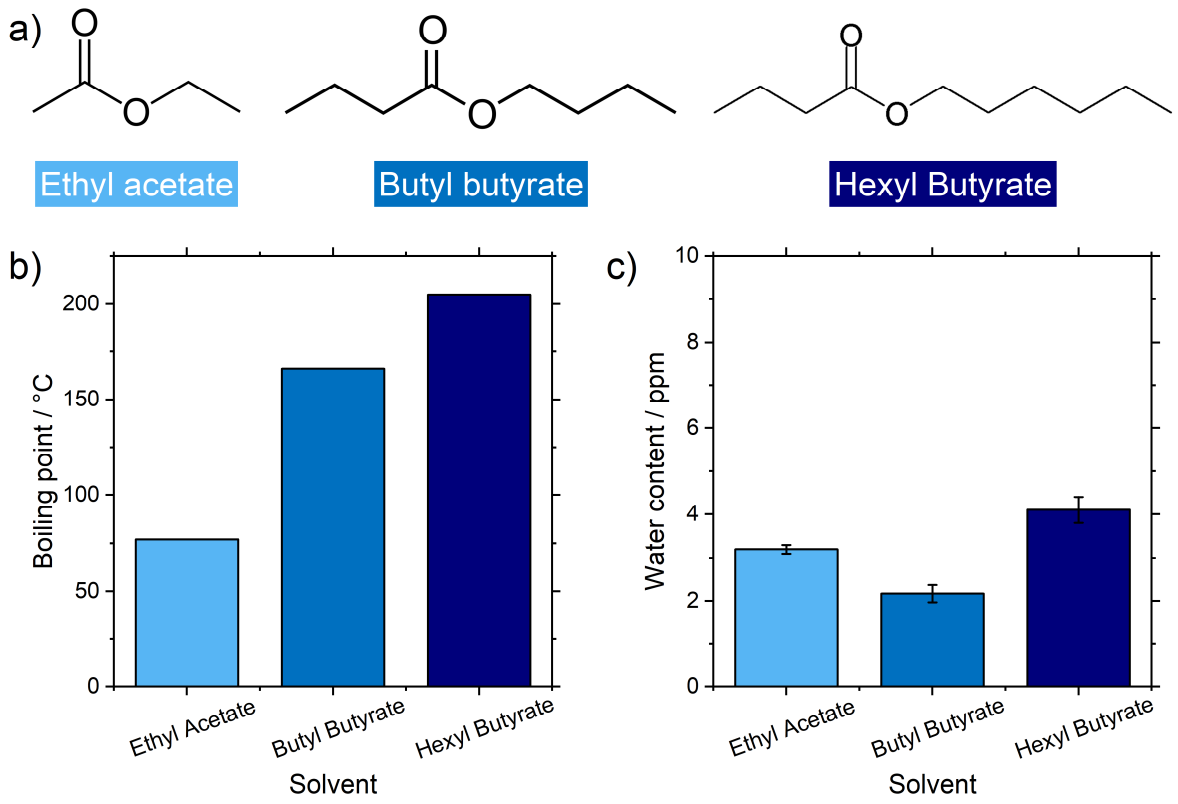

Figure 3.1 (a) Chemical formulas of employed solvents and their respective (b) reported boiling points[175–177] and (c) measured water content.

To prepare the solid-state tapes using these solvents, we initially dried them over 4Å molecular sieves to remove any residual water and prevent Li_6PS_5Cl degradation. All solvents achieved low water levels, below 5 ppm, as measured by Karl-Fischer titration (**Figure 3.1c**).

We chose PVDF-HFP for the manufacturing of our solid-state tapes due to its ability to adjust the ratio of the HFP comonomer, which modifies its physical properties. Moreover, PVDF-HFP is readily available commercially, as it is already employed in both Li-ion and Li metal-polymer technologies.[81] Thermal analysis was performed on two of these binders, with HFP contents of 15 and 30-35 mol.% (information given by the suppliers: Solvay and Arkema, respectively). Thermogravimetric analysis (TGA) shows a lower and broader temperature range for binder degradation with a higher content of HFP (442°C for 30-35 mol.% versus 493°C for 15 mol.% - **Figure 3.2a**), suggesting reduced thermal stability. However, these temperature limits are more than adequate considering the processing and operation of SSBs within the range of room temperature to 100°C.

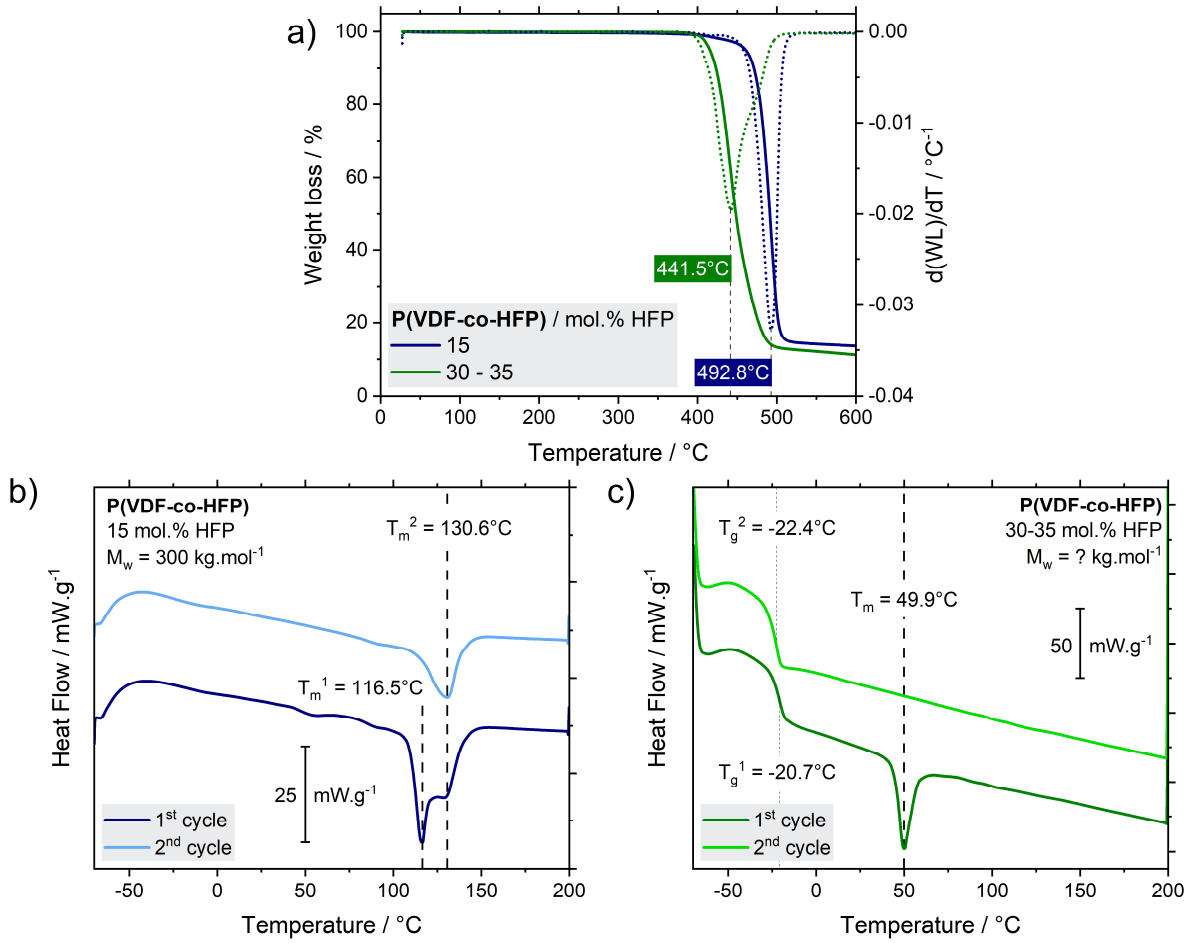

Figure 3.2 Thermal analysis of two types of P(VDF-co-HFP) with 15 mol.% (blue) and 30-35 mol.% of HFP comonomer. (a) Thermogravimetric analysis (TGA) from room temperature to 600°C with weight loss and its first derivative according to temperature. (b-c) Differential scanning calorimetry (DSC) measurements with first and second heating scans between -70 and 200°C. All experiments were performed under argon atmosphere at a rate of 10°C.min^{-1}.

Differential scanning calorimetry (DSC) highlights two distinct thermal behaviours. The low HFP content binder displays a dual event around 120°C (α and β phases melting)[178] which is partly reversible, as assessed by the presence of a melting peak (T_m^2 = 130.6°C) on the second heating step. This binder behaves as a thermoplastic, which is semi-crystalline at room temperature.[179] On the other hand, increasing the HFP content to 30-35 mol.% drastically modifies the thermal properties and the amorphous binder then possesses elastomeric properties. Indeed, no melting event appears on the second heating step and the melting temperature on the first cycle is much lower (50°C) than for the low HFP content binder. These two distinct mechanical behaviours will influence the mechanical properties of our solid-state tapes, which will be discussed in the following sections.

Finally, we assessed the solubility of these binders in the three chosen alkyl-ester solvents. For this, we mixed various amount of binder (1, 2.5, 5 and 10 wt.%) in each solvent and qualitatively observed the clarity and homogeneity of the prepared solution. The maxima of solubility that we obtained for each combination are summarised in **Table 3.1**.

		HFP content / mol.%	
		15	30 - 35
Solvent	Ethyl acetate	5 wt.% (100°C) Gel at 25°C	10 wt.% (25°C)
	Butyl Butyrate	2.5 wt.% (100°C) Gel at 25°C	10 wt.% (25°C)
	Hexyl butyrate	Not soluble at 1 wt.% (100°C)	5 wt.% (100°C)

Table 3.1 Maxima of PVDF-HFP solubility in various alkyl-ester solvents (EA, BB and HB) according to the HFP comonomer content and the temperature.

Natural tendencies emerged from these solubility tests. Small solvent molecules can better dissolve the binder, at higher contents. The elastomer $PVDF_{70}$-HFP_{30} is soluble in ethyl and butyl butyrate up to 10 wt.%, without the assistance of temperature. Its solubility is lower in hexyl butyrate and needs some heat to dissolve fully. However, the thermoplastic $PVDF_{85}$-HFP_{15} is difficult to dissolve in large amounts and systematically requires some heating to obtain a clear solution. Interestingly, these solutions jellify when cooled down to room temperature. Being less fluorinated, $PVDF_{85}$-HFP_{15} have less sites for intermolecular bonding with the solvent, possibly explaining weaker solubility compared to $PVDF_{70}$-HFP_{30}. Altogether, the binders that we selected can be used at sufficient concentrations in the alkyl-ester solvents, although some heating is required in the case of $PVDF_{85}$-HFP_{15}.

3.2.2 Argyrodite stability with the processing solvent

In our study, we selected three types of Li_6PS_5Cl powders, varying in the particle size and supplier. Two materials were sourced from NEI Corporation, labelled as *normal* (*n*Li_6PS_5Cl) and *fine* (*f*Li_6PS_5Cl). Observation of the powders by scanning electron microscopy (SEM – **Figure 3.1**) revealed no significant difference in particle size. Only the largest particles (around 30 µm in diameter) seemed to have been removed, likely through sieving or grinding. As displayed on **Figure 3.4a**, conductivity measurements revealed a slightly lower ionic

conductivity at room temperature for *f*Li_6PS_5Cl (1.6 $mS.cm^{-1}$) compared to *n*Li_6PS_5Cl (2.6 $mS.cm^{-1}$). These measurements were performed on densified pellets (400MPa) in an ion-blocking electrodes (carbon paper) configuration, at 100 MPa within a dedicated cell (**Figure S3.1**).

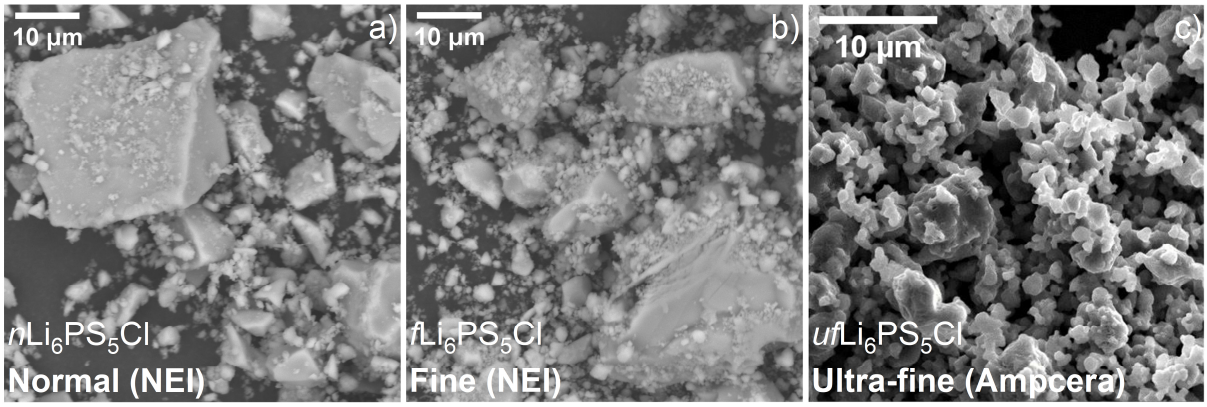

Figure 3.3 Scanning electron microscopy (SEM) pictures of Li_6PS_5Cl powders from different suppliers: (a) normal and (b) fine argyrodite commercialised by NEI Corporation; (c) ultra-fine argyrodite commercialised by Ampcera.

As an alternative, we sourced argyrodite from another supplier (Ampcera) because they recently commercialised so-called ultra-fine powder with a D_{50} of 1 µm, consistent with the SEM image showing smaller particles. Interestingly, the ionic conductivity of *uf*Li_6PS_5Cl is not suffering from its higher specific surface area, as it is comparable to the conductivity of the most conductive material, *n*Li_6PS_5Cl (2.6 $mS.cm^{-1}$).

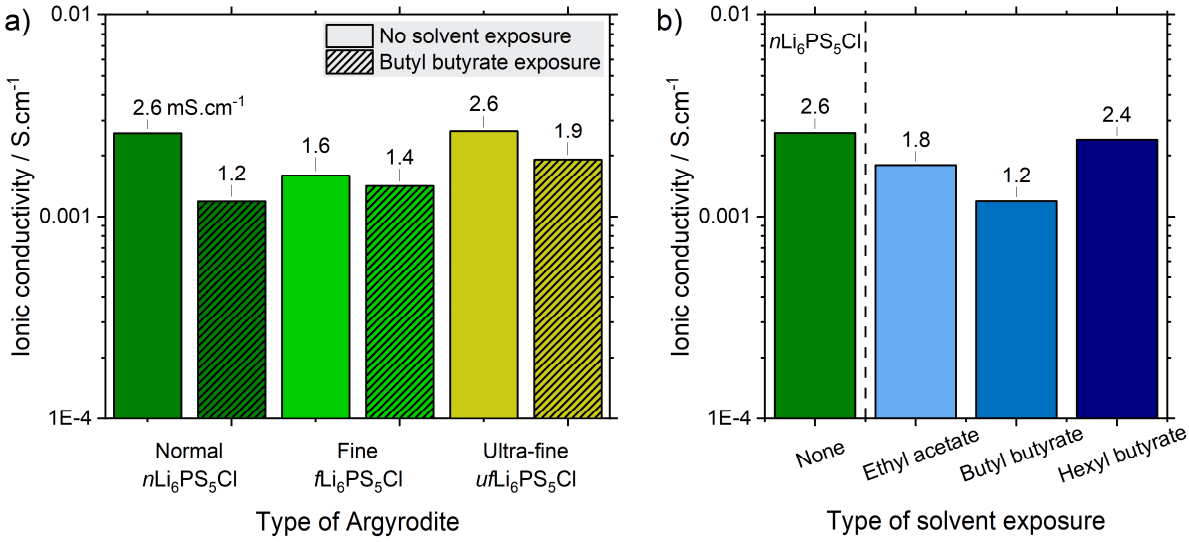

Figure 3.4 Effect of solvent exposure on Li_6PS_5Cl ionic conductivity at room temperature. (a) Butyl butyrate exposure on argyrodite powders of different sizes and suppliers. (b) Normal argyrodite exposed to various alkyl-ester solvents.

We further studied the retention of ionic conductivity in these argyrodites when exposed to our processing solvents (EA, BB and HB - **Figure 3.4b**). Overall, all the samples exposed retained a minimum of 1.2 $mS.cm^{-1}$ after undergoing high-energy ball-milling with the solvent for 10 min. The resulting suspension was then tape-casted and dried at 100°C, followed by vacuum drying, to mimic the procedure used for fabricating tape electrodes and separators. We consider the observed decrease in ionic conductivity to be acceptable for the wet processing of Li_6PS_5Cl, as it remains above 1 $mS.cm^{-1}$. Furthermore, we confirmed that the electronic conductivity did not increase after solvent treatment (**Figure S3.2**). X-ray diffractograms (XRD) of the exposed samples did not reveal any modification of the crystallographic structure (**Figure S3.3**). Altogether, these measurements confirm the satisfactory stability of Li_6PS_5Cl when exposed to the alkyl-ester solvents, providing a solid foundation for subsequent experiments involving the manufacture of tape cathodes and separators.

3.3 – Solid-state cathode composites: from powder to tapes

The transition from pellet-type to sheet-type SSBs introduces complexity to the system, requiring the incorporation of a polymeric binder for handling and mechanical integrity. However, the binder, intrinsically insulative, is an obstacle for the movement of lithium ions and electrons within the battery, thereby affecting overall performance. The main objective of the subsequent study, which focusses on the cathode, is to minimise the effect of the binder on electrochemical performance while ensuring that the prepared tape maintains the mechanical cohesion necessary for cell assembly (cutting, handling).

3.3.1 Decisive parameters for the slurry preparation

When opting for a solvent-assisted process, additional parameters must be considered compared to conventional powder grinding, which is typically used to prepare cathode composites at the laboratory scale. In this section, we explore some key parameters related to slurry preparation, including the influence of pre-grinding the cathode composite, the benefit of using a solvent mixture and the identification of the optimal mixing strategy.

The initial tests utilised the layered oxide AM $LiNi_{0.6}Mn_{0.2}Co_{0.2}O_2$ (NMC 622 – Umicore). However, to ensure consistency among our team, we subsequently shifted to the high-nickel content $LiNi_{0.82}Mn_{0.07}Co_{0.11}O_2$ (NMC 811 – MSE Supplies), which offers superior

electrochemical performance. Throughout the following sections, comparisons of cell performance will consistently employ the same AM. While cycling procedures may vary between tests (upper cut-off voltage, C-rate and active material loading), this information will be systematically provided.

○ Mixing the solid components

The initial test for preparing the tape cathode involved adding the powders to the solvent (ethyl acetate), and then subjecting the mixture to simple magnetic stirring for 10 min. Subsequently, the resulting slurry was hand-coated onto an aluminium current collector using the doctor blade technique with a 200 µm gap. The resulting tape was dried at 60°C under vacuum and cut to 8 mm discs for assembling SSBs in the dedicated cell setup (**Figure S3.1**).

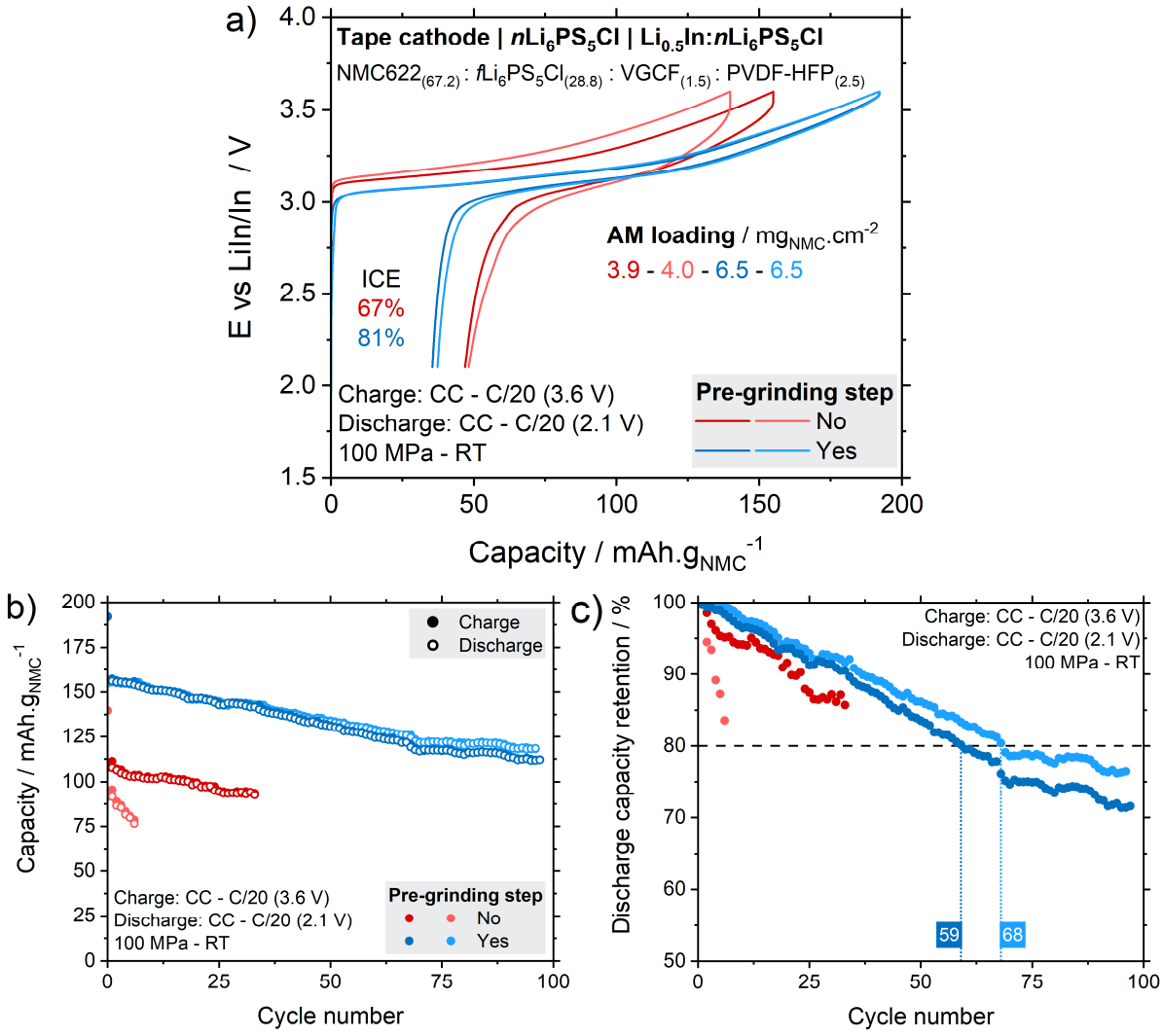

Figure 3.5 Electrochemical performance of tape cathode-based SSBs. Influence of pre-grinding the cathode composite before preparing the slurry for cathode tape casting. (a) First cycle voltage profile and initial coulombic efficiency (ICE). (b) Capacity and (c) retention at C/20.

Although the mechanical integrity and substrate adhesion were satisfactory, the AM loading appeared to be low (4 $mg_{NMC}.cm^{-2}$) compared to our standards (10 – 14 $mg_{NMC}.cm^{-2}$ / 2.7 – 3.9 $mAh.cm^{-2}$ as calculated from theoretical NMC capacity). The cycling behaviour of the cathode tape was probed in a system comprising a $n Li_6PS_5Cl$ separator and a $Li_{0.5}In$:$n Li_6PS_5Cl$ alloy anode composite. The voltage profile during the first cycle at C/20 (**Figure 3.5a**) exhibited significant polarisation between charge and discharge, resulting in a low initial coulombic efficiency (ICE = 67%). The long-term capacity was found to be non-repeatable between cells, of low magnitude (≈ 100 $mAh.g_{NMC}^{-1}$ at C/20), and displayed rapid decay (**Figure 3.5b-c**).

To circumvent the limited electrochemical performance, we implemented a preliminary step of grinding the cathode composite without the binder and solvent, aiming at enhancing the interparticle contacts between AM and SE. The resulting tape cathode displayed improved electrochemical performance, showing reduced polarization and achieving a higher ICE of 81%. Additionally, it demonstrated enhanced repeatability and higher capacity values at C/20 (155 versus 100 $mAh.g_{NMC}^{-1}$ without the pre-grinding step). To understand the origin of this improvement, we observed both cathode tapes with SEM (**Figure 3.6**). The organisation of the particles appeared more homogeneous with the pre-grinding step than with the simple suspension of powders in the slurry, potentially facilitating easier access to AM. This could result in lower tortuosity for lithium ions and electrons, leading to reduced cell polarisation. This preliminary step is therefore kept for subsequent cathode tapes fabrication.

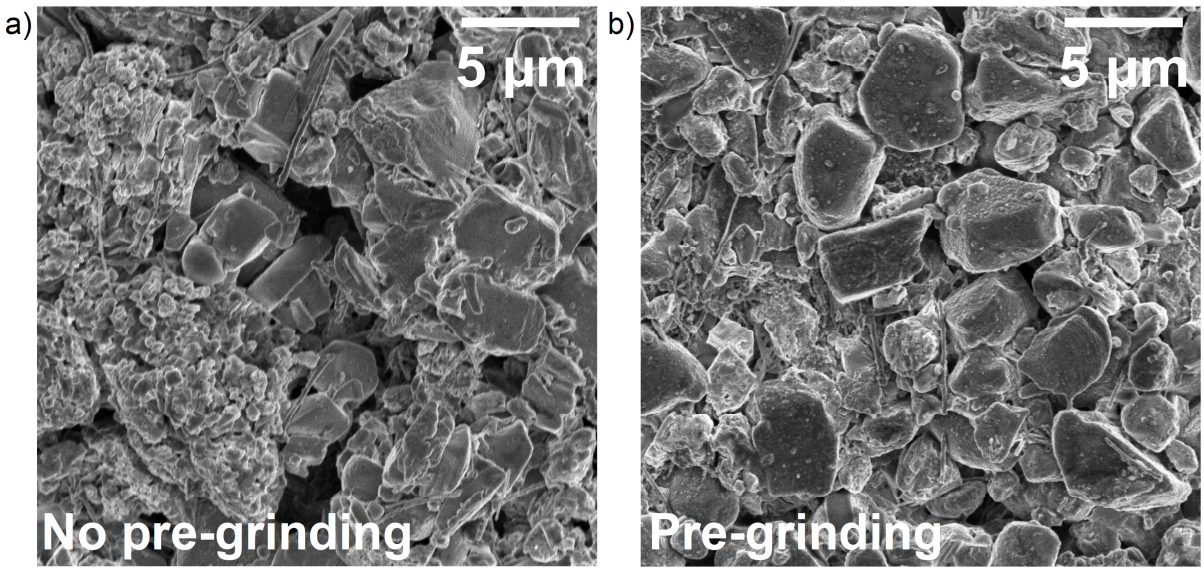

Figure 3.6 SEM pictures of tape cathode (a) without and (b) with a preliminary step of grinding the dry components (NMC, Li_6PS_5Cl and VGCF) before their addition to the solvent.

○ Influence of a solvent mixture on the processing

Working with ethyl acetate, which has a low boiling point (77°C), presents a challenge regarding the timescale for slurry preparation, mixing, and coating. During these steps, the solvent can evaporate if left uncovered, thereby modifying the initial dry mass and slurry viscosity. Although we did not experience delamination issues as reported by Kim *et al.*[162], we did face difficulties with rapid solvent evaporation when depositing the slurry onto the current collector just before using the doctor blade. In an attempt to address this issue, we prepared a cathode slurry using a mixture of ethyl acetate and hexyl butyrate (205°C). Additionally, increasing the coating gap from 200 to 600 µm allowed reaching the target of AM loadings (> 10 $mg_{NMC}.cm^{-2}$) without compromising the tape adhesion and integrity.

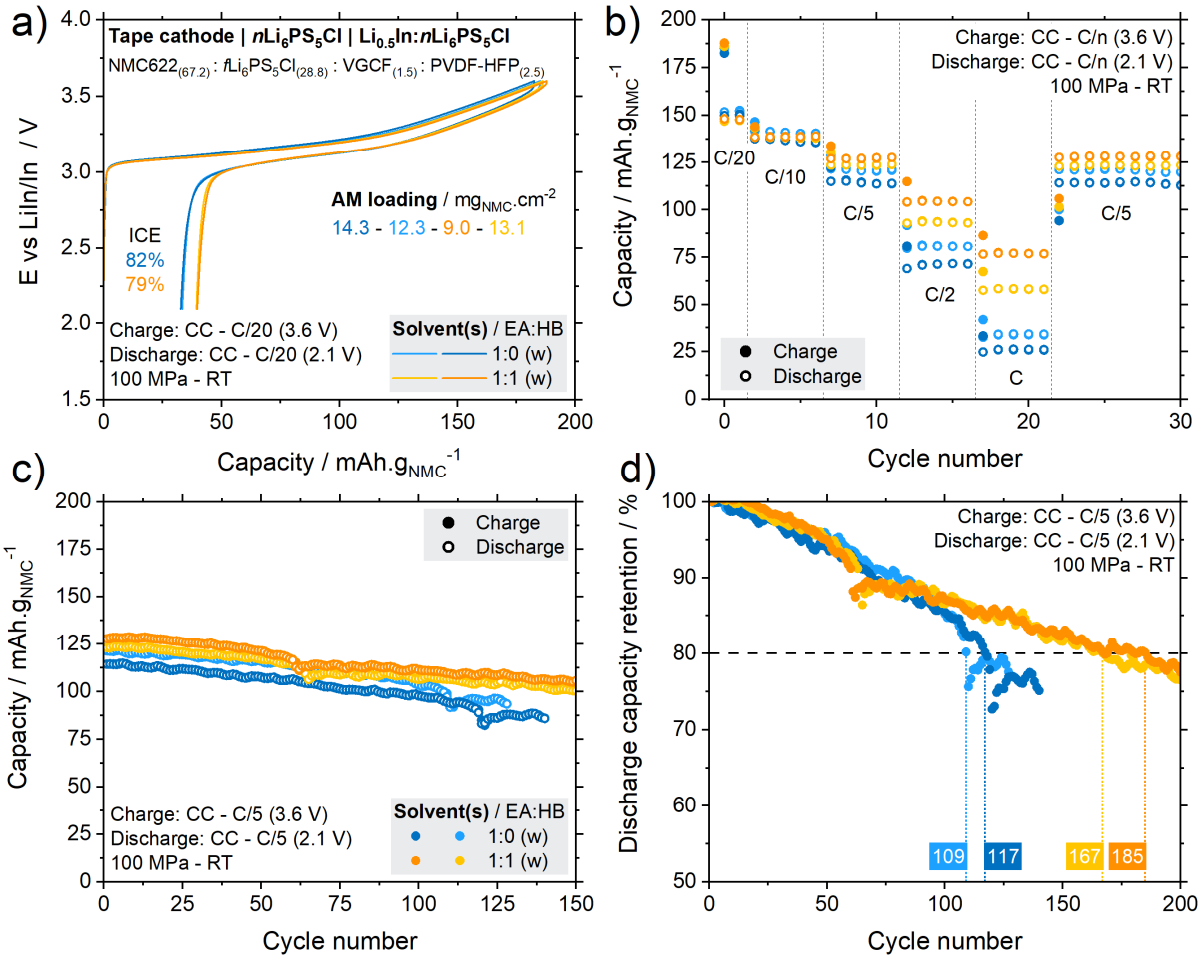

Figure 3.7 Electrochemical performance of tape cathode-based SSBs. Influence of using a mixture of solvent (EA: ethyl acetate – HB: hexyl butyrate) in the slurry preparing for cathode tape casting. (a) First cycle voltage profile and initial coulombic efficiency (ICE). (b) Capacity according to C-rate and (c) at C/5 for long cycling. (d) Smoothed discharge capacity retention at C/5.

Figure 3.7 compares the electrochemical performance of cathode tapes based on pure EA and on EA:HB = 1:1 (w) slurries. Both show similar levels of polarisation and low C-rates capacity (< C/2). However, the cathode based on solvent mixture outperforms in terms of power capability and long-term capacity retention at C/5. These differences, repeatable across two cells, might stem from the slightly lower AM loading used for the solvent mixture-based cathode. Overall, we can conclude that the use of a solvent mixture does not interfere with the electrochemistry of the cathode tape. Nevertheless, the solvent mixture does not prevent the rapid evaporation of EA, as practically experienced, prompting us to seek a third solvent as an alternative.

○ Identifying the best slurry mixing strategy

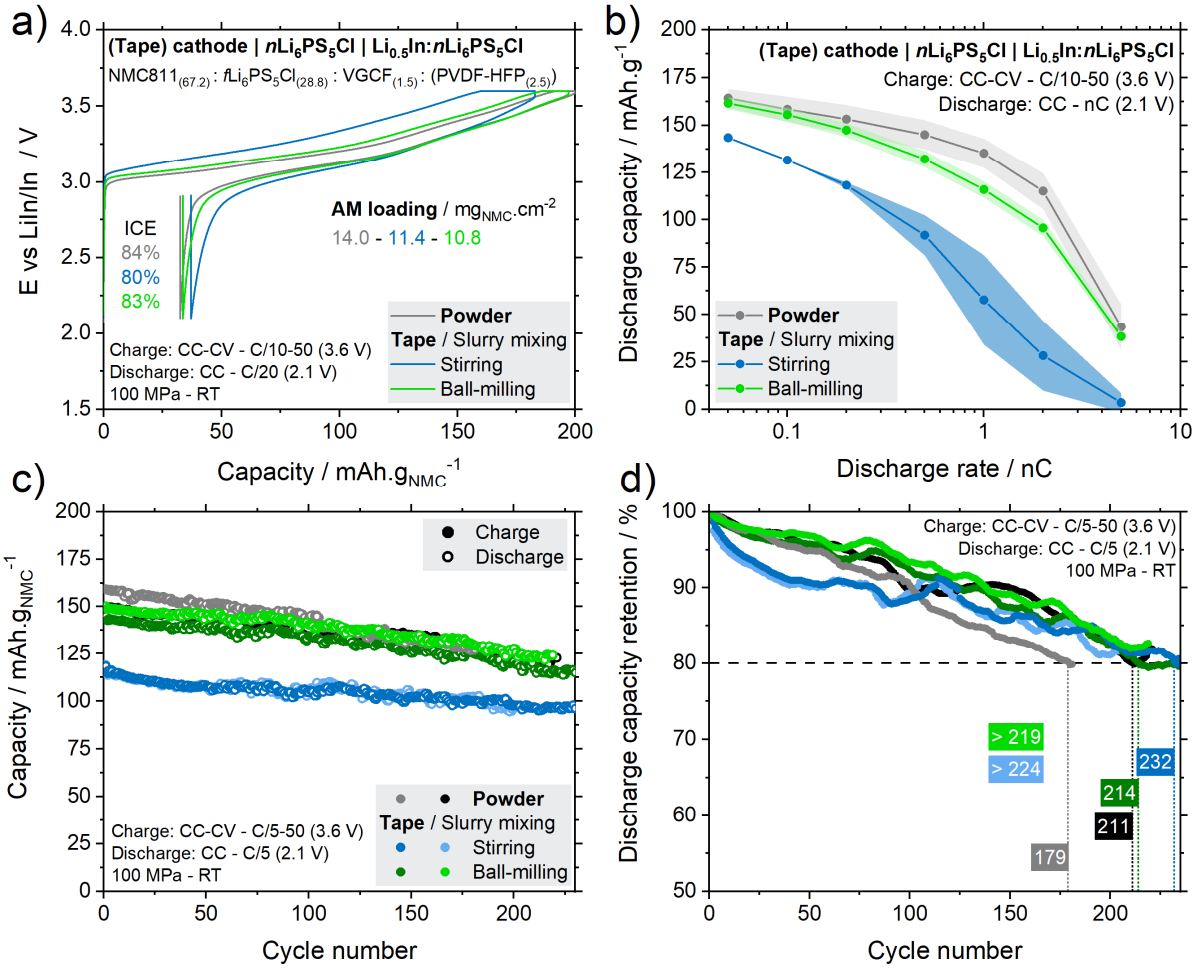

Figure 3.8 Electrochemical performance of tape cathode-based SSBs compared with the original cathode composite powder (grey). Influence of the method used to prepare the slurry: comparison between magnetic stirring (blue) and high-energy ball-milling (green). (a) First cycle voltage profile and initial coulombic efficiency (ICE). Cells repetition and their first cycle voltage profile are available on **Figure S3.4** (b) Rate capability average over 2 cells for each type of SSB. (c) Capacity at C/5 for long cycling. (d) Smoothed discharge capacity retention at C/5.

Since PVDF-HFP is not soluble in hexyl butyrate, we looked for a slightly less bulky alkyl-ester and found butyl butyrate. As shown in section **3.2**, this solvent can solubilise PVDF-HFP (15 mol.% HFP) when heated to 100°C and does not affect the stability of Li_6PS_5Cl. At this point of the study, we shifted from NMC622 to 811 and data from reference binder-free cells are displayed in grey on **Figure 3.8**. Employing a similar stirring process (blue data), the tape cathode did not yield satisfactory performance, as the initial polarisation was significantly higher than that of the reference. Consequently, it resulted in lower capacity levels in both rate capability tests and long-term cycling at C/5. Simple stirring of the slurry in a vial did not appear ideal for achieving mixing homogeneity. Therefore, we drew inspiration from a reported study and shifted to high-energy ball-milling (SPEX SamplePrep) of the dry and liquid components for a short time of 10 min. The resulting tape cathode exhibited nearly identical cycling performance compared to the binder-free system (ICE, rate capability and long-term cycling) and demonstrated improved repeatability compared to stirring-based cathodes. Interestingly, the capacity retention appeared to be independent of the mixing method and the presence of the binder, with all cells reaching 80% discharge capacity retention after approximately 200 cycles.

Overall, these optimization steps of the cathode tape revealed several key parameters to approach the performance of the binder-free reference system as closely as possible. The preliminary grinding of the cathode composite is essential to establish the necessary AM:SE:VGCF contacts, which is not guaranteed by simply suspending these components in the binder solution. The boiling point of the solvent does not appear to influence the electrochemistry of the tape cathodes. However, using a single solvent with a sufficiently high boiling point (Butyl butyrate – 166°C) simplifies the slurry processing by preventing rapid solvent evaporation while facilitating binder dissolution. Finally, the use of a high-energy mixing strategy for slurry preparation appears to promote the organization of particles within the composite, resulting in performance closer to that of the reference system.

3.3.2 Electrochemical performance of the tape cathode

Having developed a reliable method for tape cathode fabrication, we then investigated its robustness when changing cycling parameters. We assessed the repeatability between tapes, examined the impact of increased AM loading, and evaluated the effects of decreasing the operating pressure.

- Repeatability between tapes

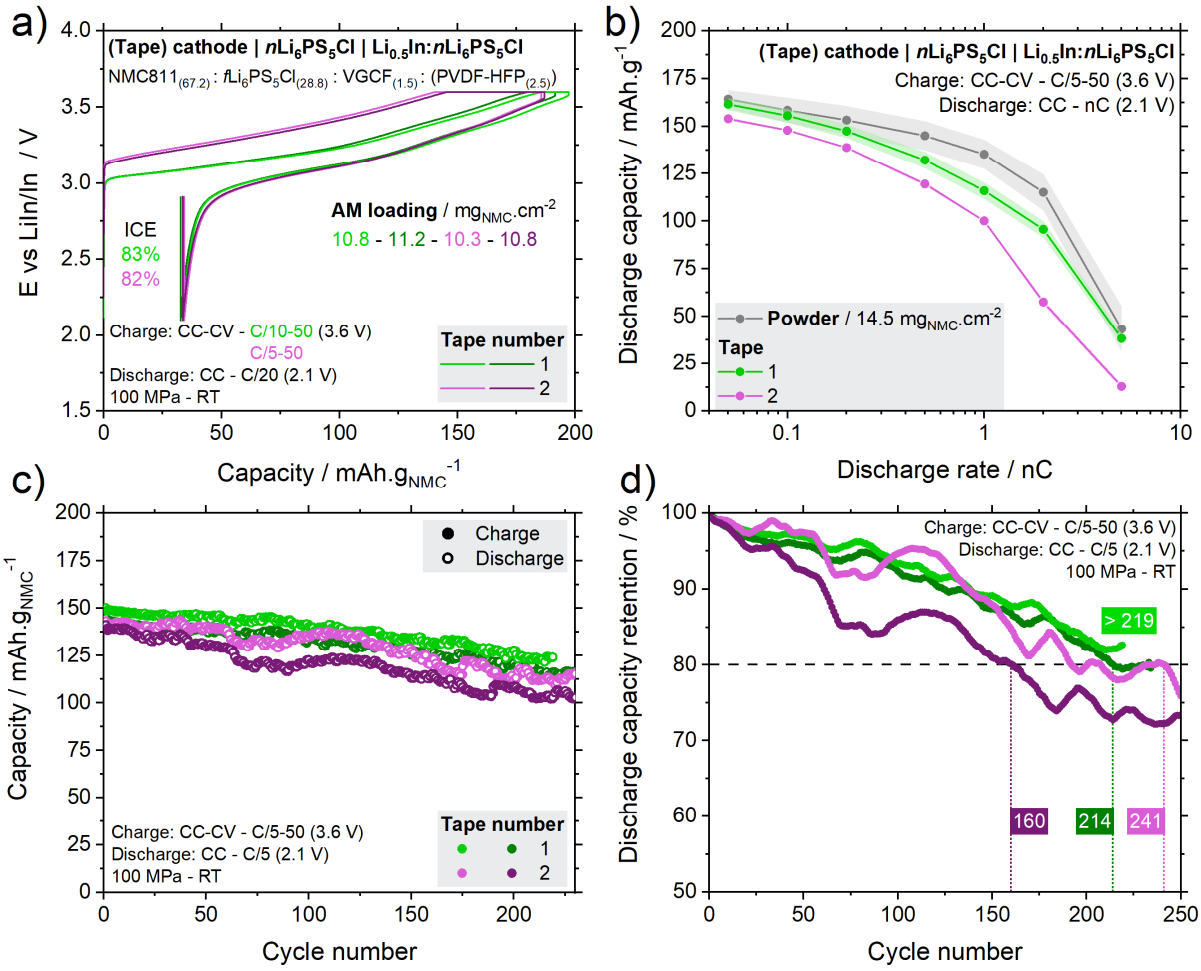

Figure 3.9 Study of repeatability between tapes of same formulation and fabrication process. Electrochemical performance of tape cathode-based SSBs for tape n°1 (green) and tape n°2 (pink) (a) First cycle voltage profile and initial coulombic efficiency (ICE). (b) Rate capability averaged over two cells for each type of SSB. (c) Capacity at C/5 for long cycling. (d) Smoothed discharge capacity retention at C/5.

To assess the repeatability of our fabrication process, we prepared two cathode tapes with identical formulation and manufacturing method. One of the greatest challenge we encountered was ensuring uniform material loading across the entire tape area, as will be further discussed in section **3.3.3**. Currently, cutting electrodes with similar loading from the same tape remains largely uncertain. Minimizing the dispersion of loadings when comparing cells was a critical limitation we sought to address throughout the study by adjusting specific parameters, as discussed in the next section. In **Figure 3.9**, identical cells with an average loading of 10.8 ± 0.4 $mg_{NMC}.cm^{-2}$ are tested with our rate capability and long-term cycling protocol. From the first cycle voltage profile, we noted that both the ICE (82.3 ± 0.7 %) and the absolute irreversible capacity (33.5 ± 0.6 $mAh.g_{NMC}^{-1}$) were similar. We also showed that

using a CC-CV (constant current – constant voltage) mode in charge with different CC rate (green: C/10 – pink: C/5) did not significantly affect the subsequent discharge capacity at C/20 (154 ± 4 mAh.g_{NMC}^{-1}). Although there was larger polarisation using C/5 in CC, the CV step consequently lasted longer to compensate for it. Concerning power capability, discharge capacity levels at different C-rates were highly repeatable within the same tape, but disparity tended to increase at higher current densities between two identical tapes (158 ± 5 mAh.g_{NMC}^{-1} at C/20 and 27 ± 15 mAh.g_{NMC}^{-1} at 5C). This can mainly be attributed to increased polarisation at high current density, exacerbated by inhomogeneities in the cathode layer (tortuosity, accessibility of AM, loading). The long-term cycling behaviour at C/5 displayed a similar tendency between tapes, reaching 80% of initial capacity around 200 cycles. Here again, the repeatability of long-term performance remains subject to larger uncertainty compared to the very repeatable behaviour of the first cycles. Large variations observed in the retention profile partly originate from fluctuations in room temperature, influenced by changes in weather conditions and the operation of machines and cyclers. Overall, we can conclude from this test that we can expect high repeatability of the initial electrochemical data (< 5% deviation in capacity levels for first cycle and rate capability test) between identical tapes if care is taken to minimise the disparity in AM loading. However, we must keep in mind that the disparity in long-term capacity retention and high C-rate behaviour is not yet predictable and understood.

○ Influence of areal loading

Going further in the repeatability assessment, we checked the influence of increasing the areal AM loading on the electrochemical performance (**Figure 3.10**). From the same cathode tape, we collected electrodes with a loading of 10.6 ± 0.4 $mg_{NMC}.cm^{-2}$ and a higher loading of 14.5 ± 0.5 $mg_{NMC}.cm^{-2}$ (+ 37%). As expected, we can notice a higher polarisation of the first charge using a higher loading, yet compensated by a longer CV step. The ICE and discharge capacity levels remains very repeatable, but disparity increases again at higher C-rates and during long-term cycling. Here again, remaining heterogeneity between cells may be exacerbated. The effect of room temperature is more clearly visible with the shape of the discharge capacity retentions, since the four cells were launched at the same time. Comparing these results with the binder-free cells at similar loading (14.5 $mg_{NMC}.cm^{-2}$ - **Figure 3.10b**) highlights the remaining gap in performance when introducing a binder, especially at high current density.

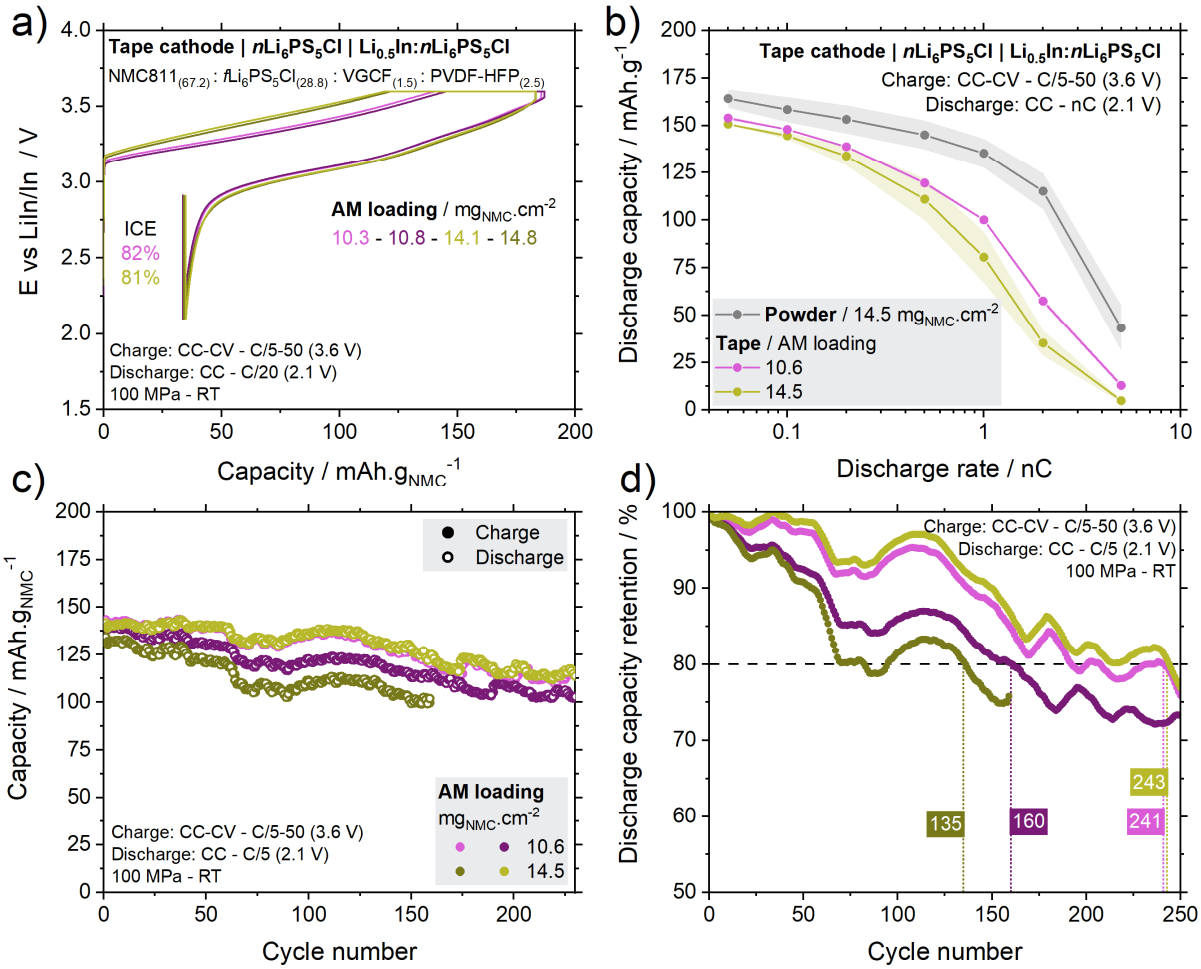

Figure 3.10 Study of the influence of cathode active material areal loading. Electrochemical performance of tape cathode-based SSBs with 10.6 (pink) and 14.5 $mg_{NMC}.cm^{-2}$ (khaki). (a) First cycle voltage profile and initial coulombic efficiency (ICE). (b) Rate capability averaged over two cells for each type of SSB. (c) Capacity at C/5 for long cycling. (d) Smoothed discharge capacity retention at C/5.

○ Effect of lowering the operation pressure

Keeping in mind the final objective of scaling up the SSB manufacturing, the ability to decrease significantly the operation pressure of our sheet-type cells is essential. Working only on the cathode tape at this stage of the study, we compared the electrochemical performance of these cells when decreasing the pressure from 100 to 2 MPa, using a dedicated setup (**Figure S3.1b**). Knowing that we employed a relatively low AM loading in this test (6.2 ± 0.6 $mg_{NMC}.cm^{-2}$), no impact of the pressure can be detected on the first cycle voltage profile (**Figure 3.11**), displaying similar polarisation and ICE (81.8 ± 0.7 %). Interestingly, capacity retention at C/20 appears to be positively affected by a lower cycling pressure.

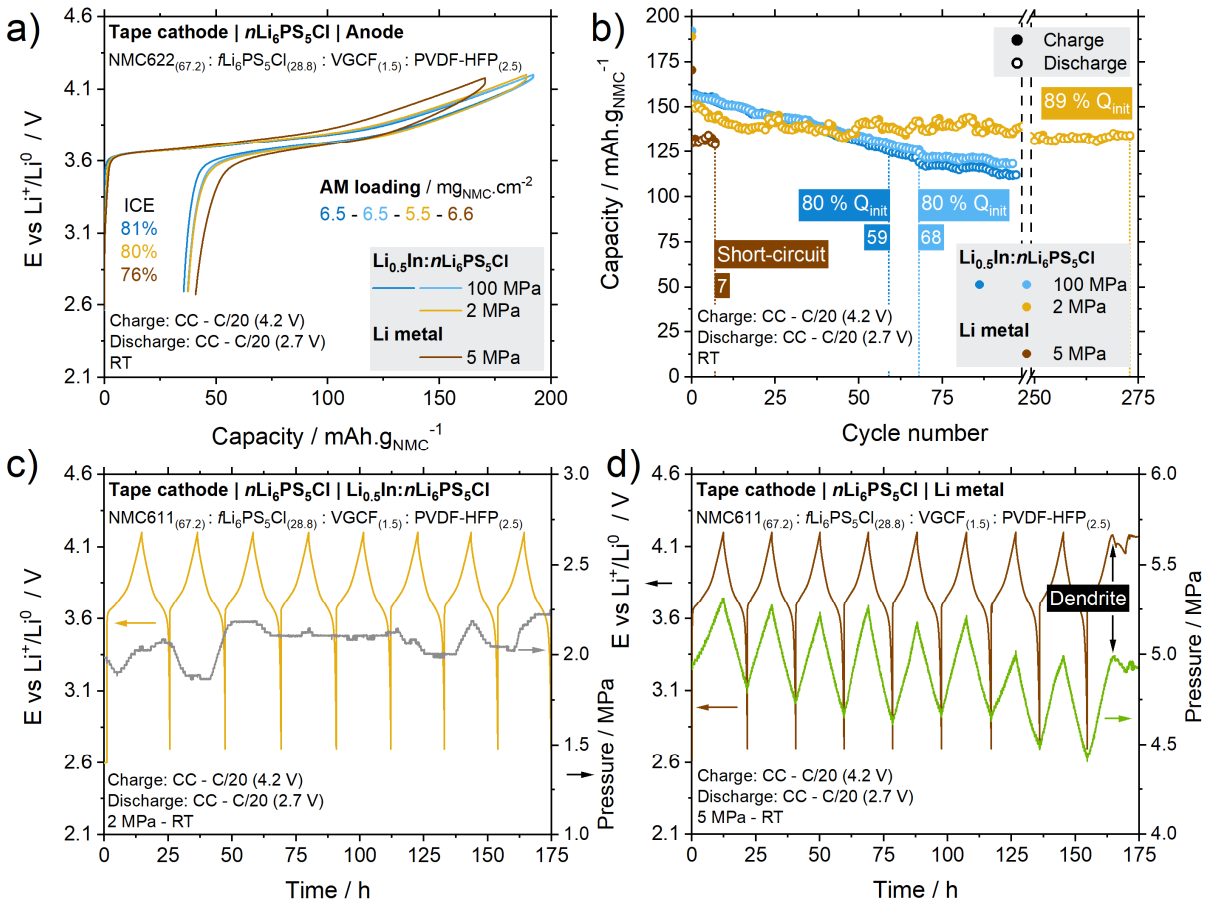

Figure 3.11 Influence of operation pressure (high pressure 100 MPa – blue; low pressure 2-5 MPa – yellow and brown) and type of anode (alloy composite LiIn and pure Li metal). Electrochemical performance of the corresponding tape cathode-based SSBs. (a) First cycle voltage profile and initial coulombic efficiency (ICE). (b) Capacity at C/20 for long cycling. Evolution of stack pressure during cycling for SSB based on (c) LiIn composite or (d) pure Li metal anode.

It preserved 89% of initial capacity after 270 cycles, while high-pressure cells quickly reach 80% after 60 cycles. It demonstrates a very high stability, which would need to be repeated with a higher AM loading. Working at such low pressure enables to replace the composite anode made of $Li_{0.5}In$ alloy and nLi_6PS_5Cl with a pure lithium metal electrode. The cycling of such a cell at 5 MPa suffers from a higher polarisation leading to poorer efficiency (76 %) and lower discharge capacity level (130 versus 154 ± 3 $mAh.g_{NMC}^{-1}$). Interestingly, the initial cycles at C/20 were stable in polarisation and capacity, which matches well with the reversibility of the measured pressure (via a pressure sensor) between 4.7 and 5.3 MPa. However, instabilities soon appear, most likely stemming from the Li | Li_6PS_5Cl interface. The pressure starts to decrease up to the apparition of a sudden and noisy voltage drop. It is the signature of the instable growth of lithium through the separator[172], since the plating is not mastered at the interface. However, the evolution of the pressure in a cell based on a composite alloy

anode is not reliable in the absence of constant temperature. Since the molar reaction volume of lithiation $\Delta_r V_m(Li)$[41] is lower for indium (+ 7.89 $cm^3.mol^{-1}$) than for lithium (+ 13.02 $cm^3.mol^{-1}$), the volume change is smaller and temperature variation can affect the reliability of the measurement. With these simple tests, we revealed a potentially enhanced stability of our tape cathode-based cells at an operation pressure close to the industrial requirements (< 1 MPa). This pressure range enables the use of a lithium metal anode, which exhibits satisfactory initial cycling but still suffers from the instability of the non-mastered Li | Li_6PS_5Cl interface.

We continued the study on lower operation pressure, transitioning from the NMC622-based cathode to the more optimised NMC811-based cathode. As shown on **Figure 3.12**, lowering the pressure from 100 to 2 MPa leads to a significant increase in polarisation during the first cycle, ultimately resulting in lower ICE (77.5 ± 0.2 % at 2 MPa versus 83.0 ± 0.2 % at 100 MPa) and initial discharge capacity (109 ± 3 mAh.gNMC-1 at 2 MPa versus 161 ± 4 mAh.gNMC-1 at 100 MPa). The performance of the cell kept at 2 MPa (orange data) is significantly affected by its initial polarisation, both regarding rate capability and long-term cycling. Interestingly, we submitted the other low-pressure cell to 100 MPa for the third cycle (**Figure 3.12b**), and the polarisation and capacity naturally caught up with the reference cells at 100 MPa (green). Lowering the pressure back to 2MPa (dotted red line), the cell surprisingly delivered 37% more capacity, benefiting from lower polarisation. The following rate capability test demonstrates the beneficial effect of one high-pressure cycle on the capacity levels. The principal limitation of going to low pressure with SSBs is the likely loss of inter-particle contacts, especially in the cathode where the AM experiences significant volume change during cycling (up to 7% for NMC811). The application of a high pressure greatly helps to mitigate this contact loss during cycling. During this test, submitting the cell to one cycle at 100 MPa helps maintaining these contacts, even after going back to low pressure. Regarding discharge capacity retention (**Figure 3.12e**), the low pressure cell exhibits excellent performance, reaching 80% of its initial C/5 capacity after more than 550 cycles, significantly outperforming its counterparts cycling at 100 MPa (around 220 cycles). However, it is important to analyse these results with caution as they are tricky to replicate, and the AM loading was relatively low.

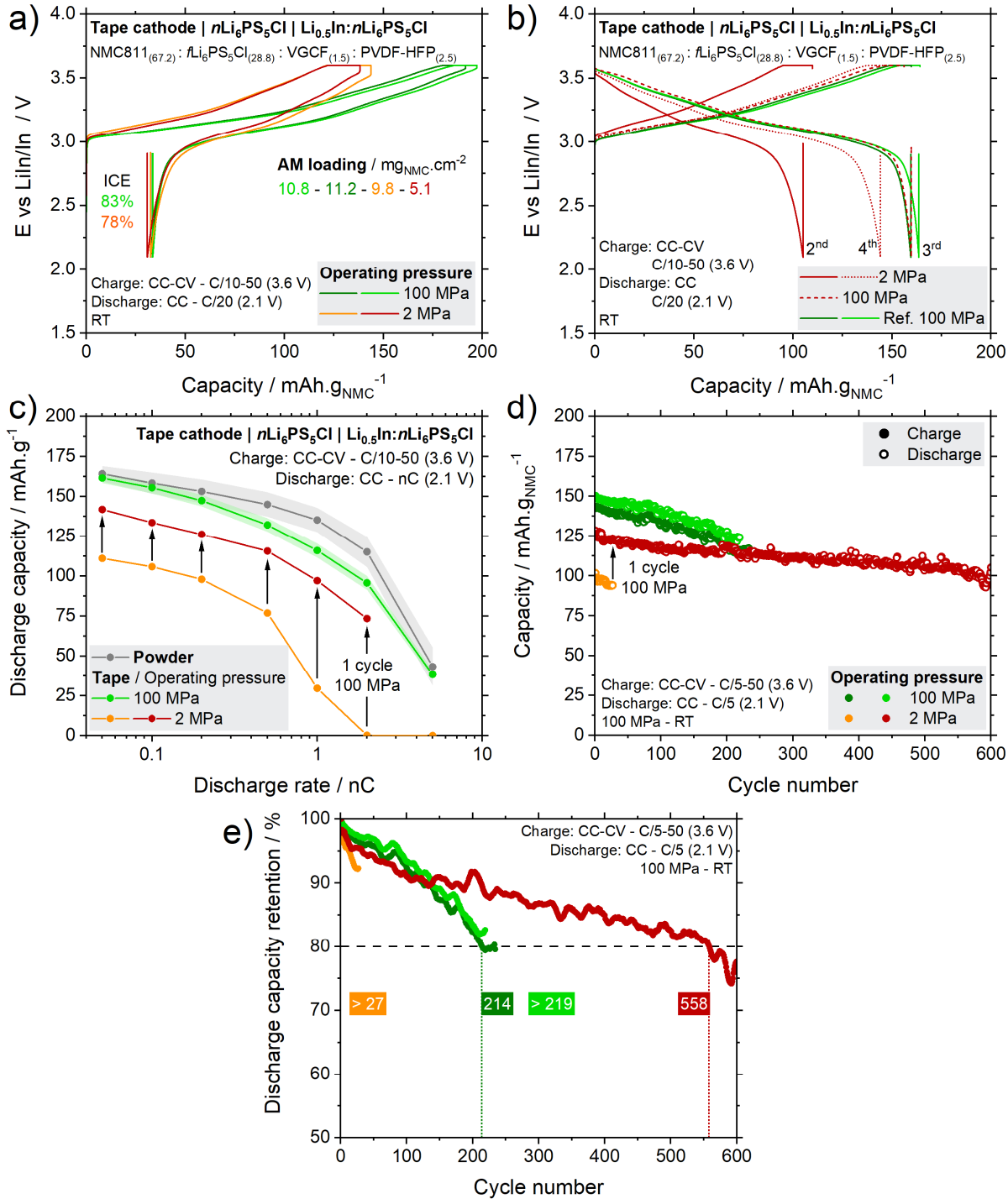

Figure 3.12 Effect of lowering the operating pressure on tape cathode-based SSB. (a) First cycle voltage profile and initial coulombic efficiency (ICE) of cells running at 100 MPa (green) and at 2 MPa (orange and red). (b) Effect of an intermediate cycle at 100 MPa on subsequent cycling back to 2 MPa. (c) Rate capability and (d) capacity at C/5 for long cycling. (e) Smoothed discharge capacity retention at C/5.

These tests on lowering the cell operating pressure pave the way for future experiments on self-standing SSB, which will be discussed in subsequent section **3.5.2**. From both cell configuration (NMC 622 and 811), it seems that cycling at a low pressure of 2 MPa is

achievable, while difficult to reproduce, and the capacity retention is in both cases greatly enhanced compared to the reference systems at 100 MPa.

3.3.3 Towards enhanced cathode composite tapes

In the preceding subsections, we highlighted several essential parameters to prepare and cycle a tape cathode with robust electrochemical performance, approaching the binder-free cell behaviour. However, to obtain even better reliability and understanding of the ruling phenomena in this cathode tape, we explored other parameters reported crucial in the literature: the binder content and the particle size of Li_6PS_5Cl.[162,180] For higher repeatability, we transitioned from tape casting by hand to an automated coater inside the glovebox.

○ Advantages and limitations of an automated coating process

Shifting to an automated coating process, we naively thought that it would enhance the homogeneity of the material loading, thanks to the constant speed of coating. However, it appeared that tape thickness standard deviation was still not negligible, around 40 µm for an average thickness between 50 and 100 µm, depending on the formulation (**Figure 3.13a**). However, it was clear that the first half of the tape was systematically thicker than the second half. The amount of available slurry decreases during the coating process, resulting in a thinner tape at the end of the deposition. We also probed qualitatively the influence of slurry viscosity by varying the binder content keeping a constant dry mass ratio of 50%. The formulation based on 1.5 wt.% PVDF-HFP, being less viscous, gives thinner and more heterogeneous coating, with extremal thicknesses of 122 and 12 µm (**Figure 3.13c**). The mechanical integrity of the tape is also affected by decreasing the binder content, compromising the cutting and handling of such an electrode. Using a higher amount of 2.5 wt.% binder results in more homogeneous coatings, regardless of the SE particle (*n*Li_6PS_5Cl versus *uf*Li_6PS_5Cl). However, it is important to keep in mind that this edge effect is exacerbated by the small quantity of slurry that is coated, around one gram. Future test should include the evaluation of the slurry viscosity to ensure better repeatability of the tape thickness.

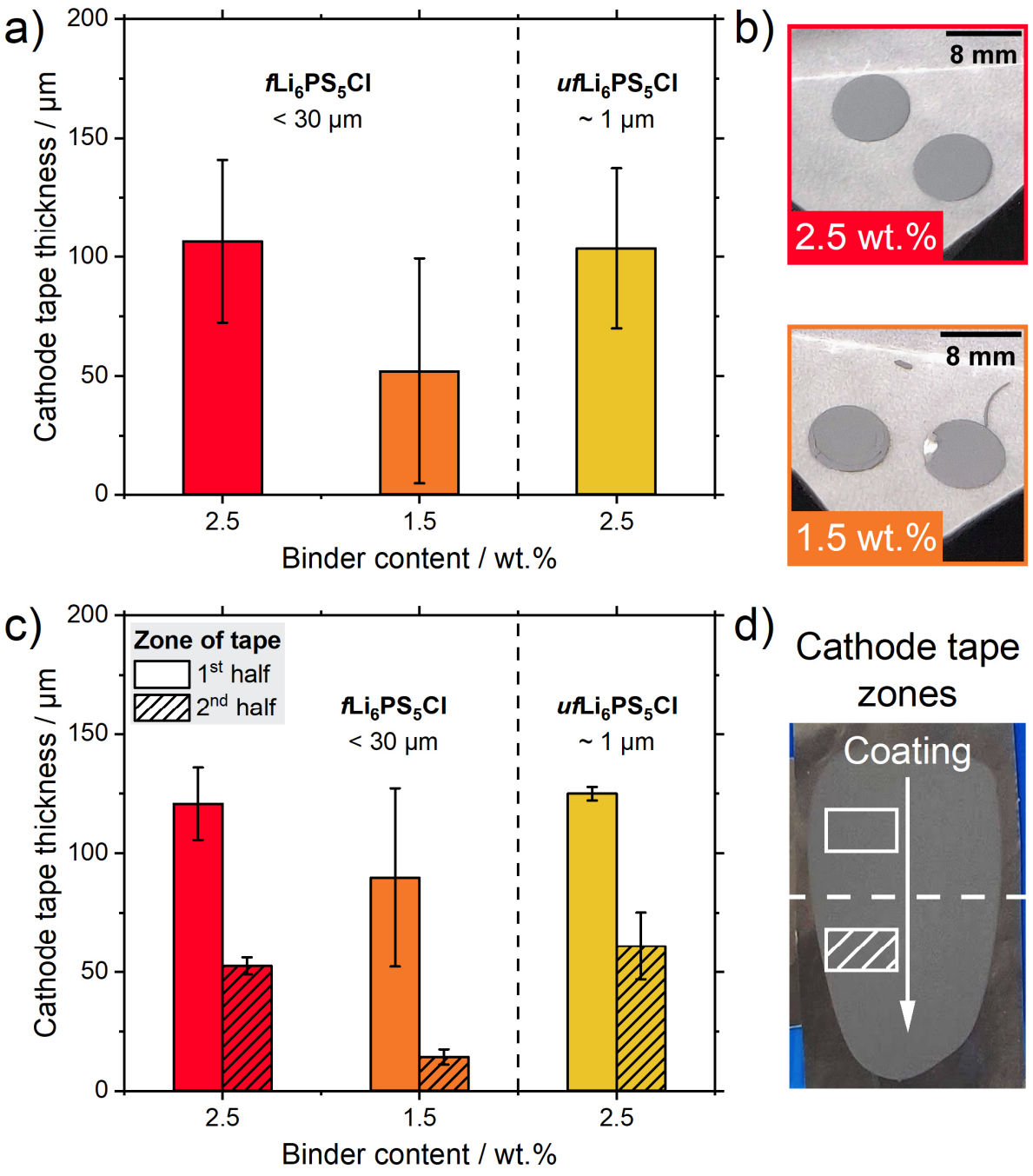

Figure 3.13 (a) Average thickness and deviation of whole tape cathode after coating and drying, according to binder content and SE particle size. (b) Pictures of discs of cathode tape after cutting to highlight the mechanical cohesion according to binder content. (c) Average thickness of first and second zones of tape cathode, according to binder content and SE particle size. (d) Designation of zones related to the coating direction.

Carrying out further characterisation of our tape cathodes, we observed their cross-section by SEM, revealing a highly homogeneous coating at the level of observation (**Figure 3.14a**). Energy-dispersive X-ray spectroscopy (EDS) mapping confirmed a uniform distribution between AM and Li_6PS_5Cl, as revealed by nickel (Ni) and sulphur (S) maps. Additionally, we confirmed the effective distribution of the fluorinated binder throughout the height of the

electrode, consistent with its macroscopic mechanical integrity and strong adhesion to the aluminium current collector. Altogether, these results support the enhanced cycling performance of this tape cathode, displayed on **Figure 3.15**. The two other cathode tapes, with lower binder content or smaller SE particles, also exhibit good homogeneity (**Figure S3.5**).

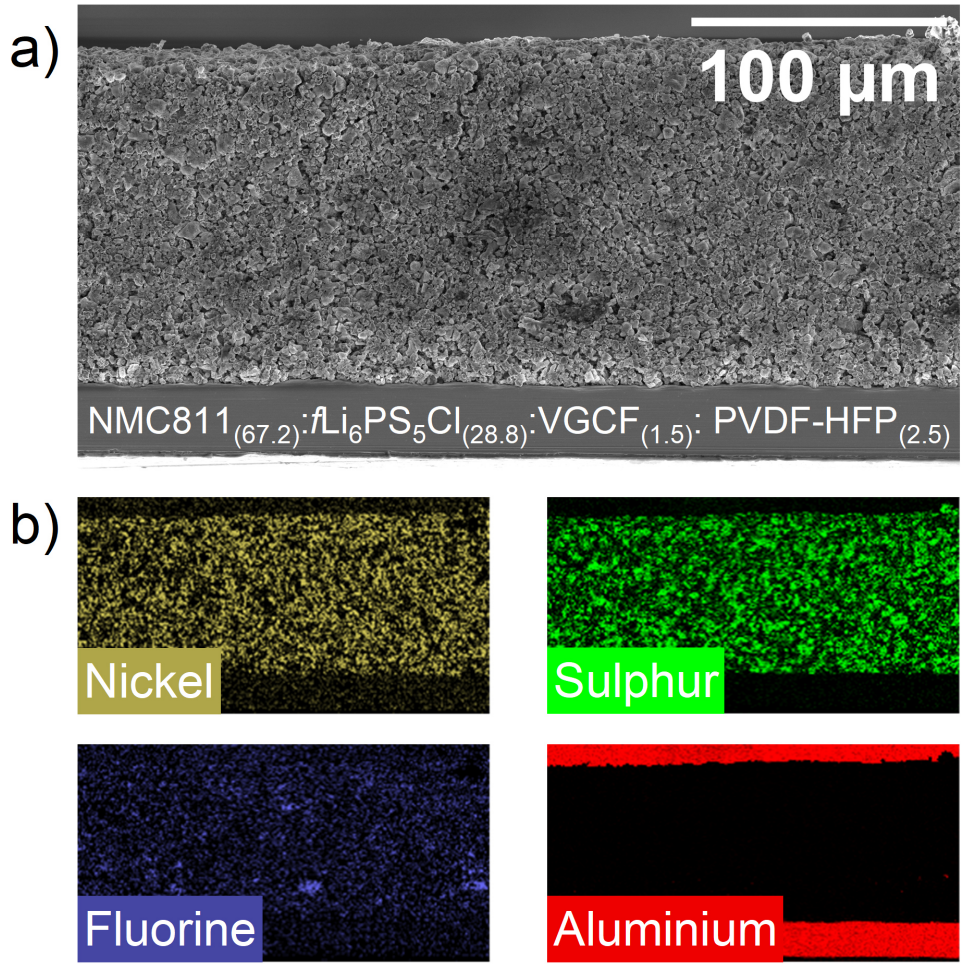

Figure 3.14 (a) SEM cross-section image of tape cathode after drying. The composition of cathode is NMC811 : *f*Li_6PS_5Cl : VGCF : PVDF-HFP = 67.2 : 28.8 : 1.5 : 2.5 (w). (b) Energy-dispersive X-ray spectroscopy (EDS) mapping for nickel (yellow), sulphur (green), fluorine (blue) and aluminium (red).

We first evaluated the influence of binder content on the cycling performance. Intuitively, decreasing the amount of PVDF-HFP, which is electrochemically inactive, should reduce the performance gap with the binder-free system. Indeed, the rate capability test highlights less degraded capacity at high C-rates for the cathode with low binder content (1.5 wt.%) compared to the higher binder content (2.5 wt.%), almost overlapping with the binder-free cells. However, the AM loading is 20% lower due to the thinner coating obtained with only 1.5 wt.% of binder, stemming from the less viscous slurry. Despite some variability

between repetitions of tape cathode-based cells (around 10 mAh.g_{NMC}^{-1} deviation at current densities < 2C), the long-term cycling behaviour is currently very similar, with overlapping discharge capacity retentions.

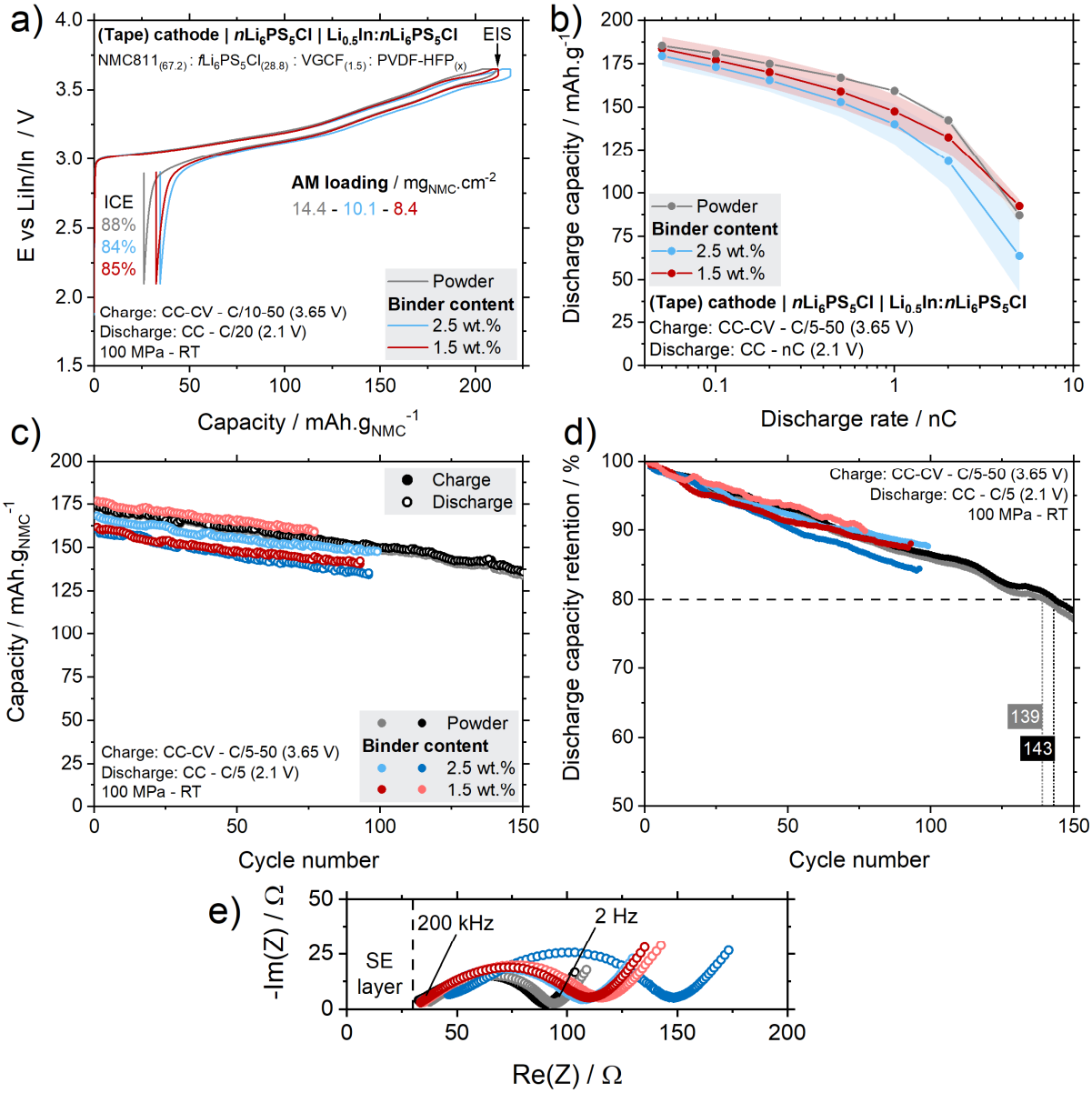

Figure 3.15 Study of the influence of binder content in the tape cathode. Electrochemical performance of tape cathode-based SSBs with 2.5 wt.% (blue) and 1.5 wt.% (red) of PVDF-HFP (15 mol.% HFP), compared with the initial cathode composite powder. (a) First cycle voltage profile and initial coulombic efficiency (ICE). Cells repetition and their first cycle voltage profile are available on **Figure S3.6** (b) Rate capability averaged over 2 cells for each type of SSB. (c) Capacity at C/5 for long cycling. (d) Smoothed discharge capacity retention at C/5. (e) Electrochemical impedance spectra (EIS) of cells after the first charge, in 25°C oven.

To gain insights into the internal resistance of the cell, we performed electrochemical impedance spectroscopy (EIS) at the end of the first charge and at a constant temperature of 25°C (**Figure 3.15e**). Qualitatively, we probed the influence of the binder on the cathode

contribution. The high-frequency region (> 200 kHz) is primarily governed by the separator layer, here pure *n*Li_6PS_5Cl. The resistance value of around 30 Ω corresponds well with the amount of SE (m ≈ 30 mg) and the separator thickness after densification (e ≈ 400 µm). The mid-frequency contribution (2 Hz < f < 200 kHz) is attributed to the electrodes. In our two-electrode system, we cannot distinguish between the cathode and the anode contributions. Yet, it is possible to compare spectra between cells with different binder content, as the anode remains identical. An increase of the resistance is observed with the addition of binder, indicating more difficult access to the AM, impeded by the presence of non-conductive binder. However, the repetition over two cells did not allow us to confirm confidently this effect based on binder content. For a deeper understanding of the binder's influence, we should perform EIS on a three-electrode cell to isolate the cathode's contribution, using $Li_{0.5}In$: *n*Li_6PS_5Cl as a reference electrode with a voltage plateau at 0.622 V vs Li^+/Li^0, and fit the data with a transmission line model to extract the ionic and electronic resistances.[181,182] Overall, we can conclude from this data that the binder indeed negatively influences electrochemical performance, as predicted. However, the balance between mechanical integrity and cycling behaviour tends to favour the use of 2.5 wt.% binder, with which the tape cathode already delivers reliable and almost unimpaired performance at reasonable current densities (< 1C).

○ Decreasing SE particle size

The last parameter we investigated to improve our tape cathode was the particle size of the SE. We replaced our conventional *f*Li_6PS_5Cl (D < 30 µm) with the *uf*Li_6PS_5Cl (D_{50} ≈ 1 µm) in the cathode composite, as better AM:SE contact and enhanced performance were reported with smaller SE particles.[180] We first studied its effect on the binder-free composite cathode (**Figure 3.16**). On the first cycle, the voltage profiles overlapped well, indicating no influence of the reduced SE particle size, with an identical AM loading. However, the ICE is slightly lower using *uf*Li_6PS_5Cl (85.0 ± 0.4 %) than with *f*Li_6PS_5Cl (87.5 ± 0.2 %). This higher first cycle irreversibility can originate from either kinetic limitation or higher irreversible reactivity. The latter may be explained by a higher surface of contact between the SE, the AM and VGCF, possibly triggering more degradation.[181]

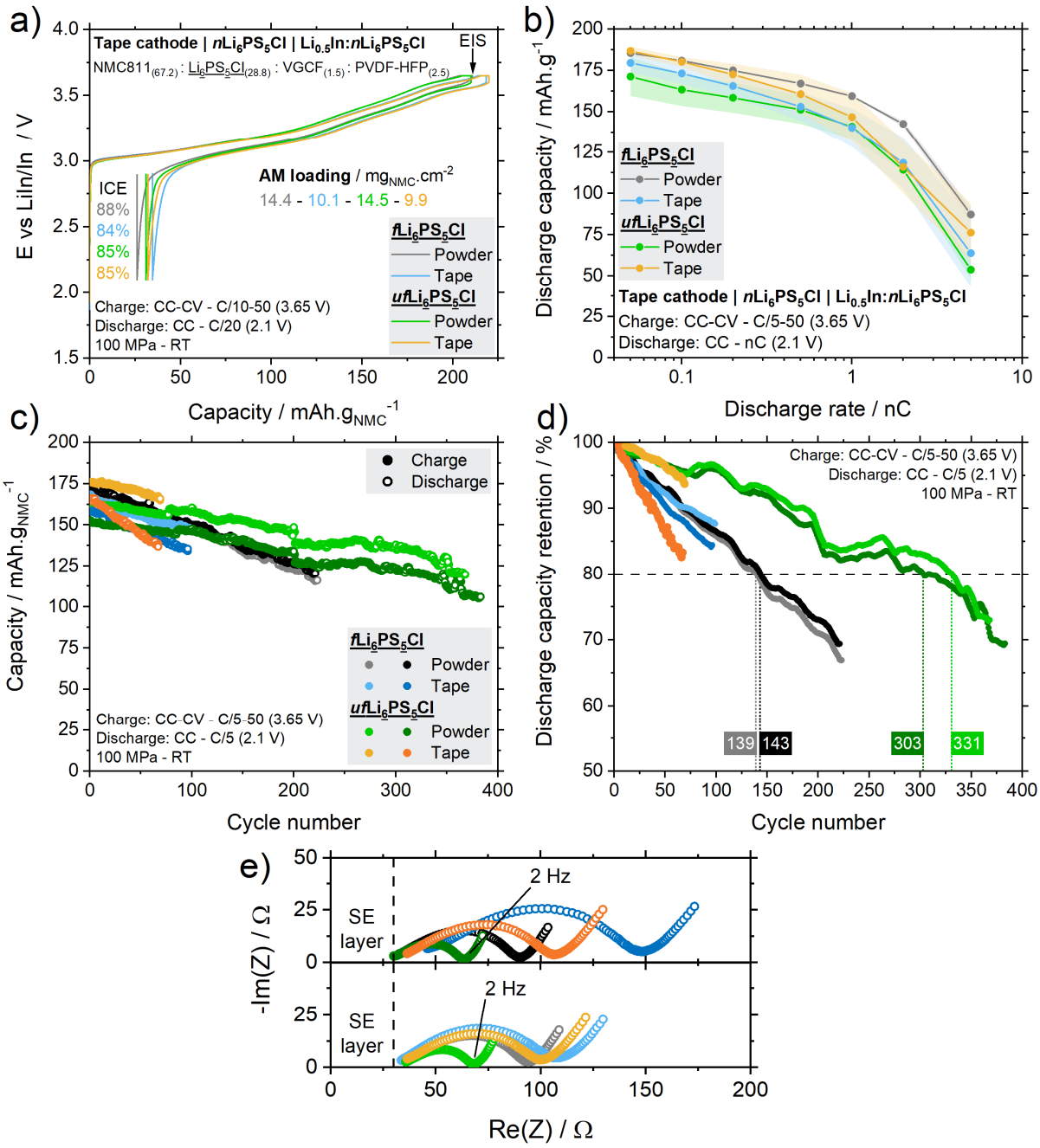

Figure 3.16 Study of the influence of the particle size of Li_6PS_5Cl in the cathode composite, both as powder and tape. Electrochemical performance of powder cathode-based SSBs with larger (< 30µm - grey) and smaller (≈ 1 µm - green) particles of SE, and their respective tape cathode-based SSBs (large: blue – small: yellow). (a) First cycle voltage profile and initial coulombic efficiency (ICE). Cells repetition and their first cycle voltage profile are available on **Figure S3.7**. (b) Rate capability averaged over 2 cells for each type of SSB. (c) Capacity at C/5 for long cycling. (d) Smoothed discharge capacity retention at C/5. (e) Electrochemical impedance spectra (EIS) of cells after the first charge, in 25°C oven.

Regarding the rate performance, the capacity levels for the ultra-fine SE containing cathode are lower (around - 10% for C-rates < 2C), in line with the lower ICE. However, long-term cycling largely outperforms our conventional cathode composite, reaching 80% of the initial

C/5 discharge capacity after 300 cycles, which doubles the previous performance. Improved initial contacts in the cathode might help mitigate the contact loss occurring over cycling, thus maintaining better capacity retention. Some post-mortem analysis should enrich our understanding of this topic, such as examining the cathode cross-section with FIB-SEM (focus ion beam – scanning electron microscopy), for example. Integrating 2.5 wt.% of binder in these composite cathodes does not significantly modify the electrochemical performance. Surprisingly, the tape cathode with *uf*Li_6PS_5Cl outperforms its binder-free counterpart in rate capability. However, the room temperature cycling may explain this non-negligible difference in capacity since the cells were launched at different time of the year. The capacity retention is enhanced for tape with *uf*Li_6PS_5Cl for only one cell (yellow), and the fast capacity decay of the other cell (orange) suggests an unknown issue, calling for a third repetition. Regarding the EIS performed after the first charge (**Figure 3.16e**), it is clear that the resistance is minimised by using smaller SE particles. The effect is less pronounced with the associated binder-containing cathodes. Altogether, it appears that the transition to SE with small particle size improves the cell capacity retention, yet to be confirmed in the case of the tape cathode (cells still running).

As a partial conclusion to the tape casting of solid-state cathode composite electrodes, we studied a variety of parameters, from the slurry fabrication process to formulation optimization, resulting in enhanced and repeatable electrochemical performance, paving the way for future self-standing solid-state batteries. The next component to be developed is the self-standing Li_6PS_5Cl separator.

3.4 – Self-standing argyrodite-based separators

3.4.1 Preparation of separator

A similar fabrication process to the tape cathode was employed to prepare the Li_6PS_5Cl-based separator. Argyrodite powder was suspended in a solution of PVDF-HFP and butyl butyrate with a dry mass of 57%, which was mixed in a high-energy ball-miller (SPEX SamplePrep) for 10 min. The obtained slurry was then coated on a polyethylene terephthalate (PET) foil, with a silicone-coated surface to ease subsequent delamination. Drying was performed in two steps: an hour at 100°C on the coating machine, followed by an overnight storage under vacuum in the glovebox antechamber. To assess the effectiveness of our drying

procedure, we performed TGA analysis on our dried separator (**Figure 3.17**). We can confirm that no significant weight loss is observed before butyl butyrate boiling point (166°C), which certifies our procedure. Nevertheless, we detect around 1% weight loss on both pristine *n*Li_6PS_5Cl and our separator between 150 and 600°C. This is probably due to material reactivity with the atmosphere during the short transfer from the glovebox to the TGA instrument, since a small opening is needed on top of the TGA pan to prevent its explosion. After 400°C, more intense weight loss occurs for the self-standing separator, which we can be directly attributed to the binder degradation process.

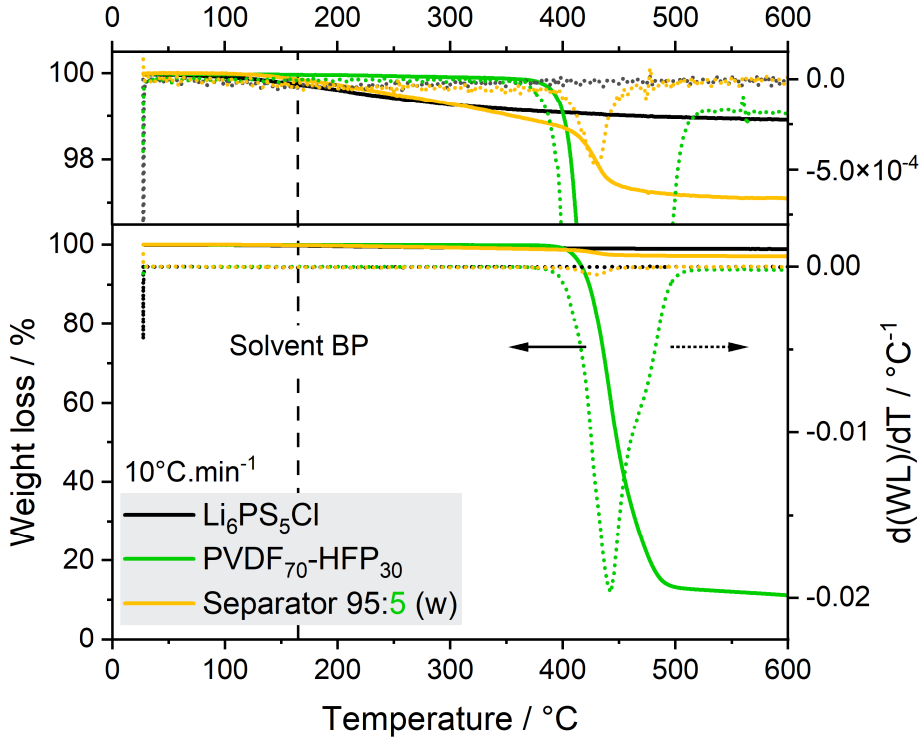

Figure 3.17 Thermogravimetric analysis (TGA) of solid-sate separator (yellow) based on Li_6PS_5Cl (black) and P(VDF-co-HFP) with 30 mol.% of HFP comonomer (green). Weight loss is measured from room temperature to 600°C under argon atmosphere at a rate of 10°C.min^{-1}. Enlargement of the graph is displayed in the upper part for easier reading.

For the separator fabrication, we preferred the PVDF-HFP with 30 mol.% of HFP comonomer instead of the initial low HFP content (15 mol.%) used in the cathode. First tests were conducted using the thermoplastic PVDF-HFP (15 mol.%) binder but difficulties in safely handling, cutting and densifying the tape motivated us to shift to the elastomer (**Figure 3.18**).

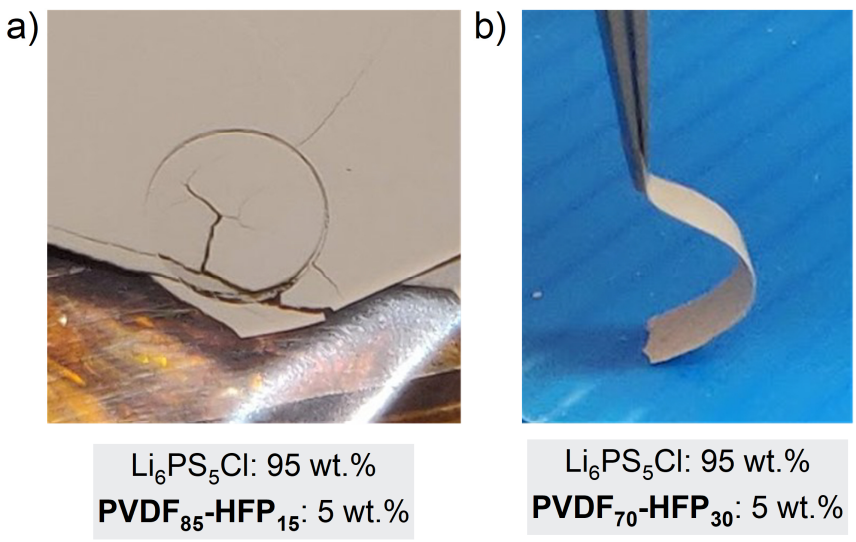

Figure 3.18 Pictures illustrating qualitatively the mechanical properties of Li_6PS_5Cl-based self-standing separators containing PVDF-HFP binders of different HFP content: (a) 15 mol.% - thermoplastic binder and fragile separator, (b) 30 mol.% - elastomeric binder and flexible separator.

Thanks to its elastomeric properties, the binder ensures the mechanical integrity and grants some flexibility to the self-standing separator, unlike the previous binder, with which the separator is brittle. Similar to the tape cathode, introducing a certain amount of non-conductive binder in the separator will impede the ionic pathway. Here, we need to balance between reaching sufficient ionic conductivity and obtaining mechanical properties suitable for self-standing cell assembly. A screening in $PVDF_{70}$-HFP_{30} content was performed, and we studied the physiochemical characteristics of the tapes. A gap of 200µm was used with the doctor blade coating, and the resulting tape thickness tends to decrease with lower binder content (**Figure 3.19a**). Again, the slurry viscosity is likely the reason since we also observe a higher disparity across the whole tape area at 1 wt.% (78 ± 9 µm) than at 5 wt.% (88 ± 3 µm). One can note that the dispersion is much lower for separators (< 10 µm) compared to the tape cathode (≈ 40 µm – **Figure 3.13**). The different nature of the binder and the resulting change in viscosity could be a possible explanation, although we did not investigate this further. Interestingly, transitioning to finer argyrodite (*uf*Li_6PS_5Cl) significantly reduces the separator thickness after drying, from 83 ± 4 to 70 ± 4 µm, which suggests a better packing of the particles. In all the case, the coating quality is satisfactory without any pinholes or irregularities, as seen on **Figure 3.19b**.

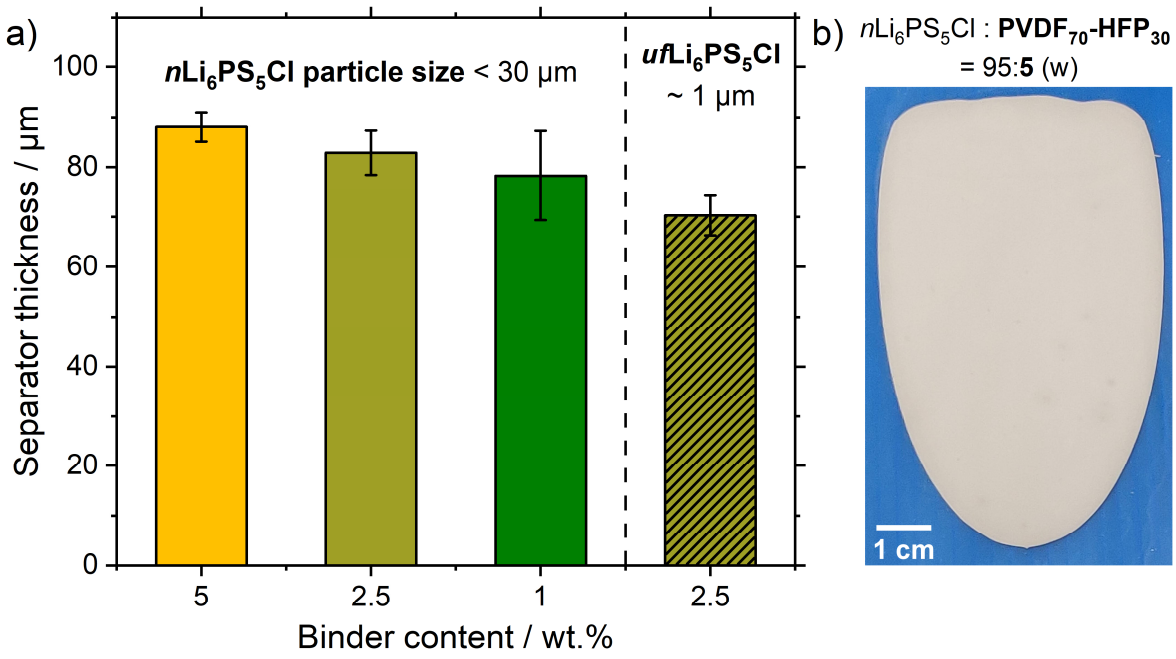

Figure 3.19 (a) Average thickness and deviation of whole tape separator after coating and drying, according to binder content and SE particle size. (b) Picture of the tape separator coated on a PET foil.

These tapes, of approximately 40 cm^2 and 0.5 g of Li_6PS_5Cl, can simply be cut into the desired shape with a blade. At this small thickness level, it is not possible to peel them off the PET foil, as they are too fragile. However, increasing the coating gap to 400 µm, leading to approximately 180 µm thick separators, makes the delamination possible yet delicate, even before densification (**Figure S3.8**). With the thinner separators presented here, we cut squares of 2 x 2 cm^2 and measured their thickness and mass to obtain an approximation of their porosity as casted (**Figure 3.20**). Averaged on five points, the thickness still suffers from significant disparity, up to 10 µm of standard deviation. We should remember that the square length represents ≈ 25% of the total length of the tape, already subjected to thickness disparity. Increasing the area of coating, thus the amount of material, should minimise this issue in future experiments. Porosity before densification lies between 30 and 45 %, without a clear tendency regarding the binder content or the SE particle size. The densification step is performed in a cold isostatic press (CIP – **Figure 3.21**). First, the tape separator is sealed under vacuum in a pouch bag, with its exposed surface protected by a PET foil. The bag is then placed in the dedicated vessel, filed with incompressible oil. The vessel is then hermetically closed by placing the upper piston. An isostatic pressure up to 500 MPa can finally be reached by subjecting the piston to 100 tons under a dedicated electric hydraulic press.

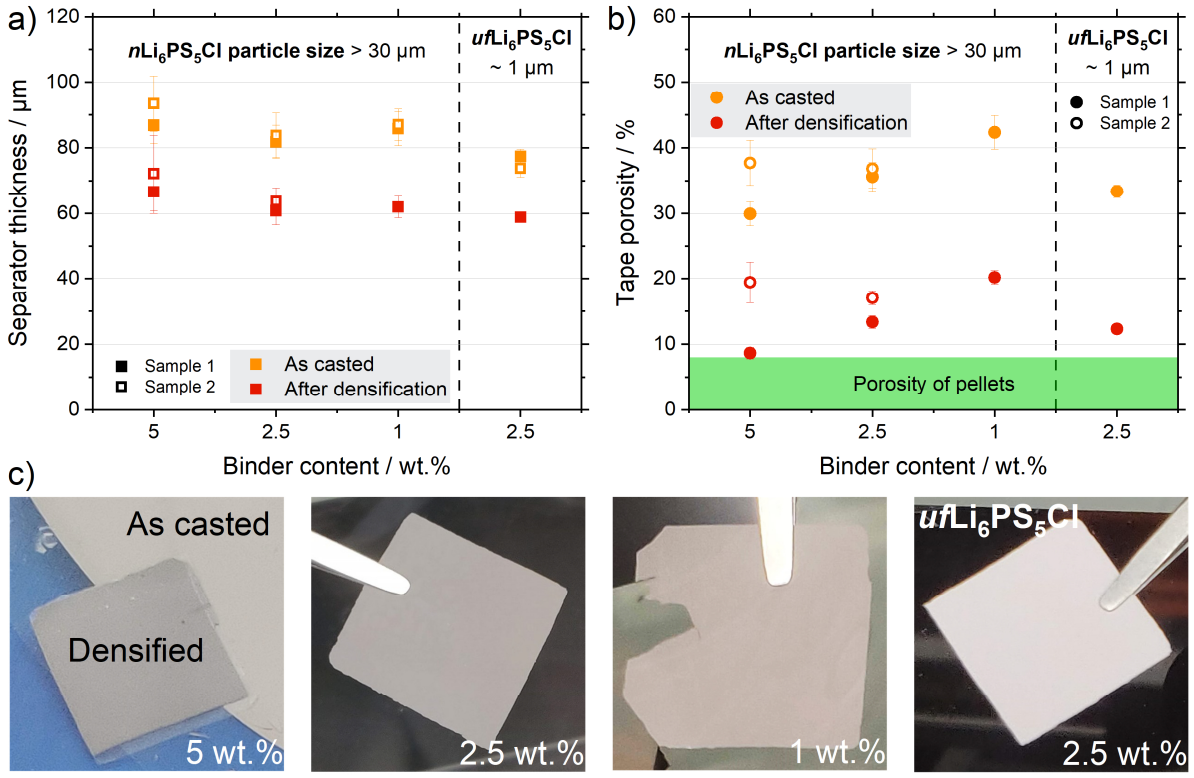

Figure 3.20 Evolution of (a) separators thickness and (b) their related porosity before and after densification at 400 MPa in isostatic press, according to binder content and SE particle size. (c) Pictures of the separators cut as 2 x 2 cm^2 squares.

We densified the samples at 400 MPa for 5 min to mimic the conditions of pellet densification under conventional hydraulic press. Once we collected the samples inside the glovebox, we were able to peel off effortlessly the PET foil and obtain self-standing tapes (**Figure 3.20c**). A clear darkening of the tape is observed, suggesting effective densification. Concerning their mechanics, only the tapes containing 1 wt.% of binder are very fragile and difficult to delaminate. We did not characterise the mechanical properties of these tapes but we could qualitatively conclude that 2.5 wt.% of PVDF-HFP gave sufficient resistance to safely handle it. Overall, the final thickness reaches around 60 µm for a decreased porosity between 10 and 20%. However, these values are significantly higher than the average porosity of densified binder-free pellet of argyrodite (< 8 % – **Figure S3.9**). The presence of binder should be the obvious explanation, yet no clear tendency on tape porosity can confirm or disprove it. Nonetheless, the error inherent to the determination of the tape surface along with heterogeneous thickness over the surface might lead to a wrong determination of the porosity. Indeed, exact cutting to desired shape is difficult in the glovebox and the handling of the tape often results in damaging the corners, which alters the mass and area measurements.

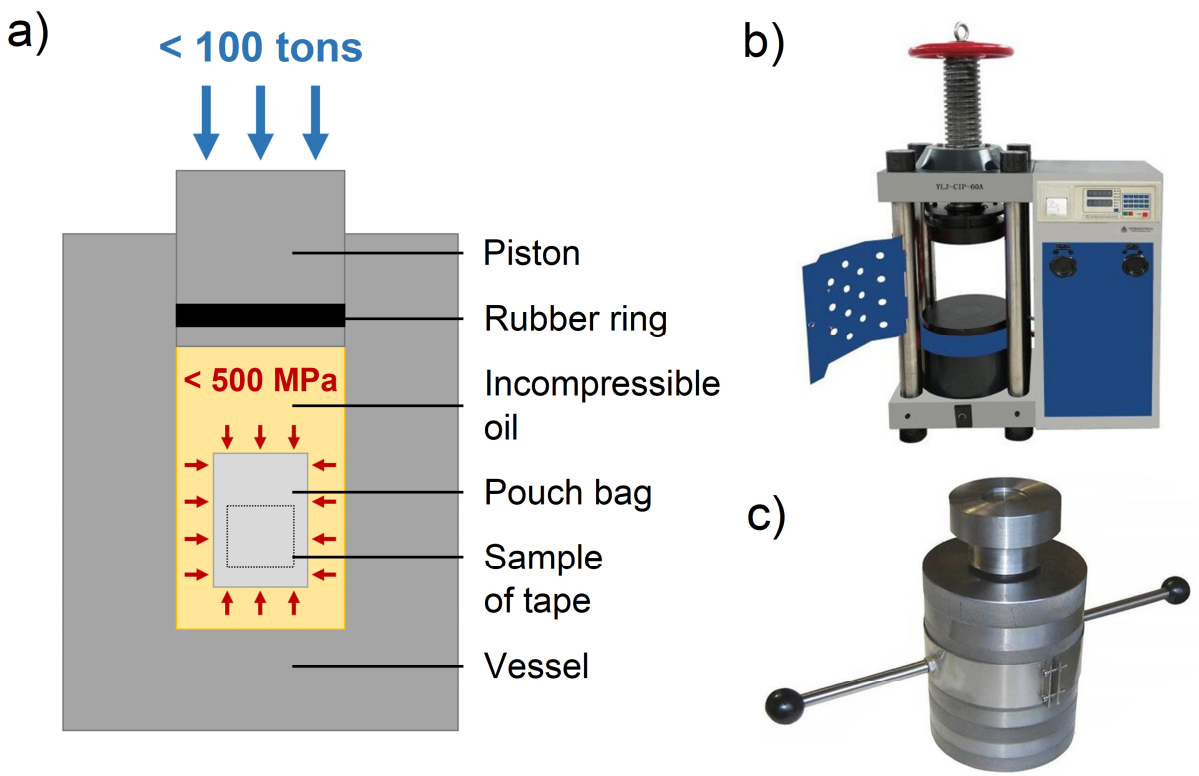

Figure 3.21 (a) Schematic of the isostatic pressing principle. Pictures of the dedicated (b) electrical hydraulic press and (c) isostatic pressing vessel and piston.

A more reliable method to determine porosity should help removing any doubt, such as FIB-SEM cross-section and 3D reconstruction of the void distribution[46] or X-ray computed tomography.[183] Keeping in mind the low melting point of the binder (50 °C – **Figure 3.2**), a possible strategy to improve densification and decrease the tape porosity would be to heat the oil before the isostatic pressing. In the melted state, the polymer would spread more easily, which could allow us to decrease the porosity. Additionally, its content could be lowered without compromising the mechanical integrity of the tape.

Continuing with the structural characterization of the tapes, we observed their cross-section by SEM before densification (**Figure 3.22**). The organisation of particles appears macroscopically homogeneous. However, it is difficult to decipher the influence of the binder content, which we cannot detect in the structure, or of the particle size since Li_6PS_5Cl reacts very quickly during the short transfer (few seconds) to the microscope chamber. Morphology of densified tapes will be observed concurrently with densified cathode in the following section **3.5.2**.

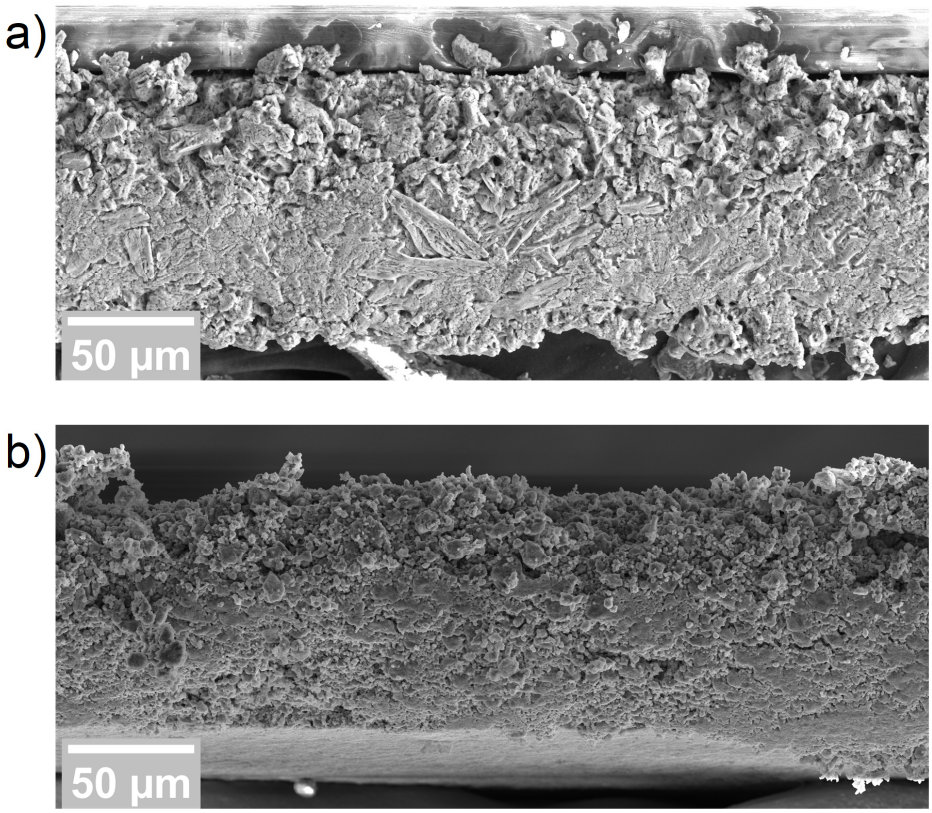

Figure 3.22 SEM cross-section images of tape separator after drying. The tape composition is (a) *n*Li_6PS_5Cl : PVDF-HFP = 95:5 (w) and (b) *uf*Li_6PS_5Cl : PVDF-HFP = 97.5:2.5 (w).

3.4.2 Conductivity of tapes

After evaluating the structure of the Li_6PS_5Cl separators, we examined how their composition influenced the tape conductivity. To perform EIS of a sheet of SE, we developed a specific pouch cell system with an ion-blocking electrode configuration (**Figure 3.23a-b**). The densified tape separator (2x2 cm^2) was positioned between two carbon paper electrodes with respective areas of 1x1 and 1.5x1.5 cm^2. Prior to this, metallic tabs for electrical connection were taped to the electrodes' external side. Once the tape electrolyte was inserted between the electrodes, the pouch was sealed under vacuum inside the glovebox and a final densification was performed at 100 MPa in the isostatic press, to ensure proper contact with the electrodes. Subsequently, the pouch cell was placed inside a custom-designed frame for characterising and operating self-standing SSB (**Figure 3.23c-d**). Applied pressure was regulated via four compressed springs exerting force onto the aluminium frame. Shoulder screws maintained a consistent and reproducible compression length. Silicon rubber squares (3x3 cm^2), protruding from the aluminium body, evenly transmitted the applied pressure on

the pouch placed in between. By adjusting the load of the springs and the length of the screws, a range of pressures from 0.2 to 5 MPa could be applied to the pouch cell with versatility.

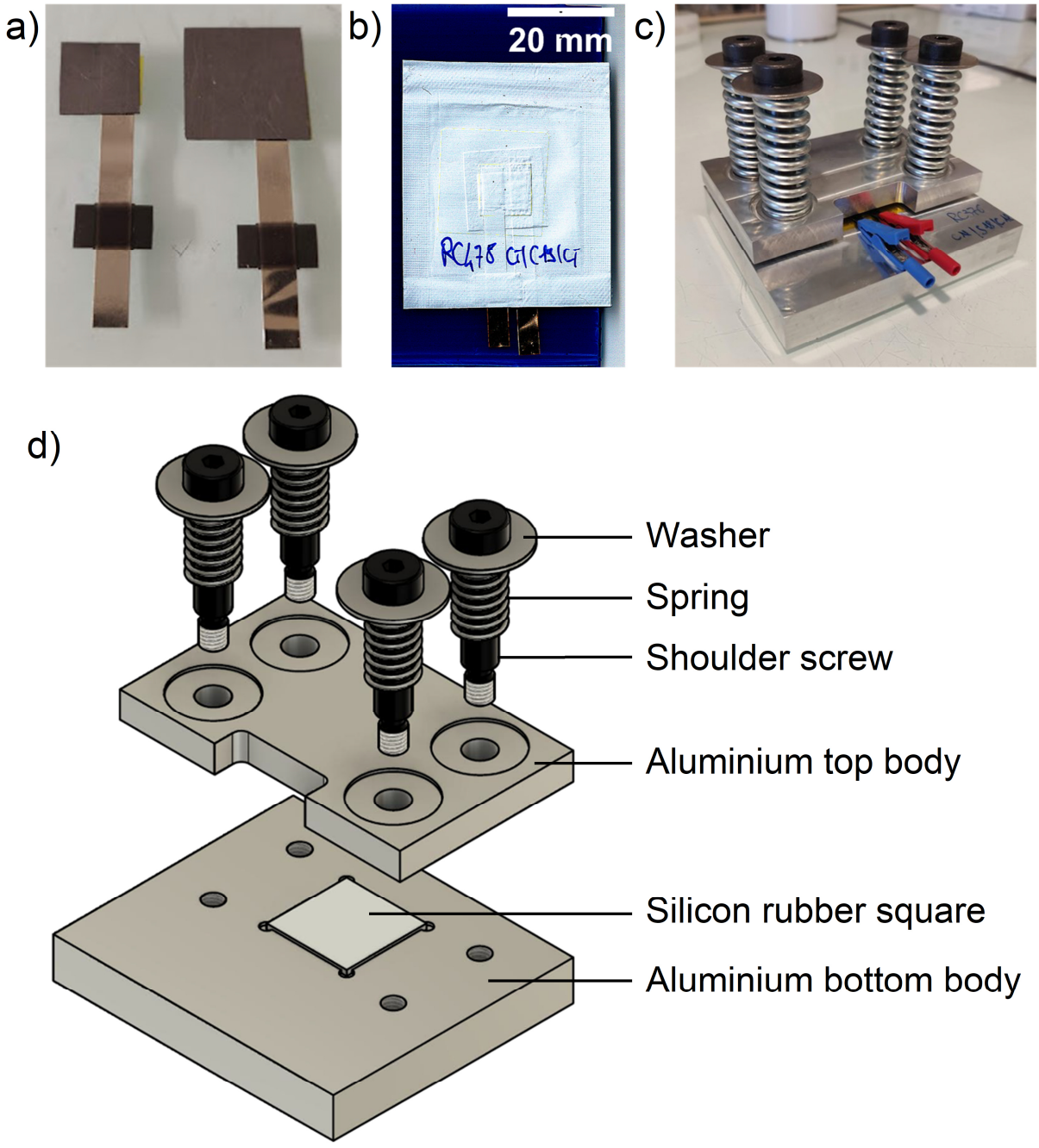

Figure 3.23 (a) Picture of the carbon paper electrodes attached on battery tabs for electrical contact. (b) Scanned image of the densified pouch cell for conductivity measurement, with the electrodes, tabs and tape electrolyte appearing in relief. (c) Photograph of the custom-designed frame for constant pressure application on SSB pouch cell. (d) Exploded view of the frame with the parts name.

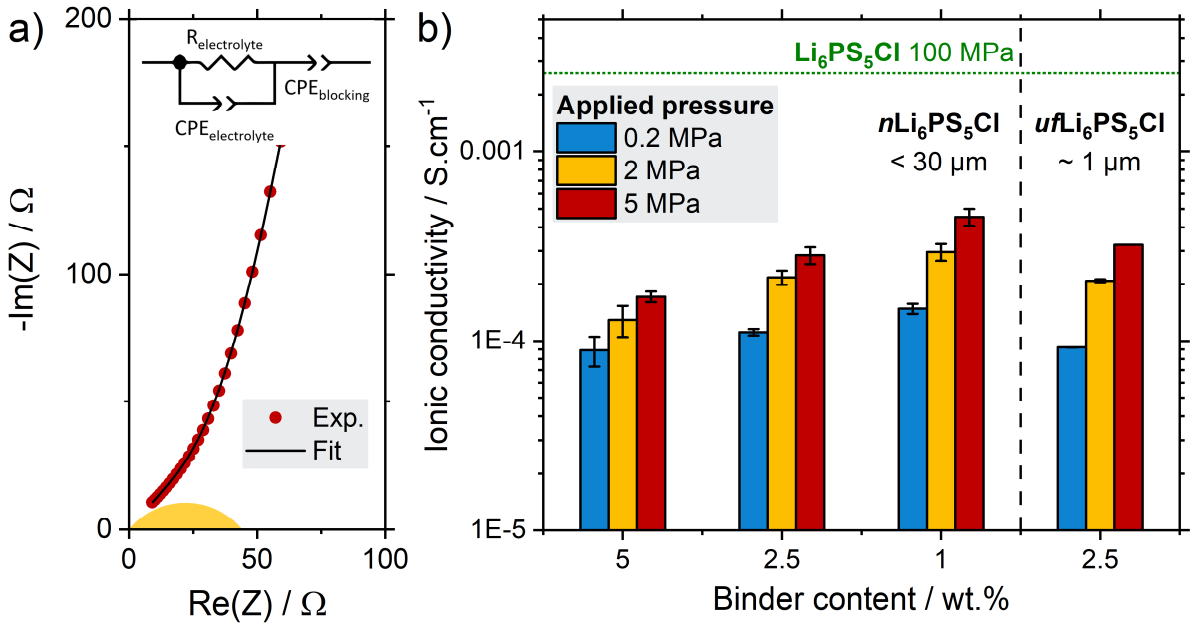

Figure 3.24 (a) EIS data for ionic conductivity measurement of Li_6PS_5Cl : PVDF-HFP = 95:5 (w) at 5 MPa and 25°C. (b) Evolution of ionic conductivity of Li_6PS_5Cl : PVDF-HFP tape separators according to applied pressure, binder content and SE particle size, measured at 25°C. Two cells were assembled per formulation.

To evaluate the conductive properties of our tape SE, we conducted EIS at 25°C and different stack pressure (0.2, 2 and 5 MPa) on the dedicated pouch cell placed in the frame. Impedance data were fitted with a model taking into account both the electrolyte and the ion-blocking interface with the carbon electrodes (**Figure 3.24a**). From $R_{electrolyte}$, $S_{electrode} \approx 1$ cm^2 (true area is measured for each pouch cell) and $e_{electrolyte}$, the ionic conductivity could be estimated and its evolution according to pressure and tape formulation is presented in **Figure 3.24b**. Firstly, the range of conductivity for tapes is around a decade lower than the reference pellet of Li_6PS_5Cl measured at 100 MPa. Both the effect of binder presence and decreased stack pressure can explain lower ionic conductivities. Interestingly, the expected tendency of higher conductivity at higher pressure is confirmed with all the samples. Moreover, decreasing the binder content results in less degraded conductivity, up to 0.5 mS.cm^{-1} with 1 wt.% PVDF-HFP at 5 MPa. The SE particle size does not have any significant influence on conductivity levels, meaning that the amount of grain boundaries between particles is not a decisive parameter, even at low pressure. Interestingly, working with such thin tape electrolyte (e ≈ 60 µm) can effectively compensate for the lower ionic conductivity. Areal resistance is approximately 20 Ω.cm^2 for 2.5 wt.% binder-containing tapes which is comparable with the value of 15 Ω.cm^2 for the binder-free layer of *n*Li_6PS_5Cl in cells cycled at 100 MPa (refer to section **3.3**). Moreover, working with thin separators will help increase the cell-level energy

density. In parallel, electronic conductivity was measured as low as 10^{-10} S.cm^{-1} for all the tapes (**Figure S3.10**).

The development of Li_6PS_5Cl-based self-standing separators with low areal resistance, reduced thickness and sufficient mechanical resistance enables their integration with our cathode tape in self-standing batteries.

3.5 – Towards self-standing solid-state batteries: pairing tape cathode and self-standing separator

In this final section, we initiated the assembly of self-standing SSBs, benefiting from the development of our solid-state cathode standing on an aluminium current collector and our self-standing solid-state separator. The initial approach consisted in evaluating how matching the binder-containing cathode and separator affected the electrochemical performance in our conventional high-pressure system. The final work delved into the assembly of electrodes and separator into a freestanding stack and its electrochemical characterisation at reduced pressure, thus approaching our final motivation of large self-standing SSBs.

3.5.1 Influence of tape separator on electrochemical performance

To evaluate the cathode – separator bilayer electrochemical performance, we assembled three type of systems: a binder-free one serving as reference (grey – **Figure 3.25**) one with only the tape cathode (blue) to assess its performance, and the advanced system with the replacement of the Li_6PS_5Cl pellet by our thin tape separator (pink). The reader may notice the relatively weaker performance of these systems, attributed to the timeline of our experiments, which, in this case, were performed before the final optimisation of the cathode and separator. Nonetheless, these data confirm the detrimental effect of integrating a tape separator, which is highlighted concurrently by the higher polarisation (**Figure 3.25a**), and the appearance of an additional high frequency (< 5 kHz) semi-circle on the EIS after first charge (**Figure 3.25e**). We can estimate the areal resistance around 250 Ω.cm^2 for this separator, which is much higher than what was measured in ion-blocking systems (refer to section **3.4.2**). The separator fabrication was not optimised yet, and the tape thickness was much higher (e ≈ 200 µm) at the time of the experiment. Regarding the rate capability, the higher initial

polarisation leads to lower and more disperse discharge capacity levels. This disparity correlates with less reproducible impedance spectra, compared to the other systems.

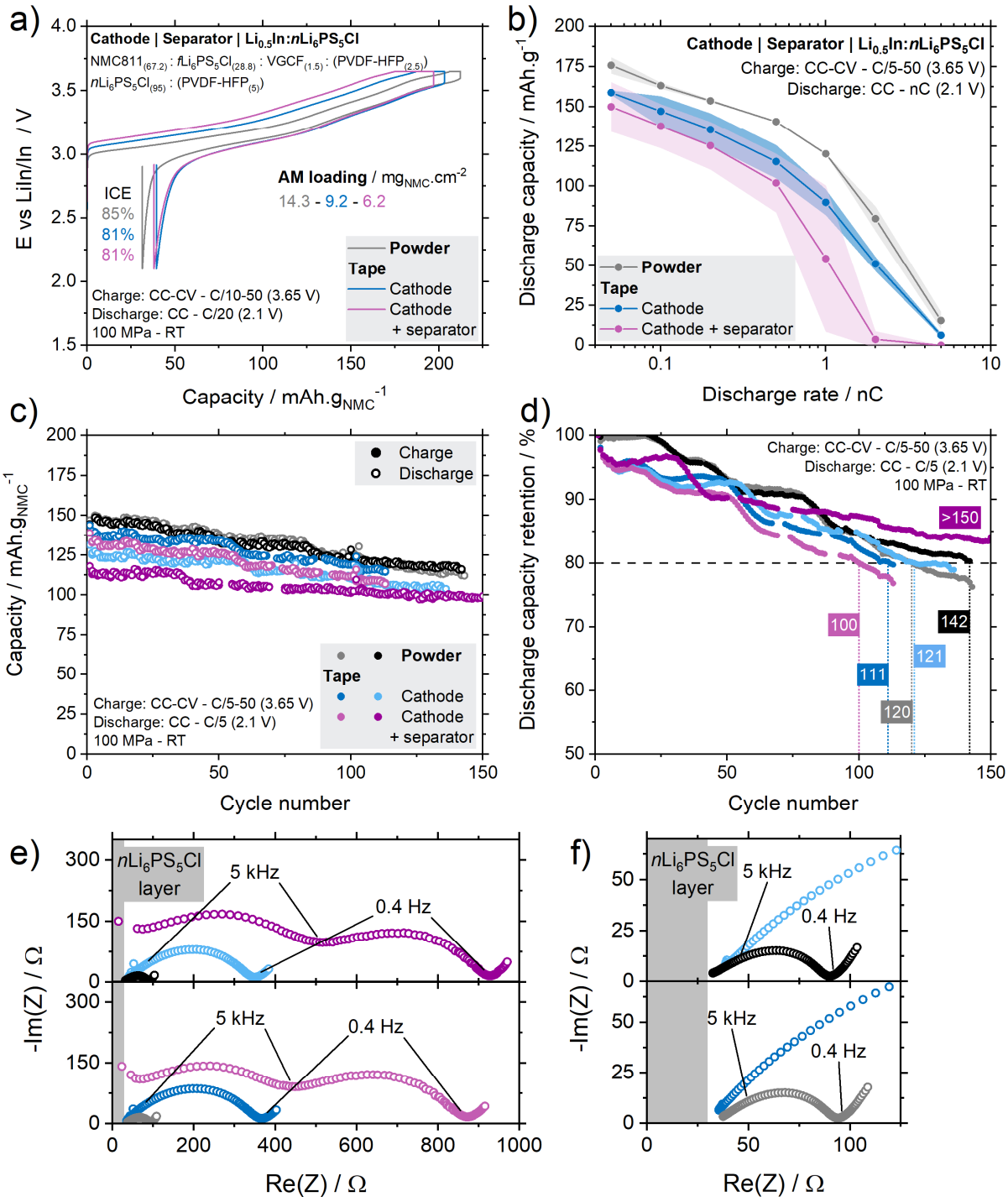

Figure 3.25 Study of the influence of replacing the SE layer (pure Li_6PS_5Cl – blue) by a tape separator (Li_6PS_5Cl : PVDF-HFP = 95:5 (w) - purple) in tape cathode-based SSBs, compared to the binder-free reference system (grey). Electrochemical performance of (a) First cycle voltage profile and initial coulombic efficiency (ICE). Cells repetition and their first cycle voltage profile are available on **Figure S3.11**. (b) Rate capability averaged over 2 cells for each type of SSB. (c) Capacity at C/5 for long cycling. (d) Smoothed discharge capacity retention at C/5. (e-f) Electrochemical impedance spectra (EIS) of cells after the first charge, in 25°C oven.

Interestingly, the discharge capacity retention is again not affected by the presence of binder in different layers of the cells, manifesting the absence of chemical instability due to the binder. The characterisation could have been performed with the optimised cathode and separator, but the low thickness of the self-standing tape prevents its densification inside the routine and high-pressure cell device since it is not possible to peel it off the substrate before densification. This is the reason why we initiated the assembly of fully self-standing SSBs, packaged in pouch cells.

3.5.2 Assembly and cycling of self-standing solid-state batteries at low pressure

One objective in transitioning to self-standing SSBs was to allow the fabrication of cells with a larger area. For this, a dedicated frame (**Figure 3.26a**) was designed by Dr. Romain Dugas, research engineer in charge of the SSB group in Collège de France. In this system, a self-standing separator is clamped within the frame (**Figure 3.26b**). Subsequently, it is densified with the tape cathode using the square stainless steel pistons, applying a unidimensional pressure under the hydraulic press. Unfortunately, the discontinuity of pressure at the edge of the piston systematically leads to the separator being cut to the tape cathode dimension. In this case, the anode cannot be larger than the cathode, resulting in edge effect issue and probable short-circuit of the cell. To take a step back, we decreased the cathode area from 4 to 0.5 cm^2 and attempted its densification onto a 11 mm diameter separator disc (**Figure 3.26d**). However not ideal as the separator is prone to cracks at the border of the cathode, we were able to obtain two crack-free bilayers that we then matched with an alloy anode. It was prepared by pressing at 50 MPa a disc of lithium metal against a disc of indium with a 1:2 molar ratio, onto a 10 mm diameter copper current collector. No optimisation of the anode has been carried out yet, resulting in a very large excess on the negative side of the cell.

Taking inspiration from our previous test at low pressure (**Figure 3.12**), we firstly cycled the self-standing cell inside the frame (**Figure 3.26a**), applying 100 MPa under a hydraulic press inside the glovebox. As shown in **Figure 3.27a**, the first cycle is more polarised than with routine system previously described (**Figure 3.25**). It leads to a lower first discharge capacity (125 versus 150 $mAh.g_{NMC}^{-1}$ at C/20). However, the ICE remains comparable with previous systems (78 versus 81%).

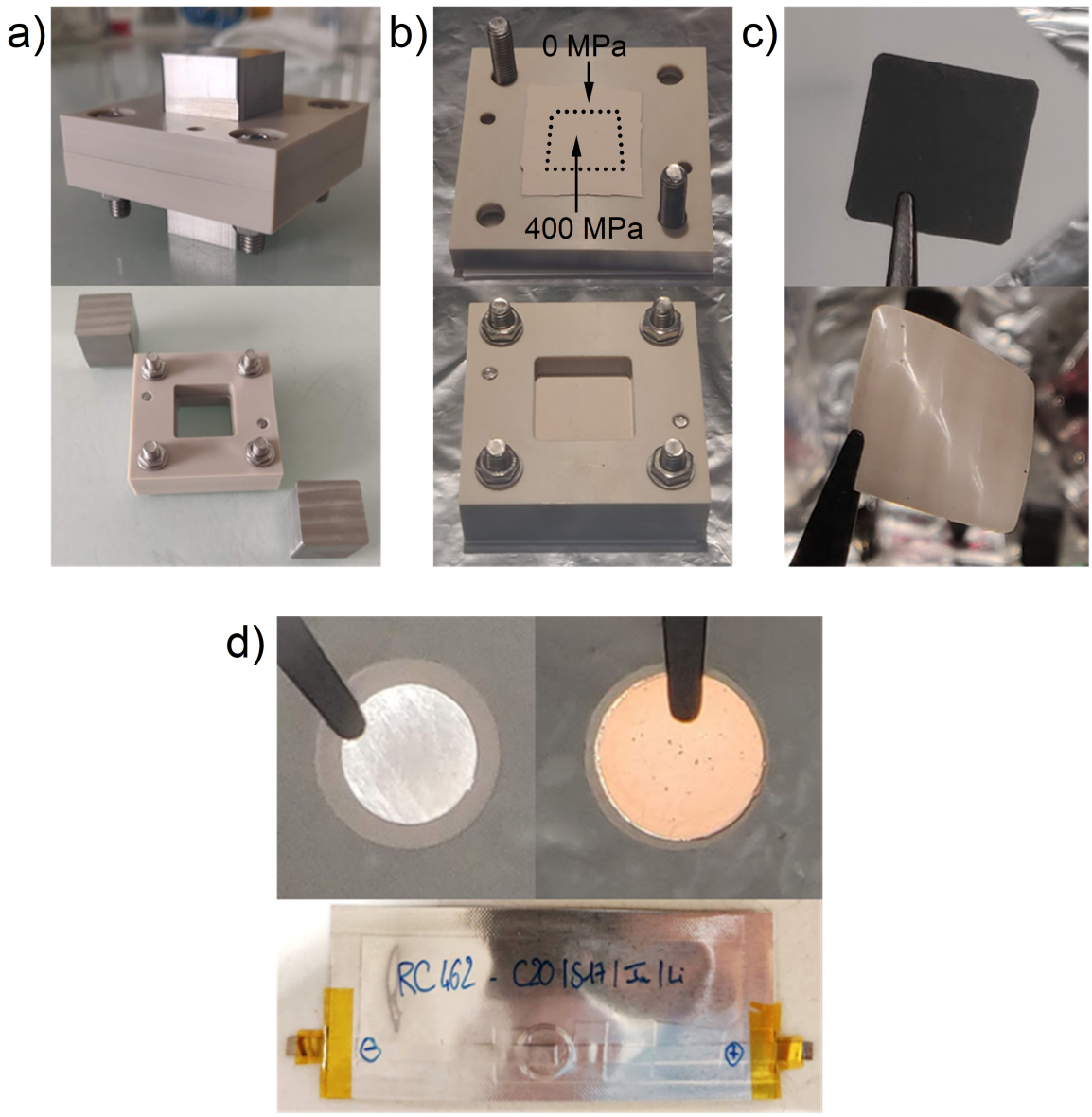

Figure 3.26 (a) Picture of frame for assembling self-standing SSB of 4cm^2 area. (b) Principle of larger separator clamped in the frame. (c) Image of cathode tape before densification (top) and after densification at 400 MPa (1D hydraulic press) with the separator (bottom). (d) Photographs of a self-standing SSB of 0.5 cm^2 area (cathode) with a $Li_{0.5}In$ alloy anode pressed onto a copper current collector (top). Pouch packaging of this cell (bottom).

After two cycles at high pressure, the self-standing cell was packaged in a pouch bag, and sealed under vacuum. It was then placed inside the pressure frame at 0.6 MPa. Surprisingly, the discharge capacity only dropped by 13% from 125 to 109 mAh.g_{NMC}^{-1}, highlighting again the beneficial effect of preliminary cycling at high pressure to sustain sufficient contact between particles and the battery's layers. The subsequent cycles lead to discharge capacity stabilisation after 25 cycles around 80 – 85 mAh.g_{NMC}^{-1}. However very low for a C/20 rate, the stable capacity is again characteristic of the cells we cycle at low pressure. To optimise this

cell further, we tested the influence of post-densification using the isostatic press. While a pressure of 50 MPa did not have a significant effect, applying 400 MPa on the pouch allowed us to recover 104 % of the initial discharge capacity, while still cycling at a very low pressure (0.6 MPa). This is another proof that sustaining interparticle contacts is crucial for the proper cycling of SSBs at low pressure required for application (< 1 MPa).

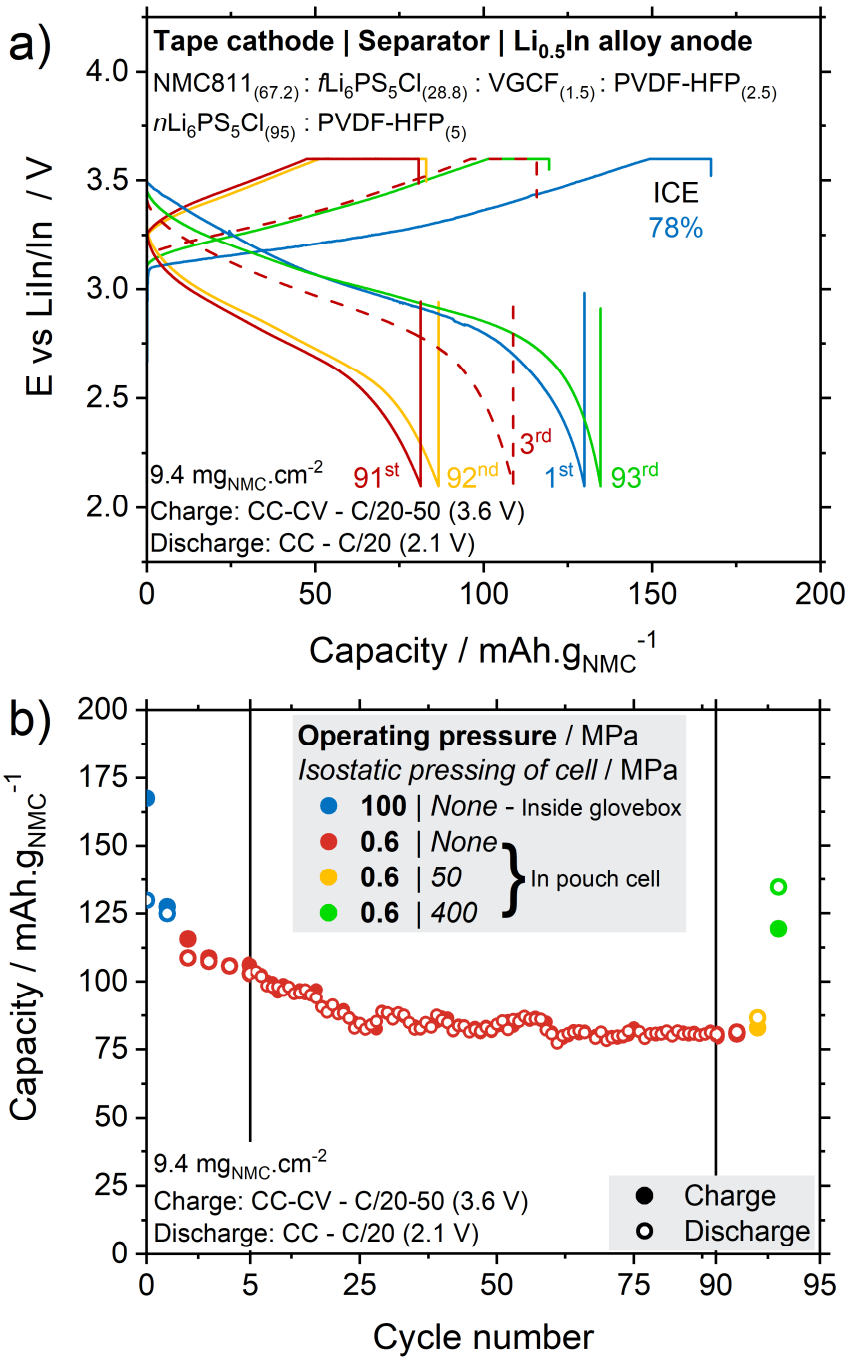

Figure 3.27 Electrochemical performance of a self-standing SSB. (a) Voltage profile at first cycle under press inside glovebox (blue), at cycle n°3 after transfer to pouch cell at 0.6 MPa (dashed red), at cycle n°91 in pouch cell (red), at cycle n°92 after submitting the pouch cell to an isostatic pressure of 50 MPa (yellow) and at cycle n°93 after an isostatic pressure of 400 MPa (green). (b) Capacity of the battery over cycles at C/20 and room temperature.

Nonetheless, cycling a self-standing SSB pressurised by a hydraulic press inside the glovebox is far from convenient. To bypass this limitation, we performed isostatic pressing on a cell packaged in a pouch. This aims to replace the preliminary cycling at high pressure. A first cycle without this pressurisation step shows the impasse of solely employing 1D densification before packaging.

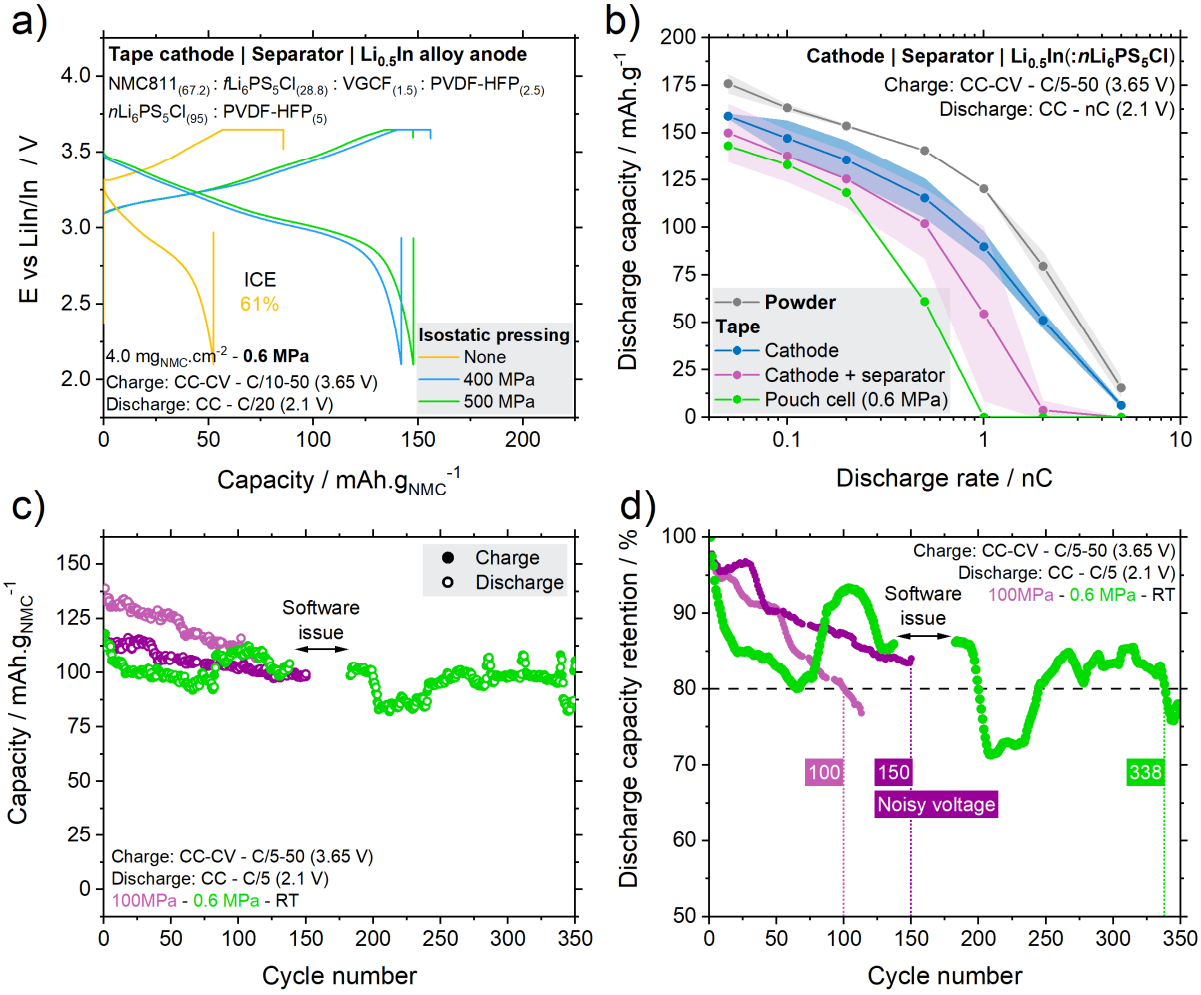

Figure 3.28 Electrochemical performance of a self-standing SSB in a pouch cell. (a) Effect of isostatic pressing on the voltage profile of the SSB pouch cell operating at 0.6 MPa. (b) Rate capability of pouch cell (green) compared to similar systems cycling at 100 MPa. (c) Capacity over cycling and (d) smoothed discharge capacity retention at C/5 and room temperature.

However, applying 400 MPa to the pouch, for only 5 min, allows retrieving a promising capacity level of 142 mAh.g_{NMC}^{-1} at C/20. Capacity was increased even more to 147 mAh.g_{NMC}^{-1} with a second treatment at 500 MPa. Interestingly, the rate capability was comparable with the similar system cycling at 100 MPa (pink), yet only at small rates < C/2. Here again, the discharge capacity retention of the cell cycling at 0.6 MPa was improved

compared to the cycling at 100 MPa. It reached over 300 cycles but was very sensitive to the ambient temperature, which fluctuated significantly over the cycling timeframe.

These very promising results steer towards an assembly process fully based on isostatic pressing. To initiate this new strategy, we packaged a tape cathode and a self-standing separator, containing both 2.5 wt.% binder, facing each other in a pouch bag. It was then placed in the isostatic press at 400 MPa for 5 min. They were both cut from the tape as casted. This process effectively densified the bilayer, yet the separator, larger than the cathode, is systematically cut around the edges of the cathode layer, which is a similar phenomenon as what we observed with uniaxial pressure in **Figure 3.28c**. Despite this constraint, we could observe the cross-section of the obtained bilayer by SEM (**Figure 3.29**). EDS maps helped distinguishing the border between the cathode and the separator. The bilayer appears properly densified, yet porosity is not evaluated here. Good contact is observed at the interface and the parallelism between layers is well preserved. We observed the same characteristics for the bilayer based on *uf*Li_6PS_5Cl (**Figure S3.12**).

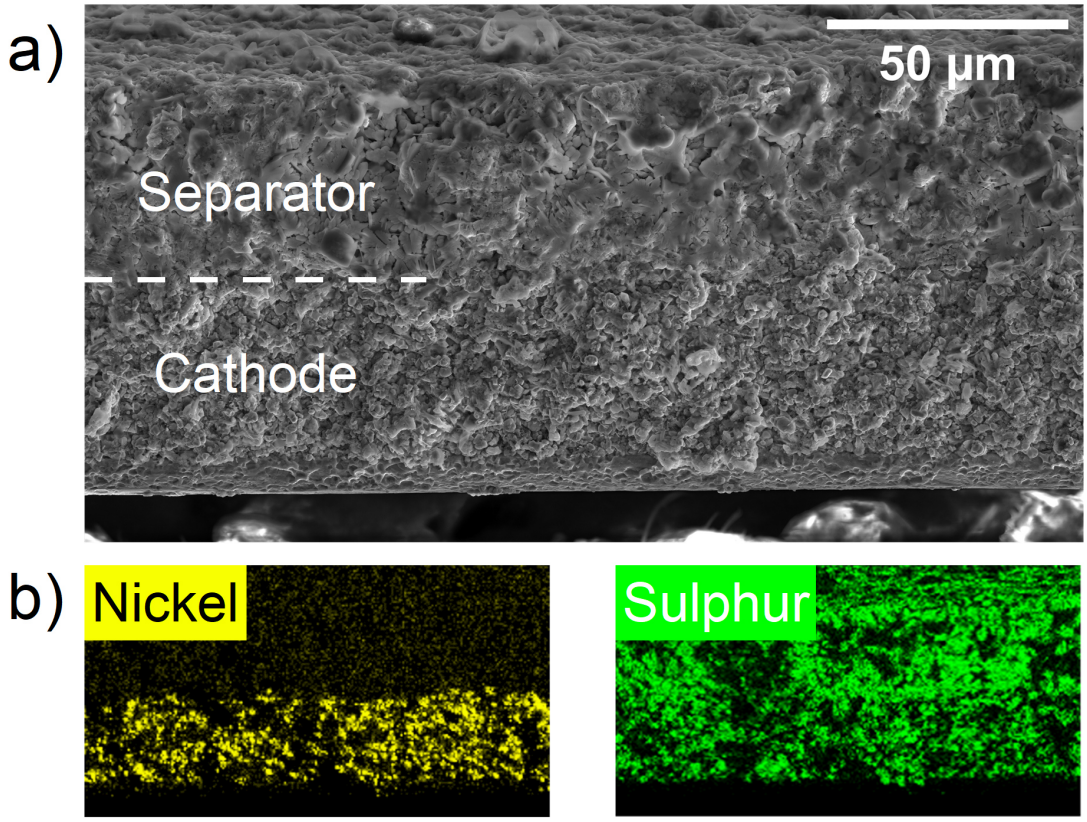

Figure 3.29 (a) SEM cross-section image of tape cathode | tape separator bilayer after densification at 400 MPa in isostatic press. The composition of cathode is NMC811 : *f*Li_6PS_5Cl : VGCF : PVDF-HFP = 67.2 : 28.8 : 1.5 : 2.5 (w) and *n*Li_6PS_5Cl : PVDF-HFP = 97.5 : 2.5 (w) for the separator. (b) Energy-dispersive X-ray spectroscopy maps for nickel (yellow) and sulphur (green).

Overall, these preliminary tests of self-standing SSBs are very promising for the future development of cells that are able to operate at low pressure, meeting the industrial requirement for application.

3.6 – Conclusion

In conclusion, **Chapter 3** delved into a strategy to transition from pellet-type to freestanding solid-state batteries, with the aim of scaling up their fabrication. Unlike the first approach detailed in **Chapter 2**, here we focused on selecting a non-conductive binder (PVDF-HFP) solely for particles cohesion within the battery.

We began by assessing the feasibility of a slurry-based process for fabricating tape cathodes and separators. Finding the right combination of solvent, binder, and solid electrolyte was crucial, and alkyl-esters emerged as promising candidates due to their ability to solubilise the binder without compromising Li_6PS_5Cl stability.

A comprehensive optimisation of cathode tape fabrication revealed several key parameters regarding the slurry preparation: the necessity of pre-grinding the composite (AM:SE:VGCF), employing a single solvent with a medium boiling point (butyl butyrate) and utilising high-energy ball milling for achieving slurry mixing and coating homogeneity. The electrochemical performance of the tape cathode was then evaluated, focusing on intra- and inter-tape repeatability, increasing the active material loading, and lowering the binder content. As a constant to SSBs scaling up, the trade-off between conductive and mechanical properties is again emerging, the binder content being here the adjustment variable. Further improvement could be achieved through the reduction of the SE particles, manifesting better and sustainable interparticle contacts within the cathode.

On the path to self-standing SSBs, the development of thin and self-supported SE-based separator is crucial. We explored the influence of binder content and particle size of Li_6PS_5Cl, finding degraded ionic conductivity for these tapes, but with areal resistivity approaching that of pure Li_6PS_5Cl pellet (15 $\Omega.cm^2$), displaying low ohmic drop in the high-pressure cycling.

Moving closer to the goal of self-standing SSBs, we evaluated the impact of pairing cathode and separators tapes at high pressure, demonstrating the feasibility of competitive

electrochemical performance. Finally, we assembled self-standing stacks packaged in pouch bags, demonstrating the feasibility of very low-pressure cycling (0.6 MPa), meeting industrial standards. Optimisation of the assembly procedure revealed key points, including the importance of isostatic pressing for tape densification and the remaining issue of separator fragility at the cathode boundary.

In summary, **Chapter 3** presented a comprehensive study on transitioning from pellet-type to sheet-type SSBs via the integration of a non-conductive polymeric binder. The industry-compatible manufacturing process and promising performance at low pressure mark significant progress, yet challenges remain in achieving a functioning self-standing SSB with competitive energy density.

Chapter 4 – General conclusions and perspectives

In an era of booming electrification of our society, batteries are at the heart of the transition, with solid-state batteries (SSBs) attracting considerable attention in the quest for enhanced performance. The translation of extensive research efforts into practical systems hinges on the capability to scale up and adapt their fabrication and operation accordingly. In this thesis, we have explored strategies to initiate the transition of SSBs into practical application and the role that polymers can play in the most advanced inorganic-based systems. In an effort to mitigate the fragility of densified ceramics, the incorporation of polymers into inorganic-based SSBs is intended to improve particle cohesion and mechanical durability.

Our initial approach was based on the hybridisation of the solid electrolyte (HSE), by employing the salt-in-polymer PEO:LiTFSI as a lithium – conductive binder to aggregate Li_6PS_5Cl argyrodite particles to form self-standing and flexible solid-state separators. In addition to the evaluation of the mechanical properties, we investigated the overall ionic conductivity mechanism according to the ratio between organic and inorganic phases. It appeared as a necessity to compromise between enhanced conductivity and self-standing property, with a threshold around 75 wt.% of Li_6PS_5Cl. To gain a deeper understanding of the interplay between the phases, we introduced a novel approach to identify the dominant activation mechanism in the HSE by fitting the ionic conductivity as a function of temperature. The distinction in conduction mechanism between the organic electrolyte, characterised by segmental motion and modelled by a Vogel-Fulcher-Tammann (VFT) equation, and the inorganic electrolyte, characterised by ion-hoping and described by an Arrhenius law, serves as a signature to identify the preferred ionic pathway through the HSE. We discovered a harmful interphase reactivity through impedance measurement, which explains the lack of a shared conduction mechanism. Nuclear magnetic resonance identified this interphase, which leads to an energetically unfavourable and slow transfer of lithium ions.

Despite this intrinsic limitation, we optimised the HSE formulation to obtain a processable material with sufficient ionic conductivity and flexibility by adjusting the polymer molar mass. The manufacturing process, based on dry mixing, has shown great potential for scaling up in dry room conditions, but is currently limited by excessive water uptake of the hybrid material. The HSE did not mitigate instability at the lithium metal interface in electrochemical systems. However, it demonstrated promising cycling performance when paired with an NMC-based cathode. Overall, our study on SE hybridisation provided valuable insights into the complex interplay within an HSE, including conduction mechanisms, reactivity, and mechanical properties. Nonetheless, it also underscored the limitation of such intricate systems when applied to practical systems.

To simplify the system and achieve self-standing SSBs, we reduced the binder content and eliminated its ability to conduct lithium ions. For this, we used the fluorinated copolymer PVDF-HFP, a conventional non-conductive binder. The wet route was used for separator and electrode preparation, relying on the appropriate binder – solvent – SE combination. Using an alkyl-ester solvent and Li_6PS_5Cl SE, this approach ensures the solubility of the binder, the chemical stability of the SE with the solvent, and the mechanical cohesion of the dried tape. The study thoroughly investigated various parameters related to the slurry and tape preparation process, their formulation and the testing conditions. It examined pre-grinding, type of mixing, and use of co-solvent in the slurry and tape preparation process, as well as pressure, loading, and repeatability in testing conditions. Furthermore, the study analysed the binder content and SE particle size in the formulation of cathode tapes with respect to mechanical and conductivity properties. As already experienced with the HSEs, we have consistently faced the trade-off between conductive properties and mechanical cohesion. However, we have successfully achieved performance levels comparable to the binder-free reference system, demonstrating the potential for self-standing SSB.

Thin self-standing films based on Li_6PS_5Cl were successfully fabricated and their ionic conductivity was assessed at low pressures ranging from 0.2 to 5 MPa using a specially designed frame. These results demonstrated the potential of these films for use in practical self-standing SSBs. The analysis of the tape porosity indicated higher values (10 – 20 %) compared to conventional binder-free pellets (< 8%). This likely led to a decrease in ionic conductivity, which ranged from 1 to 4 x 10^{-4} $S.cm^{-1}$, depending on the applied pressure and

binder content. The reduced thickness of the self-standing separator resulted in an areal resistivity of around 20 Ω.cm^2, comparable to that of conventional pellets, despite its significantly lower conductivity compared to the binder-free version that exceeds 1 mS.cm^{-1}. Therefore, it is highly suitable for integration into a SSB.

The successful development of the cathode and separator has opened the possibility of assembling self-standing SSBs. After evaluating the impact of pairing these components in conventional cells cycling at high pressure, we have transitioned to a pouch format and achieved promising results in terms of stability. This demonstrates the feasibility of cycling at a pressure lower than 1 MPa. While some assembly constraints still need to be resolved, we are now closer than ever to achieving practical SSBs.

With reliable fabrication processes in place and promising low-pressure results, we will now integrate a high-energy density anode, such as lithium metal or silicon. In both scenarios, the task is challenging as it requires addressing the chemo-mechanical instability of these anodes with the SE, developing new integration processes and reducing operation pressure simultaneously. For silicon, the major challenge is the mitigation of mechanical failure and contact loss while meeting application requirements on operation pressure (< 1 MPa).[184] For lithium metal, preventing the growth of dendrites is paramount and require a precise control of its interface with the SE. In this case, the stabilisation of the interface can be achieved through the introduction of an interlayer, which could be organic, inorganic or even hybrid. Submicrometric polymeric buffer layers are attractive as they can improve the adhesion and stability of lithium metal with the SE.[113,153] Drawing on Blue Solutions' expertise on thin lithium metal processing (< 20 µm) and its assembly with polymer electrolytes, we aim to integrate this design in our self-standing solid-state full cell. Another strategy involves coating the lithium metal foil or the separator with a nanometric inorganic layer through physical deposition. The mitigation of the interface instability is then based on an alloying reaction with various metallic elements (silver, aluminium, magnesium …)[160,185,186] or on a conversion reaction of sacrificial binary compounds (Cu_3N, AgF, CuF_2)[187–189] to form an artificial solid electrolyte interphase (SEI). Lastly, the integration of hybrid interlayers also attracts attention since they can potentially combine the mechanical benefit of polymer with the mitigation principle of the inorganic compound.[174] In all these systems, a careful evaluation of the (electro-)chemical stability and cost-benefit balance will be required considering the

integration of an additional layer. Overall, we are convinced that the success of such ambitious developments must rely on close collaboration and will benefit from each party's expertise.

Ultimately, our exploration of the potential benefits of using polymers in inorganic-based SSBs revealed similarities, irrespective of the conductive property of the binder. The development of self-standing solid-state separators or electrodes requires balancing the mechanical cohesion provided by the binder with its impeding nature, which can obstruct the flow of lithium ions and electrons. It also highlighted the porous frontier between research and engineering at this stage of SSBs development, during which the optimisation of fabrication process need to be fuelled by the observation and understanding of the underlying chemo-mechanical phenomena. Ultimately, we are confident that the advances made in this PhD brought valuable insights and greater confidence for future implementation of practical SSBs.

Supplementary information

S2 – Supplementary information for Chapter 2

S2.1 Materials and methods

o Materials and electrolytes preparation

Preparation of electrolytes was carried out in an argon-filled glovebox (O_2 < 1 ppm and H_2O < 1 ppm). PEO of different molar mass (600, 6 and 1.5 kg.mol^{-1}) were bought from Sigma-Aldrich and dried just below their respective melting point under vacuum for two days. The same procedure was applied to poly(ethylene-co-propylene oxide) (P(EO-co-PO), Meisei Chemical Works, Ltd. – 1000 kg.mol^{-1}). Poly(ethylene glycol) (PEG – 0.4 kg.mol^{-1}) and tetrahydrofuran (THF) were bought from Sigma-Aldrich and dried over molecular sieves (4Å) inside the glovebox. LiTFSI from Solvionic was vacuum dried at 110°C for two days. The ceramic solid electrolyte Li_6PS_5Cl was purchased from NEI Corporation (d ≈ 1 - 30 µm). The NMC cathode active material ($LiNi_{0.6}Mn_{0.2}Co_{0.2}O_2$ monolithic, d ≈ 4 µm) was kindly provided by Umicore. Vapour grown carbon fibres (VGCF) were bought from Sigma-Aldrich and dried at 280°C under vacuum for one day. Poly(vinylidene fluoride-co-hexafluoropropylene) (PVDF-HFP) binder was obtained from Solvay (15 mol.% - 300kg.mol^{-1}). Indium foils (99.99%) were purchased from Sigma-Aldrich. Lithium metal foils (e = 80µm) were kindly provided by Blue Solutions.

To prepare an HSE following a wet route, PEO and LiTFSI were first dissolved in THF. Li_6PS_5Cl powder was subsequently added and the ink obtained by magnetic stirring was casted in a PTFE Petri dish and let to dry in the glovebox. Further drying was performed under vacuum at 50°C, before peeling the film off.

HSEs were prepared following a dry mixing of powders in an agate mortar. First, LiTFSI was mixed with the desired quantity of polymer and the resulting gum was hot pressed (80°C) several times between PET foils to ensure homogeneity. Then, the appropriate amount of Li_6PS_5Cl powder was grinded for 5 min and the organic phase was added to Li_6PS_5Cl to agglomerate. The obtained HSE paste was spread as a thin film (e ≈ 100 µm) by hand-rolling it between PET foils. In case the processing as a film was not possible due to lack of mechanical

cohesion, the HSE was pelletised in an 8 mm diameter die-set under 100 MPa for 1 min, using a manual hydraulic press (Specac, 15T) inside the glovebox.

The organic-to-inorganic ratio is expressed in both mass and volume according to the following equation:

$$x_{inorg}^{V} = \frac{x_{inorg}^{M}}{x_{inorg}^{M} + \left(1 - x_{inorg}^{M}\right) \cdot \frac{\rho_{inorg}}{\rho_{org}}} \qquad \textbf{Equation S2.1}$$

where x_{inorg}^{V} (resp. x_{inorg}^{M}) is the volume (resp. mass) fraction of the inorganic phase, ρ_{inorg} = 1.64 g.cm^{-3} is Li_6PS_5Cl theoretical density and ρ_{org} ≈ 1.4 g.cm^{-3} is the organic phase density (for EO:Li = 10:1).

ρ_{org} is calculated according the following equation:

$$\rho_{PEO:LiTFSI} = \rho_{PEO} \cdot \frac{1 + A}{\frac{\rho_{PEO}}{\rho_{LiTFSI}} + A} \qquad \textbf{Equation S2.2}$$

where ρ_{PEO} ≈ 1.2 g.cm^{-3}, ρ_{LiTFSI} = 2.023 g.cm^{-3} and $A = EO{:}\,Li \cdot \frac{M_{EO} \cdot M_{PEO}}{(M_{PEO} - M_{H_2O}) \cdot M_{LiTFSI}}$ (**Equation S2.3**), with M_{EO} = 44.05, M_{PEO}= 600 · 10^3, M_{H_2O} = 18.02 and M_{LiTFSI} = 287.09 g.mol^{-1}.

The ratio of lithium in the organic phase is expressed as:

$$R_{org}^{Li} = \frac{n_{org}^{Li}}{n_{org}^{Li} + n_{inorg}^{Li}} = \frac{x_{org}^{V} \cdot C_{org}^{Li}}{x_{org}^{V} \cdot C_{org}^{Li} + x_{inorg}^{V} \cdot C_{inorg}^{Li}} \qquad \textbf{Equation S2.4}$$

where $C_{org}^{Li} = \left(\frac{M_{LiTFSI}}{\rho_{LiTFSI}} + EO{:}\,Li \cdot \frac{M_{EO}}{\rho_{PEO}}\right)^{-1}$ = 1.96 mmol.cm^{-3} (**Equation S2.5**) and C_{inorg}^{Li} = 36.7 mmol.cm^{-3} for EO:Li = 10:1.[95]

○ Ionic conductivity measurements

According to an ion-blocking electrodes configuration, polymer electrolytes and HSEs were placed between stainless steel discs and Li_6PS_5Cl pellets were faced with carbon electrodes to ensure good contact. Dedicated two-electrode cells (**Figure S2.1a-b**) previously developed in our laboratory, were employed to perform EIS measurements. They both consist in two stainless steel plungers acting as current collectors, placed in cylindrical body ($S_{electrolyte}$ = 0.5027 cm^2). For brittle materials, the 8 mm diameter pellet was directly placed in the PEI body. For flexible electrolytes, the film, wider than the cell section, was clamped in a modified

cell body composed of three parts (PEI and stainless steel) that are assembled together with screws. The cells were then closed with the plungers using dedicated screws at a constant torque of 1.7 N.m. Airtightness was ensured by compressed O-rings. The cells were preheated at 80°C for 1h in advance of the measurement to improve the contact between electrodes and electrolyte. EIS was performed in the frequency range of 1 MHz – 1 Hz with a voltage amplitude of 50 mV, using a VMP3 potenstiotat/galvanostat (BioLogic) controlled by EC-lab® software. Fifteen points were acquired per decade of frequency with ten repetitions per point. To determine activation mechanism and the associated energy (Arrhenius or VFT), temperature was applied to the cell through heated silicon oil traveling in a PVC pipe wrapped around the cell. It was connected to a thermal immersion circulator (ThermoFisher Scientific), controlled by EC-lab® to vary the temperature from 20 to 80°C, with step of 20°C and 3h intervals for equilibration. In parallel, real cell temperature was monitored thanks to a thermocouple inserted in the upper cell plunger, for sake of precision when calculating activation energies. Conductivities were calculated with the following equation:

$$\sigma_{ionic} = \frac{e}{S \cdot R_{tot}} \qquad \textbf{Equation S2.6}$$

where e is the membrane thickness, S the cell section and $R_{tot} = R_{ionic} + R_{interface}$ the total resistance. Resistance values were obtained by fitting the EIS data with the following model using Z-view software (Scribner):

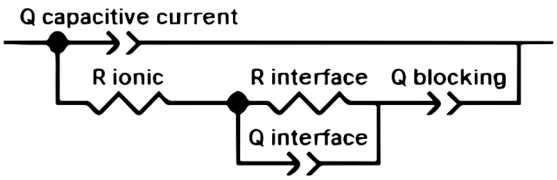

Scheme S2.1

with R_{ionic} the electrolytic resistance, $R_{interface}$ and $Q_{interface}$ the contribution of the organic-inorganic interface and $Q_{blocking}$ describing the capacitive response against blocking electrodes at low frequency. The other branch, composed only of $Q_{capacitive\ current}$, describes the capacitive current in parallel to the faradic current. For pure inorganic or organic electrolytes, $R_{interface}$ was set to 0 Ω.

○ Scanning electron microscopy

HSE cross-section morphology was observed on a FEI Magellan scanning electron microscope (SEM) and samples were prepared by blade cutting inside glovebox.

○ Differential scanning calorimetry

Thermal properties of the prepared electrolytes were studied with a differential scanning calorimeter (DSC – TA Instruments Q20) in the temperature range of -70 – 200°C, at a heating rate of 10 °C.min^{-1}. Samples of 5 – 15 mg were hermetically sealed in aluminium pans inside the argon-filled glovebox. Analysis of the melting enthalpy allows the calculation of the degree of crystallinity for PEO_x:LiTFSI electrolytes:

$$\chi_c = \frac{\Delta H^{melt}_{PEO\ in\ electrolyte}}{\Delta H^{melt}_{pure\ PEO}} \qquad \textbf{Equation S2.7}$$

○ Mechanical characterization

Tensile test was performed on a universal testing machine (Zwick Z100) located in a dry room (dew point below - 40°C). The HSE paste was first calendered as a large-area membrane (e = 100 µm) thanks to a prototyping machine. Four samples per formulation were cut to the chosen dimensions (60 x 10 mm), fixed at a distance of 41 mm between jaws and tested at a load rate of 5 mm.min^{-1}. Force was measured against the elongation until the sample fractures (F = 0 N) and the stress-strain curve ($\sigma - \varepsilon$) is obtained using these equations:

$$\sigma = \frac{F}{S}\ ;\text{in } MPa \qquad \textbf{Equation S2.8}$$

$$\varepsilon = \frac{\Delta L}{L_0}\ ;\text{in } \% \qquad \textbf{Equation S2.9}$$

$$E = \frac{\sigma}{\varepsilon}\ ;\text{in } MPa \qquad \textbf{Equation S2.10}$$

with F the force, S the sample section, ΔL the elongation and L_0 the initial distance between jaws. Young's modulus E is calculated by fitting the initial linear domain (ε = 1.22% for HSE 40 wt.% ceramic and ε = 0.14 % for HSE 75 wt.% ceramic). Yield strength σ_y is the stress at the end of the linear (i.e. elastic) limit. Ultimate strength σ_u is defined as the maximum of stress undergone by the sample. Resilience modulus U_r is calculated as the elastic energy (area under the stress-strain curve in the linear domain) and toughness modulus U_t is computed as the total energy absorbed before fracturing.

$$U_r = \frac{\sigma_y^2}{2E}\ ;\text{in } J.m^{-3} \qquad \textbf{Equation S2.11}$$

$$U_t = \int_0^{\varepsilon_f} \sigma \cdot d\varepsilon \; ; \text{in } J.m^{-3}$$ **Equation S2.12**

○ Water content determination

Water content in the HSE and the precursor materials was determined by Karl-Fischer titration (Metrohm coulometer).

○ EIS to determine interfacial resistance

To measure the interfacial resistance between the organic and inorganic phases, trilayer stacks of PEO_x:LiTFSI | Li_6PS_5Cl | PEO_x:LiTFSI were assembled (x = 10, 20 and 40). Polymer electrolyte membranes were prepared by hot pressing (80°C) the material between PET foils to reach a film thickness of 35 µm. Ceramic powder was densified as a pellet at 400 MPa using an 8 mm diameter die-set. Then, polymer membranes were carefully attached to the cell stainless steel plungers and the ceramic pellet was place in between them before closing. A pressure of 4.5 MPa was applied via a spring assisted setup, so that the polymer does not creep at high temperature (**Figure S2.1c**). EIS was performed at room temperature before and after an hour stabilization at 80°C. Afterwards, temperature-dependent EIS was carried out in the same conditions as previously described. Impedance data were fitted using the previously described model (**Scheme S2.1**).

○ X-ray photoelectron spectroscopy

XPS spectra were collected on an Omicron Argus X-ray photoelectron spectrometer, using a monochromatic Al Kα (hν = 1486.6 eV) radiation source having a 300 W electron beam power. The samples were analysed under ultra-high vacuum conditions (1 x 10^{-8} Pa). After recording a broad range spectrum (pass energy 100 eV), high resolution spectra were recorded for all core XPS levels (pass energy 20 eV). Spectrum processing was carried out using the Casa XPS software package. The spectra were fitted by applying a Gaussian/Lorentzian function with a ratio G/L equal to 70:30.

○ Nuclear magnetic resonance

^{7}Li NMR spectra were recorded on a 20T (850 MHz for ^{1}H, 330 MHz for ^{7}Li) Bruker WB Avance spectrometer equipped with 1.3 mm ^{1}H-^{19}F/X double resonance probe head. The Magic Angle Sinning (MAS) rate was set at 40 kHz to prevent unwanted pressure gradients on the polymer sample inside the ZrO_2 rotor, and the bearing and drive gas were pure nitrogen. The samples were prepared inside an argon-filled glovebox. The ^{7}Li chemical shift was

referenced with 1M ^{7}LiCl in water, and the RF strength was set to 86 kHz (90° pulse of 2.9 µs). The longitudinal relaxation times of ^{7}Li in argyrodite and the polymer phase were measured in the same conditions at 526 ms and 1.0 s respectively. All 1D spectra were recorded using a rotor synchronised Hahn echo sequence (with a half echo time equal to a single rotor period), using a recovery delay of 5 s to ensure quantitative measurements, and 16 transients were recorded for each. The EXchange SpectroscopY 2D experiment was recorded with a 1.5 s recovery delay, 64 transients were recorded for each one of the 512 time increments, and the sweep width in the indirect dimension was set to 2000 Hz, using the States method for quadrature detection. NMR data treatment was performed using Dmfit software. The spectra were fitted with Gaussian/Lorentzian functions to extract the intensity and chemical shift of each contribution.

- Powder X-ray diffraction

XRD analysis was conducted utilising an airtight holder fitted with a beryllium (Be) window. The XRD patterns were recorded in reflection mode, employing the Bragg–Brentano geometry, and data acquisition was carried out with a Bruker D8 ADVANCE diffractometer. A copper (Cu) Kα X-ray source (λ_1 = 1.54056 Å and λ_2 = 1.54439 Å) was utilised in conjunction with a LynxEye detector for data collection.

- Battery assembly and electrochemical testing

Symmetric cells were assembled by clamping the HSE film (d = 11 mm – e ≈ 100-250 µm) in the cell body, before placing two lithium metal electrodes (d = 8 mm – e ≈ 80 µm) on each sides. The cells were then closed with the plungers using dedicated screws at a constant torque of 1.5 N.m. The cells were preheated at 80°C for 1h in advance of the measurement to improve the contact between electrodes and electrolyte. The CCD determination protocol was done in an oven at 25°C, following a staircase test with pulses of 1 hour from a starting current of 20 µA.cm^{-2} and step increase of 20 µA.cm^{-2} per cycle. An impedance spectrum was acquired between every cycle in the frequency range of 1 MHz – 1 Hz with a voltage amplitude of 50 mV, using a VMP3 potenstiotat/galvanostat (BioLogic) controlled by EC-lab® software.

Battery assembly and electrochemical tests were carried out in the same cells as for ionic conductivity measurement (**Figure S2.1a-b**). The assembly followed a first step of placing the electrolyte: either by clamping an HSE membrane (e ≈ 100 µm) or by compressing

30 mg of Li_6PS_5Cl (e ≈ 400 µm) in the cell body at 100 MPa for few seconds, thanks to a manual hydraulic press. The next steps were identical for both battery configurations. A disc of cathode was placed on one side (m ≈ 4 mg – e ≈ 30 µm) and the appropriate amount of counter electrode powder ($Li_{0.5}In$: Li_6PS_5Cl = 60:40 (w)) was spread on the other side (m ≈ 30 mg – e ≈ 250 µm). The whole stack was finally densified under 400 MPa for 15 min (e_{tot} ≈ 700 µm). The closure was carried out by applying 2.3 N.m to each screw to obtain an internal pressure of 100 MPa. All assembly steps were performed in an argon-filled glovebox to prevent any potential contamination from moisture. Cathode tape was prepared by hand-grinding powders in an agate mortar to reach the desired ratio NMC622 : Li_6PS_5Cl : VGCF = 67.2 : 28.8 : 1.5 (w). 2.5 wt.% of PVDF-HFP was then added to the mix. To prepare the slurry, powders and the appropriate amount of ethyl acetate (extra dry 99.9%, Thermo Scientific) were stirred together for 15 min. It was then casted onto the aluminium current collector using the doctor blade method and tape was vacuum dried at 60°C for 12h.

Galvanostatic cycling was performed in the voltage range of 2.1 – 3.6 V vs LiIn/In (2.72 – 4.22 V vs Li^+/Li) at a varying C-rate (calculated according to theoretical capacity Q_{NMC622} = 276.5 $mAh.g^{-1}$): two cycles at C/20 followed by five cycles steps of C/10, C/5, C/2 and C before long cycling at C/5. Measurements were conducted on a BCS potentiostat/galvanostat (BioLogic) controlled with EC-Lab® software.

S2.2 Supplementary figures

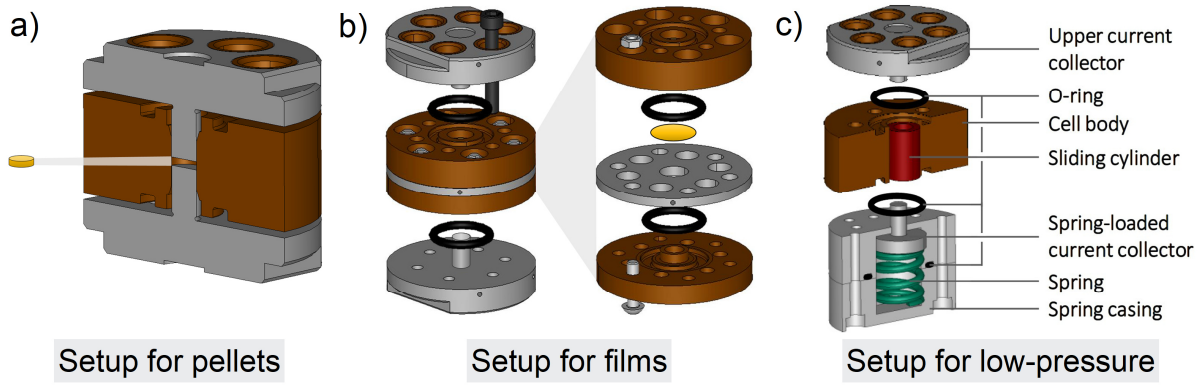

Figure S2.1 Schematics of the electrochemical cells. (a) Simple version of the two-electrode cell for pellet measurement. (b) Specific design for an HSE membrane clamped in the cell body. (c) Constant-pressure spring-loaded setup for low-pressure measurements. Courtesy of Dr. Romain Dugas.

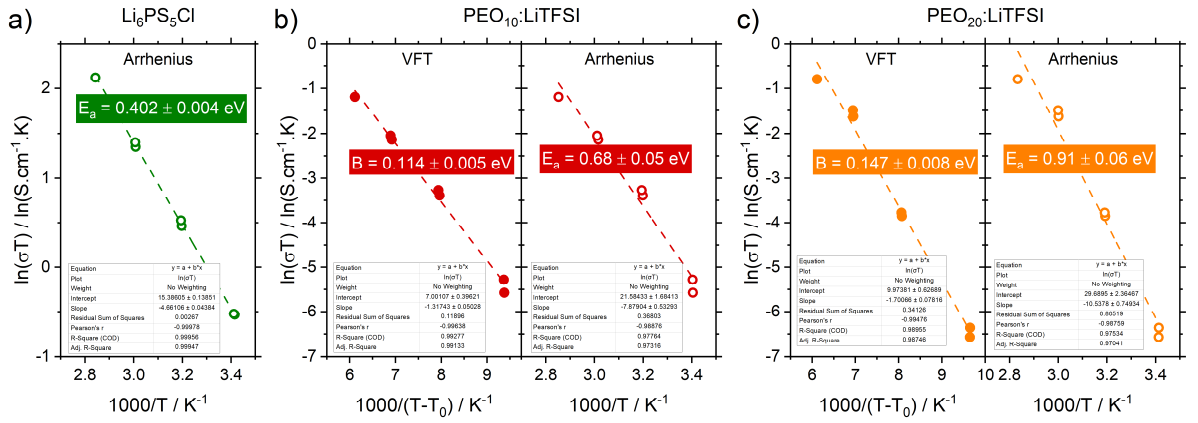

Figure S2.2 Fitting of ionic conductivity in temperature and choice of the appropriate activation mechanism (VFT versus Arrhenius): (a) Li_6PS_5Cl, (b) PEO_{10}:LiTFSI and (c) PEO_{20}:LiTFSI.

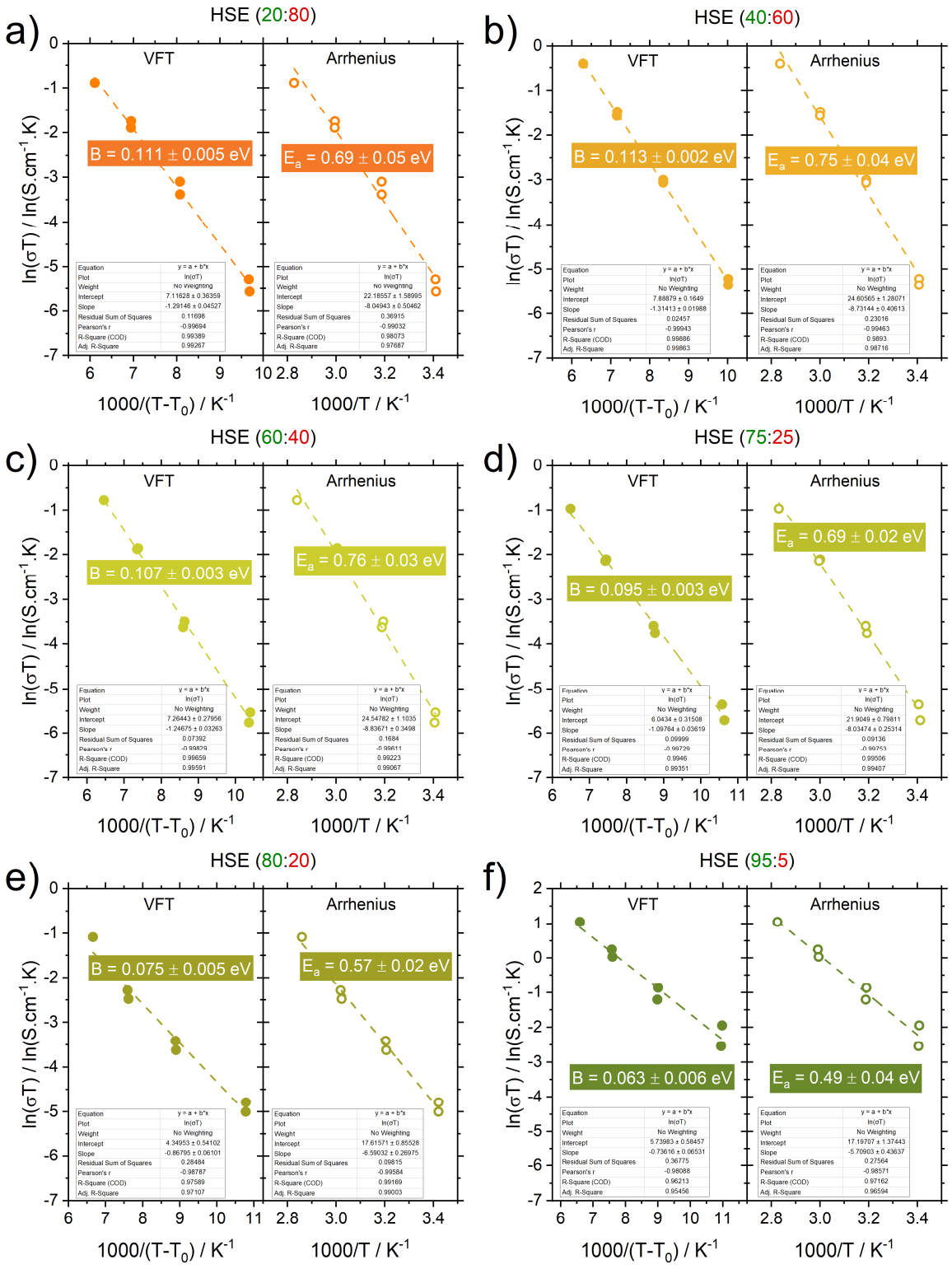

Figure S2.3 Fitting of ionic conductivity in temperature and choice of the appropriate activation mechanism (VFT versus Arrhenius) for HSEs containing (a) x = 20, (b) 40, (c) 60, (d) 75, (e) 80 and (f) 95 wt.% of Li_6PS_5Cl and 100-x wt.% of PEO_{10}:LiTFSI.

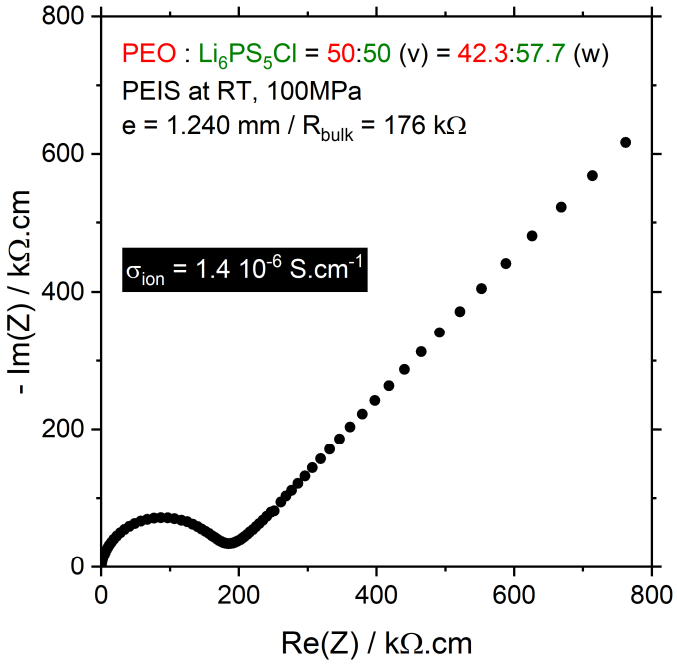

Figure S2.4 Impedance spectrum of a PEO:Li_6PS_5Cl = 50:50 (v) = 42.3:57.7 (w) pellet to obtain the ionic conductivity of an HSE in the absence of LiTFSI salt, i.e. with a non Li^+-conductive organic phase.

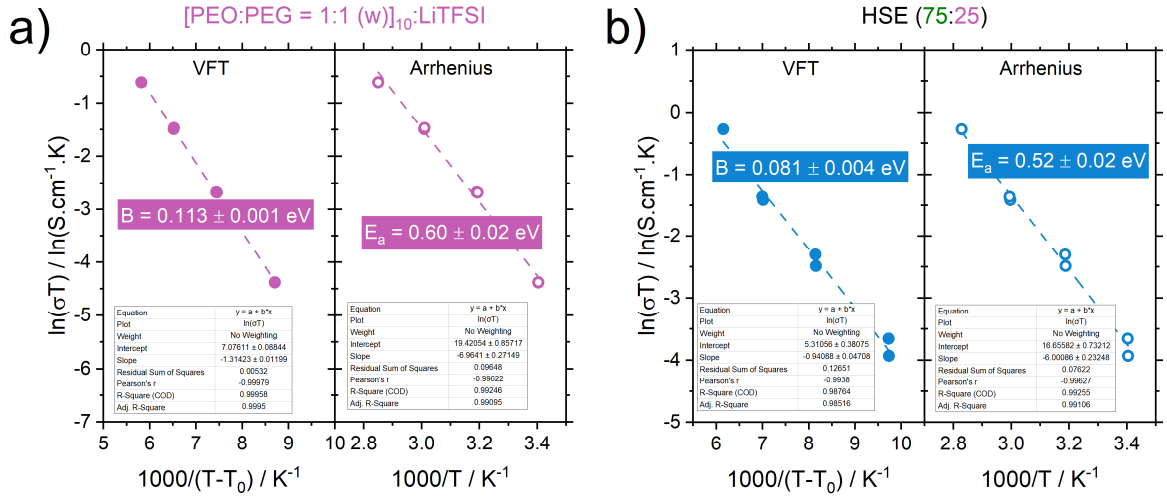

Figure S2.5 Fitting of ionic conductivity in temperature and choice of the appropriate activation mechanism (VFT versus Arrhenius) for (a) the modified organic phase [PEO:PEG = 1:1 (w)]$_{10}$:LiTFSI and (b) the associated HSE containing 75 wt.% of Li_6PS_5Cl.

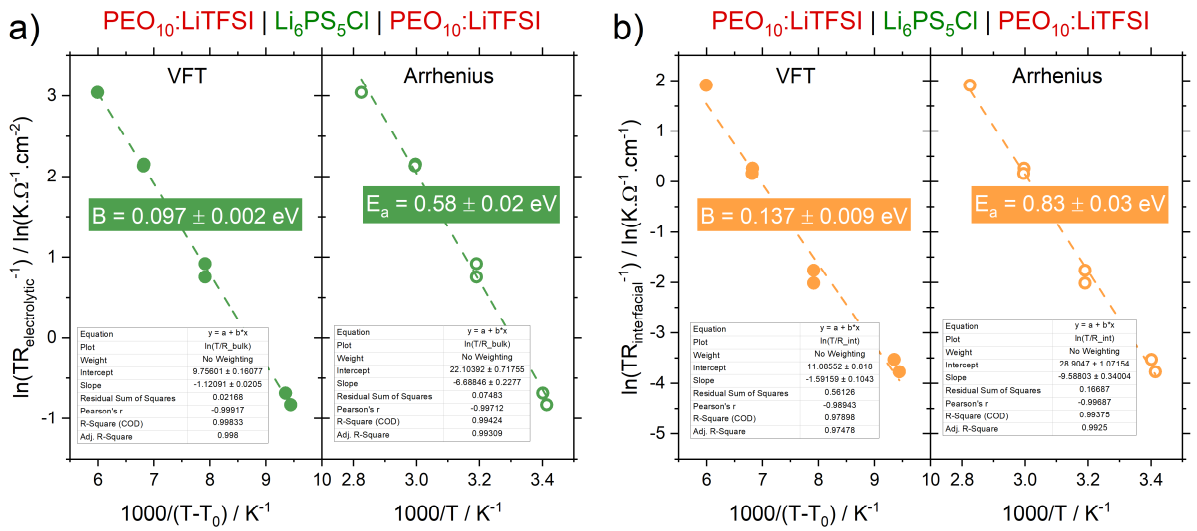

Figure S2.6 Fitting of (a) electrolytic and (b) interfacial resistances in temperature measured for the layered system PEO_{10}:LiTFSI | Li_6PS_5Cl | PEO_{10}:LiTFSI. Choice of the appropriate activation mechanism (VFT versus Arrhenius) according to highest adjusted R^2 value.

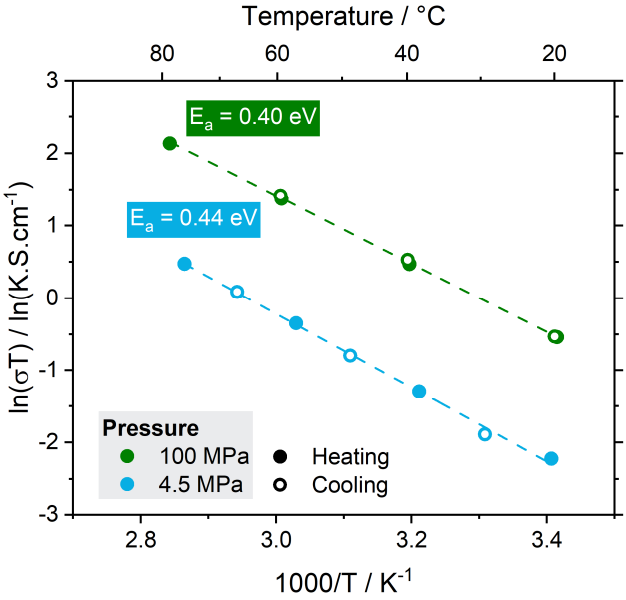

Figure S2.7 Effect of the stack pressure on pelletised Li_6PS_5Cl conductivity. Carbon electrodes were used to ensure best possible contact with pistons.

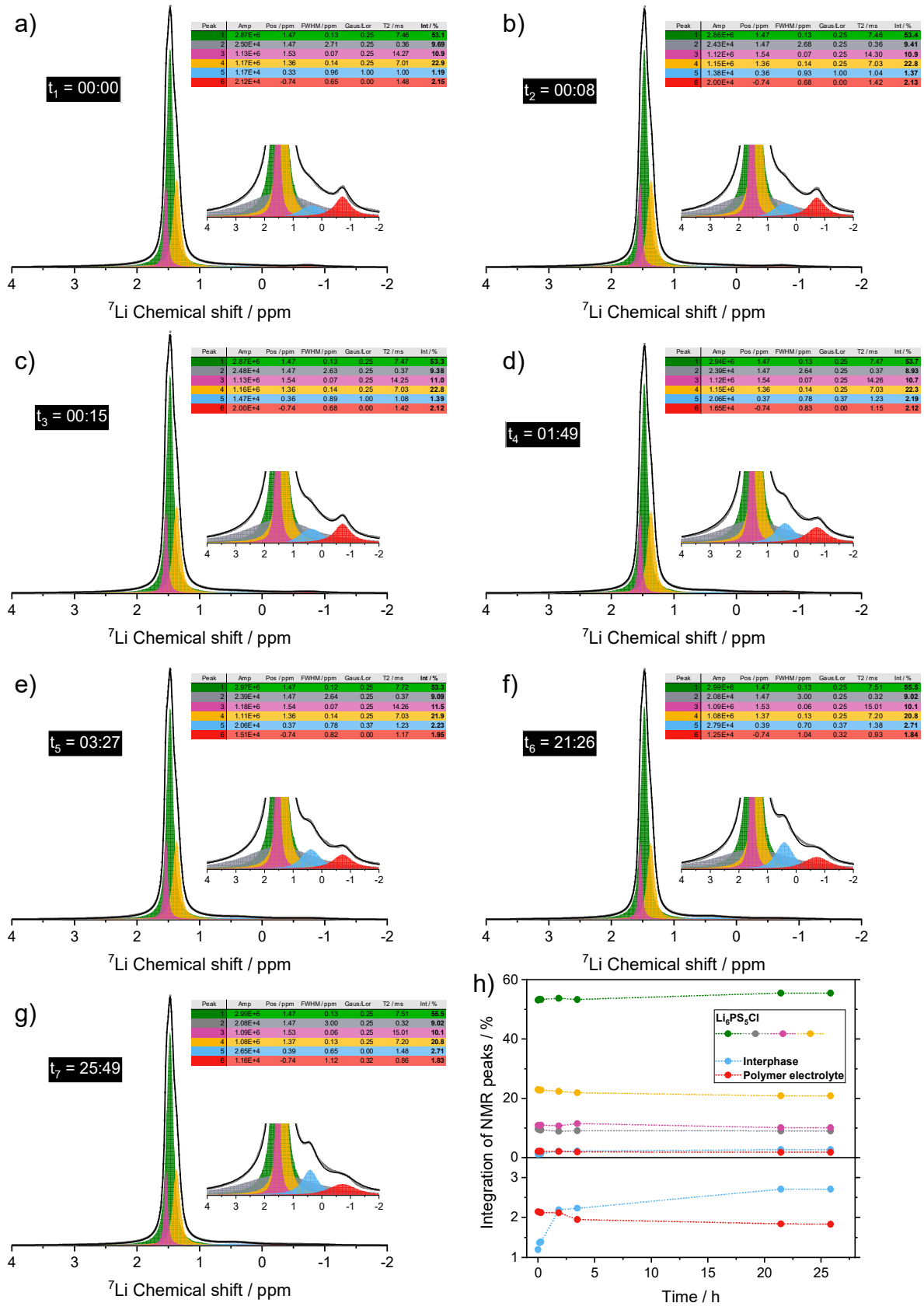

Figure S2.8 (a-g) ^{7}Li MAS NMR spectra of an HSE acquired over one day. (h) Evolution of peaks intensity over time.

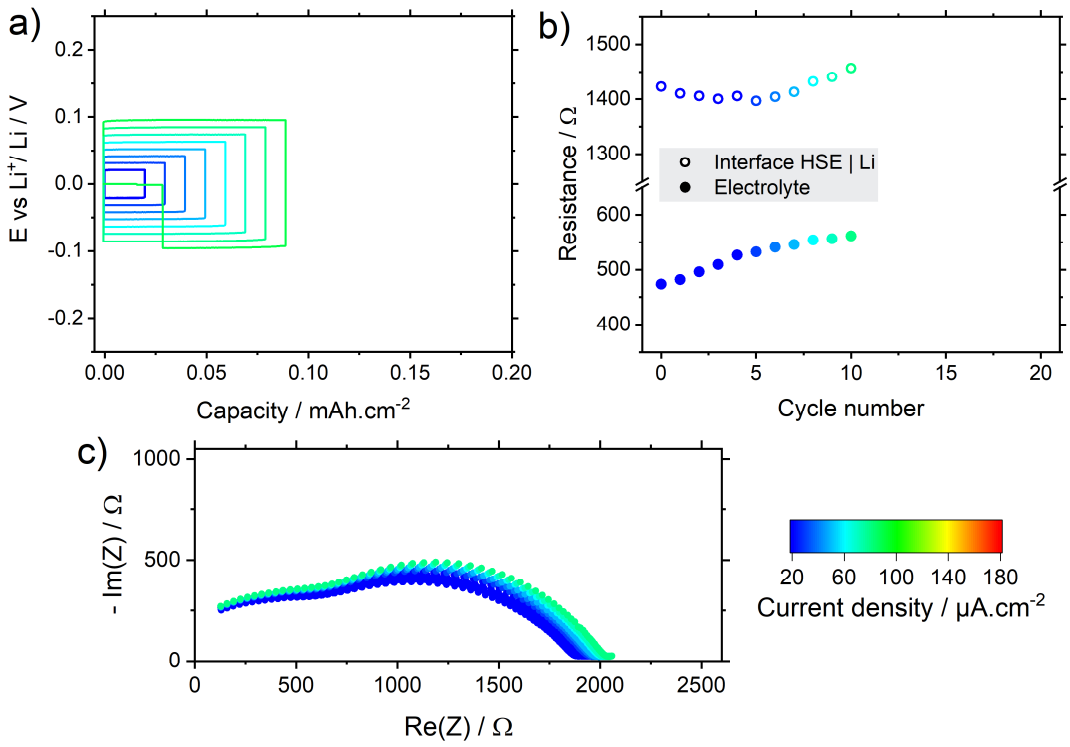

Figure S2.9 Determination of CCD of the symmetric cell with the optimised HSE based on homopolymer PEO. (a) Voltage profile according to capacity. (b) Evolution of electrolytic and interfacial resistances over cycles. (c) EIS over cycles. Colours represent the current density applied to the symmetric cell.

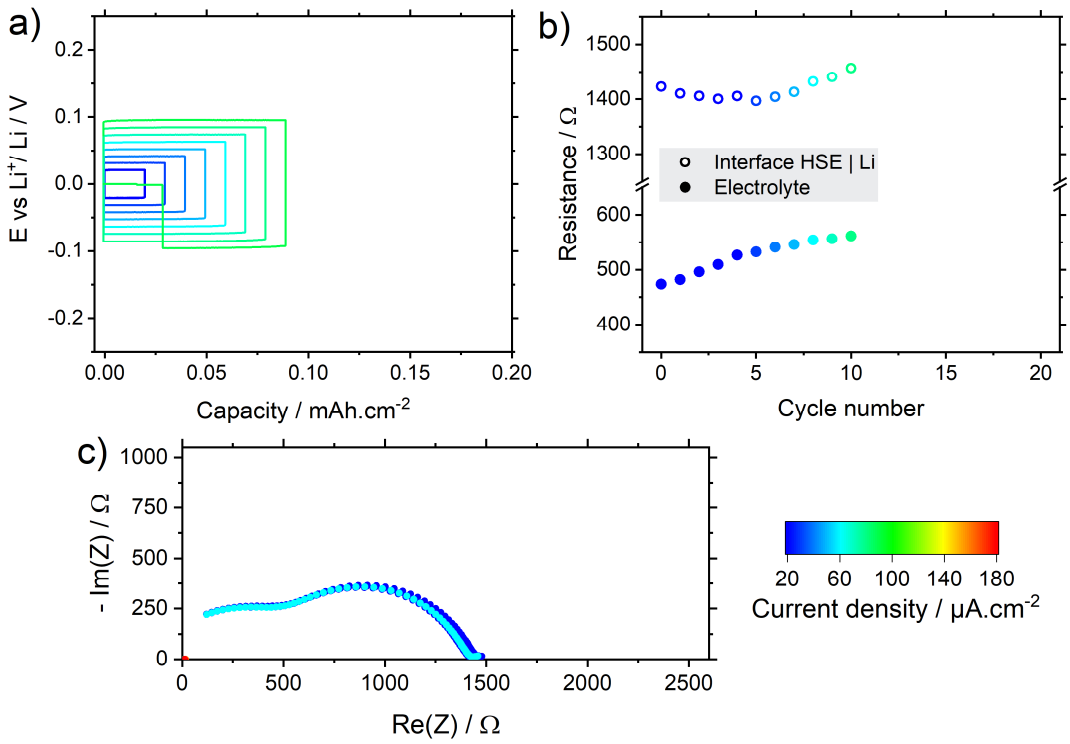

Figure S2.10 Determination of CCD of the symmetric cell with the optimised HSE based on homopolymer PEO. (a) Voltage profile according to capacity. (b) Evolution of electrolytic and interfacial resistances over cycles. (c) EIS over cycles. Colours represent the current density applied to the symmetric cell.

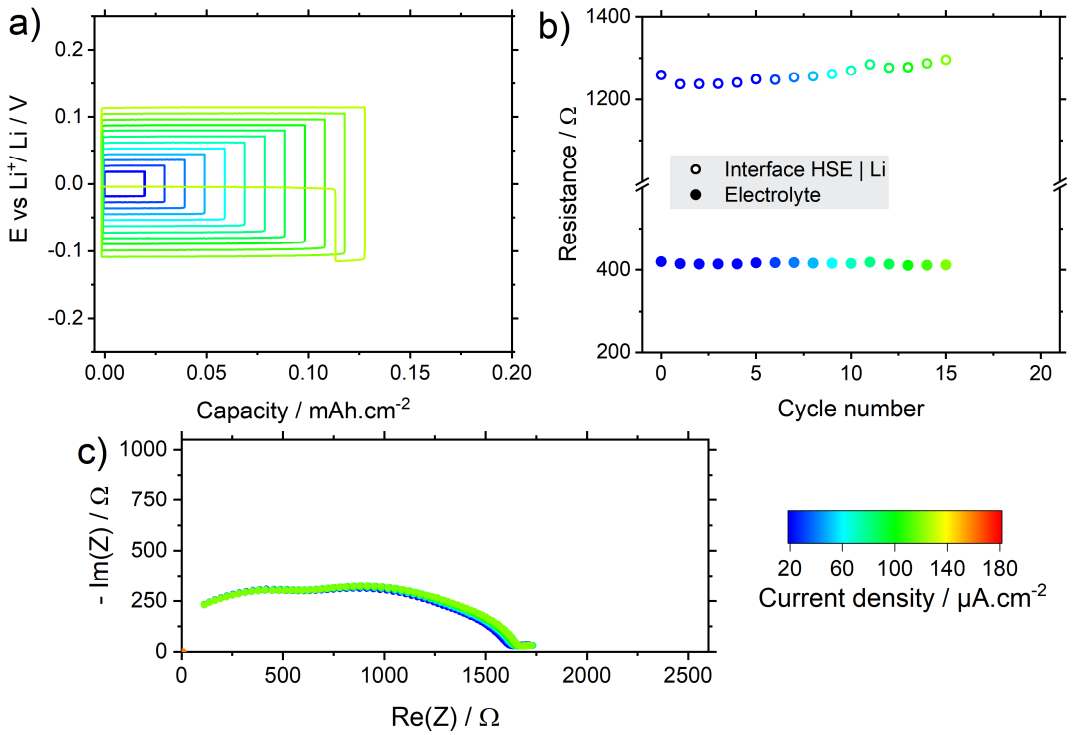

Figure S2.11 Determination of CCD of the symmetric cell with the optimised HSE based on copolymer P(EO-co-PO). (a) Voltage profile according to capacity. (b) Evolution of electrolytic and interfacial resistances over cycles. (c) EIS over cycles. Colours represent the current density applied to the symmetric cell.

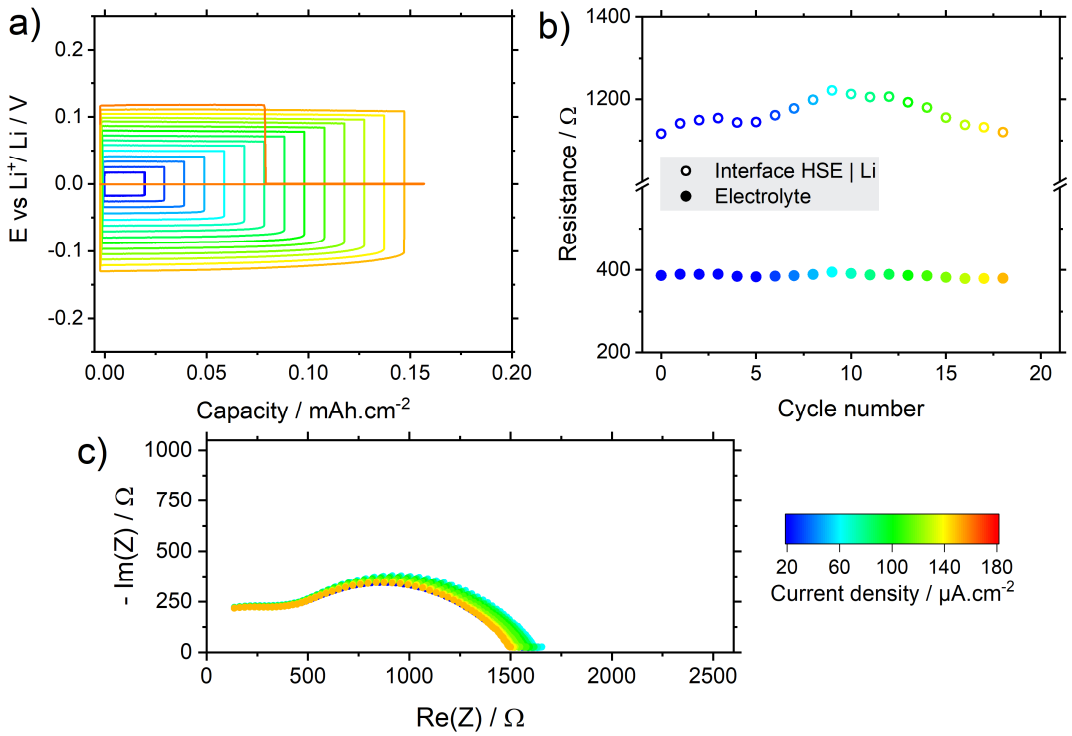

Figure S2.12 Determination of CCD of the symmetric cell with the optimised HSE based on copolymer P(EO-co-PO). (a) Voltage profile according to capacity. (b) Evolution of electrolytic and interfacial resistances over cycles. (c) EIS over cycles. Colours represent the current density applied to the symmetric cell.

S3 – Supplementary information for Chapter 3

S3.1 Materials and methods

○ Materials

The handling of all materials and all processing steps were conducted inside an argon-filled glovebox (O_2 < 0.1 ppm, H_2O < 1 ppm), unless described differently. The argyrodite solid electrolytes *n*Li_6PS_5Cl (*normal* – 1-30 µm) and *f*Li_6PS_5Cl (*fine* – 1-20 µm) were purchased from NEI Corporation. The *ultra-fine* powder (D_{50} ≈ 50 µm) was kindly provided by Ampcera. Poly(vinylidene fluoride-co-hexafluoropropylene) (PVDF-HFP) binders were obtained from Solvay (15 mol.% HFP) and kindly provided by Arkema (> 30 mol.% HFP). Ethyl acetate (99.9 % - extra dried over molecular sieves) was purchased from Thermo Scientific and used as received. Butyl butyrate (≥ 98%) and hexyl butyrate (≥ 98%) were bought from Sigma-Aldrich. Dioxygen was removed from the bottles by bubbling argon for one hour and the solvents were dried over molecular sieves (4Å) inside the glovebox. The NMC622 cathode active material ($LiNi_{0.6}Mn_{0.2}Co_{0.2}O_2$ monolithic, d ≈ 4 µm) was kindly provided by Umicore. The NMC811 AM was purchased from MSE Supplies ($LiNi_{0.82}Mn_{0.07}Co_{0.11}O_2$ monolithic, D_{50} ≈ 3 - 5 µm). Vapor grown carbon fibers (VGCF) were bought from Sigma-Aldrich and dried at 280°C under vacuum for one day. Indium foils (99.99%) were purchased from Sigma-Aldrich. Lithium metal foils (e = 80µm) were kindly provided by Blue Solutions. Aluminium (e = 12 µm) and copper (e = 10 µm) current collectors were kindly provided LRCS, Amiens. Polyethylene terephthalate (PET) silicone-coated foils (e = 19 µm) were kindly provided by Blue Solutions. Carbon paper electrodes were sourced from Papyex.

○ Water content determination

Water content in the solvents dried over molecular sieves was determined by Karl-Fischer titration (Metrohm coulometer), with three repetitions per solvent.

○ Powder X-ray diffraction

XRD analysis was conducted utilising an airtight holder fitted with a beryllium (Be) window. The diffractograms were recorded in reflection mode, employing the Bragg−Brentano geometry, and data acquisition was carried out with a Bruker D8 ADVANCE diffractometer. A copper (Cu) Kα X-ray source (λ_1 = 1.54056 Å and λ_2 = 1.54439 Å) was utilised in conjunction with a LynxEye detector for data collection.

○ Thermal analysis

Thermal stability of materials (tapes, binder, powder) was measured by thermogravimetric analysis (TGA – Mettler Toledo TGA/DSC 3+) from room temperature to 600°C, at a heating rate of 10 °C.min^{-1}. The PVDF-HFP binders were further characterised by differential scanning calorimetry (DSC – TA Instruments Q20) in the temperature range of -70 – 200°C, at a heating rate of 10 °C.min^{-1}. In all cases, samples of 10 – 20 mg were hermetically sealed in aluminum pans inside the argon-filled glovebox. A pinhole was punch on the top of the TGA pan to avoid its explosion due to gas formation.

○ Scanning electron microscopy

Powder and tapes cross-section micrographs were obtained on an FEI Magellan scanning electron microscope equipped with an Oxford Instruments energy dispersive X-ray spectroscopy (EDS) detector. EDX of the composite cathode was carried out using an acceleration voltage of 15 kV. Cross-section samples were prepared by blade cutting inside glovebox.

○ Tape casting of cathode and separator

Cathode composite powder was initially prepared by hand-grinding NMC, Li_6PS_5Cl and VGCF in agate mortar until homogenisation. Solutions of PVDF-HFP were prepared by dissolving the binder powder in the chosen solvent, under magnetic stirring and with heating to 60°C when needed. The cathode (resp. separator) slurry was prepared by placing the composite powder (resp. Li_6PS_5Cl powder) and the binder solution in stainless steel jar with two balls of 0.5 g, hermetically closed. The mixing was done by high-energy ball-milling for 10 min with the SPEX SamplePrep machine. The obtained homogeneous slurry was then hand-coated on an aluminium current collector (resp. PET silicone-coated foil) by the doctor blade technique with a gap of 400 µm (resp. 200 µm). The tape were dried overnight at 100°C under vacuum in a Büchi. When specified, the tapes were coated using an automatic film coater (TFC 200H, Automatic Research) placed inside the glovebox, at a speed of 20 mm.s^{-1}. The tapes were dried first at 100°C on the coater for 1h, then under vacuum in the glovebox antechamber overnight.

○ Solid electrolyte stability with solvents

We exposed the three types of Li_6PS_5Cl to the processing solvent by mixing them at equal mass ratio via high-energy ball milling for 2 x 5min, to mimic the previously detailed procedure of slurry preparation. The resulting suspension was coated and dried in the same way and then the powder was collected for further characterization.

○ Conductivity measurement

For pellets, Li_6PS_5Cl powder (pristine or solvent-exposed) was densified in an 8 mm die-set at 400 MPa for 5 min. The obtained pellet was then placed in the dedicated two-electrode cell (**Figure S3.1a**) with carbon paper discs and closed at 100 MPa.

For tape separators, they were cut to 2x2 cm^2 squares and packaged in pouch bags, sealed under vacuum. Densification was performed in the isostatic press at 400 MPa for 5 min. The tapes were then peeled off the PET substrate and positioned between two carbon paper electrodes with respective areas of 1x1 and 1.5x1.5 cm^2. The stack was sealed under vacuum with metallic tabs for electrical connection. A final densification was performed at 100 MPa in the isostatic press, to ensure proper contact with the electrodes. Pouch cell was placed under the frame at various pressures (0.2, 2 and 5 MPa).

EIS was performed at room temperature in the frequency range of 35 MHz – 1 Hz with a voltage amplitude of 50 mV, using an MTZ impedance analyser (BioLogic). Conductivities were calculated with the following equation:

$$\sigma_{ionic} = \frac{e}{S \cdot R_{electrolyte}}$$ **Equation S3.1**

where e is the pellet / membrane thickness, S the cell section and $R_{electrolyte}$ the resistance for ionic transport across the pellet. Resistance values were obtained by fitting the EIS data with the following model using Z-view software (Scribner):

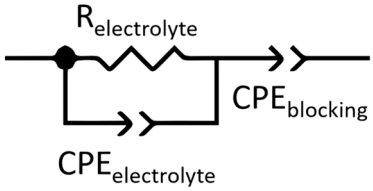

Scheme S3.1

with $CPE_{electrolyte}$ the capacitive contribution of the pellet and $CPE_{blocking}$ describing the capacitive response against blocking electrodes at low frequency.

Electronic conductivity was measured at 25°C on the identical cells using the DC polarization technique by imposing a constant voltage of 0.25 V for 1 hour. Resulting current was averaged over the last 300 seconds.

○ Battery assembly and electrochemical testing

Battery assembly and high-pressure electrochemical tests were carried out in dedicated two electrode cells (**Figure S3.1a**). The assembly followed a first step of cold-pressing 30 mg of *n*Li_6PS_5Cl (e ≈ 400 µm) in the cell body at 100 MPa for few seconds, thanks to a manual hydraulic press. Then, a disc of cathode was placed on one side and the appropriate amount of counter electrode powder ($Li_{0.5}In$: *n*Li_6PS_5Cl = 60:40 (w)) was homogeneously spread on the other side. Lithium-indium composite was prepared by laminating Li and In foils until the resulting alloy became brittle. The obtained alloy was mixed with *n*Li_6PS_5Cl in an agate mortar, until a homogeneous powder was obtained. The battery stack was finally densified under 400 MPa for 5 min. The closure was carried out by applying 2.3 N.m to each screw to obtain an internal pressure of 100 MPa. All assembly steps were performed in an argon-filled glovebox to prevent any potential contamination from moisture.

For self-standing batteries, a disc of cathode (d = 8 mm) was pressed against a disc of separator (d = 11 mm), between stainless steel pistons at 400 MPa under a hydraulic press. The alloy anode $Li_{0.5}In$ was prepared by pressing at 50 MPa a disc of lithium metal against a disc of indium with a 1:2 molar ratio, onto a 10 mm diameter copper current collector. The anode was then attached to bilayer of separator and cathode, and the stack was packaged in a pouch bag with metallic tabs. When specified, the pouch cell was further densified in the isostatic press.

Galvanostatic cycling was performed in the voltage range of 2.1 – 3.6(5) V vs LiIn/In (2.72 – 4.22 (4.27) V vs Li^+/Li). Details of C-rates are indicated in the figures and were calculated according to theoretical capacity Q_{NMC622} = 276.5 $mAh.g^{-1}$ and Q_{NMC811} = 275.2 $mAh.g^{-1}$. Measurements were conducted on a BCS potentiostat/galvanostat (BioLogic) controlled with BT-Lab® software. EIS was acquired after 4 hours of rest at the end of the first charge, between 1 MHz and 10 mHz at 25°C on a VMP3 potentiostat/galvanostat (BioLogic).

S3.2 Supplementary figures

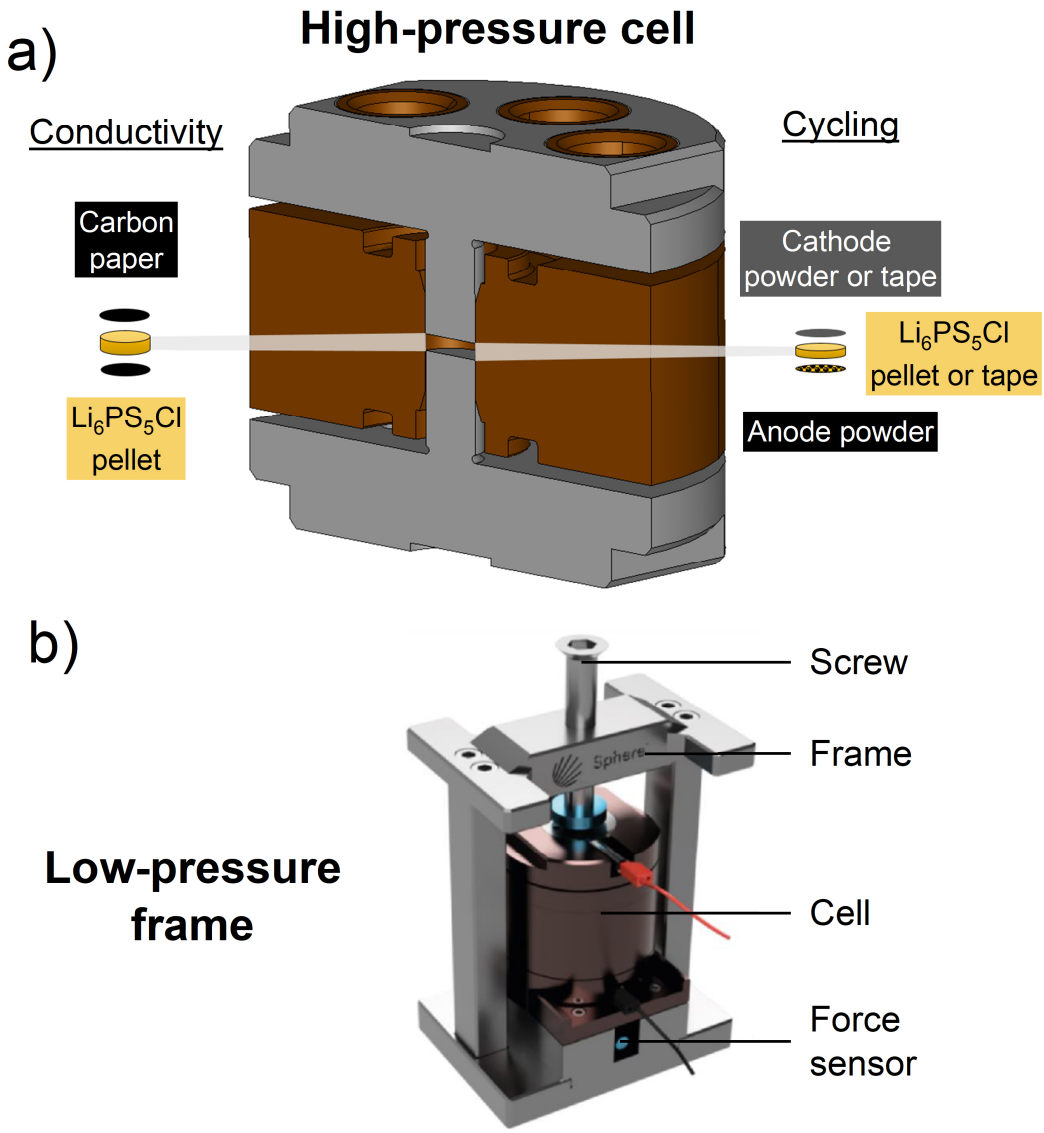

Figure S3.1 (a) Schematics of the two-electrode cell for high-pressure and airtight cell cycling and conductivity measurement. (b) Schematic of the fixed-gap cell design used for low pressure cycling.

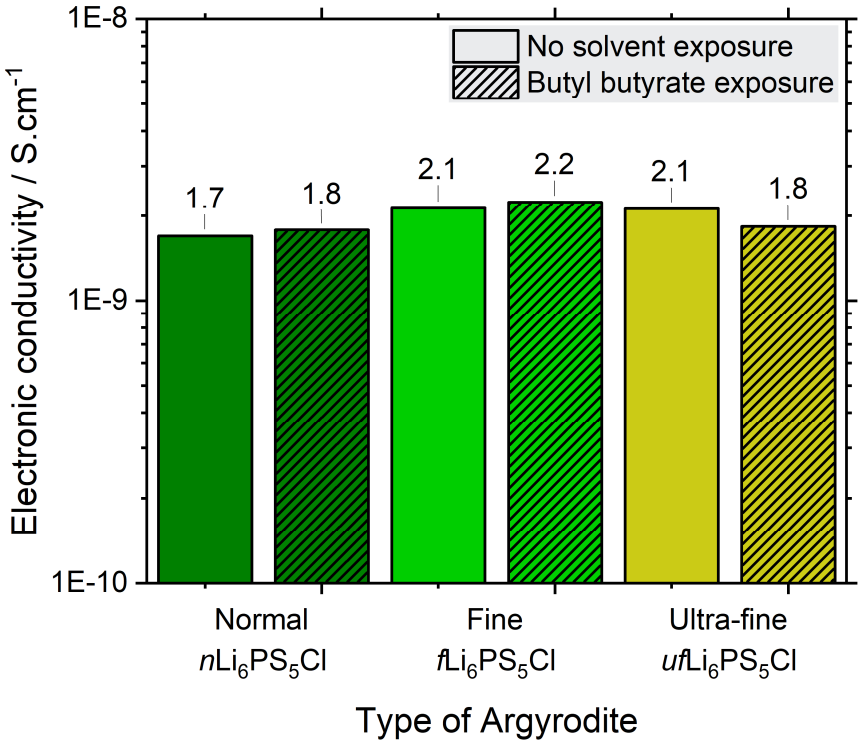

Figure S3.2 Effect of butyl butyrate exposure on Li_6PS_5Cl electronic conductivity at room temperature. Argyrodite powders are of different sizes and from various suppliers (NEI and Ampcera).

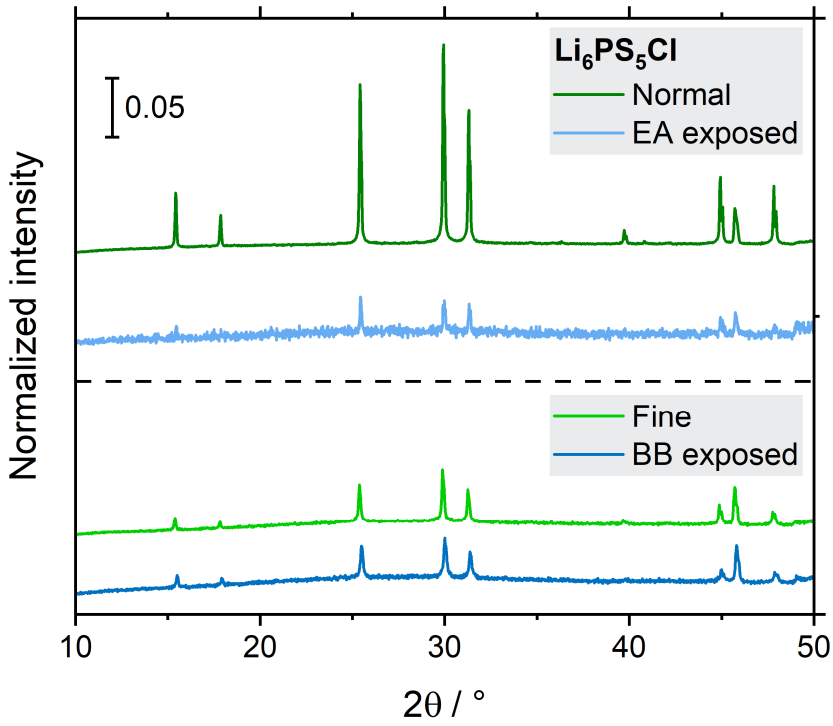

Figure S3.3 X-ray diffractograms of Li_6PS_5Cl powder at pristine state (green) and after a solvent exposure of 20min during ball milling followed by drying steps at 100°C and under vacuum (blue). EA and BB stands for ethyl acetate and butyl butyrate respectively.

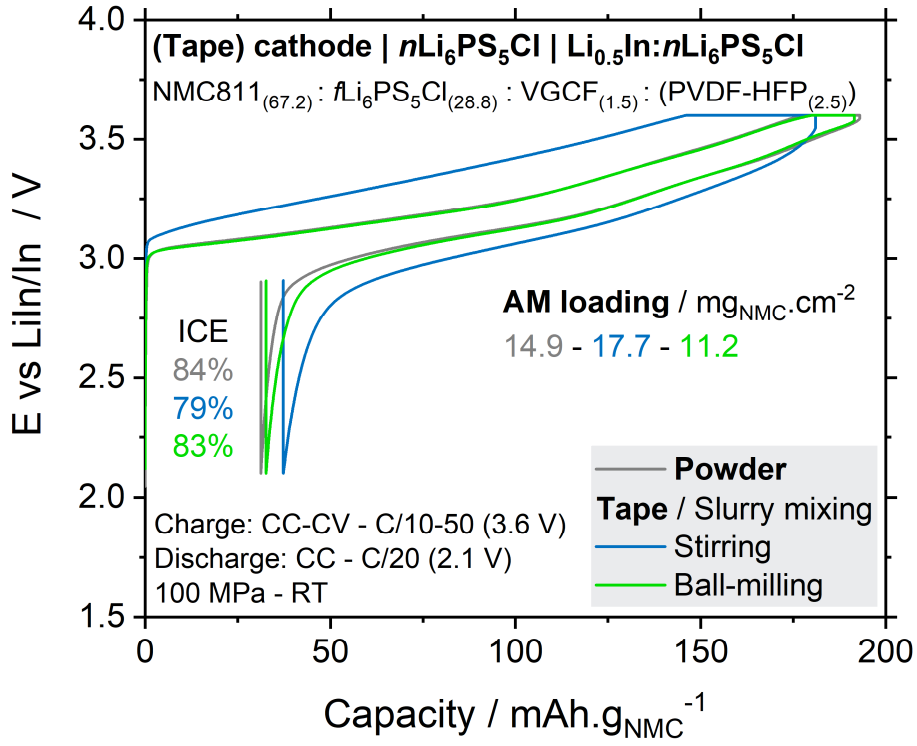

Figure S3.4 First cycle voltage profile and initial coulombic efficiency (ICE) of tape cathode-based SSBs for comparison of the chosen strategy for slurry mixing.

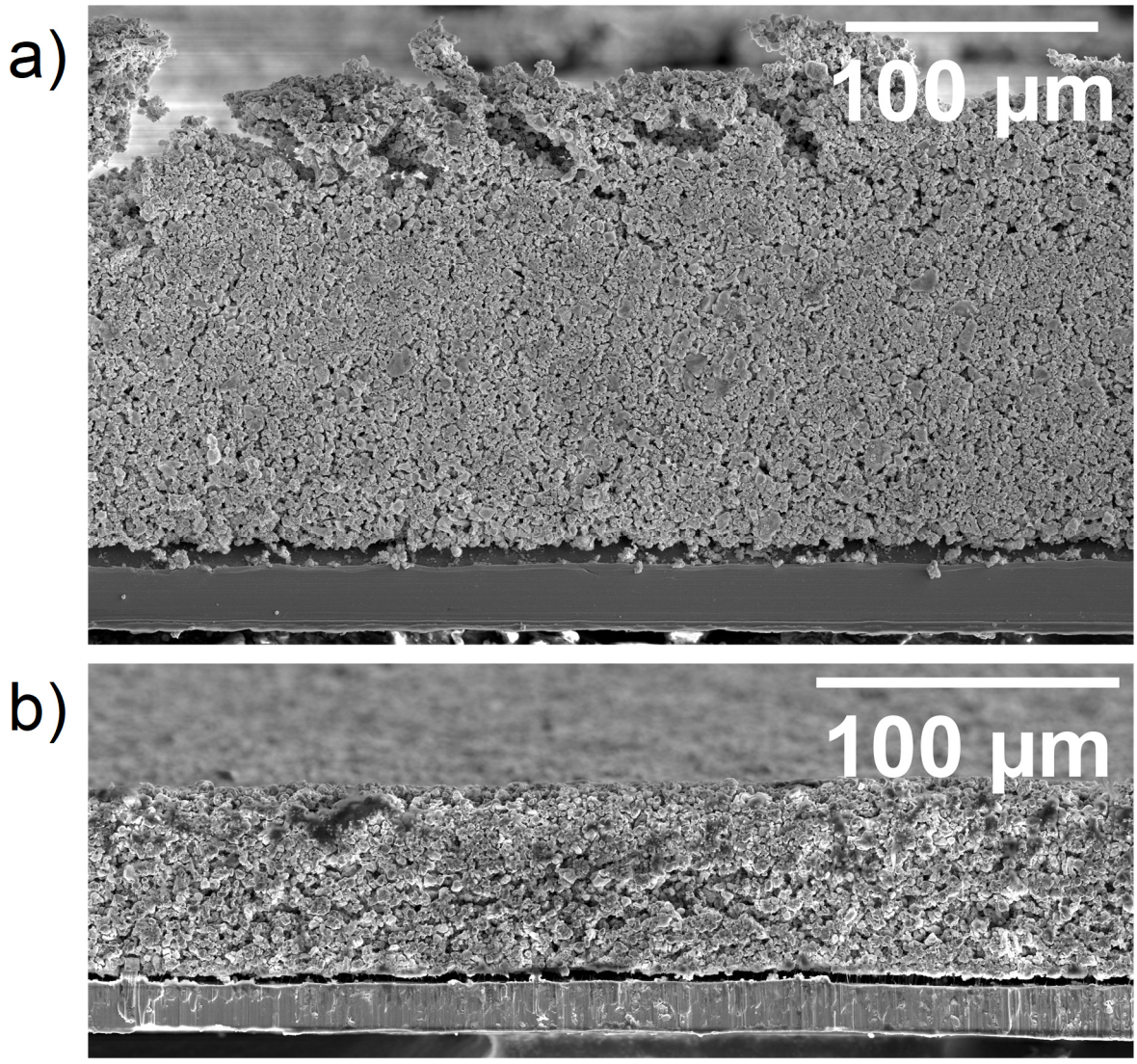

Figure S3.5 SEM cross-section images of tape cathode after drying. (a) The composition of cathode is NMC811 : *f*Li_6PS_5Cl : VGCF : **PVDF-HFP** = 67.8 : 29.1 : 1.5 : **1.5** (w). (b) The composition of cathode is NMC811 : ***uf*Li$_6$PS$_5$Cl** : VGCF : PVDF-HFP = 67.2 : 28.8 : 1.5 : 2.5 (w).

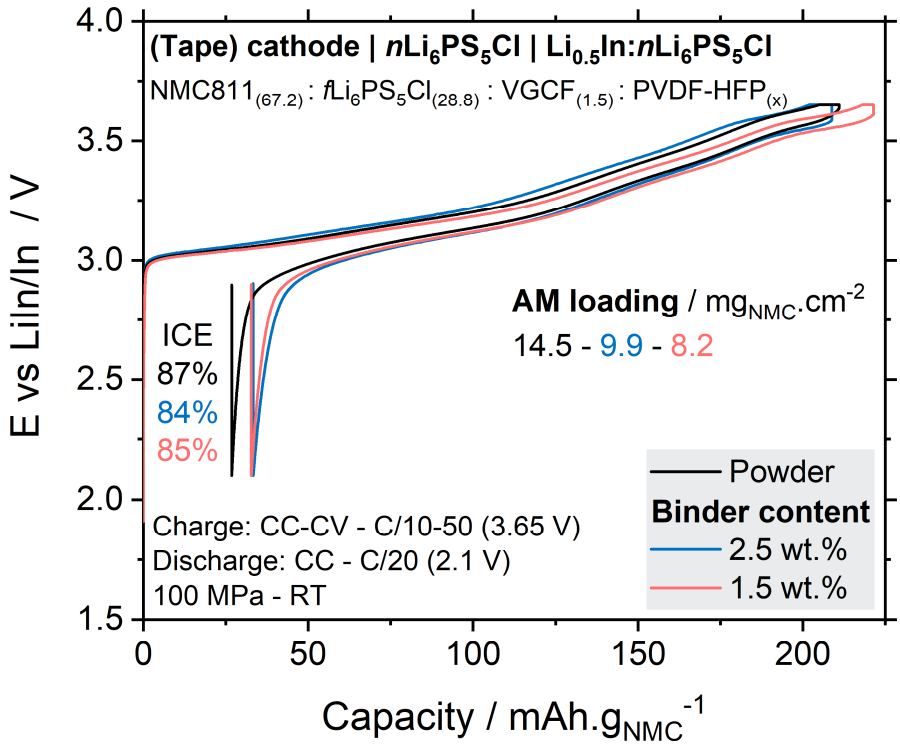

Figure S3.6 First cycle voltage profile and initial coulombic efficiency (ICE) of tape cathode-based SSBs for comparison of binder content.

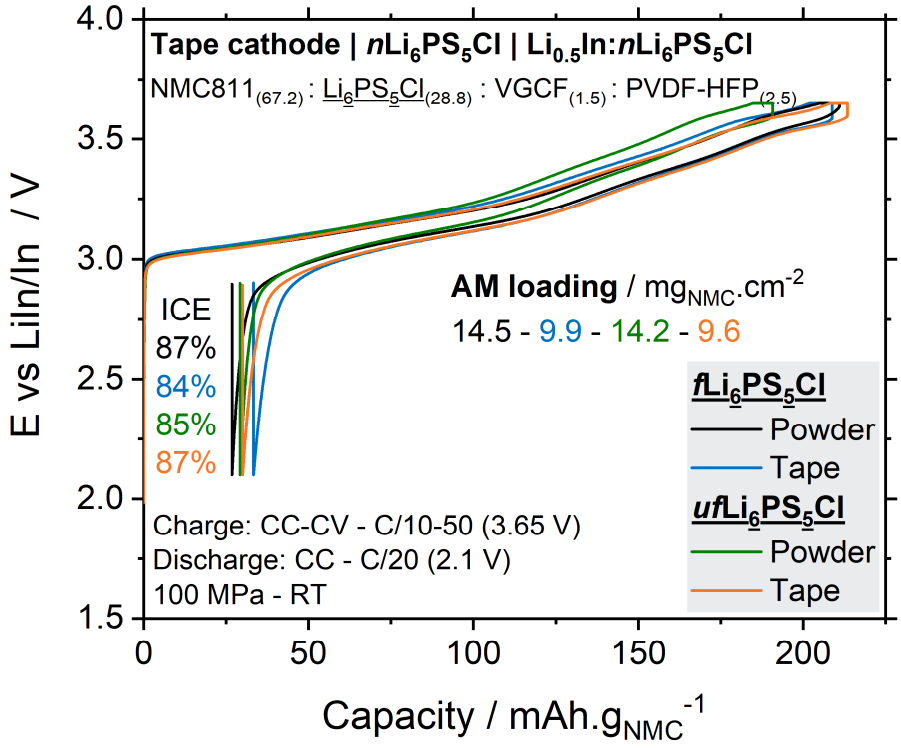

Figure S3.7 First cycle voltage profile and initial coulombic efficiency (ICE) of tape cathode-based SSBs for comparison of SE particle size in the cathode composite, both as powder and tape.

Li_6PS_5Cl: 95 wt.%
$PVDF_{85}$-HFP_{15}: 5 wt.%

Figure S3.8 Image of separator peeled off its PET substrate, average thickness of 180 µm.

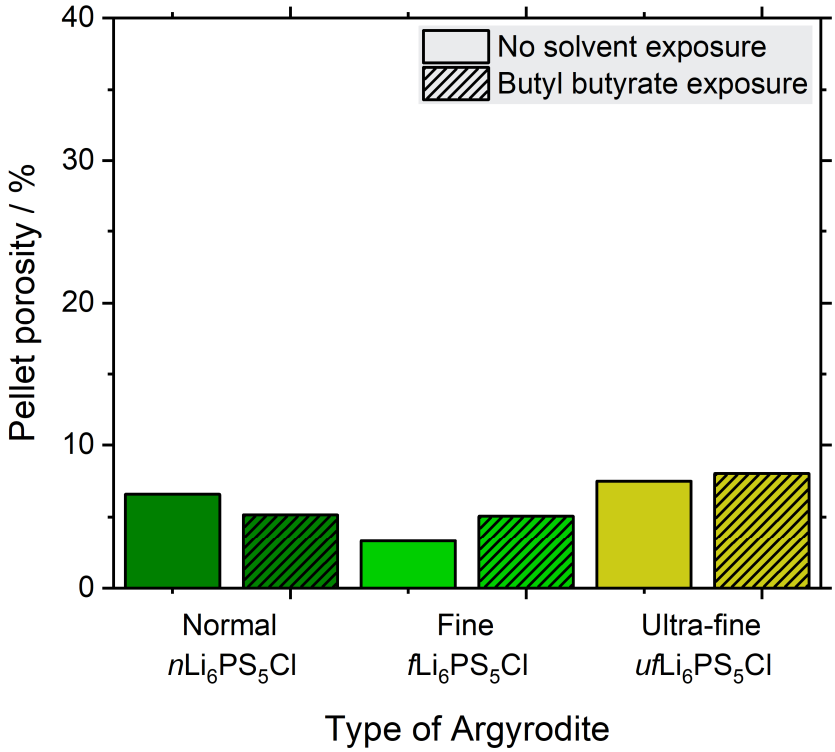

Figure S3.9 Calculated porosity of argyrodite pellets used for conductivity measurements. Porosity is estimated from measured mass and thickness.

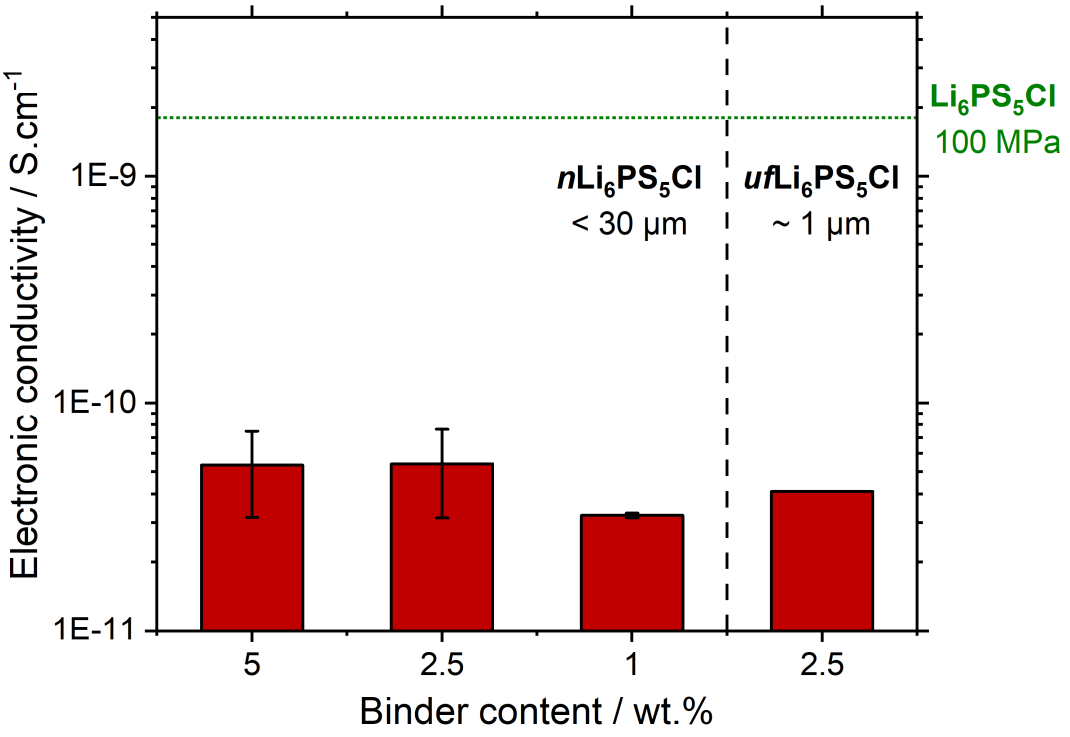

Figure S3.10 Evolution of electronic conductivity of Li_6PS_5Cl : PVDF-HFP tape separators according to binder content and SE particle size, measured at 5 MPa and 25°C. Two cells were assembled per formulation.

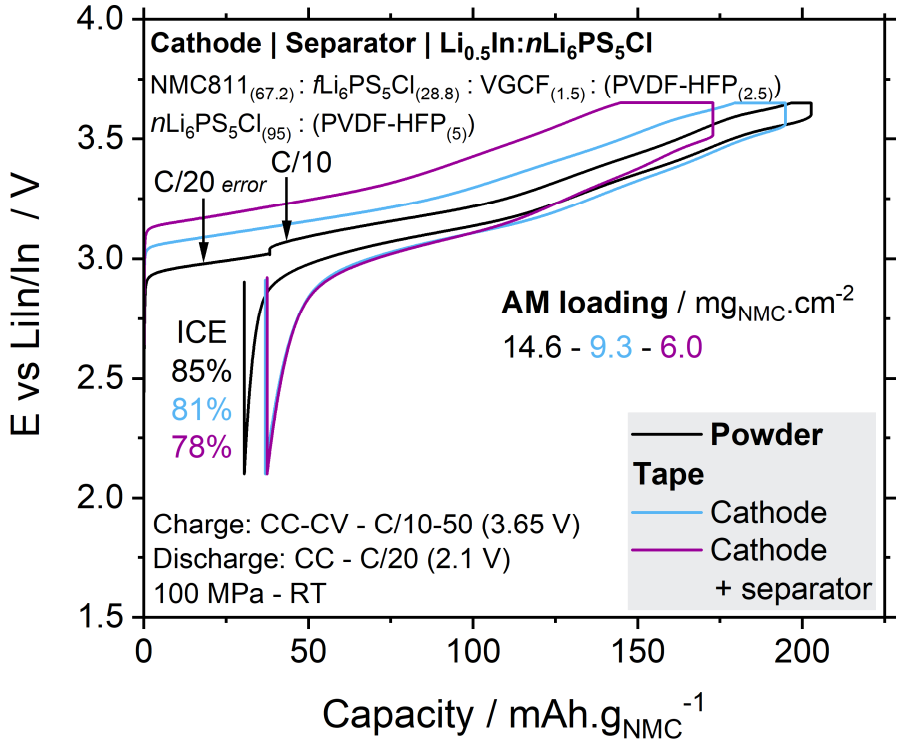

Figure S3.11 First cycle voltage profile and initial coulombic efficiency (ICE) of tape cathode-based SSBs for assessing the influence of a tape separator (purple) replacing the pure SE layer (blue), compared to the binder-free reference system (black).

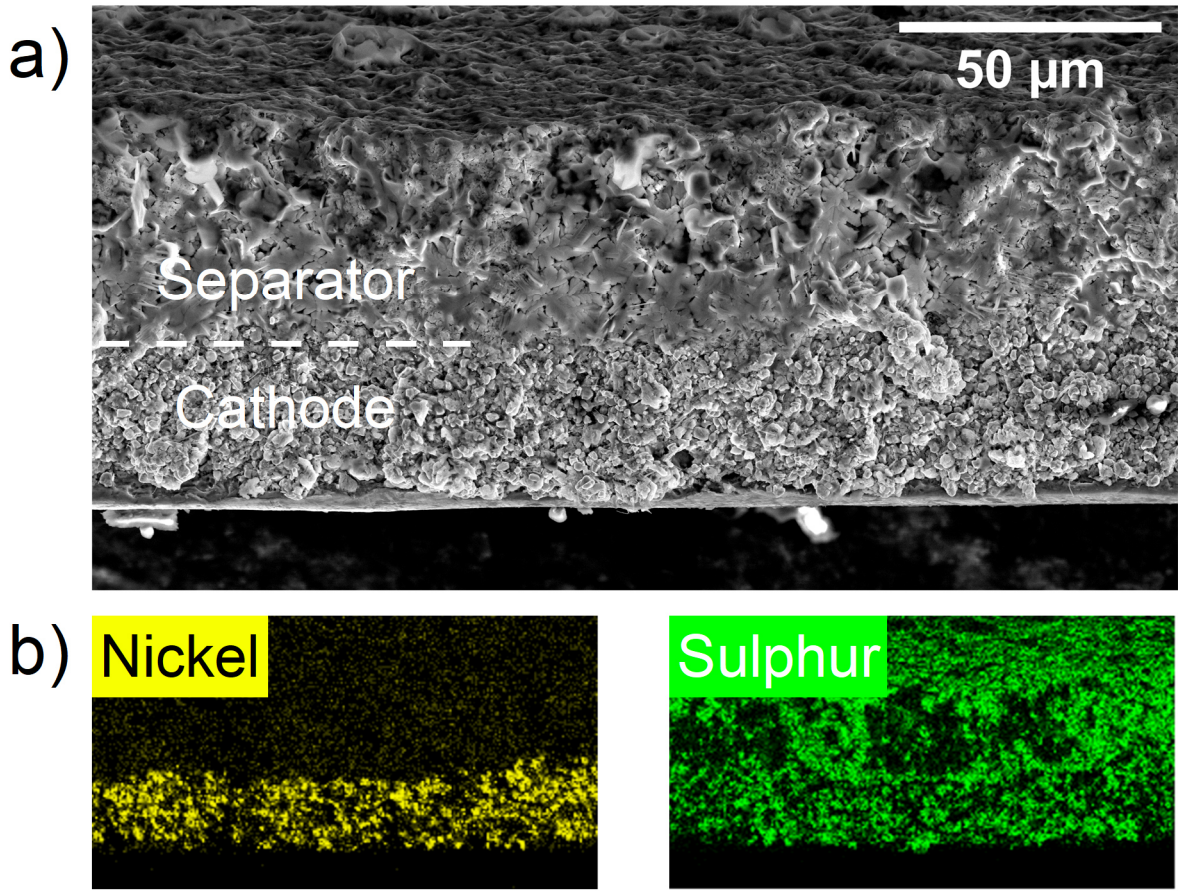

Figure S3.12 (a) SEM cross-section image of tape cathode | tape separator bilayer after densification at 400 MPa in isostatic press. The composition of cathode is NMC811 : *uf*Li_6PS_5Cl : VGCF : PVDF-HFP = 67.2 : 28.8 : 1.5 : 2.5 (w) and *uf*Li_6PS_5Cl : PVDF-HFP = 97.5 : 2.5 (w) for the separator. (b) Energy-dispersive X-ray spectroscopy maps for nickel (yellow) and sulphur (green).

References

1. Energy density. *Wikipedia* (2023). at <https://en.wikipedia.org/w/index.php?title=Energy_density&oldid=1175711730>
2. Calvin, K., Dasgupta, D., Krinner, G., Mukherji, A., Thorne, P. W., Trisos, C., Romero, J., Aldunce, P., Barrett, K., Blanco, G., Cheung, W. W. L., Connors, S., Denton, F., Diongue-Niang, A., Dodman, D., Garschagen, M., Geden, O., Hayward, B., Jones, C., Jotzo, F., Krug, T., Lasco, R., Lee, Y.-Y., Masson-Delmotte, V., Meinshausen, M., Mintenbeck, K., Mokssit, A., Otto, F. E. L., Pathak, M., Pirani, A., Poloczanska, E., Pörtner, H.-O., Revi, A., Roberts, D. C., Roy, J., Ruane, A. C., Skea, J., Shukla, P. R., Slade, R., Slangen, A., Sokona, Y., Sörensson, A. A., Tignor, M., van Vuuren, D., Wei, Y.-M., Winkler, H., Zhai, P., Zommers, Z., Hourcade, J.-C., Johnson, F. X., Pachauri, S., Simpson, N. P., Singh, C., Thomas, A., Totin, E., Arias, P., Bustamante, M., Elgizouli, I., Flato, G., Howden, M., Méndez-Vallejo, C., Pereira, J. J., Pichs-Madruga, R., Rose, S. K., Saheb, Y., Sánchez Rodríguez, R., Ürge-Vorsatz, D., Xiao, C., Yassaa, N., Alegría, A., Armour, K., Bednar-Friedl, B., Blok, K., Cissé, G., Dentener, F., Eriksen, S., Fischer, E., Garner, G., Guivarch, C., Haasnoot, M., Hansen, G., Hauser, M., Hawkins, E., Hermans, T., Kopp, R., Leprince-Ringuet, N., Lewis, J., Ley, D., Ludden, C., Niamir, L., Nicholls, Z., Some, S., Szopa, S., Trewin, B., van der Wijst, K.-I., Winter, G., Witting, M., Birt, A., Ha, M., Romero, J., Kim, J., Haites, E. F., Jung, Y., Stavins, R., Birt, A., Ha, M., Orendain, D. J. A., Ignon, L., Park, S., Park, Y., Reisinger, A., Cammaramo, D., Fischlin, A., Fuglestvedt, J. S., Hansen, G., Ludden, C., Masson-Delmotte, V., Matthews, J. B. R., Mintenbeck, K., Pirani, A., Poloczanska, E., Leprince-Ringuet, N. & Péan, C. *IPCC, 2023: Climate Change 2023: Synthesis Report. Contribution of Working Groups I, II and III to the Sixth Assessment Report of the Intergovernmental Panel on Climate Change [Core Writing Team, H. Lee and J. Romero (eds.)]. IPCC, Geneva, Switzerland.* (Intergovernmental Panel on Climate Change (IPCC), 2023). doi:10.59327/IPCC/AR6-9789291691647
3. Misconceptions about electric vehicles | Carbone 4. at <https://carbone4.com/en/analysis-faq-electric-vehicles>
4. Knobloch, F., Hanssen, S. V., Lam, A., Pollitt, H., Salas, P., Chewpreecha, U., Huijbregts, M. A. J. & Mercure, J.-F. Net emission reductions from electric cars and heat pumps in 59 world regions over time. *Nat Sustain* **3,** 437–447 (2020).
5. Trends in batteries – Global EV Outlook 2023 – Analysis. *IEA* at <https://www.iea.org/reports/global-ev-outlook-2023/trends-in-batteries>
6. Alessandro Volta - La pile électrique | BNF ESSENTIELS. at <https://gallica.bnf.fr/essentiels/node/5584>
7. Daniell cell. *Wikipedia* (2023). at <https://en.wikipedia.org/w/index.php?title=Daniell_cell&oldid=1165854764>
8. Lead/acid batteries. at <https://www.doitpoms.ac.uk/tlplib/batteries/batteries_lead_acid.php>
9. Whittingham, M. S. Electrical Energy Storage and Intercalation Chemistry. *Science* **192,** 1126–1127 (1976).
10. Whittingham, M. S. The Role of Ternary Phases in Cathode Reactions. *J. Electrochem. Soc.* **123,** 315–320 (1976).
11. Whittingham, M. S. Chemistry of intercalation compounds: Metal guests in chalcogenide hosts. *Progress in Solid State Chemistry* **12,** 41–99 (1978).

12. Winter, M., Barnett, B. & Xu, K. Before Li Ion Batteries. *Chem. Rev.* **118,** 11433–11456 (2018).
13. Mizushima, K., Jones, P. C., Wiseman, P. J. & Goodenough, J. B. LixCoO2 (0<x<-1): A new cathode material for batteries of high energy density. *Materials Research Bulletin* **15,** 783–789 (1980).
14. Armand, M. B. in *Materials for Advanced Batteries* (eds. Murphy, D. W., Broadhead, J. & Steele, B. C. H.) 145–161 (Springer US, 1980). doi:10.1007/978-1-4684-3851-2_7
15. Lazzari, M. & Scrosati, B. A Cyclable Lithium Organic Electrolyte Cell Based on Two Intercalation Electrodes. *J. Electrochem. Soc.* **127,** 773 (1980).
16. Yoshino, A. The Birth of the Lithium-Ion Battery. *Angewandte Chemie International Edition* **51,** 5798–5800 (2012).
17. The Nobel Prize in Chemistry 2019. *NobelPrize.org* at <https://www.nobelprize.org/prizes/chemistry/2019/popular-information/>
18. Fujimoto, M., Yoshinaga, N., Ueno, K., Furukawa, N., Nohma, T. & Takahashi, M. Lithium secondary battery. (1993). at <https://patents.google.com/patent/EP0541889A1/en>
19. Fong, R., Sacken, U. von & Dahn, J. R. Studies of Lithium Intercalation into Carbons Using Nonaqueous Electrochemical Cells. *J. Electrochem. Soc.* **137,** 2009 (1990).
20. International Energy Agency. *Global EV Outlook 2023: Catching up with Climate Ambitions*. (OECD, 2023). doi:10.1787/cbe724e8-en
21. Noh, H.-J., Youn, S., Yoon, C. S. & Sun, Y.-K. Comparison of the structural and electrochemical properties of layered Li[NixCoyMnz]O2 (x = 1/3, 0.5, 0.6, 0.7, 0.8 and 0.85) cathode material for lithium-ion batteries. *Journal of Power Sources* **233,** 121–130 (2013).
22. Thackeray, M. M., David, W. I. F., Bruce, P. G. & Goodenough, J. B. Lithium insertion into manganese spinels. *Materials Research Bulletin* **18,** 461–472 (1983).
23. Padhi, A. K., Nanjundaswamy, K. S. & Goodenough, J. B. Phospho-olivines as Positive-Electrode Materials for Rechargeable Lithium Batteries. *J. Electrochem. Soc.* **144,** 1188 (1997).
24. Graetz, J., Ahn, C. C., Yazami, R. & Fultz, B. Highly Reversible Lithium Storage in Nanostructured Silicon. *Electrochem. Solid-State Lett.* **6,** A194 (2003).
25. Besenhard, J. O., Yang, J. & Winter, M. Will advanced lithium-alloy anodes have a chance in lithium-ion batteries? *Journal of Power Sources* **68,** 87–90 (1997).
26. Hess, S., Wohlfahrt-Mehrens, M. & Wachtler, M. Flammability of Li-Ion Battery Electrolytes: Flash Point and Self-Extinguishing Time Measurements. *J. Electrochem. Soc.* **162,** A3084–A3097 (2015).
27. Li, Q., Yang, Y., Yu, X. & Li, H. A 700 W·h·kg−1 Rechargeable Pouch Type Lithium Battery. *Chinese Phys. Lett.* **40,** 048201 (2023).
28. Janek, J. & Zeier, W. G. A solid future for battery development. *Nat Energy* **1,** 16141 (2016).
29. Bachman, J. C., Muy, S., Grimaud, A., Chang, H.-H., Pour, N., Lux, S. F., Paschos, O., Maglia, F., Lupart, S., Lamp, P., Giordano, L. & Shao-Horn, Y. Inorganic Solid-State Electrolytes for Lithium Batteries: Mechanisms and Properties Governing Ion Conduction. *Chem. Rev.* **116,** 140–162 (2016).
30. Kato, Y., Hori, S., Saito, T., Suzuki, K., Hirayama, M., Mitsui, A., Yonemura, M., Iba, H. & Kanno, R. High-power all-solid-state batteries using sulfide superionic conductors. *Nat Energy* **1,** 16030 (2016).

31. Pang, M.-C., Wei, Y., Wang, H., Marinescu, M., Yan, Y. & Offer, G. J. Large-Format Bipolar and Parallel Solid-State Lithium-Metal Cell Stacks: A Thermally Coupled Model-Based Comparative Study. *J. Electrochem. Soc.* **167,** 160555 (2021).
32. Lewis, J. A., Tippens, J., Cortes, F. J. Q. & McDowell, M. T. Chemo-Mechanical Challenges in Solid-State Batteries. *Trends in Chemistry* **1,** 845–857 (2019).
33. Kasemchainan, J., Zekoll, S., Spencer Jolly, D., Ning, Z., Hartley, G. O., Marrow, J. & Bruce, P. G. Critical stripping current leads to dendrite formation on plating in lithium anode solid electrolyte cells. *Nat. Mater.* **18,** 1105–1111 (2019).
34. Lewis, J. A., Cortes, F. J. Q., Liu, Y., Miers, J. C., Verma, A., Vishnugopi, B. S., Tippens, J., Prakash, D., Marchese, T. S., Han, S. Y., Lee, C., Shetty, P. P., Lee, H.-W., Shevchenko, P., De Carlo, F., Saldana, C., Mukherjee, P. P. & McDowell, M. T. Linking void and interphase evolution to electrochemistry in solid-state batteries using operando X-ray tomography. *Nat. Mater.* **20,** 503–510 (2021).
35. Cheng, E. J., Sharafi, A. & Sakamoto, J. Intergranular Li metal propagation through polycrystalline Li6.25Al0.25La3Zr2O12 ceramic electrolyte. *Electrochimica Acta* **223,** 85–91 (2017).
36. Porz, L., Swamy, T., Sheldon, B. W., Rettenwander, D., Frömling, T., Thaman, H. L., Berendts, S., Uecker, R., Carter, W. C. & Chiang, Y.-M. Mechanism of Lithium Metal Penetration through Inorganic Solid Electrolytes. *Advanced Energy Materials* **7,** 1701003 (2017).
37. Rosso, M., Brissot, C., Teyssot, A., Dollé, M., Sannier, L., Tarascon, J.-M., Bouchet, R. & Lascaud, S. Dendrite short-circuit and fuse effect on Li/polymer/Li cells. *Electrochimica Acta* **51,** 5334–5340 (2006).
38. Wang, C., Adair, K. & Sun, X. All-Solid-State Lithium Metal Batteries with Sulfide Electrolytes: Understanding Interfacial Ion and Electron Transport. *Acc. Mater. Res.* **3,** 21–32 (2022).
39. Singer, C., Töpper, H.-C., Kutsch, T., Schuster, R., Koerver, R. & Daub, R. Hydrolysis of Argyrodite Sulfide-Based Separator Sheets for Industrial All-Solid-State Battery Production. *ACS Appl. Mater. Interfaces* **14,** 24245–24254 (2022).
40. Ruhl, J., Riegger, L. M., Ghidiu, M. & Zeier, W. G. Impact of Solvent Treatment of the Superionic Argyrodite Li_6PS_5Cl on Solid-State Battery Performance. *Adv Energy Sustain Res* **2,** 2000077 (2021).
41. Koerver, R., Zhang, W., de Biasi, L., Schweidler, S., Kondrakov, A. O., Kolling, S., Brezesinski, T., Hartmann, P., Zeier, W. G. & Janek, J. Chemo-mechanical expansion of lithium electrode materials – on the route to mechanically optimized all-solid-state batteries. *Energy Environ. Sci.* **11,** 2142–2158 (2018).
42. Koerver, R., Dursun, I., Leichtweiß, T., Dietrich, C., Binder, J., Hartmann, P., Zeier, W. G. & Janek, J. Capacity fade in solid-state batteries: Interphase formation and chemo-mechanical processes in nickel-rich layered oxide cathodes and lithium thiophosphate solid electrolytes. *Chemistry of Materials*
43. Walther, F., Koerver, R., Fuchs, T., Ohno, S., Sann, J., Rohnke, M., Zeier, W. G. & Janek, J. Visualization of the Interfacial Decomposition of Composite Cathodes in Argyrodite-Based All-Solid-State Batteries Using Time-of-Flight Secondary-Ion Mass Spectrometry. *Chem. Mater.* **31,** 3745–3755 (2019).
44. Shi, T., Tu, Q., Tian, Y., Xiao, Y., Miara, L. J., Kononova, O. & Ceder, G. High Active Material Loading in All-Solid-State Battery Electrode via Particle Size Optimization. *Advanced Energy Materials* **10,** 1902881 (2020).

45. Zhang, F., Guo, Y., Zhang, L., Jia, P., Liu, X., Qiu, P., Zhang, H. & Huang, J. A review of the effect of external pressure on all-solid-state batteries. *eTransportation* **15,** 100220 (2023).
46. Doux, J.-M., Yang, Y., Tan, D. H. S., Nguyen, H., Wu, E. A., Wang, X., Banerjee, A. & Meng, Y. S. Pressure effects on sulfide electrolytes for all solid-state batteries. *J. Mater. Chem. A* **8,** 5049–5055 (2020).
47. Doux, J.-M., Nguyen, H., Tan, D. H. S., Banerjee, A., Wang, X., Wu, E. A., Jo, C., Yang, H. & Meng, Y. S. Stack Pressure Considerations for Room-Temperature All-Solid-State Lithium Metal Batteries. *Advanced Energy Materials* **10,** 1903253 (2020).
48. Faraday, M. *Experimental Researches in Electricity*. (Taylor and Francis, 1839).
49. Whittingham, M. S. & Huggins, R. A. in **364,** 139–154 (1972).
50. Goodenough, J. B., Hong, H. Y.-P. & Kafalas, J. A. Fast Na+-ion transport in skeleton structures. *Materials Research Bulletin* **11,** 203–220 (1976).
51. Fenton, D. E., Parker, J. M. & Wright, P. V. Complexes of alkali metal ions with poly(ethylene oxide). *Polymer* **14,** 589 (1973).
52. Armand, M. & Duclot, M. Nouveaux matériaux élastomères à conduction ionique. (1980).
53. Kwak, H., Wang, S., Park, J., Liu, Y., Kim, K. T., Choi, Y., Mo, Y. & Jung, Y. S. Emerging Halide Superionic Conductors for All-Solid-State Batteries: Design, Synthesis, and Practical Applications. *ACS Energy Lett.* **7,** 1776–1805 (2022).
54. Aono, H., Sugimoto, E., Sadaoka, Y., Imanaka, N. & Adachi, G. Ionic Conductivity of Solid Electrolytes Based on Lithium Titanium Phosphate. *J. Electrochem. Soc.* **137,** 1023–1027 (1990).
55. Thokchom, J. S., Gupta, N. & Kumar, B. Superionic Conductivity in a Lithium Aluminum Germanium Phosphate Glass–Ceramic. *J. Electrochem. Soc.* **155,** A915 (2008).
56. Inaguma, Y., Liquan, C., Itoh, M., Nakamura, T., Uchida, T., Ikuta, H. & Wakihara, M. High ionic conductivity in lithium lanthanum titanate. *Solid State Communications* **86,** 689–693 (1993).
57. Murugan, R., Thangadurai, V. & Weppner, W. Fast Lithium Ion Conduction in Garnet-Type Li7La3Zr2O12. *Angewandte Chemie International Edition* **46,** 7778–7781 (2007).
58. Wan, T., Zhang, L., Du, H., Lin, X., Qu, B., Xu, H., Li, S. & Chu, D. Recent Developments in Oxide-Based Ionic Conductors: Bulk Materials, Nanoionics, and Their Memory Applications. *Critical Reviews in Solid State and Materials Sciences* **43,** 47–82 (2018).
59. Ren, Y., Chen, K., Chen, R., Liu, T., Zhang, Y. & Nan, C.-W. Oxide Electrolytes for Lithium Batteries. *Journal of the American Ceramic Society* **98,** 3603–3623 (2015).
60. Farzanian, S., Vazquez Mercado, J., Shozib, I., Sivadas, N., Lacivita, V., Wang, Y. & Tu, Q. H. Mechanical Investigations of Composite Cathode Degradation in All-Solid-State Batteries. *ACS Appl. Energy Mater.* **6,** 9615–9623 (2023).
61. Mercier, R., Malugani, J.-P., Fahys, B. & Robert, G. Superionic conduction in Li2S - P2S5 - LiI - glasses. *Solid State Ionics* **5,** 663–666 (1981).
62. Kanno, R., Hata, T., Kawamoto, Y. & Irie, M. Synthesis of a new lithium ionic conductor, thio-LISICON–lithium germanium sulfide system. *Solid State Ionics* **130,** 97–104 (2000).
63. Murayama, M., Kanno, R., Irie, M., Ito, S., Hata, T., Sonoyama, N. & Kawamoto, Y. Synthesis of New Lithium Ionic Conductor Thio-LISICON—Lithium Silicon Sulfides System. *Journal of Solid State Chemistry* **168,** 140–148 (2002).

64. Murayama, M., Sonoyama, N., Yamada, A. & Kanno, R. Material design of new lithium ionic conductor, thio-LISICON, in the Li2S–P2S5 system. *Solid State Ionics* **170,** 173–180 (2004).
65. Kamaya, N., Homma, K., Yamakawa, Y., Hirayama, M., Kanno, R., Yonemura, M., Kamiyama, T., Kato, Y., Hama, S., Kawamoto, K. & Mitsui, A. A lithium superionic conductor. *Nature Mater* **10,** 682–686 (2011).
66. Deiseroth, H.-J., Kong, S.-T., Eckert, H., Vannahme, J., Reiner, C., Zaiß, T. & Schlosser, M. Li6PS5X: A Class of Crystalline Li-Rich Solids With an Unusually High Li+ Mobility. *Angewandte Chemie International Edition* **47,** 755–758 (2008).
67. Adeli, P., Bazak, J. D., Park, K. H., Kochetkov, I., Huq, A., Goward, G. R. & Nazar, L. F. Boosting Solid-State Diffusivity and Conductivity in Lithium Superionic Argyrodites by Halide Substitution. *Angewandte Chemie International Edition* **58,** 8681–8686 (2019).
68. Sakuda, A., Hayashi, A. & Tatsumisago, M. Sulfide Solid Electrolyte with Favorable Mechanical Property for All-Solid-State Lithium Battery. *Sci Rep* **3,** 2261 (2013).
69. Ginnings, D. C. & Phipps, T. E. Temperature-conductance curves of solid salts. III. Halides of lithium. *J. Am. Chem. Soc.* **52,** 1340–1345 (1930).
70. Li, X., Liang, J., Chen, N., Luo, J., Adair, K. R., Wang, C., Banis, M. N., Sham, T.-K., Zhang, L., Zhao, S., Lu, S., Huang, H., Li, R. & Sun, X. Water-Mediated Synthesis of a Superionic Halide Solid Electrolyte. *Angewandte Chemie International Edition* **58,** 16427–16432 (2019).
71. Asano, T., Sakai, A., Ouchi, S., Sakaida, M., Miyazaki, A. & Hasegawa, S. Solid Halide Electrolytes with High Lithium-Ion Conductivity for Application in 4 V Class Bulk-Type All-Solid-State Batteries. *Advanced Materials* **30,** 1803075 (2018).
72. Wang, S., Bai, Q., Nolan, A. M., Liu, Y., Gong, S., Sun, Q. & Mo, Y. Lithium Chlorides and Bromides as Promising Solid-State Chemistries for Fast Ion Conductors with Good Electrochemical Stability. *Angewandte Chemie International Edition* **58,** 8039–8043 (2019).
73. Hennequart, B., Platonova, M., Chometon, R., Marchandier, T., Benedetto, A., Quemin, E., Dugas, R., Lethien, C. & Tarascon, J.-M. Atmospheric-Pressure Operation of All-Solid-State Batteries Enabled by Halide Solid Electrolyte. *ACS Energy Lett.* 454–460 (2024). doi:10.1021/acsenergylett.3c02513
74. Wang, S., Xu, X., Cui, C., Zeng, C., Liang, J., Fu, J., Zhang, R., Zhai, T. & Li, H. Air Sensitivity and Degradation Evolution of Halide Solid State Electrolytes upon Exposure. *Advanced Functional Materials* **32,** 2108805 (2022).
75. Armand, M. & Moursli, F. Bisperhaloacyl or bisperhalosulfonyl imides of alkali metals, their solid solutions with polymers, and their use as battery electrolytes. (1983).
76. Capuano, F., Croce, F. & Scrosati, B. Composite Polymer Electrolytes. *J. Electrochem. Soc.* **138,** 1918–1922 (1991).
77. Xue, Z., He, D. & Xie, X. Poly(ethylene oxide)-based electrolytes for lithium-ion batteries. *J. Mater. Chem. A* **3,** 19218–19253 (2015).
78. Aldalur, I., Zhang, H., Piszcz, M., Oteo, U., Rodriguez-Martinez, L. M., Shanmukaraj, D., Rojo, T. & Armand, M. Jeffamine® based polymers as highly conductive polymer electrolytes and cathode binder materials for battery application. *Journal of Power Sources* **347,** 37–46 (2017).
79. Stolz, L., Hochstädt, S., Röser, S., Hansen, M. R., Winter, M. & Kasnatscheew, J. Single-Ion *versus* Dual-Ion Conducting Electrolytes: The Relevance of Concentration

Polarization in Solid-State Batteries. *ACS Appl. Mater. Interfaces* acsami.2c00084 (2022). doi:10.1021/acsami.2c00084

80. Zhang, H., Oteo, U., Zhu, H., Judez, X., Martinez-Ibañez, M., Aldalur, I., Sanchez-Diez, E., Li, C., Carrasco, J., Forsyth, M. & Armand, M. Enhanced Lithium-Ion Conductivity of Polymer Electrolytes by Selective Introduction of Hydrogen into the Anion. *Angewandte Chemie International Edition* **58,** 7829–7834 (2019).
81. Technologie de batteries - Bollore - Blue Solutions. at <https://www.blue-solutions.com/technologie-de-batteries/>
82. Bi, S., Sun, C.-N., Zawodzinski Jr., T. A., Ren, F., Keum, J. K., Ahn, S.-K., Li, D. & Chen, J. Reciprocated suppression of polymer crystallization toward improved solid polymer electrolytes: Higher ion conductivity and tunable mechanical properties. *Journal of Polymer Science Part B: Polymer Physics* **53,** 1450–1457 (2015).
83. Edman, L., Doeff, M. M., Ferry, A., Kerr, J. & De Jonghe, L. C. Transport Properties of the Solid Polymer Electrolyte System P(EO)nLiTFSI. *J. Phys. Chem. B* **104,** 3476–3480 (2000).
84. Zhou, L., Minafra, N., Zeier, W. G. & Nazar, L. F. Innovative Approaches to Li-Argyrodite Solid Electrolytes for All-Solid-State Lithium Batteries. *Acc. Chem. Res.* **54,** 2717–2728 (2021).
85. Li, C., Zhang, S., Miao, X., Wang, C., Wang, C., Zhang, Z., Wang, R. & Yin, L. Designing Lithium Argyrodite Solid-State Electrolytes for High-Performance All-Solid-State Lithium Batteries. *Batteries & Supercaps* **5,** e202100288 (2022).
86. Samara, G. A. in *Solid State Physics* **38,** 1–80 (Elsevier, 1984).
87. Hanghofer, I., Brinek, M., Eisbacher, S. L., Bitschnau, B., Volck, M., Hennige, V., Hanzu, I., Rettenwander, D. & Wilkening, H. M. R. Substitutional disorder: structure and ion dynamics of the argyrodites Li_6PS_5Cl, Li_6PS_5Br and Li_6PS_5I. *Phys. Chem. Chem. Phys.* **21,** 8489–8507 (2019).
88. Simon, F. J., Hanauer, M., Richter, F. H. & Janek, J. Interphase Formation of PEO_{20}:LiTFSI–Li_6PS_5Cl Composite Electrolytes with Lithium Metal. *ACS Appl. Mater. Interfaces* **12,** 11713–11723 (2020).
89. Ratner, M. A. & Shriver, D. F. Ion transport in solvent-free polymers. *Chem. Rev.* **88,** 109–124 (1988).
90. Stolz, L., Röser, S., Homann, G., Winter, M. & Kasnatscheew, J. Pragmatic Approaches to Correlate between the Physicochemical Properties of a Linear Poly(ethylene oxide)-Based Solid Polymer Electrolyte and the Performance in a High-Voltage Li-Metal Battery. *J. Phys. Chem. C* acs.jpcc.1c03614 (2021). doi:10.1021/acs.jpcc.1c03614
91. Vogel, D. H. Das Temperaturabhaengigkeitsgesetz der Viskositaet von Fluessigkeiten. *Phys. Z.* **22,** 645 (1921).
92. Fulcher, G. S. Analysis of recent measurements of the viscosity of glasses. *J American Ceramic Society* **8,** 339–355 (1925).
93. Tammann, G. & Hesse, W. Die Abhängigkeit der Viscosität von der Temperatur bie unterkühlten Flüssigkeiten. *Z. Anorg. Allg. Chem.* **156,** 245–257 (1926).
94. MacCallum, J. R. & Vincent, C. A. *Polymer Electrolyte Reviews*. (Springer Science & Business Media, 1989).
95. Devaux, D., Bouchet, R., Glé, D. & Denoyel, R. Mechanism of ion transport in PEO/LiTFSI complexes: Effect of temperature, molecular weight and end groups. *Solid State Ionics* **227,** 119–127 (2012).
96. Janek, J. & Zeier, W. G. Challenges in speeding up solid-state battery development. *Nat Energy* **8,** 230–240 (2023).

97. Zhu, Y., He, X. & Mo, Y. Origin of Outstanding Stability in the Lithium Solid Electrolyte Materials: Insights from Thermodynamic Analyses Based on First-Principles Calculations. *ACS Appl. Mater. Interfaces* **7,** 23685–23693 (2015).
98. Tan, D. H. S., Wu, E. A., Nguyen, H., Chen, Z., Marple, M. A. T., Doux, J.-M., Wang, X., Yang, H., Banerjee, A. & Meng, Y. S. Elucidating Reversible Electrochemical Redox of Li_6PS_5Cl Solid Electrolyte. *ACS Energy Lett.* **4,** 2418–2427 (2019).
99. Wenzel, S., Sedlmaier, S. J., Dietrich, C., Zeier, W. G. & Janek, J. Interfacial reactivity and interphase growth of argyrodite solid electrolytes at lithium metal electrodes. *Solid State Ionics* **318,** 102–112 (2018).
100. Homann, G., Stolz, L., Nair, J., Laskovic, I. C., Winter, M. & Kasnatscheew, J. Poly(Ethylene Oxide)-based Electrolyte for Solid-State-Lithium-Batteries with High Voltage Positive Electrodes: Evaluating the Role of Electrolyte Oxidation in Rapid Cell Failure. *Scientific Reports* **10,** 4390 (2020).
101. W. Andersson, E. K., Sångeland, C., Berggren, E., L. Johansson, F. O., Kühn, D., Lindblad, A., Mindemark, J. & Hahlin, M. Early-stage decomposition of solid polymer electrolytes in Li-metal batteries. *Journal of Materials Chemistry A* **9,** 22462–22471 (2021).
102. Nie, K., Wang, X., Qiu, J., Wang, Y., Yang, Q., Xu, J., Yu, X., Li, H., Huang, X. & Chen, L. Increasing Poly(ethylene oxide) Stability to 4.5 V by Surface Coating of the Cathode. *ACS Energy Lett.* **5,** 826–832 (2020).
103. Faucher, J. A., Koleske, J. V., Santee, E. R., Stratta, J. J. & Wilson, C. W. Glass Transitions of Ethylene Oxide Polymers. *Journal of Applied Physics* **37,** 3962–3964 (1966).
104. Homann, G., Stolz, L., Winter, M. & Kasnatscheew, J. Elimination of "Voltage Noise" of Poly (Ethylene Oxide)-Based Solid Electrolytes in High-Voltage Lithium Batteries: Linear versus Network Polymers. *iScience* **23,** 101225 (2020).
105. Dolle, M., Sannier, L., Beaudoin, B., Trentin, M. & Tarascon, J.-M. Live Scanning Electron Microscope Observations of Dendritic Growth in LithiumÕPolymer Cells. 4
106. Liu, X., Garcia-Mendez, R., Lupini, A. R., Cheng, Y., Hood, Z. D., Han, F., Sharafi, A., Idrobo, J. C., Dudney, N. J., Wang, C., Ma, C., Sakamoto, J. & Chi, M. Local electronic structure variation resulting in Li 'filament' formation within solid electrolytes. *Nat. Mater.* **20,** 1485–1490 (2021).
107. Deng, Z., Wang, Z., Chu, I.-H., Luo, J. & Ong, S. P. Elastic Properties of Alkali Superionic Conductor Electrolytes from First Principles Calculations. *J. Electrochem. Soc.* **163,** A67–A74 (2016).
108. Lopez, J., Sun, Y., Mackanic, D. G., Lee, M., Foudeh, A. M., Song, M., Cui, Y. & Bao, Z. A Dual-Crosslinking Design for Resilient Lithium-Ion Conductors. *Adv. Mater.* **30,** 1804142 (2018).
109. Ning, Z., Li, G., Melvin, D. L. R., Chen, Y., Bu, J., Spencer-Jolly, D., Liu, J., Hu, B., Gao, X., Perera, J., Gong, C., Pu, S. D., Zhang, S., Liu, B., Hartley, G. O., Bodey, A. J., Todd, R. I., Grant, P. S., Armstrong, D. E. J., Marrow, T. J., Monroe, C. W. & Bruce, P. G. Dendrite initiation and propagation in lithium metal solid-state batteries. *Nature* **618,** 287–293 (2023).
110. Croce, F., Curini, R., Martinelli, A., Persi, L., Ronci, F., Scrosati, B. & Caminiti, R. Physical and Chemical Properties of Nanocomposite Polymer Electrolytes. *J. Phys. Chem. B* **103,** 10632–10638 (1999).
111. Fan, L.-Z., He, H. & Nan, C.-W. Tailoring inorganic–polymer composites for the mass production of solid-state batteries. *Nat Rev Mater* (2021). doi:10.1038/s41578-021-00320-0

112. Croce, F., Persi, L., Scrosati, B., Serraino-Fiory, F., Plichta, E. & Hendrickson, M. A. Role of the ceramic fillers in enhancing the transport properties of composite polymer electrolytes. *Electrochimica Acta* **46,** 2457–2461 (2001).
113. Simon, F. J., Hanauer, M., Henss, A., Richter, F. H. & Janek, J. Properties of the Interphase Formed between Argyrodite-Type Li_6PS_5Cl and Polymer-Based PEO_{10}:LiTFSI. *ACS Appl. Mater. Interfaces* **11,** 42186–42196 (2019).
114. Weiss, M., Simon, F. J., Busche, M. R., Nakamura, T., Schröder, D., Richter, F. H. & Janek, J. From Liquid- to Solid-State Batteries: Ion Transfer Kinetics of Heteroionic Interfaces. *Electrochem. Energ. Rev.* **3,** 221–238 (2020).
115. Mankovsky, D., Lepage, D., Lachal, M., Caradant, L., Aymé-Perrot, D. & Dollé, M. Water content in solid polymer electrolytes: the lost knowledge. *Chem. Commun.* **56,** 10167–10170 (2020).
116. Foran, G., Mankovsky, D., Verdier, N., Lepage, D., Prébé, A., Aymé-Perrot, D. & Dollé, M. The Impact of Absorbed Solvent on the Performance of Solid Polymer Electrolytes for Use in Solid-State Lithium Batteries. *iScience* **23,** 101597 (2020).
117. Horowitz, Y., Lifshitz, M., Greenbaum, A., Feldman, Y., Greenbaum, S., Sokolov, A. P. & Golodnitsky, D. Review—Polymer/Ceramic Interface Barriers: The Fundamental Challenge for Advancing Composite Solid Electrolytes for Li-Ion Batteries. *J. Electrochem. Soc.* **167,** 160514 (2020).
118. Jung, Y.-C., Lee, S.-M., Choi, J.-H., Jang, S. S. & Kim, D.-W. All Solid-State Lithium Batteries Assembled with Hybrid Solid Electrolytes. *J. Electrochem. Soc.* **162,** A704–A710 (2015).
119. Keller, M., Appetecchi, G. B., Kim, G.-T., Sharova, V., Schneider, M., Schuhmacher, J., Roters, A. & Passerini, S. Electrochemical performance of a solvent-free hybrid ceramic-polymer electrolyte based on Li7La3Zr2O12 in P(EO)15LiTFSI. *Journal of Power Sources* **353,** 287–297 (2017).
120. Langer, F., Bardenhagen, I., Glenneberg, J. & Kun, R. Microstructure and temperature dependent lithium ion transport of ceramic–polymer composite electrolyte for solid-state lithium ion batteries based on garnet-type Li7La3Zr2O12. *Solid State Ionics* **291,** 8–13 (2016).
121. Zheng, J., Tang, M. & Hu, Y. Lithium Ion Pathway within $Li_7La_3Zr_2O_{12}$-Polyethylene Oxide Composite Electrolytes. *Angew. Chem. Int. Ed.* **55,** 12538–12542 (2016).
122. Zheng, J., Wang, P., Liu, H. & Hu, Y.-Y. Interface-Enabled Ion Conduction in $Li_{10}GeP_2S_{12}$–Poly(ethylene Oxide) Hybrid Electrolytes. *ACS Appl. Energy Mater.* **2,** 1452–1459 (2019).
123. Liu, M., Cheng, Z., Ganapathy, S., Wang, C., Haverkate, L. A., Tułodziecki, M., Unnikrishnan, S. & Wagemaker, M. Tandem Interface and Bulk Li-Ion Transport in a Hybrid Solid Electrolyte with Microsized Active Filler. *ACS Energy Lett.* **4,** 2336–2342 (2019).
124. Roman, H. E. A continuum percolation model for dispersed ionic conductors. *J. Phys.: Condens. Matter* **2,** 3909–3917 (1990).
125. Liu, M., Zhang, S., van Eck, E. R. H., Wang, C., Ganapathy, S. & Wagemaker, M. Improving Li-ion interfacial transport in hybrid solid electrolytes. *Nat. Nanotechnol.* **17,** 959–967 (2022).
126. Chen, Y.-T., Marple, M. A. T., Tan, D. H. S., Ham, S.-Y., Sayahpour, B., Li, W.-K., Yang, H., Lee, J. B., Hah, H. J., Wu, E. A., Doux, J.-M., Jang, J., Ridley, P., Cronk, A., Deysher, G.,

Chen, Z. & Meng, Y. S. Investigating dry room compatibility of sulfide solid-state electrolytes for scalable manufacturing. *J. Mater. Chem. A* **10,** 7155–7164 (2022).

127. BAuA - Technical Rules - Technical Rules for Hazardous Substances (TRGS) - Federal Institute for Occupational Safety and Health. at <https://www.baua.de/EN/Service/Technical-rules/TRGS/TRGS.html>
128. Sulfure d'hydrogène (FT 32). Généralités - Fiche toxicologique - INRS. at <https://www.inrs.fr/publications/bdd/fichetox/fiche.html?refINRS=FICHETOX_32>
129. Kim, K. T., Woo, J., Kim, Y.-S., Sung, S., Park, C., Lee, C., Park, Y. J., Lee, H.-W., Park, K. & Jung, Y. S. Ultrathin Superhydrophobic Coatings for Air-Stable Inorganic Solid Electrolytes: Toward Dry Room Application for All-Solid-State Batteries. *Advanced Energy Materials* **13,** 2301600 (2023).
130. Hood, Z. D., Mane, A. U., Sundar, A., Tepavcevic, S., Zapol, P., Eze, U. D., Adhikari, S. P., Lee, E., Sterbinsky, G. E., Elam, J. W. & Connell, J. G. Multifunctional Coatings on Sulfide-Based Solid Electrolyte Powders with Enhanced Processability, Stability, and Performance for Solid-State Batteries. *Advanced Materials* **35,** 2300673 (2023).
131. Zhang, X., Li, X., Weng, S., Wu, S., Liu, Q., Cao, M., Li, Y., Wang, Z., Zhu, L., Xiao, R., Su, D., Yu, X., Li, H., Chen, L., Wang, Z. & Wang, X. Spontaneous gas–solid reaction on sulfide electrolytes for high-performance all-solid-state batteries. *Energy Environ. Sci.* **16,** 1091–1099 (2023).
132. Randau, S., Weber, D. A., Kötz, O., Koerver, R., Braun, P., Weber, A., Ivers-Tiffée, E., Adermann, T., Kulisch, J., Zeier, W. G., Richter, F. H. & Janek, J. Benchmarking the performance of all-solid-state lithium batteries. *Nat Energy* **5,** 259–270 (2020).
133. Doerrer, C., Capone, I., Narayanan, S., Liu, J., Grovenor, C. R. M., Pasta, M. & Grant, P. S. High Energy Density Single-Crystal NMC/Li_6PS_5Cl Cathodes for All-Solid-State Lithium-Metal Batteries. *ACS Appl. Mater. Interfaces* **13,** 37809–37815 (2021).
134. Bielefeld, A., Weber, D. A. & Janek, J. Modeling Effective Ionic Conductivity and Binder Influence in Composite Cathodes for All-Solid-State Batteries. *ACS Appl. Mater. Interfaces* **12,** 12821–12833 (2020).
135. Kim, S. Y., Cha, H., Kostecki, R. & Chen, G. Composite Cathode Design for High-Energy All-Solid-State Lithium Batteries with Long Cycle Life. *ACS Energy Lett.* **8,** 521–528 (2023).
136. Cronau, M., Duchardt, M., Szabo, M. & Roling, B. Ionic Conductivity versus Particle Size of Ball-Milled Sulfide-Based Solid Electrolytes: Strategy Towards Optimized Composite Cathode Performance in All-Solid-State Batteries. *Batteries & Supercaps* **5,** e202200041 (2022).
137. Kim, J., Kim, M. J., Kim, J., Lee, J. W., Park, J., Wang, S. E., Lee, S., Kang, Y. C., Paik, U., Jung, D. S. & Song, T. High-Performance All-Solid-State Batteries Enabled by Intimate Interfacial Contact Between the Cathode and Sulfide-Based Solid Electrolytes. *Adv Funct Materials* 2211355 (2023). doi:10.1002/adfm.202211355
138. Lee, J., Lee, T., Char, K., Kim, K. J. & Choi, J. W. Issues and Advances in Scaling up Sulfide-Based All-Solid-State Batteries. *Acc. Chem. Res.* **54,** 3390–3402 (2021).
139. Hippauf, F., Schumm, B., Doerfler, S., Althues, H., Fujiki, S., Shiratsuchi, T., Tsujimura, T., Aihara, Y. & Kaskel, S. Overcoming binder limitations of sheet-type solid-state cathodes using a solvent-free dry-film approach. *Energy Storage Materials* **21,** 390–398 (2019).
140. Lee, D. J., Jang, J., Lee, J., Wu, J., Chen, Y., Holoubek, J., Yu, K., Ham, S., Jeon, Y., Kim, T., Lee, J. B., Song, M., Meng, Y. S. & Chen, Z. Physio-Electrochemically Durable Dry-

Processed Solid-State Electrolyte Films for All-Solid-State Batteries. *Adv Funct Materials* **33,** 2301341 (2023).

141. Oh, D. Y., Kim, K. T., Jung, S. H., Kim, D. H., Jun, S., Jeoung, S., Moon, H. R. & Jung, Y. S. Tactical hybrids of Li+-conductive dry polymer electrolytes with sulfide solid electrolytes: Toward practical all-solid-state batteries with wider temperature operability. *Materials Today* **53,** 7–15 (2022).
142. Nam, Y. J., Cho, S.-J., Oh, D. Y., Lim, J.-M., Kim, S. Y., Song, J. H., Lee, Y.-G., Lee, S.-Y. & Jung, Y. S. Bendable and Thin Sulfide Solid Electrolyte Film: A New Electrolyte Opportunity for Free-Standing and Stackable High-Energy All-Solid-State Lithium-Ion Batteries. *Nano Lett.* **15,** 3317–3323 (2015).
143. Song, Y. B., Baeck, K. H., Kwak, H., Lim, H. & Jung, Y. S. Dimensional Strategies for Bridging the Research Gap between Lab-Scale and Potentially Practical All-Solid-State Batteries: The Role of Sulfide Solid Electrolyte Films. *Advanced Energy Materials* **13,** 2301142 (2023).
144. Krauskopf, T., Richter, F. H., Zeier, W. G. & Janek, J. Physicochemical Concepts of the Lithium Metal Anode in Solid-State Batteries. *Chem. Rev.* **120,** 7745–7794 (2020).
145. Markowitz, M. M. & Boryta, D. A. Lithium Metal-Gas Reactions. *J. Chem. Eng. Data* **7,** 586–591 (1962).
146. Li, Y., Li, Y., Sun, Y., Butz, B., Yan, K., Koh, A. L., Zhao, J., Pei, A. & Cui, Y. Revealing Nanoscale Passivation and Corrosion Mechanisms of Reactive Battery Materials in Gas Environments. *Nano Lett.* **17,** 5171–5178 (2017).
147. Tan, D. H. S., Chen, Y.-T., Yang, H., Sreenarayanan, B., Doux, J.-M., Li, W., Lu, B., Ham, S.-Y., Sayahpour, B., Wu, E. A., Deysher, G., Han, H. E., Hah, H. J., Jeong, H. & Meng, Y. S. Carbon Free High Loading Silicon Anodes Enabled by Sulfide Solid Electrolytes for Robust All Solid-State Batteries. 13
148. Santhosha, A. L., Medenbach, L., Buchheim, J. R. & Adelhelm, P. The Indium–Lithium Electrode in Solid-State Lithium-Ion Batteries: Phase Formation, Redox Potentials, and Interface Stability. *Batteries & Supercaps* **2,** 524–529 (2019).
149. Kato, A., Suyama, M., Hotehama, C., Kowada, H., Sakuda, A., Hayashi, A. & Tatsumisago, M. High-Temperature Performance of All-Solid-State Lithium-Metal Batteries Having Li/Li $_3$ PS $_4$ Interfaces Modified with Au Thin Films. *J. Electrochem. Soc.* **165,** A1950–A1954 (2018).
150. Sang, L., Bassett, K. L., Castro, F. C., Young, M. J., Chen, L., Haasch, R. T., Elam, J. W., Dravid, V. P., Nuzzo, R. G. & Gewirth, A. A. Understanding the Effect of Interlayers at the Thiophosphate Solid Electrolyte/Lithium Interface for All-Solid-State Li Batteries. *Chem. Mater.* **30,** 8747–8756 (2018).
151. Hou, G., Ma, X., Sun, Q., Ai, Q., Xu, X., Chen, L., Li, D., Chen, J., Zhong, H., Li, Y., Xu, Z., Si, P., Feng, J., Zhang, L., Ding, F. & Ci, L. Lithium Dendrite Suppression and Enhanced Interfacial Compatibility Enabled by an Ex Situ SEI on Li Anode for LAGP-Based All-Solid-State Batteries. *ACS Appl. Mater. Interfaces* **10,** 18610–18618 (2018).
152. Davis, A. L., Garcia-Mendez, R., Wood, K. N., Kazyak, E., Chen, K.-H., Teeter, G., Sakamoto, J. & Dasgupta, N. P. Electro-chemo-mechanical evolution of sulfide solid electrolyte/Li metal interfaces: operando analysis and ALD interlayer effects. *J. Mater. Chem. A* **8,** 6291–6302 (2020).
153. Ates, T., Keller, M., Kulisch, J., Adermann, T. & Passerini, S. Development of an all-solid-state lithium battery by slurry-coating procedures using a sulfidic electrolyte. *Energy Storage Materials* **17,** 204–210 (2019).

154. Deng, S., Sun, Y., Li, X., Ren, Z., Liang, J., Doyle-Davis, K., Liang, J., Li, W., Norouzi Banis, M., Sun, Q., Li, R., Hu, Y., Huang, H., Zhang, L., Lu, S., Luo, J. & Sun, X. Eliminating the Detrimental Effects of Conductive Agents in Sulfide-Based Solid-State Batteries. *ACS Energy Lett.* **5,** 1243–1251 (2020).
155. Frith, J. T., Lacey, M. J. & Ulissi, U. A non-academic perspective on the future of lithium-based batteries. *Nat Commun* **14,** 420 (2023).
156. Vanleeuw, D., Sapundjiev, D., Sibbens, G., Oberstedt, S. & Salvador Castiñeira, P. Physical vapour deposition of metallic lithium. *J Radioanal Nucl Chem* **299,** 1113–1120 (2014).
157. Schönherr, K., Schumm, B., Hippauf, F., Lissy, R., Althues, H., Leyens, C. & Kaskel, S. Liquid lithium metal processing into ultrathin metal anodes for solid state batteries. *Chemical Engineering Journal Advances* **9,** 100218 (2022).
158. The Role of Isostatic Pressing in Large-Scale Production of Solid-State Batteries. doi:10.1021/acsenergylett.2c01936
159. Tan, D. H. S., Meng, Y. S. & Jang, J. Scaling up high-energy-density sulfidic solid-state batteries: A lab-to-pilot perspective. *Joule* **6,** 1755–1769 (2022).
160. Lee, Y.-G., Fujiki, S., Jung, C., Suzuki, N., Yashiro, N., Omoda, R., Ko, D.-S., Shiratsuchi, T., Sugimoto, T., Ryu, S., Ku, J. H., Watanabe, T., Park, Y., Aihara, Y., Im, D. & Han, I. T. High-energy long-cycling all-solid-state lithium metal batteries enabled by silver–carbon composite anodes. *Nat Energy* **5,** 299–308 (2020).
161. Zhou, L., Zuo, T.-T., Kwok, C. Y., Kim, S. Y., Assoud, A., Zhang, Q., Janek, J. & Nazar, L. F. High areal capacity, long cycle life 4 V ceramic all-solid-state Li-ion batteries enabled by chloride solid electrolytes. *Nat Energy* **7,** 83–93 (2022).
162. Kim, K. T., Kwon, T. Y., Song, Y. B., Kim, S.-M., Byun, S. C., Min, H.-S., Kim, S. H. & Jung, Y. S. Wet-slurry fabrication using PVdF-HFP binder with sulfide electrolytes via synergetic cosolvent approach for all-solid-state batteries. *Chemical Engineering Journal* **450,** 138047 (2022).
163. Keller, M., Varzi, A. & Passerini, S. Hybrid electrolytes for lithium metal batteries. *Journal of Power Sources* **392,** 206–225 (2018).
164. Verdier, N., Foran, G., Lepage, D., Prébé, A., Aymé-Perrot, D. & Dollé, M. Challenges in Solvent-Free Methods for Manufacturing Electrodes and Electrolytes for Lithium-Based Batteries. *Polymers* **13,** 323 (2021).
165. Comer, A. C., Kalika, D. S., Kusuma, V. A. & Freeman, B. D. Glass-transition and gas-transport characteristics of polymer nanocomposites based on crosslinked poly(ethylene oxide). *Journal of Applied Polymer Science* **117,** 2395–2405 (2010).
166. Jee, A.-Y., Lee, H., Lee, Y. & Lee, M. Determination of the elastic modulus of poly(ethylene oxide) using a photoisomerizing dye. *Chemical Physics* **422,** 246–250 (2013).
167. Li, M., Kolek, M., Frerichs, J. E., Sun, W., Hou, X., Hansen, M. R., Winter, M. & Bieker, P. Investigation of Polymer/Ceramic Composite Solid Electrolyte System: The Case of PEO/LGPS Composite Electrolytes. *ACS Sustainable Chem. Eng.* **9,** 11314–11322 (2021).
168. Marzantowicz, M., Dygas, J. R. & Krok, F. Impedance of interface between PEO:LiTFSI polymer electrolyte and blocking electrodes. *Electrochimica Acta* **53,** 7417–7425 (2008).
169. Huynh, T. V., Messinger, R. J., Sarou-Kanian, V., Fayon, F., Bouchet, R. & Deschamps, M. Restricted lithium ion dynamics in PEO-based block copolymer electrolytes measured by high-field nuclear magnetic resonance relaxation. *The Journal of Chemical Physics* **147,** 134902 (2017).

170. Scholz, E. *Karl Fischer Titration: Determination of Water*. (Springer Science & Business Media, 2012).
171. Lee, J., Howell, T., Rottmayer, M., Boeckl, J. & Huang, H. Free-Standing PEO/LiTFSI/LAGP Composite Electrolyte Membranes for Applications to Flexible Solid-State Lithium-Based Batteries. *J. Electrochem. Soc.* **166,** A416–A422 (2019).
172. Lu, Y., Zhao, C.-Z., Yuan, H., Cheng, X.-B., Huang, J.-Q. & Zhang, Q. Critical Current Density in Solid-State Lithium Metal Batteries: Mechanism, Influences, and Strategies. *Advanced Functional Materials* **31,** 2009925 (2021).
173. Fuchs, T., Haslam, C. G., Richter, F. H., Sakamoto, J. & Janek, J. Evaluating the Use of Critical Current Density Tests of Symmetric Lithium Transference Cells with Solid Electrolytes. *Advanced Energy Materials* **n/a,** 2302383
174. Huo, H., Jiang, M., Mogwitz, B., Sann, J., Yusim, Y., Zuo, T., Moryson, Y., Minnmann, P., Richter, F. H., Veer Singh, C. & Janek, J. Interface Design Enabling Stable Polymer/Thiophosphate Electrolyte Separators for Dendrite-Free Lithium Metal Batteries. *Angew Chem Int Ed* (2023). doi:10.1002/anie.202218044
175. PubChem. Ethyl Acetate. at <https://pubchem.ncbi.nlm.nih.gov/compound/8857>
176. PubChem. Butyl butyrate. at <https://pubchem.ncbi.nlm.nih.gov/compound/7983>
177. PubChem. Hexyl butyrate. at <https://pubchem.ncbi.nlm.nih.gov/compound/17525>
178. Yuan, D., Li, Z., Thitsartarn, W., Fan, X., Sun, J., Li, H. & He, C. β phase PVDF-hfp induced by mesoporous SiO2 nanorods: synthesis and formation mechanism. *J. Mater. Chem. C* **3,** 3708–3713 (2015).
179. Kumar, D., Dolui, S., Banerjee, S. & Ameduri, B. in *Thermoplastic Elastomers* (ed. N. Singha, S. J.) sous presse (Elsevier, 2023). doi:10.1016/B978-0-323-91758-2.00010-6
180. Schlautmann, E., Weiß, A., Maus, O., Ketter, L., Rana, M., Puls, S., Nickel, V., Gabbey, C., Hartnig, C., Bielefeld, A. & Zeier, W. G. Impact of the Solid Electrolyte Particle Size Distribution in Sulfide-Based Solid-State Battery Composites. *Advanced Energy Materials* 2302309 (2023). doi:10.1002/aenm.202302309
181. Quemin, E., Dugas, R., Koç, T., Hennequart, B., Chometon, R. & Tarascon, J.-M. Decoupling Parasitic Reactions at the Positive Electrode Interfaces in Argyrodite-Based Systems. *ACS Appl. Mater. Interfaces* acsami.2c13150 (2022). doi:10.1021/acsami.2c13150
182. Dugas, R., Dupraz, Y., Quemin, E., Koç, T. & Tarascon, J.-M. Engineered Three-Electrode Cells for Improving Solid State Batteries. *J. Electrochem. Soc.* **168,** 090508 (2021).
183. Dixit, M. B., Regala, M., Shen, F., Xiao, X. & Hatzell, K. B. Tortuosity Effects in Garnet-Type Li7La3Zr2O12 Solid Electrolytes. *ACS Appl. Mater. Interfaces* **11,** 2022–2030 (2019).
184. Huo, H. & Janek, J. Silicon as Emerging Anode in Solid-State Batteries. *ACS Energy Lett.* **7,** 4005–4016 (2022).
185. Oh, J., Choi, S. H., Kim, J. Y., Lee, J., Lee, T., Lee, N., Lee, T., Sohn, Y., Chung, W. J., Bae, K. Y., Son, S. & Choi, J. W. Anode-Less All-Solid-State Batteries Operating at Room Temperature and Low Pressure. *Advanced Energy Materials* **13,** 2301508 (2023).
186. Wan, H., Wang, Z., Zhang, W., He, X. & Wang, C. Interface design for all-solid-state lithium batteries. *Nature* **623,** 739–744 (2023).
187. Gao, Q., Wu, D., Zhu, X., Lu, P., Ma, T., Yang, M., Chen, L., Li, H. & Wu, F. Dendrite-free lithium-metal all-solid-state batteries by solid-phase passivation. *Nano Energy* **117,** 108922 (2023).

188. Huo, H., Chen, Y., Li, R., Zhao, N., Luo, J., Silva, J. G. P. da, Mücke, R., Kaghazchi, P., Guo, X. & Sun, X. Design of a mixed conductive garnet/Li interface for dendrite-free solid lithium metal batteries. *Energy Environ. Sci.* **13,** 127–134 (2020).
189. Lee, J., Choi, S. H., Im, G., Lee, K.-J., Lee, T., Oh, J., Lee, N., Kim, H., Kim, Y., Lee, S. & Choi, J. W. Room-Temperature Anode-Less All-Solid-State Batteries via the Conversion Reaction of Metal Fluorides. *Advanced Materials* **34,** 2203580 (2022).

Exploring the role of polymers in scaling up the manufacturing of solid-state batteries

Abstract: The imperative transition toward renewable energy sources and the ongoing electrification of transportation position battery technologies at the forefront of this transformation. While the lithium-ion technology is already well-established, the quest for higher energy density has drawn significant attention to the emerging solid-state batteries (SSBs). Their working principle is based on ion and electron transfers through solid-solid contacts, which are complex to master and sustain, giving rise to most of the challenges associated with their realisation. Especially, the capability to scale up SSBs' fabrication process is critical for future implementation and calls for a shift from pellet-type to sheet-type assembly. Thus, this doctoral research delved into the role of polymers in facilitating this transition by exploring two strategies differing on the binder's ability to conduct lithium ions. In the first approach, we capitalised on the polymer electrolyte PEO:LiTFSI favourable mechanical properties to prepare self-standing films of hybrid solid electrolyte with a high content of Li_6PS_5Cl, using a dry process. However, the instability between the organic and inorganic phases resulted in a resistive interphase that prevents a shared conduction mechanism within the hybrid. After that, we pursued a simpler approach to fabricate self-standing SSBs by employing a conventional non-conductive binder, PVDF-HFP, and using a slurry-based tape casting process. The thorough optimisation of the formulation and preparation of the electrodes and solid-state separators gave promising results, closely approaching the electrochemical performance of binder-free reference SSBs, even under low operating pressure. The reliability of our fabrication process thus paves the way for assembling self-standing solid-state full cells, integrating high energy density anodes such as lithium metal.

Keywords: Solid-state batteries, hybrid electrolyte, argyrodite, tape casting, low pressure, interfaces

Le rôle des polymères dans les batteries tout-solide et leur mise à l'échelle

Résumé : Dans un contexte de transition vers les énergies renouvelables et d'électrification de la mobilité, les batteries sont un rouage indispensable à cette transformation. Alors que la technologie lithium-ion est aujourd'hui largement établie, la course à la performance en matière de densité d'énergie mise sur les batteries tout-solide, encore à l'état de prototype. Elles sont basées sur le principe du transfert de charge au travers de contacts purement solides, complexes à former et à maintenir, et donc sources de nombreux problèmes associés à leur fonctionnement. La mise à l'échelle des procédés de fabrication des batteries tout-solide est particulièrement critique et nécessite un changement de stratégie d'assemblage, en abandonnant le format en pastille pour tendre vers un montage en feuillets. Dans ce contexte, nos travaux de recherche ont porté sur le rôle des polymères dans l'adaptation du procédé d'assemblage, en tant que liant des particules inorganiques. Nous avons exploré deux stratégies qui se distinguent par rapport à la nature de ce liant, pouvant être conducteur ou non des ions lithium. Dans une première approche, l'électrolyte polymère PEO:LiTFSI a été utilisé pour préparer des films autosupportés d'électrolyte hybride à haut taux de charges inorganiques Li_6PS_5Cl, suivant un procédé à sec. L'instabilité des deux électrolytes en contact génère cependant une interphase trop résistive pour assurer une conduction ionique conjointe au sein de l'hybride. Dans un souci de simplification du système, une nouvelle approche a été adoptée, se basant sur un liant non conducteur, le PVDF-HFP, pour la préparation et le coulage en bande d'une encre afin d'obtenir des films d'électrodes et de séparateurs. Une optimisation minutieuse des paramètres a permis d'obtenir des résultats encourageants puisque que proches du système de référence ne contenant pas de liant, et ce même à basse pression de cyclage. La fiabilité du procédé développé au cours de cette thèse ouvre maintenant la voie vers l'assemblage de cellules tout-solide complètes, intégrant une anode à haute densité d'énergie telle que le lithium métal.

Mots-clés : Batteries tout-solide, électrolyte hybride, argyrodite, coulage en bande, basse pression, interfaces